



Gas-Solid Heat Exchanger for Cement Production

Maarup, Claus; Dam-Johansen, Kim; Clement, Karsten; Hjuler, Klaus

Publication date:
2013

Document Version
Publisher's PDF, also known as Version of record

[Link back to DTU Orbit](#)

Citation (APA):

Maarup, C., Dam-Johansen, K., Clement, K., & Hjuler, K. (2013). Gas-Solid Heat Exchanger for Cement Production. Technical University of Denmark, Department of Chemical and Biochemical Engineering.

DTU Library

Technical Information Center of Denmark

General rights

Copyright and moral rights for the publications made accessible in the public portal are retained by the authors and/or other copyright owners and it is a condition of accessing publications that users recognise and abide by the legal requirements associated with these rights.

- Users may download and print one copy of any publication from the public portal for the purpose of private study or research.
- You may not further distribute the material or use it for any profit-making activity or commercial gain
- You may freely distribute the URL identifying the publication in the public portal

If you believe that this document breaches copyright please contact us providing details, and we will remove access to the work immediately and investigate your claim.



CHEC Research Centre
Department of Chemical and Biochemical Engineering

Ph.D. Dissertation

Gas-Solid Heat Exchanger for Cement Production

Claus Maarup, M.Sc. Eng.

October 2013

*Being a PhD-student is not difficult,
but the life you try to live beside your studies is.
Thank you for your understanding, support,
and patience, Nina.*

Preface

The present Ph.D. dissertation is submitted as a partial fulfillment of the requirements for obtaining the Ph.D. degree at the Technical University of Denmark (DTU). It summarizes activities performed in the Combustion and Harmful Emission Control (CHEC) group at the Department for Chemical and Biochemical Engineering between January 2010 and September 2013. The work has been supervised by Professor Kim Dam-Johansen and Associate Professor Karsten H. Clement from DTU, and Research Engineer Ph.D. Klaus Hjuler, FLSmidth A/S.

The project is a part of the research platform New Cement Production Technology, and has been financed by the Danish National Advanced Technology Foundation. Some experimental activities has been funded by grants received from the Proof of Concept pool under The Danish Council for Technology and Innovation.

A number of people have been contributing to this project. Firstly, I would like to express my gratitude to my supervisors for their counseling and guiding: Kim for always throwing ideas in the air, Klaus for providing me with an insight in the cement industry, and Karsten for always having time for discussions.

I would also like to thank my colleagues and fellow Ph.D.-students for the we time spend together both during and off work, the students I had the pleasure of guiding through their B.Sc. and M.Sc. projects, and the people at Dania for taking me in as one of their own, especially Jesper Lebæk and Klaus Nielsen.

Finally, I am especially grateful to my friend and colleague Peter J. Herslund for the hours of fruitful discussions over cups of coffee, fortunately not all about our work and problems, Brian B. Hansen for the time shared in the office, and my family for always being there.

Claus Maarup
DTU, September 2013

Abstract

This Ph.D. dissertation presents the results of the investigation of a gas/solid heat exchanger, developed for application as a preheater in the cement industry.

Traditionally, the process of transferring energy from hot combustion gases to raw materials in a cement plant is carried out in a process consisting of cyclones and riser ducts. This technology has been the preferred the last fifty years, despite several attempts to introduce alternative processes.

Still, the cyclone-based process has some inherent undesired properties, such as high pressure drop ($> 35 - 45$ mbar), tall preheating structure (> 100 m), lack of options for integration of steam generating processes, and increased construction costs due to the cylindrical geometries, why it has been desired to develop a feasible alternative.

A gas/solid heat exchange design, called the two-dimensional heat exchanger (2D-HX), has been designed and patented. The 2D-HX consists of a series of mixing and separation processes, similar to the cyclone-based process, while the 2D-HX has a more compact design with planar and square geometries, and a modular construction.

The performance of the 2D-HX has been investigated experimentally, providing an insight in the internal processes of particle transport and heat exchange. For the 2D-HX, it was found that: (a) Stable operation could be achieved at industrial conditions, (b) the particle transport properties, measured as a transport efficiency, were in the same range as the cyclone preheater, $\eta_{transport} = 0.7 - 0.8$, (c) the separation process was driven by gravity in a process termed *accelerated settling*, and (d) the thermal efficiencies were around 20 % lower than for the cyclone process.

A model consisting of mass- and energy balances was developed to describe the 2D-HX performance and verified against experimental data. The separation and entrainment processes were modeled analogous to pneumatic powder transport processes.

Model predictions for full-scale facilities were compared with the results obtained from classic upscaling theory, indicating that the two methods produced similar results, thereby enabling use of the model for upscaling purposes.

Full-scale cement preheaters with production rates equivalent to 3000 and 6000 tons per day of clinker (TPDc) were evaluated. A 6000 TPDc facility with four heat exchange stages was

estimated to be 46 m x 13 m x 12 m in size, a structure around 40 – 60 % lower than a corresponding cyclone preheater.

Estimations suggested that the 2D-HX performs 5 – 10 % poorer than the cyclone-based process in terms of dust loss, and that the capital costs of the two processes, quantified by the equipment volume, were found to be in the same order of magnitude.

Several suggestions for optimizing the 2D-HX concept were provided, and an integrated preheating facility capable of superheating steam was presented, increasing the production and efficiency of waste heat recovery processes producing electricity.

Concluding the work, it was found that implementing the suggested optimizations, a 2D-HX preheater process competitive with the cyclone-based processes could be designed.

Finally, it has been recommended to further investigate and optimize the design, to realize the full potential of the 2D-HX concept.

Dansk Resumé

Denne ph.d.-afhandling præsenterer resultaterne af et studie af en gas-faststof varmeveksler, udviklet til anvendelse som råmels forvarmer i cementindustrien.

På en cementfabrik sker energioverførslen af varme fra forbrændingsgas til råstof i en proces bestående af cykloner og stigrør. Denne teknologi har været den foretrukne de sidste halvtreds år, på trods af flere forsøg på at introducere andre teknologier, herunder skaktforvarmere.

Den cyclon-baserede proces har dog nogle designmæssige uønskede egenskaber, såsom højt trykfald ($> 35 - 45$ mbar), høj forvarmerstruktur (> 100 m), manglende muligheder for integration af processer, der kan udnytte restvarme, samt øgede opførselsomkostninger grundet de cylindriske geometrier, hvorfor det har været ønsket at udvikle et konkurrencedygtigt alternativ.

En gas/faststof varmeveksler, navngivet todimensional varmeveksler (2D-HX), er blevet designet og patenteret. Ligesom cyclonprocessen består 2D-HX af en serie af processer, hvor gas og faststof blandes og efterfølgende separeres, men 2D-HX har et mere kompakt design, samt plane og retvinklede geometrier og en modulær konstruktion.

Designet er blevet undersøgt eksperimentelt i en større laboratorieopstilling, hvilket gav et indblik i den interne partikeltransport og varmevekslingen. Det konstateres at: (a) Stabil drift kunne opnås ved industrielle betingelser, (b) partikeltransporten, målt som en transporteffektivitet, lå i samme område som cyclonforvarmeren, (c) separationsprocessen var drevet af tyngdekraften i en proces klassificeret som accelereret sedimentering, samt (d) de termiske virkningsgrader var omkring 20 % lavere end for cyclonprocessen

En model bestående af masse- og energi-balancer blev opstillet til beskrivelse af 2D-HX-konceptet. Separation- og medrivningsprocesser blev modelleret med inspiration fra pneumatiske pulvertransport processer.

Modelforudsigelser for fuldskalaanlæg blev sammenlignet med resultater fra klassisk opskaleringsteori. De fremkomne resultater var sammenfaldende, hvorfor modellen kunne anvendes til opskaleringsformål.

Driftsparametre for fuldskala anlæg med en produktionsrate på 3000 og 6000 tons klinker om dagen (TPDc) blev evalueret. En firetrins forvarmer med en kapacitet 6000 TPDc blev anslået

til en størrelse på 46 m x 13 m x 12 m; omkring 40-60 % lavere end en tilsvarende cyklonforvarmer.

Endvidere blev det fundet, at støvtabet var mellem 5 og 10 % højere i 2D-HX processen, og at anlægsudgifter af de to typer anlæg, beskrevet ved den indre volumen af udstyret, var i samme størrelsesorden.

Sluttelig er flere forslag til optimering af 2D-HX konceptet givet, og der er præsenteret en integreret forvarmningsenhed, der kan anvendes til overhedning af damp, hvorved en øget produktion og effektivitet for spildvarmeprocesserne, der producerer strøm, opnås.

Rapporten konkluderer, at hvis de foreslåede optimeringsforslag implementeres vil en konkurrencedygtig udgave af 2D-HX kunne fremstilles.

Det anbefales at undersøge og optimere designet yderligere for at realisere det fulde potentiale af 2D-HX konceptet.

List of Contents

CHAPTER 1 INTRODUCTION	11
1.1 Background	11
1.2 Objectives.....	16
1.3 Structure of Thesis	16
CHAPTER 2 PREHEATING TECHNOLOGIES IN CEMENT PRODUCTION.....	19
2.1 Historic Development	19
2.2 Current Industrial Technologies.....	21
2.2.1 The Cyclone	21
2.2.2 Cement Preheater Cyclones.....	34
2.2.3 The Cyclone Preheater Process and Operational Conditions	39
2.2.4 Current Preheater Research.....	45
2.3 Shaft Preheaters.....	49
2.3.1 Counter-current Shaft Preheaters.....	49
2.3.2 Multistage Shaft Preheaters.....	52
2.4 Summary of shaft preheaters	59
2.5 Other Preheater Designs.....	60
2.6 Preheater Design Summary	62
CHAPTER 3 PREHEATER EFFICIENCY	65
3.1 Model Boundaries.....	65
3.2 Model Set Up	67
3.3 Process Efficiency.....	69
3.3.1 Thermal Efficiency.....	69
3.3.2 Transport Efficiency.....	71
3.4 Assumptions, Parameters, and Physical Properties.....	71
3.5 Model Results.....	72
3.6 Summary	77
CHAPTER 4 DESIGN DEVELOPMENT	79
4.1 Desired Properties	79

4.2	Idea Generation.....	80
4.2.1	Draft Tube Spouted Bed (DTSB) Concept	81
4.2.2	Two Dimensional Heat Exchanger (2D-HX) Concept	82
4.3	Summary	86
CHAPTER 5 EXPERIMENTAL APPROACH, SET-UPS, AND MATERIALS.....		87
5.1	Single-stage Set-up	89
5.2	Multi-stage set-up	90
5.3	Proof of Concept Set-up	92
5.3.1	Data Acquisition	95
5.4	Materials.....	96
CHAPTER 6 INVESTIGATION OF TRANSPORT PROCESSES		99
6.1	Definition of Efficiencies.....	99
6.2	Results: Single-stage Set-up	100
6.3	Results: Multi-stage Set-up	102
6.4	Results: PoC Set-up.....	104
6.5	Overview and Comparison of Data	107
6.6	Visual Observations	109
6.6.1	Separation Process	109
6.6.2	Entrainment Process	112
6.7	Identification of Governing Mechanisms	114
6.7.1	Separation Process	114
6.7.2	Entrainment Process	116
6.8	Comparison with Industrial Preheater Cyclone	116
6.9	Summary	117
CHAPTER 7 INVESTIGATION OF HEAT EXCHANGE PERFORMANCE.....		121
7.1	Results: Thermal Performance	121
7.2	Results: Heat Loss.....	125
7.3	Results: Observations	127
7.4	Results: Pressure drop.....	129
7.5	Evaluation of Thermal Performance	130
7.6	Comparison of Heat Exchanger Design with Industrial Standard	131

7.7	Summary	132
CHAPTER 8 MODELING OF 2D-HX.....		135
8.1	Modeling of the Internal Processes	135
8.1.1	Separation Process	136
8.1.2	Entrainment	141
8.2	Pressure Drop.....	144
8.3	Modeling of 2D-HX.....	148
8.3.1	Mass and Energy Balances	148
8.3.2	Assumptions	151
8.3.3	Solution Method	151
8.3.4	Verification	152
8.4	Summary	156
CHAPTER 9 DETERMINATION OF UPSCALING PRINCIPLE		159
9.1	Upscaling Strategies	159
9.2	Selection of Upscaling Parameters	163
9.3	Parametric Design and Reference Cases.....	164
9.4	Screening of Upscaling Parameters	166
9.5	Comparison of Classic and Model-based Upscaling.....	168
9.6	Summary	170
CHAPTER 10 FULL-SCALE APPLICATION OF THE 2D-HX CONCEPT.....		171
10.1	Determination of Operation Conditions	172
10.2	Full-scale 2D-HX Facilities.....	177
10.3	Comparison of the Upscaled 2D-HX and Cyclone Preheaters.....	177
10.4	Implementation in a Cement Plant	182
10.5	Pilot-Scale Facility.....	184
10.6	Optimization of 2D-HX Design	185
10.6.1	Alternative Parametric Design	185
10.6.2	Addition of Exit Cyclone	186
10.6.3	Alternative Separation Geometry	187
10.6.4	Summary of Optimizations.....	190
10.7	Identified Issues	190

10.8 Other Applications.....	192
10.8.1 Co-generation of Power	192
10.8.2 Integration of Calciner/Combustion Chamber	194
10.8.3 Application for drying purposes	195
10.9 Industry Remarks.....	196
10.10 Summary	197
CHAPTER 11 CONCLUSIONS AND OUTLOOK.....	199
11.1 Outlook and Future work	202
CITED LITERATURE	203
LIST OF SYMBOL AND ABBREVIATIONS	215
APPENDIX A EXPERIMENTAL PROCEDURES	A
APPENDIX B DATA TREATMENT.....	C
APPENDIX C EXPERIMENTAL DATA.....	K
APPENDIX D PRESSURE DROP MODEL	Q
APPENDIX E 2D-HX MODEL AND IMPLEMENTATION.....	Y
APPENDIX F INSPECTIONAL AND DIMENSIONAL ANALYSIS.....	CC
APPENDIX G PUBLICATIONS.....	GG

Chapter 1

Introduction

"Innovation is the process of turning ideas into a manufacturable and marketable form"

– Watts Humphrey, American software engineer

1.1 Background

Cement and cementitious products are one of the corner stones of the modern civilization, being the central component of concrete, the preferred construction material of the twentieth and twenty-first centuries. The cement clinker, which creates the strength and durability of concrete and mortar, is produced in a process containing a number of different operations of which the most important are shown in Figure 1 [1].

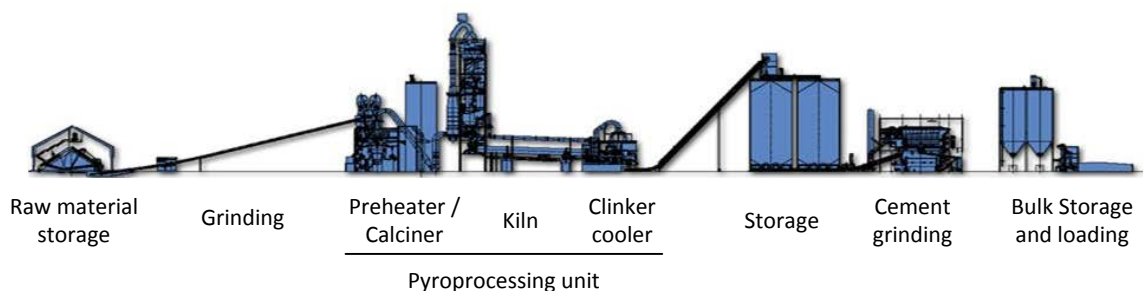


Figure 1 – Schematic overview of the major processes in cement production [2].

The raw materials, approximately 75 wt% limestone and 25 wt% clay materials containing alumina and iron, are stored in raw material silos when delivered to the cement plant. The production process is initiated by grinding and mixing the raw materials, thereby obtaining a powderous mixture with a particle diameter of 5 – 125 μm called the raw mix or raw meal [3]. The raw meal is stored in agitated silos for homogenization, before entering the hot part of the cement plant, called the pyroprocessing unit, consisting of the preheating and calciner¹ facility, the rotary kiln, and the clinker cooler.

In the preheating facility the raw meal is heated using the exhaust gases from the combustion processes in a stepwise counter-current suspension process. The preheating process consist of three to five stages, each containing a riser duct, in which the gas and particles are mixed and exchange heat, and a cyclone separating the two phases. Each stage increase particle temperatures by 150 °C – 250 °C [3]. The temperature of the preheated particles is 700 °C – 800 °C [4].

The preheated raw meal enters the calciner, where at least 85 wt% of the limestone is calcined at 870 °C – 900 °C. The calcined raw meal is then fed to the rotary kiln, where further heating and partially melting of the solids at temperatures up to 1450 °C – 1500 °C is facilitated, forming the desired chemical composition of the clinker. In standard inline calciner (ILC) facilities, 60 % of the fuel is combusted in the calciner and 40 % in the rotary kiln [1].

Leaving the rotary kiln, the clinker is rapidly cooled in the clinker cooler, thereby preserving the crystalline structure and ensuring a high content of alite [5], which is the strength giving crystal phase in the clinker. The heated cooling air is used as combustion air in the main burner in the rotary kiln and typically also as tertiary combustion air in the calciner. Additional hot gas streams from the clinker cooler may be utilized for waste heat recovery (WHR) purposes.

A schematic drawing of a pyroprocessing unit, including typically encountered temperatures are provided in Figure 2.

The cooled clinker is grinded to achieve a uniform, fine powder. For some types of cement additional mineral components such as gypsum, fly ash, or slag is added, before being stored in the final product silo, ready for transport [3].

Besides the above mentioned, processes such as gas cleaning, drying of raw meal, fuel preparation, and mixing processes are also vital parts of a cement production.

¹ The calciner carries out the calcination of the limestone releasing CO₂, and is also often termed the precalciner in the literature and industry. Here only the former name will be used.

In modern cement plants the total thermal energy consumption is 3.0 – 3.5 MJ/kg clinker, indicating that between 48 – 60 % of the energy is lost through heat losses from equipment surfaces, and as uncooled gas and dust flows leaving the pyroprocessing unit.

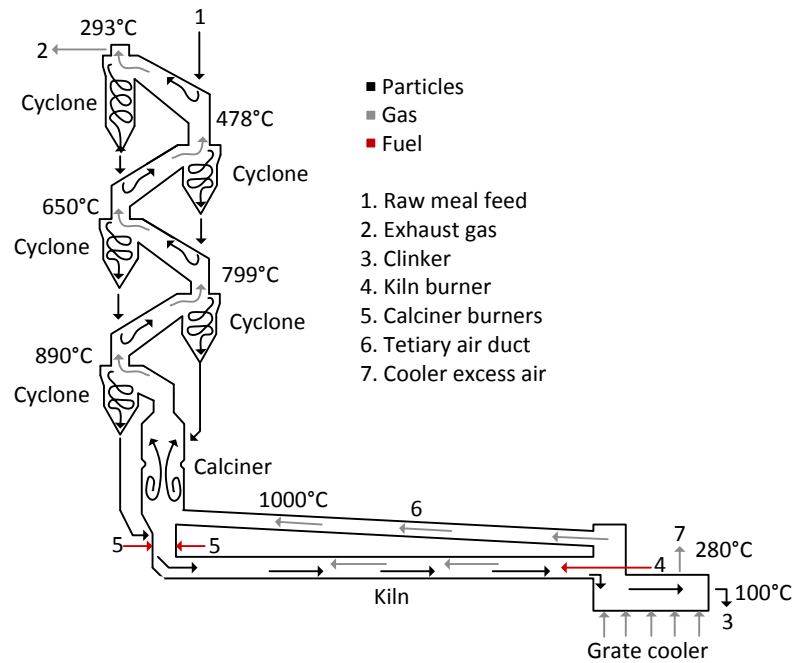


Figure 2 – Schematic illustration of the pyroprocessing unit of a five stage preheater, inline calciner (ILC) cement plant. Typical temperatures are given [4].

Table 1 – Summarized heat balance for a pyroprocessing system for a modern cement plant [3].

Processes	Energy consumption
Theoretical:	
Heating and drying of raw materials	1.5 MJ/kg clinker
Calcination	2.0 MJ/kg clinker
Heating of calcined materials	0.6 MJ/kg clinker
Formation of liquid phases and clinker chemistry	- 0.3 MJ/kg clinker
Cooling of clinker	- 1.5 MJ/kg clinker
Cooling of exhaust	- 0.6 MJ/kg clinker
Theoretical thermal energy consumption	1.7 MJ/kg clinker
Inefficiencies:	
Gas and dust leaving the pyroprocessing unit	0.8 MJ/kg clinker
Heat loss (convention and radiation)	0.7 MJ/kg clinker
Total thermal energy consumption	3.2 MJ/kg clinker

Besides the thermal energy requirement approximately additional 10 % of electrical energy is required, mainly for crushing and fan work.

Detailed descriptions of the cement production and cement chemistry can be found elsewhere [1,3,5–8]. Bhatta [3] provides an in-depth description of all aspects of cement production processes, Duda [8] describes extensively the historical development, while Nielsen [6] has made a short and concise review, describing the major processes of cement production.

The global demand for cement continues to increase, as shown in Figure 3, driven by the economic growth of countries such as China, India, Brazil, and the countries in the Middle East.

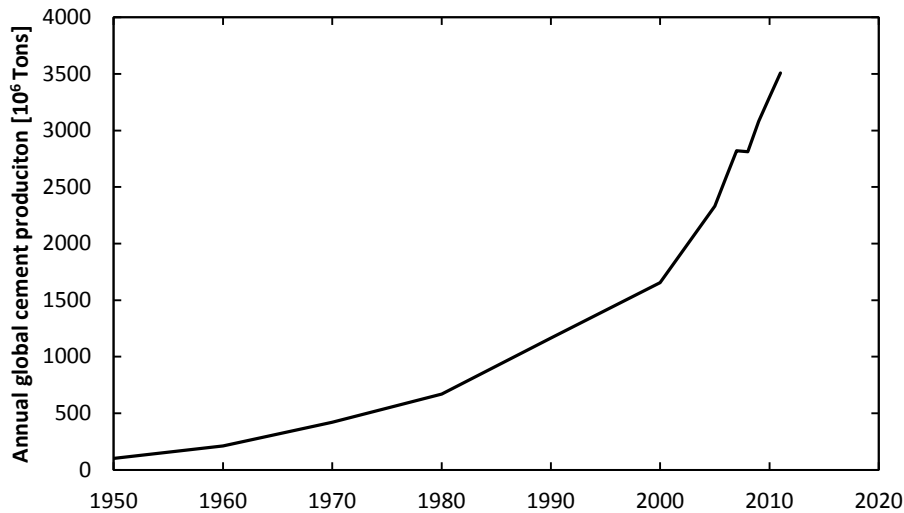


Figure 3 – Annual global cement production in million tons of cement [1,11].

The effect of the global economic recession, starting in mid-2008, can be witnessed as a temporary hold in the annual production. The increase following the recession is driven mainly by the Chinese demand. In 2006, 47.4 % of the global cement production took place in China, 6.2 % in India while the European Union, and USA contributed with 10.5 % and 3.9 %, respectively [1]. In 2010, the Chinese production accounted for 55 % of the global annual production [9].

Commercially available turnkey cement plants are mainly supplied by five major contractors, with FLSmidth and Sinoma holding the largest market shares outside China, as indicated in Figure 4. The market share of Sinoma on the domestic Chinese market is higher than 90 % [10].

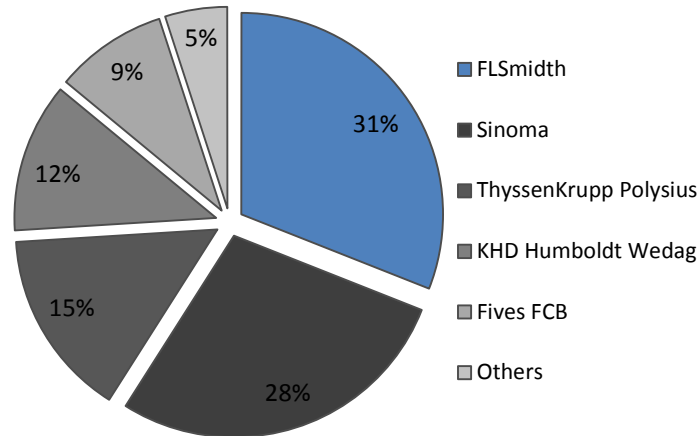


Figure 4 – Market shares of sold kiln capacity, China excluded [12].

The environmental footprint of the global cement production is significant. Around 5 % of the annual global emitted CO₂ can be attributed cement production [13]. The CO₂ release during cement production is approximately one kilo per kilo clinker. Approximately 60 % originates from the calcination process, where CO₂ is released from CaCO₃, the remaining 40 % is a product of the combustion of fuels. Other major emission species are CO, NO_x and SO₂.

Typical production capacities of cement plants range from a few thousand tons per day of clinker (TPDc) to 12000 TPDc [14], thus the amount of energy and raw materials required are of similar proportions.

The price tag of a cement plant is between 500 – 1100 DKK per ton of annual capacity, corresponding to a combined price of around 1 – 2 billion DKK for a standard 5000 TPDc facility [15,16], equivalent to approximately three years of turnover. This makes cement production a capital intensive industry with long payback periods. Therefore even marginal improvements are crucial for the cement plant providers and their customers.

To reduce capital costs and also the environmental impact, the cement plant is continuously being improved. This includes substitution of fossil fuels with alternative fuels, utilization of thermal waste energy, and development of equipment with reduced cost.

The cement industry is generally conservative with respect to adopting new technologies and a significant amount of resources is going into developing, testing, and verifying equipment performance before a commercialization is possible.

This PhD-thesis summarizes the development of a particle-gas heat exchanger for application in the cement plant as a raw meal preheater, replacing the traditional cyclone-based process.

1.2 Objectives

The objective of this project is to lower the operational and capital costs related to the preheater in a cement plant. This is done by reconsideration and a redesign of the preheater facility. Therefore, the objective of this project is not to further optimize the existing technology, but to rethink the entire preheating process and, if possible, to suggest a design with an integrated power generation system.

In bullets, the objectives summarize to:

- Investigate and suggest a novel preheater facility with lower capital costs without reducing the performance.
- Suggest a facility where a power generation system is integrated in the cement plant preheater.
- Design and carry out experiments to verify the suggested design.
- Set up and verify a model describing the experimental behavior.
- Estimate full-scale facility characteristics.

The objectives are focused on developing a cheaper preheater alternative to the cement plant, instead of seeking to reduce the emissions or improve efficiency. Therefore, estimations of emissions have not been included in the present work.

1.3 Structure of Thesis

This dissertation contains a total of 11 chapters and seven appendices. Publications can be found in appendix G. A bibliography is provided following Chapter 11, as well as list of symbols and abbreviations. A short overview of the chapters of the thesis is given hereafter:

- Chapter 2 reviews the current and selected past preheater technologies, focusing on describing the modern cyclone preheater. This chapter contains operational and equipment related data as well as presents the major areas of research related to the preheating facility. This chapter serves as a starting point for the following design considerations.

- Chapter 3 presents a model capable of predicting the internal flows and temperatures of a cyclone preheater. Two thermal efficiencies are evaluated for use as comparison parameters for preheaters.
- Chapter 4 describes the idea generation and selection process, as well as outlines the requirement for a new preheating process and introduces the developed heat exchanger design.
- Chapter 5 presents the experimental set-ups used in this work, including detailed equipment descriptions, experimental procedure, raw materials, and method of data acquisition.
- Chapter 6 reports the obtained experimental results related to the internal particle transport properties in the heat exchanger set-ups. The governing mechanisms are identified and the data from the novel design is compared with corresponding data for the cyclone preheater facility.
- Chapter 7 presents data related to the heat exchange performance of the 2D-HX. Data is analyzed and compared with similar data for the cyclone preheaters. The heat exchange data also provides a proof of concept at industrial-like process conditions.
- Chapter 8 describes the work related to setting up a model capable of representing the observed experimental behavior, and the verification of the model using experimental data.
- Chapter 9 provides an insight in the upscaling work, identifying the relevant dimensionless groups and determining the upscaling procedure.
- Chapter 10 presents the estimated full-scale data for the 2D-HX preheater when applied in a cement plant. The data is compared with relevant cyclone preheater data to evaluate the potential of the 2D-HX design.
- Chapter 11 concludes the work and outlines suggestions for future work regarding the further development of the novel preheater technology.

Chapter 2

Preheating Technologies in Cement Production

“I don't know anything, but I do know that everything is interesting if you go into it deeply enough”

– Richard Feynman, American theoretical physicist

The purpose of the preheating processes in cement production is to facilitate the heat exchange between the hot flue gases created by the combustions in the rotary kiln and calciner and the cold powdery raw material, raw meal. This process is of great importance for the overall design and economy of the cement plant, as the energy recovered in the preheating process increases the thermal efficiency of the plant, reduces kiln length, and increases production capacity.

2.1 Historic Development

With the development of technologies for continuous cement production, especially with the introduction of the first rotary kilns at the end of the 19th century, the concept of a preheating process was introduced. Before the continuous methods, cement was produced batchwise: The ancient Greeks and Romans produced cement and mortar in open pits, which were later replaced by crude, dome, or shaft kilns [3].

Up to the beginning of the 20th century the preheating and calcination of the raw meal and the burning of the cement clinker were facilitated in the rotary kilns. These processes would be

classified as either a dry or a wet process, depending on the state of the raw materials (powder or slurry). Both were carried out in long rotary kilns with length/diameter (L/D) ratios of up to 40, and were characterized by a relatively poor heat exchange between the particle bed and the hot flue gases, resulting in gas exit temperatures of up to 700 °C and correspondingly poor fuel efficiencies. Chains and internally fitted ceramic heat exchangers installed in the cold end of the dry kilns, divided the cross sectional area into three or four zones, thereby improving the energy efficiency with up to 35 % (compared to the wet processes) and reduced exit gas temperatures to around 400 °C [3]. Structural limitations of the long kilns limited the production capacity to around 2000 TPDc [3].

In the late 1920s Lellep [17] invented a new process, named the Lepol process, where the raw materials were pelletized before entering the kiln. The pellets made it possible to establish an efficient heat exchange between raw meal and combustion gases in a travelling grate heat exchanger before the raw meal entered the rotary kiln, reducing kiln L/D ratios to around 12 – 15, the exit gas temperature to 100 °C, and improved the fuel economy by 50 % compared to the wet process. The mechanical properties of the formed pellets were essential as their ability to withstand the thermal and mechanical treatment in the travelling grate heat exchange influenced the process efficiency: If the pellets broke apart, the efficiency of the system would be greatly reduced. The Lepol kiln reached production rates of up to 3000 TPDc.

The suspension preheating processes containing riser ducts and cyclones, which is the preheating technology still used, led to further reduced kiln lengths and improved thermal efficiencies without the need of pelletization. The concept was invented in the 1930s by FLSmidth A/S and made commercially available by KHD Humboldt Wedag AG in the 1950s [8].

The introduction of the calciner in the 1970s, where additional fuel were combusted and the raw meal calcined before entering the rotary kiln, further reduced kiln L/D ratios to 10 – 14 and increased production capacity to more than 12000 TPDc in a single kiln [14,18].

The design and operating conditions of the preheaters are defined by overall cement plant economics, especially energy consumption, pressure drop, and capital costs are of importance. Furthermore, emission control and operational stability are vital parameters.

2.2 Current Industrial Technologies

Since the 1950s, the dominating preheating process has been the cyclone-based preheater [19], which consists of a series of stages each comprising of a riser duct and a cyclone. In the risers, gas and particles are mixed and transported to the cyclone inlet. In the cyclone, the two flows are separated.

The performance, operation, and design of the preheaters are the focus in the following sections, starting with a detailed description of the major component in the preheater, namely the cyclone.

2.2.1 The Cyclone

Cyclones are classic unit operations used to separate dense particles from a lighter fluid by centrifugal forces. In gas cyclones, the gas rotates in a helical pattern, accelerating denser suspended particles towards the inner walls of the cyclone, where they are deposited. At the wall the particles move downwards driven by gravity and the downward gas flow [20]. An illustration of the flows in a cyclone is depicted in Figure 5, while the nomenclature of the dimensions on a cyclone with a slot type² inlet is given in Figure 6.

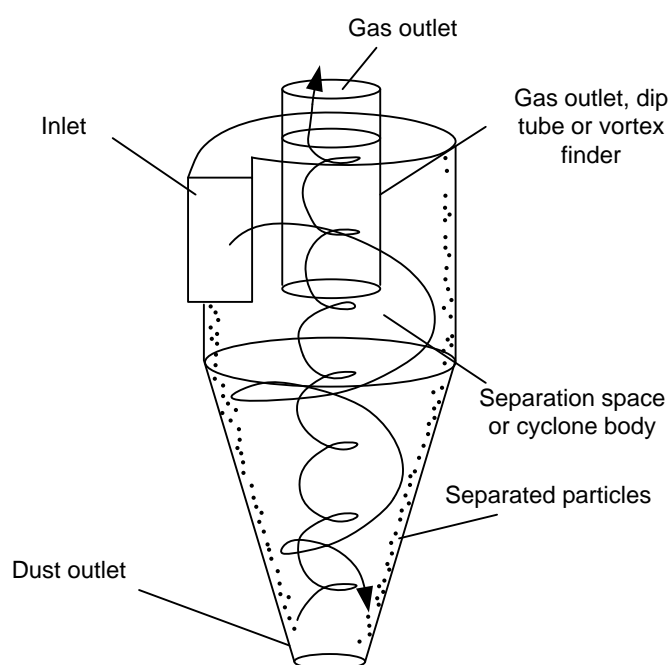


Figure 5 – Internal flows of a gas cyclone.

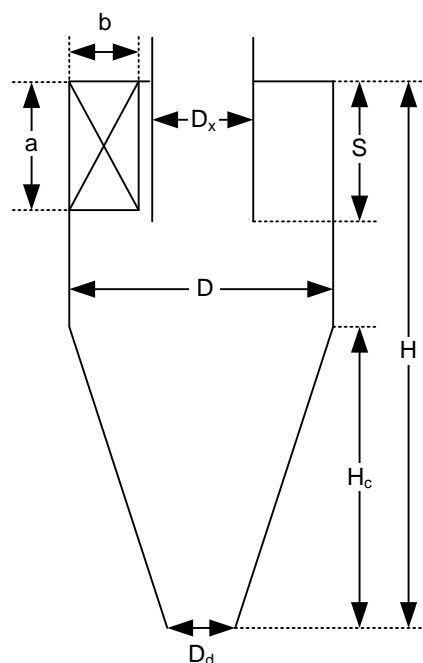


Figure 6 – Cyclone with slot type inlet and design dimensions.

² The slot type inlet is also termed tangential inlet in literature.

An overview of classic cyclone designs have been compiled by Leith and Mehta [21]. Selected data are provided in Table 2. The cyclone dimensions are normalized by the diameter of the cyclone body, D . All but one of the designs shown has slot type inlets, similar to the one shown in Figure 6. The remaining design has a wrap-around³ inlet. Generally wrap-around type inlets are used to achieve higher collection efficiencies and lower pressure drops at the cost of a more complex cyclone geometry and thereby higher installation cost [20]. The diameter of the cyclone body, D , can be estimated from the desired cut-size and pressure drop, as shown later in this section.

Table 2 – Standard cyclone design ratios [21].

Source	Recommended duty	a/D	b/D	D_x/D	S/D	$(H-H_c)/D$	H/D	D_d/D
Stairmand [22]	High efficiency	0.5	0.2	0.5	0.5	1.5	4.0	0.375
Swift [23]	High efficiency	0.44	0.21	0.4	0.5	1.4	3.9	0.4
Lapple [24]	General purpose	0.5	0.25	0.5	0.625	2.0	4.0	0.24
Swift [23]	General purpose	0.5	0.25	0.5	0.6	1.75	3.75	0.4
Stairmand [22]	High throughput ^A	0.75	0.375	0.75	0.875	1.5	4.0	0.375
Swift [23]	High throughput	0.8	0.35	0.75	0.85	1.7	3.7	0.4

^A With wrap-around type gas entry

For cyclones in general, the most important operational parameters are fractional efficiency, collection efficiency⁴, and pressure drop. The collection efficiency, η , of a cyclone is the ratio between the mass of collected solids and the mass of particles fed to the cyclone in a given time, while the fractional efficiency, η_i , is the collection efficiency of a given size fraction of particles. Note that fractional and overall efficiencies are identical, if the particles are uniform.

The collection efficiency of the inner vortex generated in the cyclone, η_x , can be calculated from the fractional efficiency and the particle size distribution of the feed.

$$\eta_x = \sum_{i=1}^N \eta_i \cdot \Delta MF_i \quad \text{Eq. 1}$$

where ΔMF_i is the i 'th mass fraction of the particles. The relation between η and η_x depends on the cyclone operation characteristic, as will be shown shortly here after in Eq. 2 to Eq. 15.

³ The wrap-around inlet is also termed scroll inlet in the literature.

⁴ Collection efficiency is also termed separation efficiency and overall efficiency in the literature.

Modeling of cyclone performance

The operational parameters of interest: Pressure drop, fractional, and collection efficiencies can be approximated from cyclone geometry, particle properties, and operational conditions. The basis of the algebraic models is approximations of the velocity field within the cyclones. The most common models for describing the velocity field have been developed by Barth [25], Alexander [26], and Muschelknautz [27,28]. Based on the velocity field, expressions and methods for determining the cut-size diameter have been suggested by several authors, including Barth [25], Muschelknautz [27,28], Lapple [29], and Leht-Licht [30].

The method and model developed by Muschelknautz and various co-workers is considered the most accurate and comprehensive of the general algebraic cyclone models [20,31,32]. What sets Muschelknautz's method (MM) apart from other models, is that it encompasses three phenomena of special interest; (a) wall roughness, (b) mass loading effects at the inlet of the cyclone, and (c) an inner feed with a different particle size distribution than the feed to the cyclone.

In the following, the work of Muschelknautz will be outlined. The model has been developed over several decades, and the full model is comprehensive. In the following the fundamental aspects will be presented. For further details on the model, please refer to [27,28,33,34] or Hoffmann and Stein [20], who made a comprehensive review covering the majority of the model.

In this context the effect of the mass loading on the inner feed, mentioned as point (c) above, will be omitted as it according to [20] has limited effect on the collection efficiency. However, if the particle size distribution of the dust leaving the cyclone is of high importance, this effect should be included in the cyclone description.

The applied cyclone nomenclature is illustrated by Figure 7, while the cyclone proportions are shown in Figure 6. The input parameters include gas flow, m_G , cyclone geometry, and solid load, c_o .

MM is based on the work of Barth [25], considering a particle rotating in a cylindrical control surface (CS) located below the vortex finder, as shown in Figure 8.

In order to determine the collection efficiency, the cut size diameter, d_{50} , which is the particle size for which 50 % of the particles are collected, must be determined. In order to achieve this, three velocity components inside the cyclone, $v_{\theta w}$, v_{zw} , and $v_{\theta CS}$, and the friction factor must be determined.

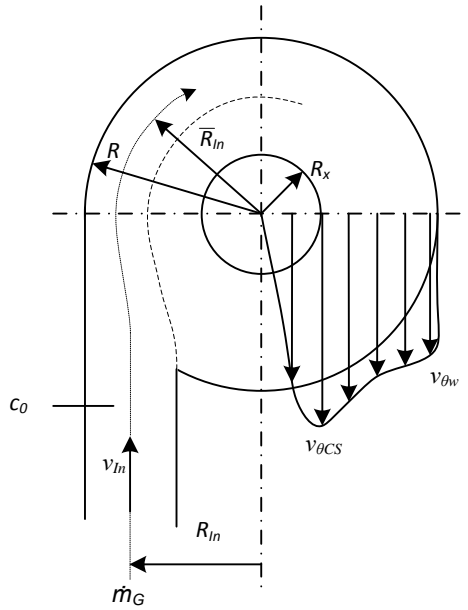


Figure 7 – Top view of the cyclone including nomenclature used in the model of Muschelknautz. The control surface is located below the vortex finder at $r = R_x$ [20].

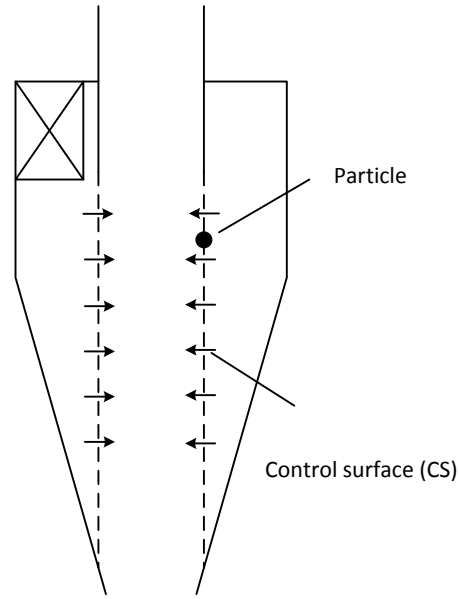


Figure 8 – Depiction of the control surface (CS) and a particle rotating at the CS.

At the inlet of a cyclone, the gas is accelerated from v_{in} to $v_{\theta w}$ by the force of the rotating vortex. According to MM the tangential velocity after the inlet at the wall, $v_{\theta w}$ is given as [34]:

$$v_{\theta w} = \frac{v_{in} \cdot R_{in}}{\alpha \cdot R} \quad \text{Eq. 2}$$

where α is a constriction factor describing the ratio between the tangential momentum based on inlet and the cyclone body geometry. For slot type cyclones α is given by Eq. 3 [27]. For wrap around inlets, α is given by Eq. 4 [28].

$$\alpha = \frac{1}{\beta} \cdot \left(1 - \sqrt{1 + 4 \cdot \left(\left(\frac{\beta}{2} \right)^2 - \frac{\beta}{2} \right) \cdot \sqrt{1 - \frac{(1 - \beta^2) \cdot (2 \cdot \beta - \beta^2)}{1 + c_o}}} \right) \quad \text{Eq. 3}$$

$$\alpha = 1 + \frac{\sqrt{3} \cdot \pi \cdot f \cdot R_{in}}{\sqrt{a \cdot b}} \quad \text{Eq. 4}$$

where β is the geometric ratio b/R and c_o is the solid load. The axial wall velocity, $v_{z w}$, is given as:

$$v_{zw} = \frac{0.9 \cdot \dot{m}_G}{\pi \cdot (R^2 - R_m^2)} \quad \text{Eq. 5}$$

where R_m is the mean radius: $R_m = \sqrt{R_x \cdot R}$, and \dot{m}_G , is the known volumetric flow rate. The factor 0.9 is based on a 10 % lip leakage assumption, where gas shortcuts the cyclone and leaves through the vortex finder directly after entering the cyclone.

The friction factor, f , needed to determine $v_{\theta CS}$ is approximated by an empiric expression, which consists of two additive parts; friction created by the gas and particles, respectively [33].

$$f = f_G + f_P \quad \text{Eq. 6}$$

The air friction factor, f_G , depends on a cyclone Reynolds number and roughness of the cyclone walls. Muschelknautz define the Reynolds number for cyclones as [33]:

$$Re_C = \frac{R_{In} \cdot R_M \cdot v_{zw} \cdot \rho_G}{H \cdot \mu \cdot \left(1 + \left(\frac{v_{zw}}{v_{\theta w}} \right)^2 \right)} \quad \text{Eq. 7}$$

where $v_{\theta m}$ is the mean tangential velocity: $v_{\theta m} = \sqrt{v_{\theta w} \cdot v_{\theta CS}}$, ρ_G is the density of the gas and μ is the viscosity of the gas. $v_{\theta CS}$ is the tangential velocity of the gas at the CS, which depends on the friction and thereby also Re_C . However, the fraction in the denominator can often be neglected, yielding: $1 + (v_{zw}/v_{\theta w})^2 \approx 1$. The friction of the air, f_G , is determined graphically. At $Re_C > 2000$, the values are independent of Re_C and ranges from 0.005 for a smooth cyclone to around 0.03 for cyclones with a relative roughness on the inner walls, k_s/R , of $6 \cdot 10^{-3}$. For the full graphical dependence, please refer to [28]. The solid friction, f_P , can be approximated by [27]:

$$f_P = 0.25 \cdot \sqrt{\frac{c_o \cdot \eta_x \cdot Fr_x \cdot \rho_G}{\rho_{Str}}} \cdot \left(\frac{D}{D_x} \right)^{-5/8} \quad \text{Eq. 8}$$

Fr_x is the Froude number at the vortex finder, $Fr_x = v_x / \sqrt{2 \cdot R_x \cdot g}$, and η_x is the collection efficiency of the inner vortex, which is the fast rotating upward moving column of gas in the center of the cyclone. ρ_{Str} is the density of the particle strands inside the cyclone. Typical values are around $0.4 \cdot \rho_p$.

Finally the tangential velocity at CS, $v_{\theta CS}$, is given as [27]:

$$v_{\theta CS} = v_{\theta w} \cdot \frac{R/R_x}{1 + \frac{f \cdot A_{Tot} \cdot v_{\theta w} \sqrt{R/R_x}}{2 \cdot \dot{m}_G}} \quad \text{Eq. 9}$$

where A_{Tot} is the total inside area of the cyclone, including roof, cylinder, cone, and outer surface of the vortex finder:

$$A_{Tot} = \pi \cdot \left(R^2 - R_x^2 + 2 \cdot (H - H_c) + (R + R_D) \cdot \sqrt{H_c^2 + (R - R_D)^2} + 2 \cdot R_x \cdot S \right) \quad \text{Eq. 10}$$

At this point, the flow field inside the cyclone is described, and consists of the velocities v_m , $v_{\theta w}$, $v_{z w}$, and $v_{\theta CS}$. From this information, the cut-size of the inner vortex of the cyclone can be determined [27]:

$$d_{50} = d_{Fact} \sqrt{\frac{18 \cdot \mu (0.9 \dot{m}_G)}{2\pi (\rho_p - \rho_g) \cdot v_{\theta CS}^2 \cdot (H - S)}} \quad \text{Eq. 11}$$

d_{Fact} is a correction factor which may be applied to match experimental data. Typically values are around 0.9 to 1.4. The $0.9 \cdot \dot{m}_G$ refers to the 10 % lip leakage assumption. The expression given in Eq. 11 is based on Stokes law and should only be applied when Stokes law is valid, $Re_p \leq 0.5$ [20]. If Stokes law does not apply the force balance on the particle with the dependency of Re_p must be set up and solved.

The fractional efficiency curve is defined from two parameters; (a) the cut-size diameter and (b) a slope, m . Several different expressions are available for evaluating the efficiency curve. One of the most applied and practical (although empirical) are [20,35]:

$$\eta_i = \frac{1}{1 + \left(\frac{d_{50}}{d_i} \right)^m} \quad \text{Eq. 12}$$

where d_i is the average particle diameter of the i 'th mass fraction. According to Hoffmann and Stein [20] a value of the exponent, m , between 4 and 6 fits well for laboratory-scale cyclones and between 2 to 4 for industrial-scale applications [20]. Generally values have been found to vary between 2 and 7. A depiction of Eq. 12 with $m = 2$ is given in Figure 9.

The separation mechanism considered until this point takes place at the inner vortex of the cyclone, which under light solid load is the only process of relevance. According to Muschelknautz, at high solid loads an additional separation mechanism is present. This is a mass loading process occurring at the inlet of the cyclone similar to the salting processes found

in horizontal pneumatic transport systems. A fraction of the incoming particles are in the first turn of the gas in the cyclone deposited on cyclone walls, thus they do not influence the inner vortex of the cyclone. The cyclone operating principle consist then of a mass loading process followed by a classification type process, as illustrated in Figure 10.

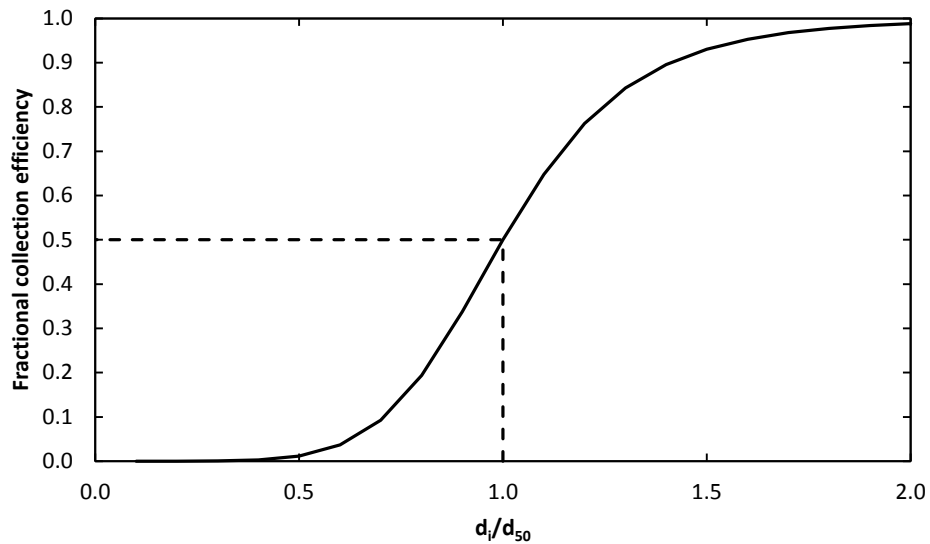


Figure 9 – A general fractional collection efficiency function with $m = 2$ as a function of particle diameter. d_{50} is the cut-size diameter.

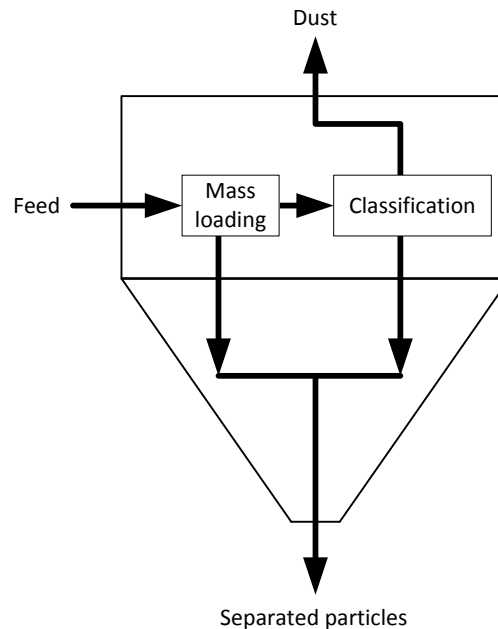


Figure 10 – Principal processes taking place inside a cyclone operating above the critical solid load. Modified from [20].

The limit for the mass loading process to occur is described as a critical solid load, c_{oL} [27]:

$$c_{oL} = 0.025 \cdot \left(\frac{d_{50}}{d_{med}} \right) \cdot (10 \cdot c_o)^k \quad \text{for } \begin{cases} c_o \geq 0.1 & k = 0.15 \\ c_o < 0.1 & k = -0.11 - 0.10 \cdot \ln(c_o) \end{cases} \quad \text{Eq. 13}$$

where d_{med} is the median particle size of the feed.

When $c_o < c_{oL}$ the mass loading effect does not take place, and the collection efficiency, is given as:

$$\eta = \eta_x \quad \text{Eq. 14}$$

When $c_o > c_{oL}$ the cyclone separation is given as [28]:

$$\eta = \left(1 - \frac{c_{oL}}{c_o} \right) + \left(\frac{c_{oL}}{c_o} \right) \cdot \eta_x \quad \text{Eq. 15}$$

The solution procedure of the MM can be summarized as illustrated in Figure 11.

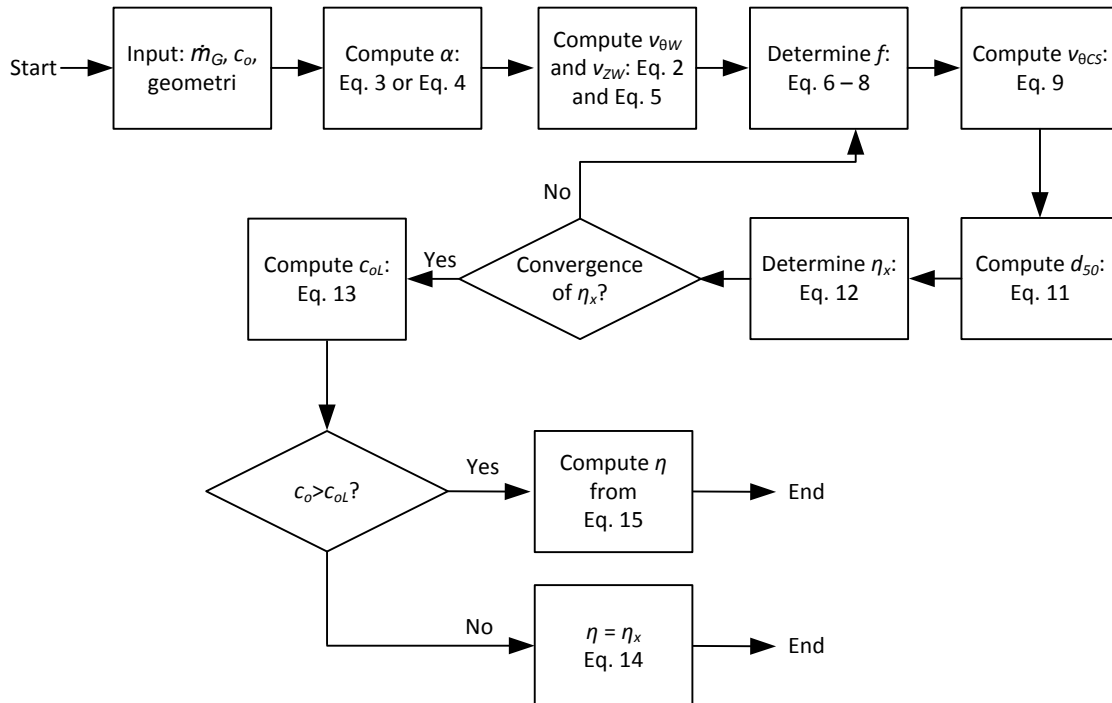


Figure 11 – Algorithm for computing cyclone collection efficiency using the method of Muschelknautz.

Note that collection efficiency enters in Eq. 8, thereby making the solution process iterative.

Pressure drop

From the known flow field within the cyclone, the pressure drop can be estimated. According to Muschelknautz, the pressure drop of the cyclone can be attributed three phenomena. Pressure drop in (a) the cyclone body, ΔP_{Body} , (b) the vortex finder, ΔP_X , and (c) pressure drop caused by acceleration of gas and particles at the inlet, ΔP_{Acc} . The pressure drops are estimated as:

$$\Delta P_{Body} = \frac{f \cdot A_{Tot} \cdot \rho \cdot (v_{\theta CS} \cdot v_{\theta w})^{1.5}}{2 \cdot 0.9 \cdot \dot{m}_G} \quad \text{Eq. 16}$$

$$\Delta P_X = \frac{1}{2} \cdot \rho \cdot v_x^2 \left(2 + \left(\frac{v_{\theta CS}}{v_x} \right)^2 + 3 \cdot \left(\frac{v_{\theta CS}}{v_x} \right)^{\frac{4}{3}} \right) \quad \text{Eq. 17}$$

$$\Delta P_{acc} = (1 + c_o) \cdot \frac{\rho \cdot (v_1^2 - v_2^2)}{2} \quad \text{Eq. 18}$$

where v_1 and v_2 are upstream and downstream gas velocities of the cyclone, respectively.

Discussion

The model presented exemplify the models in literature that enables estimations of the vital cyclone operation parameters using algebraic equations obtained partly from theoretical considerations, partly from empirical data. The presented model has been selected due to the applicability and relatively high accuracy.

The application of the model is limited by some assumptions, e.g. the applicability of Stokes law and $Re_C > 2000$. These assumptions should not be problematic under normally encountered operation conditions and cyclone geometry. However, due to the use of empirical expressions and constants, it is important to verify predictions with experimental observations.

When the mass loading effect occurs in a cyclone, this process contributes with the majority of the separated particles by mass, typically more than 90 % [31], with a very weak, if any, classification of particles. Thus, from a collection efficiency point of view the classification properties of the mass loading separation process is insignificant, which is the reason for not providing the more recent additions to the MM, concerning particle size distribution of the inner

feed. These additions are necessary if the particle size distribution of the dust outlet is of interest, however.

An example of the application of the MM is provided by Dewil et al. [36], who investigated a full-scale circulating fluidized bed (CFB) plant operating at 775 °C with a maximum thermal capacity of 58 MW and a cyclone with a diameter of 3960 mm. When comparing the full-scale cyclone performance with several cyclone models, including Barth, Leigh-licht, and Muschelknautz, Dewill et al. [36] found poor agreement between measured and estimated data, except for the Muschelknautz model.

As defined by Treftz and Muschelknautz [27] (Eq. 13), the critical load may be reached at either high solid load or large difference between the median size of the fed particles and the cut-size diameter of inner vortex. Due to the exponent of the solid load, the effect of this parameter is reduced, indicating the ratio of diameters as the more important parameter. As an example a solid load of 1.0 kg/kg with a median particle size of 20 μm is considered. In this case, the cut size diameter of the inner vortex should be 28 times lower than the particle feed for this load to be critical. This results in a cut size diameter of 0.7 μm for the inner vortex, which is a very low value. However, Hoffman et al. [37] states that the critical load might be as low as 0.001 kg/m^3 gas, which is difficult to reproduce with MM. This apparent disagreement between the experimental results and the predictions of critical load indicates that despite MM being a complex model, it is not universal, and that the fundamental mechanisms of the cyclones are still not fully described.

From the equations presented in the previous sections, it is possible to predict some general cyclone behavior:

- The effect of the solid load on the friction factor, and thereby the collection efficiency, is not clear from the expressions stated Eq. 8, as both solid load and overall efficiency enters the expression.
- If gas inlet velocity increases, the overall efficiency and pressure drop increases.

The latter statement is a general rule of thumb applied in cyclone design. The former statement is unclear with respect to the influence on the solid load. Normally accepted is that collection efficiency increases with solid load, which is especially evident when $c_o > c_{oL}$.

Experimental cyclone data reveals the complex behavior of the collection efficiency of cyclones, and the dependency of solid load. The effect of the solid load have been investigated by several researchers, including [38–44]. Hoffmann [38] showed that increasing solid load

increases overall collection efficiency. Experiments were carried out in a cyclone similar to high efficiency Stairmand cyclone with $D = 0.2$ m and $D_v/D = 0.375$. The particles used were chalk powder with an average diameter of $3.7 \mu\text{m}$. Figure 12 displays some of the experimental results obtained by Hoffmann [38]. It is noted that especially at low solid loads, the effect on the overall collection efficiency is pronounced, i.e. the increase from 5 g/m^3 to 10 g/m^3 increases the overall collection efficiency from 89 % to 92 % at $v_{in} = 15 \text{ m/s}$.

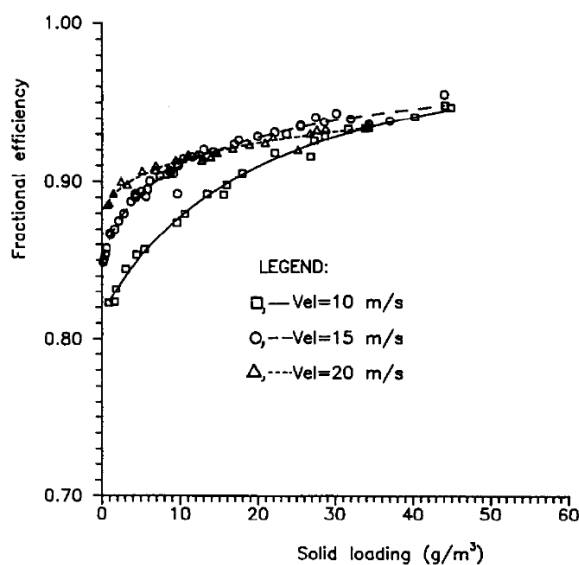


Figure 12 – Fractional efficiency as a function of solid loading and gas velocity [38].

The trend of increasing collection efficiency as a consequence of increased solid load is also reported by Zenz and Tawari [43] and Zenz [44], who investigated solid loading between $1.868 \cdot 10^{-3}$ and $1.868 \text{ kg solid/kg gas}$.

The increase of efficiency caused by higher solid loading is normally contributed two phenomena: (a) the presence of additional coarse particles sweeps fine particles to the cyclone wall for separation and (b) the formation of agglomerates, which are easier to separate from the gas. A third phenomenon, relevant for highly loaded cyclones, is the salting out of particles from the gas stream, as described by Muschelknautz.

Fassani and Goldstein [39] studied solid loadings between zero and $20 \text{ kg solid/kg gas}$ in a typical catalyst regenerator cyclone applied in cracking processes in the petroleum industry with $D = 0.154$ m. Fassani and Goldstein [39] found that the overall collection efficiency had an

optimum at around 12 kg solid/kg gas. Gas inlet velocities were varied between 7 and 27 m/s. The measured collection efficiencies are presented in Figure 13.

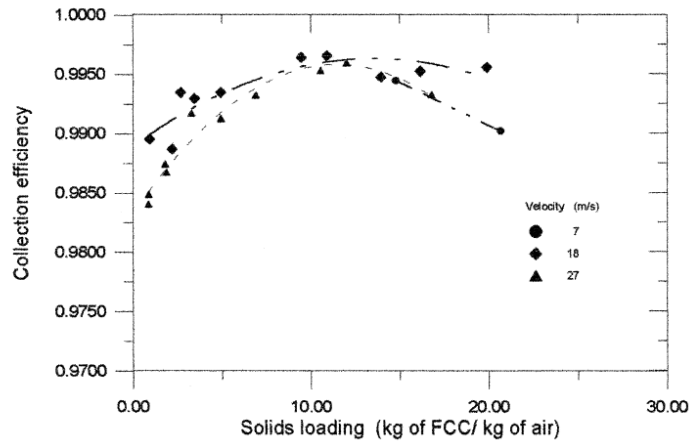


Figure 13 - Overall collection efficiency as a function of solid loading and gas velocity [39].

The optimum in collection efficiency observed by Fassani and Goldstein [39] can be caused by an increased re-entrainment of particles from the cyclone walls at high solid loadings. Tuzla and Chen [45] also reports an optimum in collection efficiency for increasing solid load without accounting for the observed phenomena.

Both Hoffmann [38] and Bricout and Lounge [41] also investigated the impact of the solid loading on pressure drop. Their results are presented in Figure 14 and Figure 15.

Hoffmann [38] reports that the pressure drop is slightly reduced as the solid loading increases, as illustrated in Figure 14. This drop is more pronounced for higher gas velocities. Bricout and Lounge [41] found that the initial addition of particles to the gas stream had large effect on the pressure drop, while the additional addition of particles above $c_o = 1$ kg/kg had little effect. Chu et al. [40] and Fassani and Goldstein [39] reports similar trends based on experiments with solid loads up to 2.5 kg and 20.0 kg/kg, receptively.

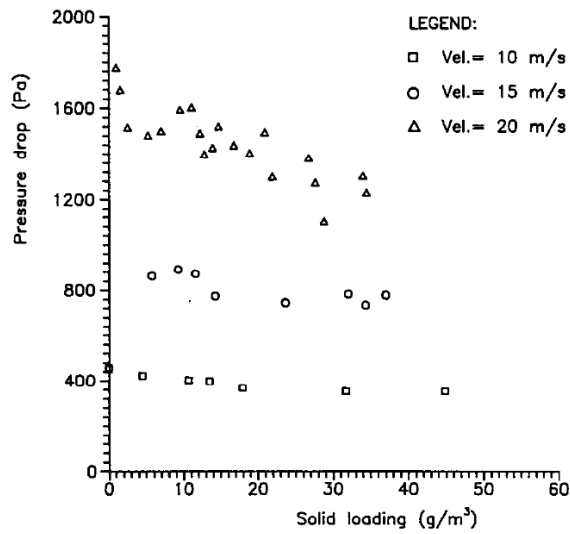


Figure 14 – Pressure drop as a function of solid loading and gas velocity [38].

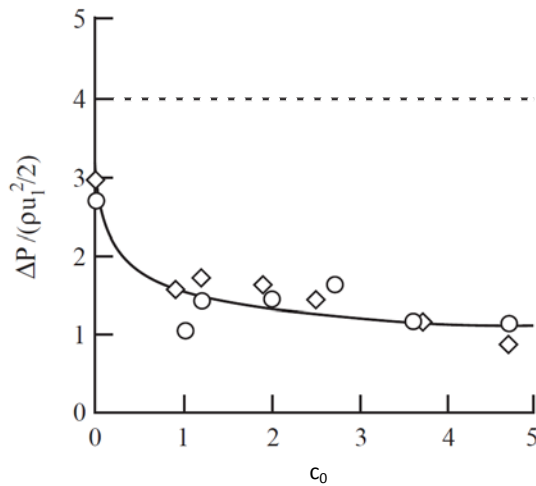


Figure 15 – Dimensionless pressure drop ratio as a function of solid loading and gas velocity [41]. Squares: Glass spheres with $d_p = 97 \mu\text{m}$, circles: plastic powder, $d_p = 136 \mu\text{m}$. Full line is model prediction by Muschelknautz and Greif [32], dashed line is model prediction by Leith and Licht [30].

Experiments carried out by Wang et al. [42] on a Lapple cyclone with $D = 0.2 \text{ m}$ confirm the rule of thumb regarding overall collection efficiency and pressure drop dependencies of the inlet velocity, as shown in Figure 16. The particles used were cement raw meal with average diameter of $29.90 \mu\text{m}$. The data indicate that the pressure drop increases by a factor of 17 when the gas velocity is increased from 5 to 35 m/s. The collection efficiency is increased from 86%

to 96 % in the same gas velocity range. The solid load during the experiments is not reported. The trends observed here are generally confirmed [20,39,40].

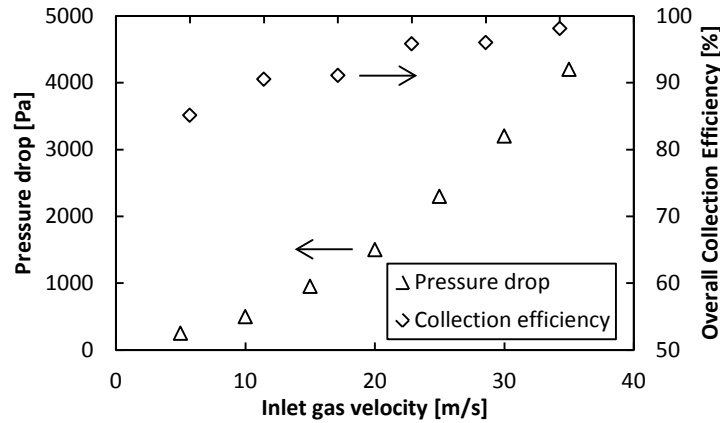


Figure 16 – Experimental data for cement raw meal with $D_p = 29.90 \mu\text{m}$ as reported by Wang et al. [42]. c_o is not provided.

The internal two phase flows in cyclones are complicated and not easily modeled in detail. Common CFD simulation tools are capable of describing gas flow with very low dust load accurately, including pressure drop [20]. However, effect of solids in the gas complicates the models. Chu et al. [40] have successfully developed a model combining CFD and discrete element methods to describe the behavior of cyclones at different solid loadings. The deviations between the model and experimental data on collection efficiency and pressure drop are less than 10%. Their findings indicate that when solid loading increases, the tangential component of the gas velocity in the cyclone decreases, which is the reason for lower pressure drops.

2.2.2 Cement Preheater Cyclones

The cyclones used in cement preheaters are generally designed to match the following criteria:

- Low pressure drop ($\Delta P < 800 \text{ Pa}$)
- Acceptable collection efficiency ($\eta > 0.80$)
- High temperature tolerance ($T_{\text{max}} \sim 850 - 890 \text{ }^\circ\text{C}$)
- Long lifetime (steel structure > 30 year, refractory and vortex finder > 5 year)
- Low thermal heat loss

The operation conditions in modern cement plants will be presented in detail in section 2.2.3 – *The Cyclone Preheater Process and Operational Conditions*, Table 6, but selected parameters are summarized in Table 3.

Table 3 – Selected operation conditions for cyclones in the cement industry.

Parameter	Value
Solid load, c_o	0.67 – 1.2 kg solid /kg gas
Inlet gas velocity	14 – 20 m/s
Outlet gas velocity (at the vortex finder)	20 – 25 m/s
Typical temperature range	50 °C – 890 °C

The preheater cyclones operate at temperatures up to around 890 °C at significantly higher solid loads than in dust removal cyclones, which complicates the design, increases wear on internal surfaces, and reduces life time of the cyclones.

The low pressure drop (LP) cyclone design used today is originally developed by FLSmidth in the 1980s. Compared to the previous cyclone designs, these cyclones reduce the pressure drop by up to 40 – 50 % [19,46]. The LP cyclones have wrap-around inlets which extends 270° as well as larger gas inlet and outlet areas [46,47]. The vortex finder is also enlarged. A comparison between a traditional cement preheater cyclone and a LP cyclone is illustrated by Figure 17.

The process conditions change down through the preheater tower, why the design of the cyclones changes to maintain optimal performance. Four examples of cyclone designs for different stages are shown in Figure 18.

The top stage cyclones are slimmer than the other stages in order to optimize collection efficiency and reduce dust loss [3], while the cones on the lower stage cyclones have several inclinations to reduce solid build-ups. Note also that the vortex finder extends further into the cyclone in the upper stages compared to the lower stages. This results in lower pressure drop and collection efficiency for the lower stage cyclones [3]. Typical overall collection efficiencies in the cement plant cyclones are between 0.70 – 0.95, with highest collection rate at the top cyclone [19].

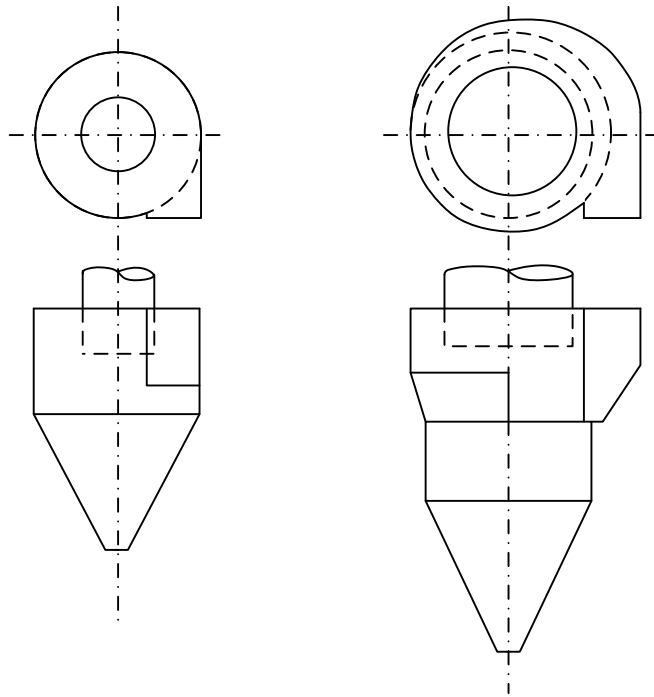


Figure 17 – Comparison between a standard cyclone (left) and a low pressure (LP) cyclone (right). Top and side views are shown.

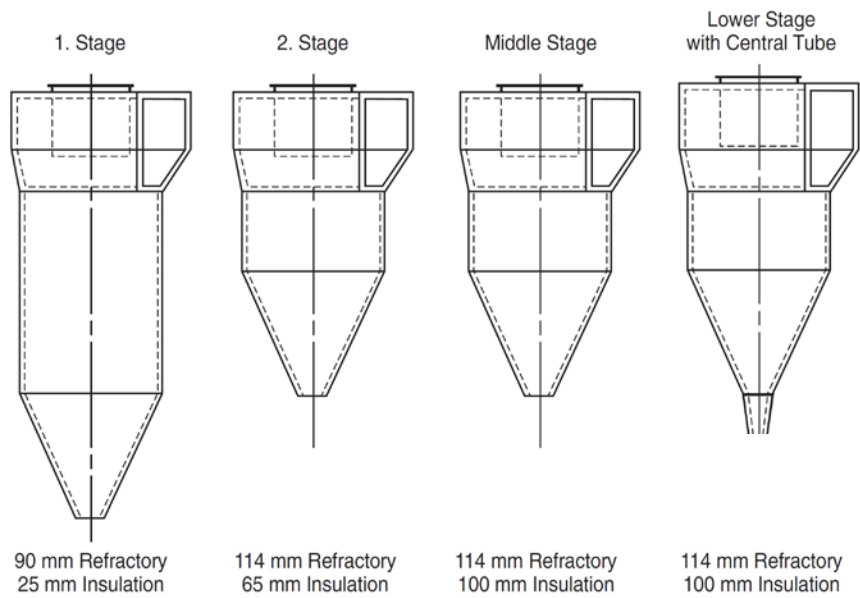


Figure 18 – Design of cyclones for use in the cement industry [3].

The cyclones are typically constructed of plain carbon steel, lined with refractory and insulation for improved lifetime and lower thermal heat loss [3]. As the top stages are colder than the bottom stages, thinner lining are used. The vortex finder of the cyclones is essential for achieving the desired collection efficiency, but especially in the lower stages, the process temperatures and the presence of chloride, sulfur and alkali reduces the lifetime of the vortex finders. To overcome this problem vortex finders constructed of special heat and corrosion resistant metal alloys or ceramics have been developed. These vortex finders can be constructed of minor segmented parts, allowing replacement through the manholes found in the cyclones [3,4,48,49], reducing replacement complexity and costs.

The most recent development within cement plant cyclones includes the addition of a double vortex finder and outlet vanes. Comparing to a standard cyclone, the pressure drop can be reduced by 50 % in addition to an improved collection efficiency; up to 98 % at 5 – 30 μm can be achieved [50]. The concept (Hurriclon®) is illustrated in Figure 19. More than 150 installations in various industries have been reported since 2000 [50,51]. The application of the Hurriclon® is typically the upper stages of the preheater, where thermal wear is less significant.

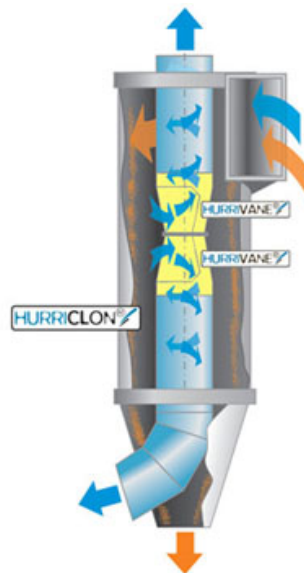


Figure 19 – Cyclone with a double dip tube installed. The unit is marketed as a Hurriclon® by ATec, Austria [51].

The size of the cyclones depends on local gas velocities in the preheater and thereby the production rate of the cement plant. Figure 20 summarizes cyclone sizes and production rates

from six sources [8,14,52–55]. The cyclone diameters are found to vary between 4.5 m and 8.5 m. Note that this applies for the middle and lower stage cyclones. Top stage cyclones are around 30 % smaller in diameter [8]. The cyclone stage heights have been reported to range from 11 m (3400 TPDc facility [55]) to 20 m (12000 TPDc facility [14]).

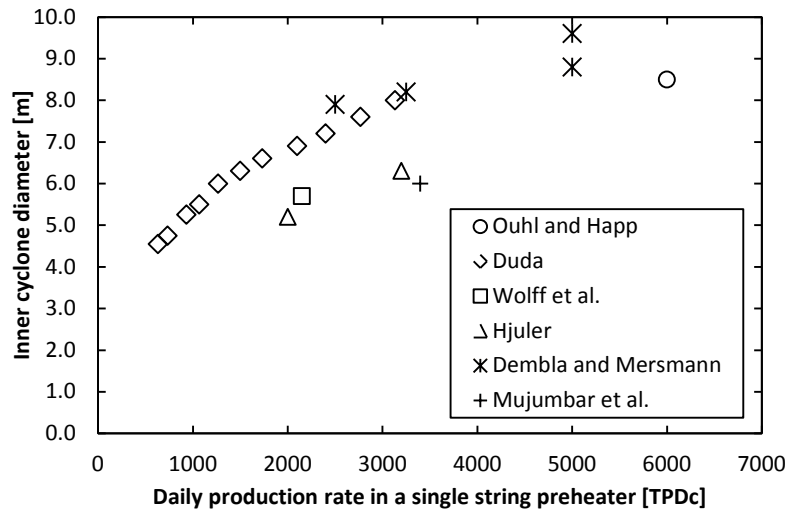


Figure 20 – Typical sizes for lower stage cyclones as a function of daily production rate in tons clinker per day (TPDc). Sizes for the top stage cyclones are typically smaller than indicated here. Data from Duda [8], Ouhl and Happ [14], Wolff et al. [52], Hjuler [53], Dembla and Mersmann [54], and Mujumbar et al. [55] are displayed.

Data describing cyclone design for application in cement plants are not commonly found in academic or patent literature, probably due to companies protecting their designs. Some available data is presented in Table 4: Bernardo et al. [56] have reported the geometric proportions of preheater cyclones. Similar proportions, except the inlet size, have been reported by Bhatti [3]. Compared to standard cyclones, exemplified by the Stairmand cyclone, cement cyclones are lower and has a shorter vortex finder.

The operation characteristics and performance of the cyclones applied in the cement industry are in many aspects similar to cyclones applied in CFB, which several research groups have worked with, including [36,39,41,45]. Selected CFB cyclone designs are provided in Table 4.

Table 4 – Cyclone geometries in CFBs and cement preheaters. The high efficiency Stairmand cyclone design is provided for comparison.

Source	Application	Inlet	a/D	b/D	D_x/D	S/D	$(H-H_c)/D$	H/D	D_d/D
Stairmand [22]	General	Tangential	0.5	0.2	0.5	0.5	1.5	4.0	0.375
Bhatty [3]	Cement preheater	Wrap-around, 270°	0.6	0.3	0.6	0.4	1.3	2.1	0.2
Bernado et al. [56]	Cement preheater	Wrap-around, 180°.	0.34	N/A	0.57	0.43	0.71	1.7	0.16
Dewil et al. [36]	CFB	Tangential	0.66	0.31	0.51	0.23	1.4	2.6	0.18
Tuzla and Chen [45]	CFB	Wrap-around, 180°.	0.61	N/A	0.62	0.75	1.3	3.5	0.32

Despite the need for a low pressure drop in the CFB systems, literature mainly considers cyclones with tangential inlet cyclones instead of wrap around inlets. Only Tuzla and Chen [45] reports an wrap-around inlet. According to Tuzla and Chen [45] the highest possible collection efficiency of the CFB cyclones is essential due to the high particle loadings in the CFB systems, typically up to 8 kg/kg. A high collection efficiency of CFB cyclones increases the system efficiency, due to a reduced loss of unreacted particles. This is contrary to the cement preheater cyclones where reductions of the pressure drop while maintaining collection efficiencies above 0.70 – 0.80 has been the major development focus of the preheater cyclones.

2.2.3 The Cyclone Preheater Process and Operational Conditions

The preheating facility of a given cement plant is designed to match the conditions at the plant site, including chemical and physical properties of raw materials and fuel, local legislation, and process specifications. Therefore generic preheater conditions can only be presented with wide intervals. The data provided in the following sections exemplifies operation characteristics and process configurations typically encountered. Site specific data may deviate significantly from the stated.

Preheater configurations

The cement plant suspension preheater consists of stages, each containing a riser duct and a cyclone. In each stage, raw meal is fed into the riser duct where it is distributed and entrained in the rising gas. A splash box is placed at the particle feed point to fan out the particles across the cross sectional area of the riser duct, thereby improving the entrainment of the particles. The gas and entrained particles are led into the cyclone, where the two phases are separated. At the bottom of the cyclone, a one-way valve ensures that gas is not moving up through the particle feed pipes. A schematic drawing of a preheater stage is illustrated by Figure 21.

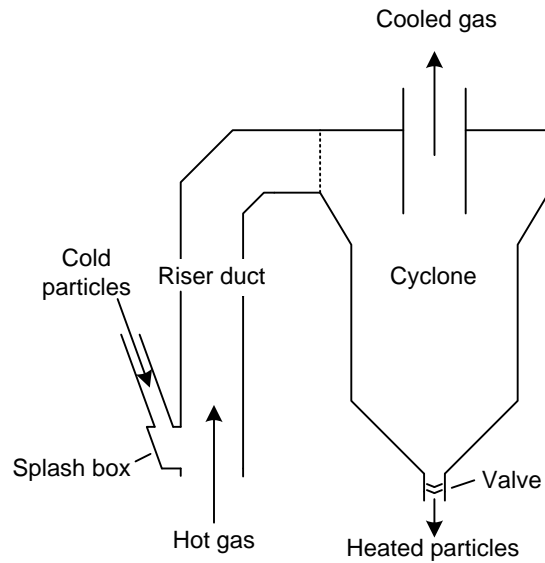


Figure 21 – Heat exchange stage in a preheating process in a cement plant.

The energy transfer from the gas to the particles flowing co-currently takes under ideal conditions less than 0.01 second [57] due to the high contact area ($d_p = 5 - 20 \mu\text{m}$), and in practice less than one second [19]. While some experiments suggest that around 80 % of the heat exchange takes place in the riser and 20 % in the cyclone [8], it is generally accepted that the energy transfer only takes place in the riser duct, as shown by Delong and Daohe [58], and the cyclones act only as separators [3,57,59]. The residence time of the particles in a preheater stage has been measured to approximately eight seconds [1,60], and the gas residence time to one to two seconds [61]. The average residence time in the preheater is around 10 seconds for the gas and 50 seconds for the particles.

To ensure a stable particle flow from the bottom of each cyclone and to prevent back flowing gas, particle gates are installed below each cyclone; typically a spring or weight controlled tipping gate, which allows particles to move down while preventing gas moving up. Depending on the raw meal flowability and the quality of the fuel, air blasters may be installed at the bottom of the cyclones to insure a stable particle flow and break up deposits. Industrial experience suggest that the particles become more sticky as temperature increases, increasing the need for air blasters at the particle outlets of the lower stages cyclones [62].

The individual preheater stages are combined in a counter-current pattern leading to a stepwise heating of the particles where the number of stages influences the overall heat exchange process. Each additional stage increases the overall heat exchange efficiency, but also increases

pressure drop, heat loss, construction costs, and building height. The increase in thermal efficiency declines for each additional stage and will, at a given point, be balanced by additional costs. Pressure drop, installed costs, and specific thermal energy consumption of selected suspension preheater systems are provided in Table 5. For comparison kiln systems with no suspension preheater are also shown.

In modern cement plants, the preheaters typically consist of four to six cyclone stages, with five stages combined with an inline calciner (ILC) being the most common state of the art [3,61].

The optimum number of stages depends especially on the moist content in the raw materials and fuel as well as the contents of sulfur, nitrogen, volatile hydrocarbons, and heavy metals [63]. Above a production capacity of 6000 TPDc multiple preheater strings are installed, as this is most economically feasible [3,19]. The thermal energy consumption of new plants is in the range 2.9 – 3.3 MJ/kg clinker [61].

Table 5 – Operation characteristics of selected suspension and kiln preheating processes [3,18].

Preheater process	Specific thermal energy consumption (MJ/kg clinker) [18]	Pressure drop (Pa) [3,4]	Normalized installation cost [3]
Wet process with internals	5.86 – 6.28	-	-
Long dry process with internals	4.60	-	-
1-stage cyclone pre-heater	4.18	-	-
2-stage cyclone pre-heater	3.77	-	-
4-stage cyclone pre-heater	3.55	-	-
4-stage cyclone pre-heater plus calciner	3.14	4000	100 %
5-stage cyclone pre-heater plus calciner ^A	3.01	4650	111 %
6-stage cyclone pre-heater plus calciner	< 2.93	5180	122 %

^A Standard configuration for new plants.

Preheater operation and process conditions

An illustration of a preheating facility in a cement plant with a five stage cyclone-based preheater and an ILC is shown in Figure 22. Despite this system being termed a five stage preheater, only four heat exchange steps are obtained before the heated raw meal is fed into the calciner. The bottom cyclone, called the calciner cyclone, does not contribute to the preheating process as it separates the gas and calcined particles.

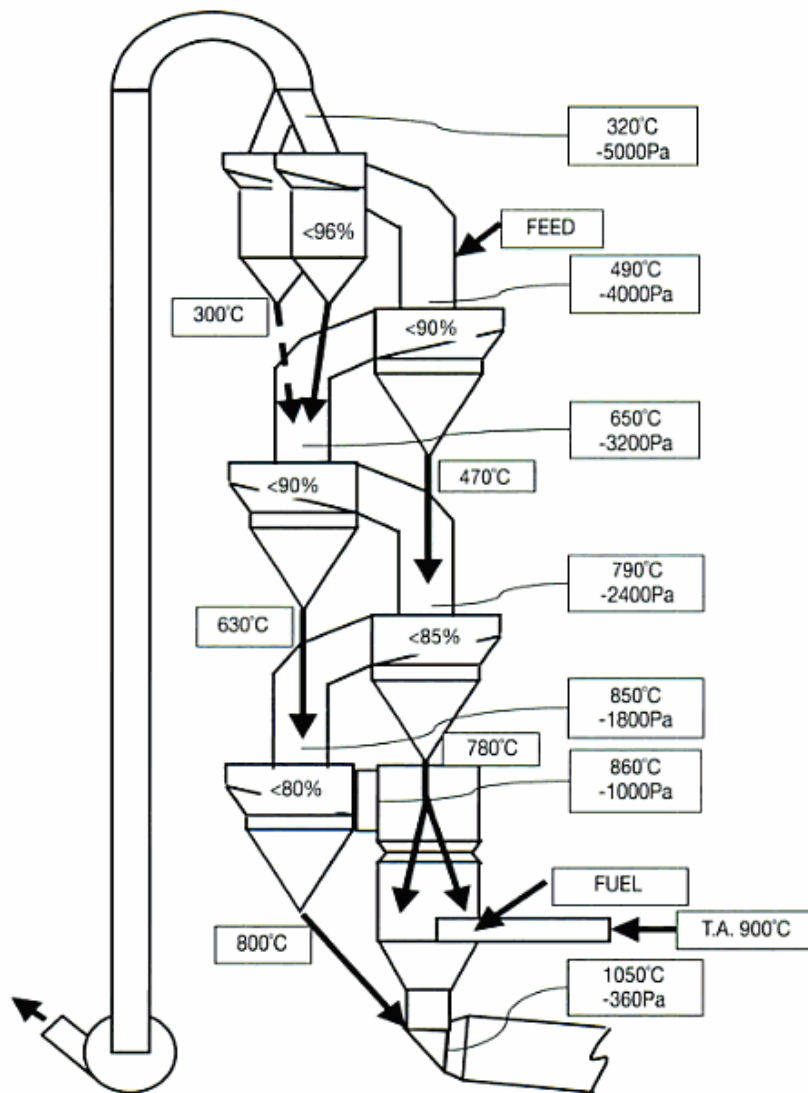


Figure 22 – A five staged cyclone preheater and calciner with relevant process conditions [19].

The gas inlet and exit temperatures shown in Figure 22 are approximate values, 850 °C and 320 °C respectively. Other sources report inlet gas temperatures of 890 °C and exit temperatures down to 270 °C [4]. Despite large contact area between particles and gas and the short thermal equilibrium time, temperature differences of up to 20 °C between gas and particles leaving a stage has been reported [19]. This is likely caused by either insufficient mixing or local surface heat loss effects.

The pressure drop in the depicted preheater facility is reported to be 4.0 kPa. Pressure drop for similar designs range from 2.7 – 4.6 kPa [3,4]. The gas is moved through the kiln, calciner, and preheater at subatmospheric pressure by the induced draft (ID) fans located after a gas

conditioning facility at the gas exit of the preheater. The ID fans utilize 5 – 8 Wh/kg clinker, corresponding to 30 % of the power consumed in the pyroprocessing part of the cement plant. The total specific electrical consumption of a plant is around 80 - 110 Wh/kg clinker [4,18,64,65].

Due to the higher temperature, the gas volume is larger in the lower stages of the preheater. To reduce the pressure drop without significantly increasing cyclone size, collection rates as low as 70 – 80 % are accepted. In the top stage, two smaller cyclones are used as high collection efficiency is desired in order to reduce the dust leaving the system with the gas. Desirable collection efficiencies for the top stages are higher than 95 % [4,19,49,66], while actual efficiencies may be as low as 80 % [59]. Typically found values range from 90 % to 95 %.

As collection efficiencies are lower than one, internal recirculation of dust in the preheater occurs. At the lower stages, the internal particle stream is at least 40 %⁵ larger than the feed stream. This recirculation is undesired as it (a) increases pressure drop (caused mostly by additional particle wall friction) and more importantly (b) reduces the thermal efficiency by moving hot material in an undesired direction. Due to the high collection efficiency at the top stage cyclones, little solid material leaves the preheater with the gas, despite the low collection efficiencies at the bottom stages.

Table 6 summarizes the typical operation conditions in the cyclone suspension preheater system.

⁵ Estimated from mass balances, based on data provided in Figure 22. For further details on the model, please refer to Chapter 3.

Table 6 – Typical operation conditions for cyclone preheaters in cement plants.

Parameter	Value	Source
Raw material fed to preheater	1.5 – 1.7 kg / kg clinker	[1,67,68]
Gas flow in preheater	1.7 – 2.7 kg / kg clinker	[57,67,68]
Solid load (fed) ^A	0.56 – 1.0	-
Solid load (internal flow) ^B	0.67 – 1.4	[19]
Gas composition	30 – 38 % CO ₂ , 3 – 5 % O ₂ , Balance N ₂	[57,67]
Inlet gas velocity ^C	14 – 20m/s	[8]
Outlet gas velocity (in the vortex finder) ^C	20 – 25 m/s	[8]
Particle inlet temperature range	50 – 60 °C	[1,59,68]
Gas temperature range	270 – 890 °C	[1,19]
Particle temperature range	50 – 790 °C	[1,19,68]
Average temperature difference between gas and solids after heat exchange	~ 20 °C	[19]
Gas residence time per stage	1 – 2 seconds	[1,60]
Particle residence time per stage	~ 8 seconds	[1,60]
Dust loss ^D	5 – 11 %	[19,59]
Pressure drop per stage	500 – 800 Pa	[3,19]
Heat loss from preheater	4 % of thermal energy input	[55,68]

^A Computed from feed rates.

^B Computed from gas feed rate and internal mass flow

^C Computed assuming a cyclone geometry as stated in Table 4, $b = 0.2 \cdot D$, and an average temperature of 500 °C.

^D Computed using collection efficiencies provided by [19,59]. Data for six different plants are available.

The preheater tower

The process equipment is mounted in a steel or concrete structure. The total height, typically ranging from 80 m to 120 m [18,61,63], is a result of (a) the cyclone geometry, (b) the length of the riser ducts, and (c) the location of the calciner cyclone. Preheater structures up to 135 - 150 m have been reported [54,69]. The calciner cyclone must be placed above than the kiln inlet, which is typically located 10 – 20 m above the ground. Furthermore, the angle of the particle transport pipe between the calciner cyclone and the kiln should be inclined about 60° – 70° to ensure stable particle flow.

The preheater tower typically contains six or seven decks with a size of 14 – 20 by 18 – 24 m [70,71]. Besides the cyclones and risers, the preheater tower also supports the kiln inlet, the

calciner, the fuel and particle lift systems, the gas exit ducts, filters, alkali bypass, access platforms, and elevators. A picture of a preheater tower is shown in Figure 23.

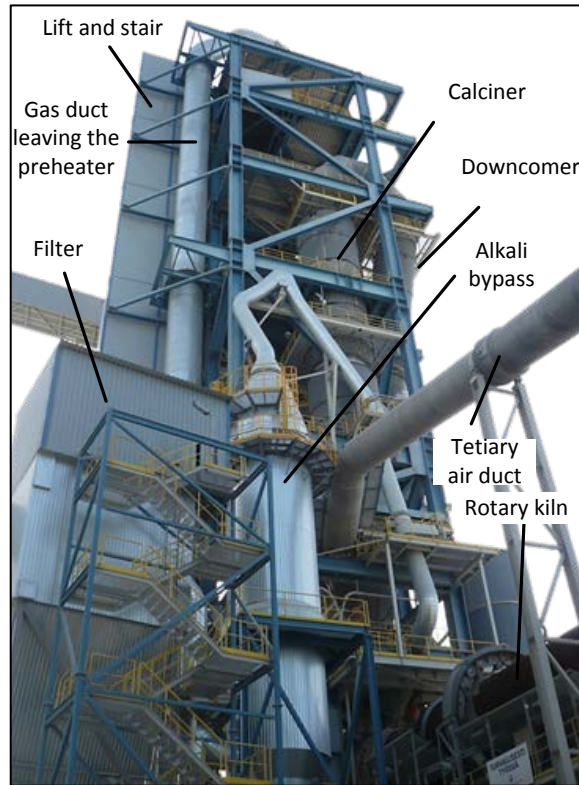


Figure 23 – A preheating facility in a cement plant. Calciner, tertiary air duct, gas exit duct, particle filters, alkali bypass, and kiln inlet are visible. Total height of tower: 110 meters [72].

2.2.4 Current Preheater Research

Current preheater research is focused on four main topics: (a) reductions of capital costs, (b) reductions of emissions, (c) adjustments for alternative fuel firing, and (d) co-generation of electricity.

Reduction of capital costs

The reduction of the capital costs is typically achieved by a reduction of cyclone vessel size, simpler cyclone geometry, and a more compact arrangement of the cyclones in the preheater tower. Several compact cyclone designs have been developed, but none are currently commercially available for cement production. An example is the co-current cyclone, originally

patented in 1934 [73], where both particles and gas leaves the cyclone in the bottom. This design can reduce the cyclone stage height by a factor of 2.5 if successfully introduced in the cement plant [63]. Horizontal cyclones [74], tilted cyclones [75], and compact cyclones [76] are other examples of designs seeking to reduce construction height. Also cyclone designs that reduces the construction costs due to a simple geometry has been available for several decades [77]. These designs have not been accepted by the cement manufactures, either due to insufficient performance, or a general conservatism in the cement industry.

Reduction of emissions

The reduction of emissions are driven by legislation on species such as; SO₂, NO_x, CO, volatile hydrocarbons, particulate matter (PM), and potentially also CO₂ [3,59,63,78].

The SO₂ emission from the cement plant originates from pyrites in the raw meal. The SO₂ formed in the combustion zones are effectively captured by the presence of active CaO, thereby forming CaSO₄. In the preheater, the temperature at the release of SO₂ is too low for the CaO in the raw meal to be active [78]. To solve this problem it has been suggested to inject hydrated lime in the top stages for the preheater system [59,78], alternatively a wet scrubber may be added for close to full capture of the SO₂. A rule of thumb is that 50 % of the sulfide content will be released in the preheater [79].

The NO_x emissions are reduced by introducing low NO_x burners in the kiln, thereby reducing the formation of thermal NO_x, by creating reducing conditions in the calciner, and by injection of ammonia in a SNCR process at the kiln inlet [78,80,81].

In modern cement plants, where fuel combustion is well controlled, the CO emissions are formed in the middle stages of the preheater, where carbon in the raw meal partly combusts. A complete combustion is not achieved due to the low oxygen levels. For sites with a high content of carbon in one of the components forming the raw meal, this component may be fired directly into the calciner, thereby completely combusting the carbon. Alternatively a regenerative thermal oxidizer may be added in the gas treatment facility, fully combustion all carbon species on the exhaust gas, including hydrocarbons [78].

The emissions of PM from cement plants originate from the pyroprocessing unit, the particle conveying systems, and the mills. Typically fabric filters or electrostatic precipitators are installed on all PM generating operations. For cleaning of the exhaust gases from the

pyroprocessing unit, electrostatic precipitators are used because of high temperatures. Precipitated material is recirculated back to the process [3].

In 1995, Klotz [63] predicted that focus would shift towards reduction of CO₂ emissions driven by a public focus on climate changes. By signing the Kyoto protocol in 2005, the European countries committed themselves to a 8 % reduction of greenhouse gases before 2012, compared to 1990-level. This led to the introduction of the EU emission trade system (ETS), where a quota system were created for CO₂ emissions for selected heavy industries [82]. Due to low quota prices and global economic recession, the EU ETS has not lead to a significant increase in the development of innovative low carbon emitting technologies [83]. For cement plants the most promising low carbon emitting technology is post process carbon capture (CC) by carbonate looping and oxyfuel firing [84]. In the CC process, the gas used for preheating of the raw materials will be the gas from a oxyfuel fired calciner, which operates at temperatures around 950 °C due to shifted calcination equilibrium caused by the high CO₂ content in the gas. The gases available from the oxycalciner will contain more than 80 % CO₂ and be of similar mass flow as the standard process, why more energy will be available for heat exchange due to higher heat capacity of CO₂. Furthermore, due to the higher molecular weight of CO₂-rich gas, the gas volume will be approximately 25 % lower [84]. The cyclone-based preheating process can still be used at these process conditions, with a potential for reducing vessel size and/or pressure drop.

Use of alternative fuels

The use of alternative fuels (AF) arose from the increased availability and need for incineration of waste. However, the complex chemical composition and physical diversity of the AF can be problematic for transport systems and burners as wells as the influence on the cement clinker chemistry and build-up of deposits in pyroprocessing unit can pose problems [6]. The moist content in AFs is up to 25 wt%, which increases the volume of the exhaust gas flow and increases the specific energy consumption for the clinker production [85].

The cost of size reduction of the AF implies that relatively large particles are fed to the calciner, and to accommodate a complete burnout, longer residence times are needed. To obtain this, the calciner is elongated and equipped with a loop and long downcomer, thereby increasing residence time at combustion conditions. In some cases, the residence time is too low to archive a complete burnout, and burning particles are found in the lower stages of the preheater tower [72]. In certain cases to achieve high residence times, a calciner modified for AF firing can be

of similar height as the preheater tower itself [54,72,85]. Other problems with the AF firing include increased deposit build-ups in the system caused by chlorides and alkali metals. The depositions are found on local cold spots in the calciner and preheater system, where alkali and chloride components condense and stick to process equipment surfaces.

The consequence of AF firing on preheater design involves larger gas flows caused by higher moist levels and lower heating values, unburned particles in lower stages of preheater, increased deposition of alkali and chloride components, and increased calciner size. Thus, when firing large amount of AF, the preheating equipment is expected to be larger or higher pressure drops need to be accepted.

Introduction of electricity cogeneration

Waste heat recovery (WHR) systems producing electricity are introduced in the cement plants for various reasons: (a) Utilization of thermal excess energy, (b) reduction of operation costs by production of electricity, and (c) compliance with local legislation.

From the clinker cooler, and in some cases also from the preheater, gas streams with temperatures of around 280 – 400 °C are available for electricity production [67]. Due to the relative low temperatures power production processes used in traditional power plants are ineffective. Instead ammonia-based Kalina cycles can be utilized with acceptable efficiencies, when gas temperatures are above 300 °C [86]. Of the available thermal energy in the exhaust gases, 20 – 25 % can be converted to electricity [64,65], covering 30 % – 44% of the plant's electricity need [65,67,87]. These facilities can be retrofitted onto existing plants and run separately without influencing the cement production. From an economy point of view, a ten percentage reduction of the overall operation costs with the introduction of a WHR system has been reported [67]. However, for plants with a need for drying raw materials, no suitable heat streams is available for a WHR system.

High temperature reservoirs that could be used for increased efficiency of the WHR process, and increase the amount of electricity produced, are from a process condition point of view available in the preheater system, but currently it is not feasible to introduce heating surfaces directly into the cyclone due to the cylindrical geometry, limited space and high dust load.

2.3 Shaft Preheaters

The shaft preheaters were developed as alternatives to the cyclone preheating processes and consist of single, closed, vertical shafts, in which a direct heat exchange between gas and solids was facilitated. The gas and particle flow patterns, and thereby also the heat exchange process, depended on the design and layout of the shaft and its internal constrictions. The shaft preheaters either facilitated a counter-current process or a stage-based co-current heat exchange process.

The two main advantages of the shaft preheaters are that they are (a) self-supported structures and (b) can facilitate a counter-current heat exchange process, which is more energy efficient than the stage-based processes. The fact that the shaft preheaters are self-supporting reduces capital costs as no additional scaffolding or structural support is needed for the preheater. Thus, the potential of the shaft preheater is to reduce both capital and operational cost of the preheating facility. Other parameters such as overall pressure drop and height of the preheater can potentially also be reduced. This is possible as the designs are not limited by the geometry of the cyclones. Furthermore, the shaft preheaters are less sensitive to build-ups and blockages of ducts, compared to the cyclone preheaters.

In the following sections, a series of shaft heat exchanger designs will be presented. The advantages and disadvantages of each design will be outlined, and a summary will conclude the presented designs. These designs are mainly found in the patent literature, whereas little can be found in the academic literature.

The shaft preheater designs will be named by their principle of operation, after their inventor, and/or by their denomination in the literature.

2.3.1 Counter-current Shaft Preheaters

The counter-current shaft preheater are characterized by facilitating a true counter-current heat exchange process, which, in terms of energy efficiency, is the most effective process possible.

FLSmidth Helix preheater

The FLSmidth Helix preheater is developed for preheating raw meal and was patented in 1969 [88]. The design consists of a vertical shaft with a smooth sloping helix shaped constriction inside. An illustration of the design is given in Figure 24. Once entering the top of the shaft, the cold particles move onto the helix and towards the central opening of the shaft due to the inward slope of the helix-shaped surface. At the central opening, the raw meal is mixed with the rising

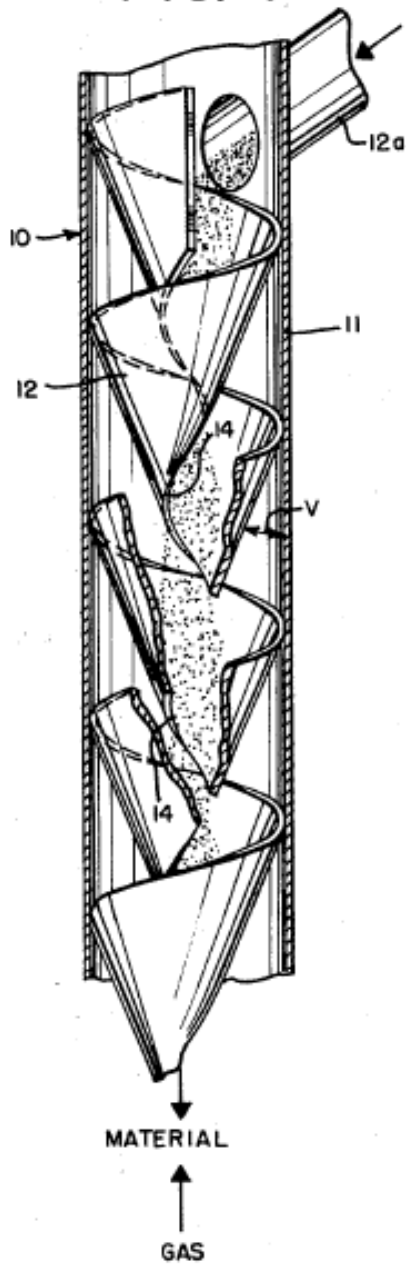
gas, which is being fed from the bottom of the shaft. The helix geometry creates a swirling motion of the gas, facilitating a separation of the two phases.

The particles and gases exchange heat and separate continuously down through the shaft, creating a continuous heat exchange process. The particles are intended to follow a combined spiral and helix movement [88]. According to the patent [88] the heat exchange is very efficient and the total height of the preheating facility can be reduced if this principle is applied in a cement plant.

The design of the FLSmidth Helix preheater will potentially allow particles to move down through the central opening, while the gas will move in a swirling upwards motion under the ceiling of the helix around the central opening, thus never coming in contact with the downward flow of particles. If this is the case, high gas exit temperatures and poor heat exchange performance must be expected.

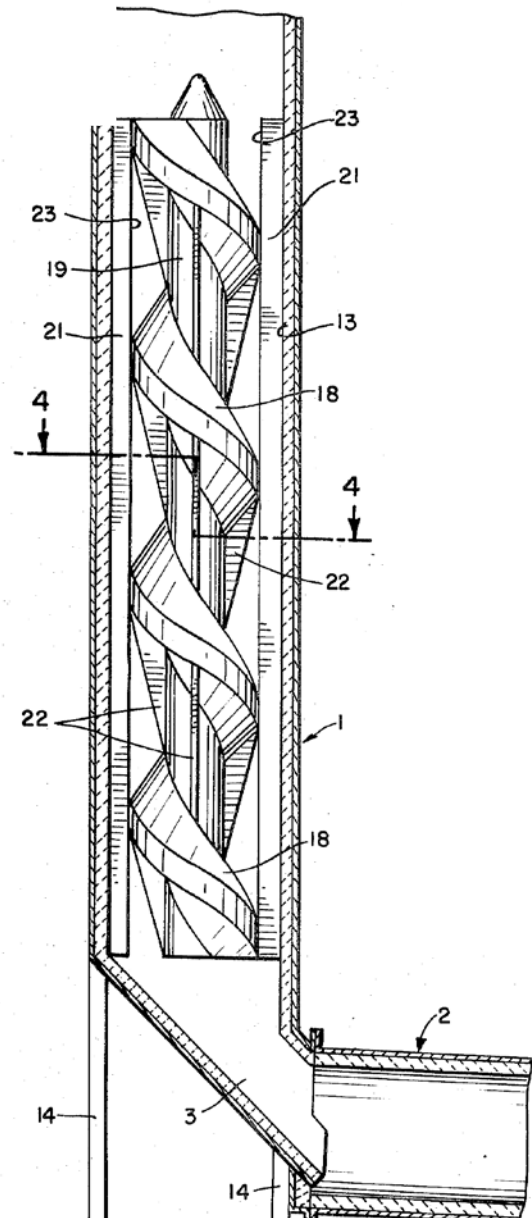
These issues have also been considered by the engineers of FLSmidth, as a modified design was patented shortly after the original helix design [89]. The modified design, presented in Figure 25, is different from the original helix preheater in several ways: (a) There is no central opening in the middle of the helix, (b) the surface of the helix is sloping towards the outer wall of the shaft and (c) baffles have been installed below the ceiling of the helix and on the shaft walls to interrupt the gas flow to ensure a more turbulent flow and a better mixing of particles and gas.

For both versions of the FLSmidth Helix preheater, cyclones are installed on top of the shaft for separating the gas and entrained dust, which is returned to the shaft. Separation efficiencies in the shaft are not high, why a substantial amount of internal recirculation would be expected.



- | |
|---------------------------------------|
| 10 Preheater |
| 11 Shaft |
| 12 Helix |
| 12a Material inlet |
| 14 Central opening |
| V Angle between helix and shaft walls |

Figure 24 – Internal view of the helix in the FLSmidth Helix shaft preheater [88].



- | | |
|--------------------------|-------------------------------|
| 1 Shaft | 18 Downwardly sloping surface |
| 2 Rotary kiln | 19 Helical column |
| 3 Kiln inlet | 21 Free space |
| 4 Cut section (not used) | 22 Baffles |
| 13 Refractory lining | 23 Vertical partitions |
| 14 Support pillars | |

Figure 25 – Schematic drawing of the modified FLSmidth Helix heat exchanger mounted in the kiln assembly [89].

Other counter-current shaft preheater designs

Several other shaft preheater designs have been patented. A few of the more promising counter-current processes are shortly summarized in Table 7.

Table 7 – List of additional counter-current shaft preheater designs.

Preheater name	Patent year	Comments	Source
Raining bed	1999	Developed for partially calcining of limestone and heating of glass cullets. Particles are distributed over the cross sectional area of the shaft and 'rains' down against the rising gas. The process is driven by gravity.	[90]
Wilhelm-Röder	1956	Developed for cooling of particles. Particles move downwards distributed on a spiral, while gas from a central vertical pipe exits through gaps in the spiral. Can work as a particle heater. Process not truly counter-current, as gas only makes one direct heat exchange with particles. Remaining heat exchange effects are indirect.	[91]
Dorst Counter-Current	1993	Developed for preheating of raw meal. Consists of a shaft with a helix structure inside. In the center of the helix is a vertical shaft. Gas slits are made in helix surface, allowing gas from beneath the helix to enter up through the slit while heat exchanging with the particles located on the helix surface.	[92]

2.3.2 Multistage Shaft Preheaters

The stage-based processes are in theory less efficient than the true counter-current processes, but for application in the cement industry the stage-based processes are easier to control and operate.

FLSmidth Zig-Zag preheater

The FLSmidth Zig-Zag preheater consists of a zig-zag shaped shaft, patented in 1963 [93]. A drawing of the system, including transport patterns for gas and particles, can be found in Figure 26.

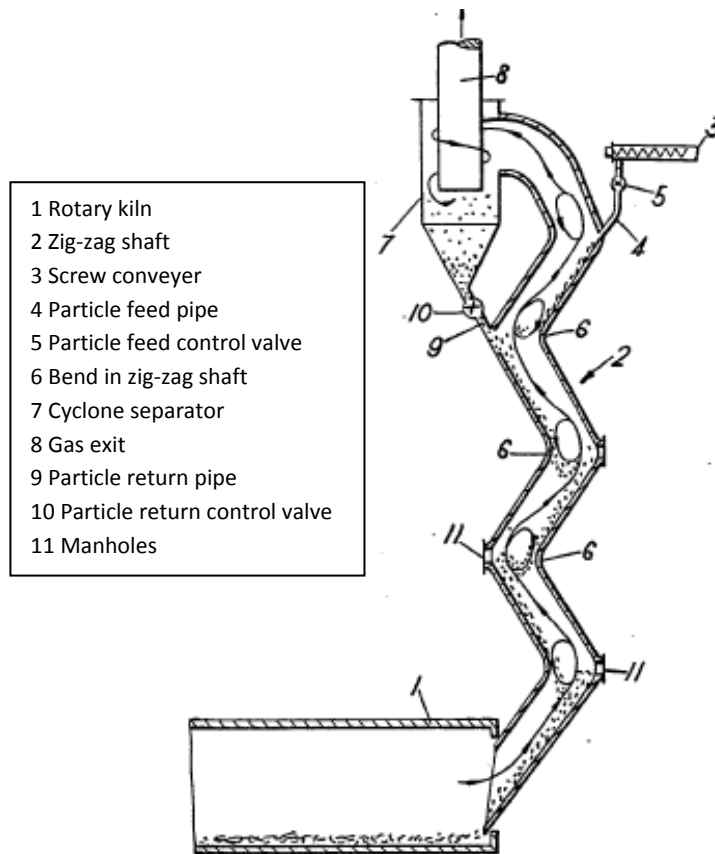


Figure 26 – Schematic drawing of the FLSmith Zig-Zag heat exchanger installed in a rotary kiln assembly [93].

At the bends in the shaft the particles moving along the downward sloping surfaces will be entrained in the gas, and as the gas also changes direction, some of the particle will be separated from the gas and collected at the walls and the sloping floor. The particles will then slide down the floor until they are reentrained at the subsequent bend. The heat exchange in the straight sections is limited due to small contact areas. According to the inventor [93], the system should internally recycles up to four times the feed stream to perform optimally. The entrained particles that leave the shaft are returned using a cyclone.

As the large recycled streams reduce the thermal efficiency, increases the pressure drop, and wear, this illustrates that at the time of patenting, the full consequences of the particle recirculation were not thought through. Later designs, such as the helix designs [88,89] try to address these issues.

FLSmidth Titan preheater

The operation principles of FLSmidth Titan⁶ preheater [94] resembles the concept of the FLSmidth Zig-Zag heat exchanger, where areas with local mixing are achieved. Internal baffles divide the shaft into chambers and guide the gas flow through the shaft.

The baffles create local eddies which ensures a good local mixing of gas and particles. The particles separated from the gas by the swirling gas motion, will end up on the sloping plates and move towards the center of the shaft, eventually being re-suspended in the gas. The gaps between the baffles are designed to obtain the desired flow patterns and gas velocities (5 to 15 m/s) [94]. To further ensure the flow of particles through the system, vibrators may be installed at each baffle. See Figure 27 for further details.

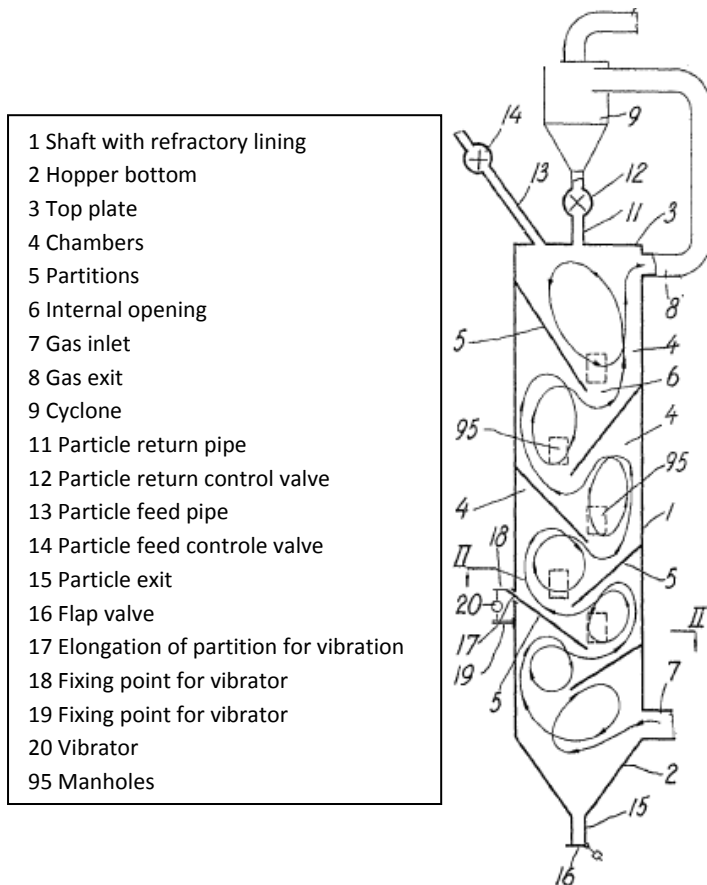


Figure 27 – Schematic drawing of the FLSmidth Titan heat exchanger [94].

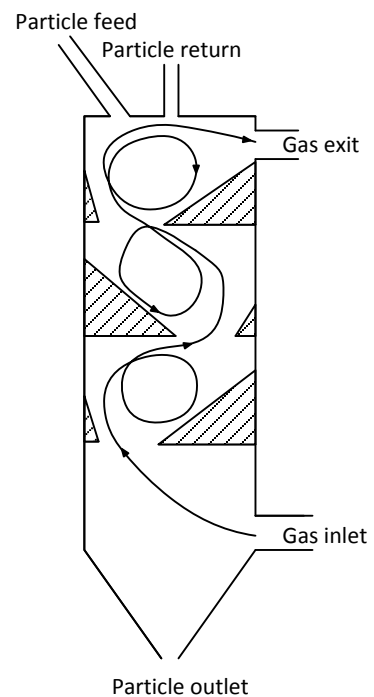


Figure 28 – Alternative baffle design and dust separation device for the FLSmidth Titan heat exchanger [94].

⁶ The name Titan refers to the name of this device internally used in FLSmidth A/S.

Several different baffle geometries have been suggested. An example of a different partition design is illustrated in Figure 28. The slopes of the partitions in the system depicted in Figure 28 are created by particles, which have settled on horizontal baffles. At the critical angle of the pile, an equilibrium is achieved, and the net deposition of particles will equal zero. Common to all the designs are that the baffles slope towards the center of the shaft and that they divide the shaft into separate chambers.

Tests performed by FLSmidth indicated that the FLSmidth Titan preheater used approximately 15 % more thermal energy pr. kg hot raw meal compared to a standard four stage cyclone preheater [95], but also revealed that the pressure drop was lower than in cyclone preheaters.

Krupp shaft preheater

The Krupp shaft preheater, developed by Krupp Polysius Company, consists of a shaft with constrictions, which separates individual chambers. At the top of the shaft, a double cyclone for reduction of dust loss is utilized. The raw meal is fed at the inlet to the cyclones, after separation the solids move down through the equipment and heat exchange with the rising gas. In each stage a solid saturation is archived, forcing a downward solid movement. The gas and raw meal is forced into contact at the narrowings between each chamber. A schematic drawing of a five stage Krupp preheater is given in Figure 29.

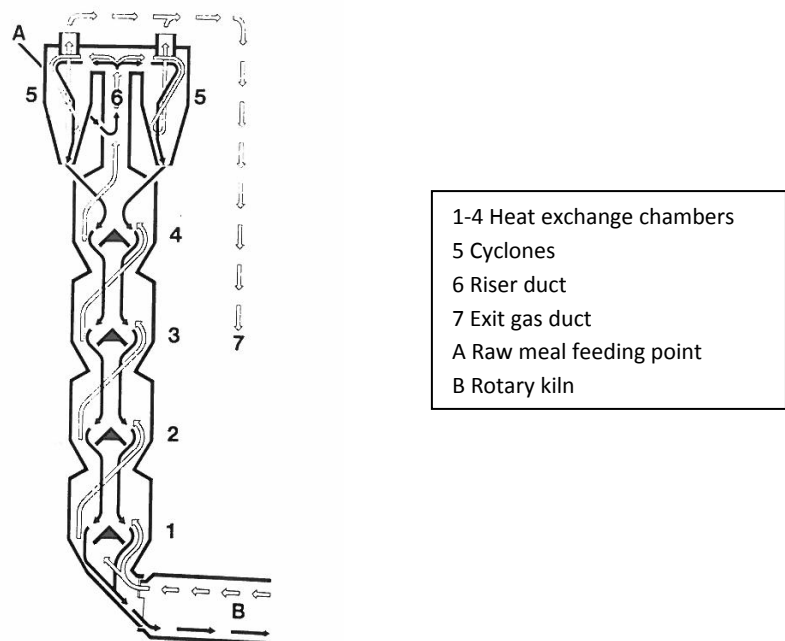


Figure 29 – Schematic drawing of the Krupp shaft preheater [8].

The Krupp shaft preheater was commercially available in the 1960's and early 1970's, and plants utilizing this technology has been constructed in Germany and China [8,96,97].

According to Duda [8], the pressure drop over the Krupp preheater was in the range of 2450 – 2650 Pa, while the specific heat consumption is around 3.6 MJ/kg clinker, and production rates up to 1650 TPDc could be archived. A 1650 TPDc facility were 7.8 m in diameter and around 60 m tall. Bohman [96] reports that a 300 TPDc facility were around 3.4 meters in diameter and 42 meters tall and had a pressure drop of around 3900 Pa.

Bohman [96] also reports that the Krupp shaft had a low labor demand and installation cost as a consequence of the simple construction. Furthermore, the design did not contain any high temperature ducts with small diameters, as found below cyclones, which rendered the Krupp shaft preheater resilient to depositions and blockages. Despite the apparently reasonable operational characteristics of the Krupp shaft preheater, the operational performance was not satisfactory [97].

In literature, the Krupp preheater is mentioned as a counter-current system. Here it is presented as a multistage system as it must be expected that a swirling motion is generated in each chamber, equaling out temperature differences within the chamber, thus making the system operates as a multistage co-current heat exchanger.

KHD preheater

In 1969 Klockner-Humboldt-Deutz (KHD) [98] patented the multistage heat exchanger concept depicted in Figure 30. The internal constrictions generate a gas flow pattern, which is flowing upwards at the feeding points of the particles, entraining the particles in the gas. Flow of gas and entrained particles undergo two 180° turns in each stage where the particles are forced toward the wall, thus resembling the cyclones, but with less rotation of the gas. The separated particles are withdrawn from material outlets and introduced at the consecutive feeding point. A depiction of the concept is shown in Figure 30.

The particle-gas separation in each stage is expected to be less efficient than in traditional cyclones due to lower gas velocities and shorter travelling path.

In 1970, KHD patented a dual shaft preheater design [99] consisting of two KHD shaft preheaters placed next to each other and where the particles are transported from one shaft to the other, increasing the number of heat exchange processes and thereby the thermal efficiency. The drawback of this concept is that twice the number of hot particle streams needs to be handled and transported horizontally.

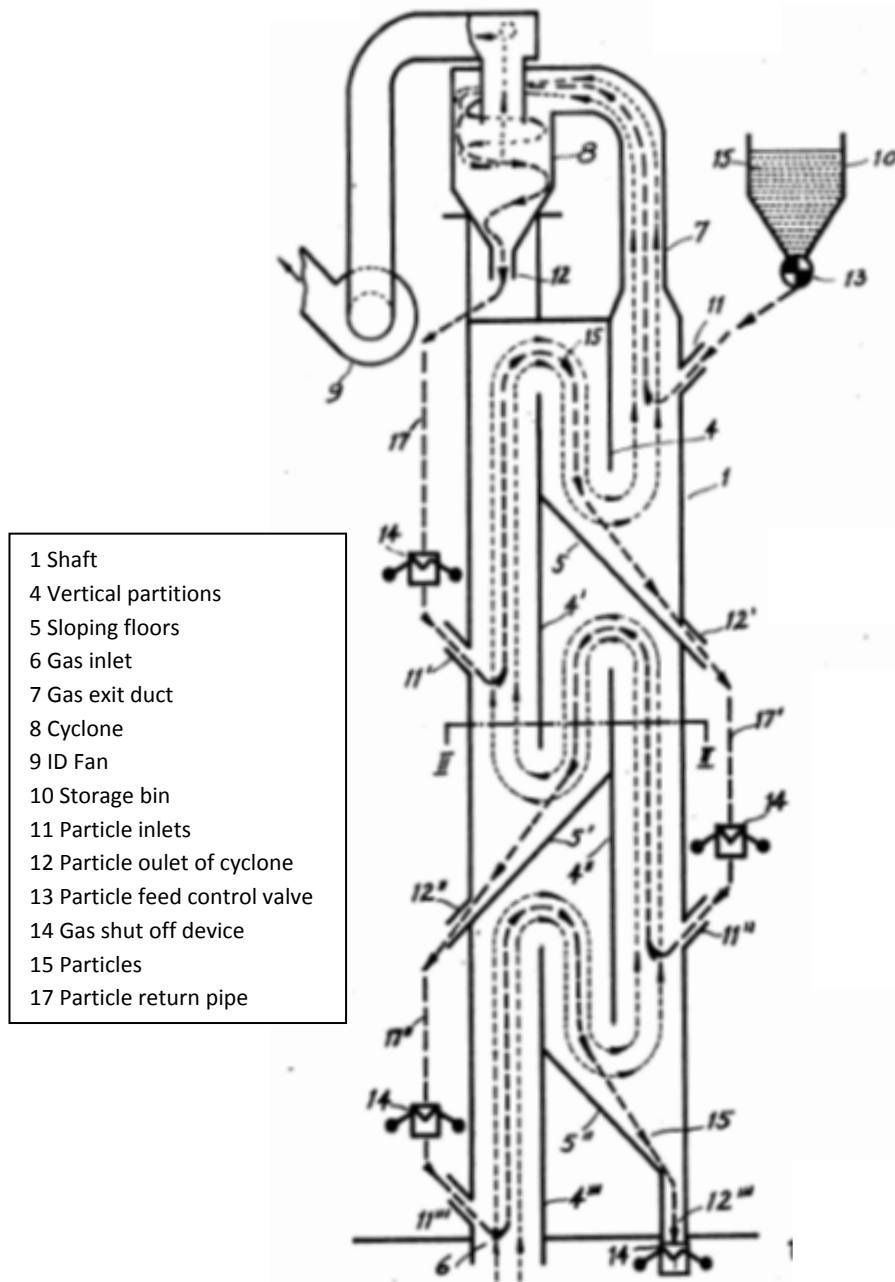


Figure 30 – Schematic drawing of the KHD heat exchanger design [98].

Sket-Zab preheater

The Sket-Zab preheater was developed for preheating of raw meal. It consists of a shaft with alternating inward sloping walls, forming a strand of particles that moves down though the upward flowing gas. Two cyclone stages are mounted on top of the shaft for recirculation of dust. A schematic drawing is provided in Figure 31.

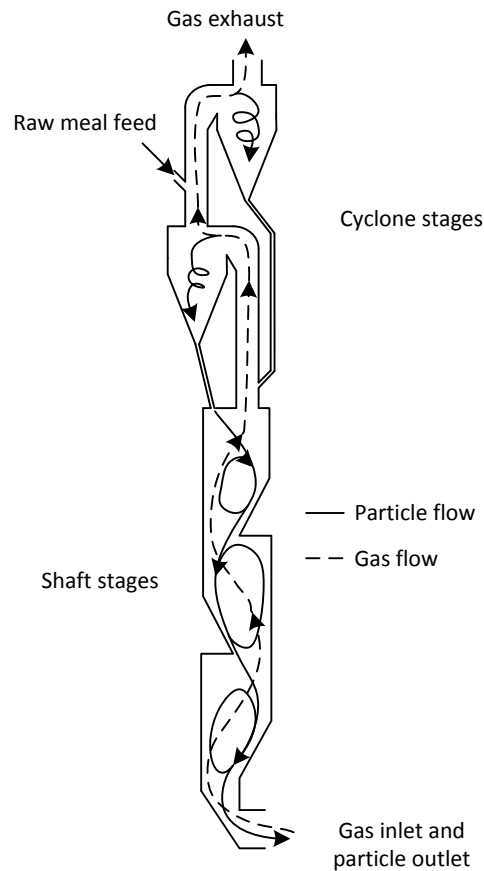


Figure 31 – Illustration of the Sket-Zab shaft preheater.

The static pressure drop has been reported to be around 2500 – 4000 Pa [8] and the thermal efficiency to be 20 % lower than cyclone preheaters with similar number of stages [69]. Mukherjee [69] reports that a five stage SKET-ZAB preheater, supplied by Voest Alpine, were in operation in an United Arab Emirate cement plant from 1982 to 1992, capable of producing 1600 TPDc. In this plant, the Sket-Zab preheater were 4.6 m in diameter and 69 m tall. It was replaced by a cyclone preheater for higher efficiency. Production rates up to 2000 TPDc have been reported using Sket-Zab preheaters [8].

Other multistage shaft preheaters

Two additional stage-based shaft preheater designs are summarized in Table 8.

Table 8 – Additional shaft preheaters with multiple stages and co-current heat exchange.

Preheater name	Patent year	Comments	Source
Polysius	1968	Developed for preheating of raw meal. Design contains cyclone like geometries mounted in a vertical shaft. Flow principles are similar to cyclone preheater. Cyclones mounted on top of each other with no external ducts in between. Internal recirculation is low.	[100]
Westfalia	1969	Developed for preheating raw meal. Consists of a shaft with narrowings separating a series of chambers, similar to the Krupp preheater. Each chamber is well mixed and particles are transported to underlying chambers via separate particle ducts, while gas exits through a central opening to the adjacent chamber. The gas velocity between chambers can be controlled by reducing the cross sectional area of the opening between chambers.	[101]

2.4 Summary of shaft preheaters

The development of the shaft preheaters in the late 1950s and 1960s followed the introduction of the cyclone suspension preheaters and operated at production rates up to 2000 TPDc [8]. The theoretical main advantage of the counter-current shaft preheaters is the potential of providing a highly efficient heat exchange process. The shaft preheater potentially can reduce the construction complexity and costs as well as pressure drop compared to the cyclone preheaters.

The present review of shaft preheater designs identified that establishing the desired flow patterns of the gas and particles is the greatest challenge for the true counter-current heat exchanger. For the multistage shaft preheater, the major challenge is to reduce internal recycling of particles.

In the table given hereafter, the identified advantages and disadvantages of the two types of shaft exchangers have been summarized.

The most interesting of the shaft designs presented seems to be the KHD shaft due to the active separation of gas and particles in each stage and a simple compact self-supporting structure. However, no evidence of the testing of this design has been found in the available scientific literature or the product portfolio of KHD Humboldt Wedag. Furthermore, no citations of the patents presented here nor any later patents with these topics have been found, indicating that the development of this technology has not been continued.

Table 9 – Overview of shaft preheater designs properties.

Advantages	Disadvantages
Shaft heat exchangers in general	
<ul style="list-style-type: none"> – Compact structure. – Simple design. – Self-supporting structure. – Lower pressure drop than cyclone preheater due to lower gas velocities. – Design not vulnerable to depositions and blockages. 	<ul style="list-style-type: none"> – Possible high internal metal temperatures, which are difficult to control or cool. – Designs not refined/optimized through decades as cyclone heat exchanger designs. – Lower separation efficiency of each stage than cyclone preheaters.
Counter-current shaft heat exchangers	
<ul style="list-style-type: none"> – Highest theoretical thermal efficiency. 	<ul style="list-style-type: none"> – Establishing a true counter-current process not practically possible for a raw meal / gas heat exchange. – Suggested designs require particle saturation, which yields low thermal efficiency.
Multi stage shaft heat exchangers	
<ul style="list-style-type: none"> – Operation principle similar to cyclone process. – Easier to facility than counter-current process. 	<ul style="list-style-type: none"> – Lower particle separation efficiency at a given stage than cyclone towers. – Heat exchange processes limited by number of stages (similar to cyclone heat exchangers).

Some operational data were available for the Krupp and Sket-Zab shaft preheaters, which were in operation in the 1960's to 1980's. They were later decommissioned due to poor performance and replaced by cyclone preheaters. This trend is general, and for the last thirty years, no evidence of a commercial available shaft preheater for application in the cement industry have been found in the scientific literature, patents, and products portfolios of relevant companies.

2.5 Other Preheater Designs

The preheating processes considered in previous sections are the shaft preheaters and the modern cyclone preheater. While the presentation of the shaft preheaters highlighted the variety of the designs, only a single version, the modern standard, of the cyclone preheaters was presented, despite numerous designs of preheaters utilizing cyclones have been developed since the introduction of the technology some 80 years ago.

Besides the suspension processes, other technologies for cement plants have also been investigated. Among these are fluidized beds and indirect heat exchangers. In the following some of these processes, including an alternative cyclone-based preheater will be briefly touched upon.

Alternative suspension preheater designs

The designs of preheaters utilizing cyclones are numerous, and the designs vary considerably: The simplest example of preheaters are the two stage cyclone systems, which were retrofitted on long dry rotary kilns in order to improve energy efficiency [8]. More complex systems has been proposed, utilizing combinations of risers, swirl tubes, furnace chambers, and multiple cyclones in each stage for improved feasibility. A single example of the numerous designs, the Dopol preheater designed by Krupp Polysius Co, shown in Figure 32, will be presented here.

The advantages of this design, according to Duda [8], are that large production capacity can be archived, up to 7200 TPDc in a single string, and that two cyclones in each stage potentially have better separation than a single large cyclone. Furthermore, the symmetric design reduces tensions in the support structure thereby reducing construction costs.

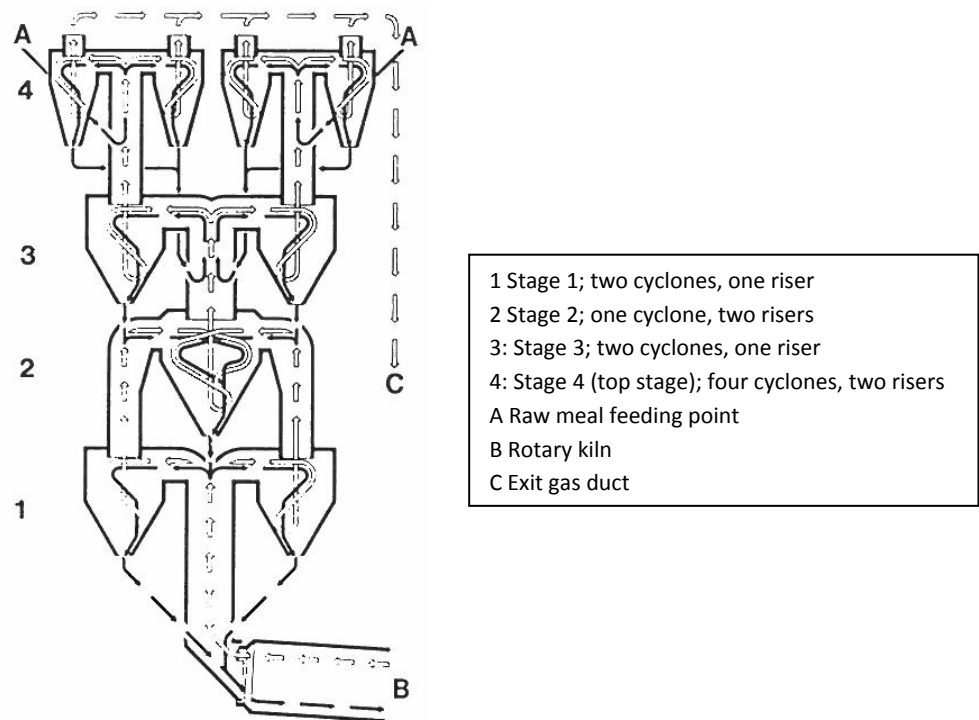


Figure 32 – Schematic drawing of the Dopol preheater [8].

Fluidization and indirect processes

The nature of the raw meal, which is classified as group C particles by Geldart [102], makes it impossible to apply simple fluidizing or bubbling beds directly. As stated in section 2.1 – *Historic Development*, the raw meal can be pelletized and then fluidized. This process is more costly than the cyclone suspension preheating process, however.

Designs such as the Solex indirect heat exchanger [103], used for sugar cooling, is not applicable for cement production either, as the large production rates of modern plants rule out indirect heat exchange processes due to limited heat transfer rates. Additionally in the Solex process, the raw meal would not flow properly through the narrow slits between the heat exchange panels. Other processes with too low heat transfer rates include rotating shell heat exchangers and modified screw conveyers [104].

2.6 Preheater Design Summary

From the development of the cyclone preheaters in the 1930's, this technology has been prevailing within cement production and subject for continuous improvement. Numerous designs utilizing cyclones and risers have been published during the last 80 years, yet the apparently simple designs containing a single cyclone and riser duct in each stage are the most successful.

The shaft preheaters were developed to compete with cyclone-based processes, especially with respect to the size of the preheater facility and the thermal performance. In practice, the shaft preheaters were not successful due to large internal recirculation, resulting in poor thermal performance, despite promising operation characteristics.

A timeline overview of the development of the preheater systems in the 20th century is shown in Figure 33.

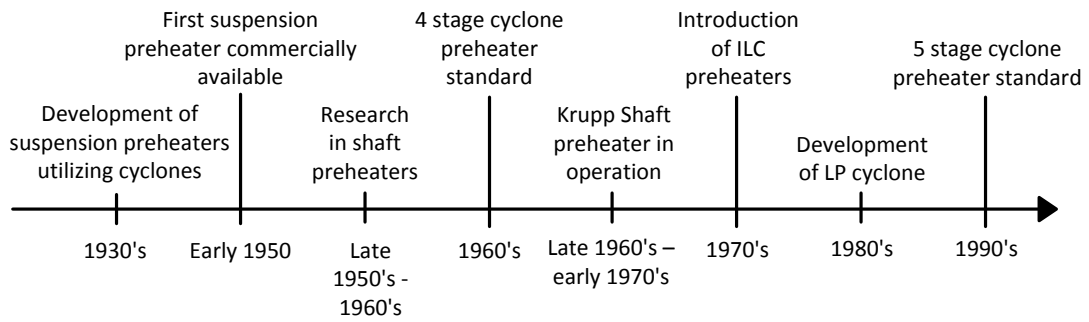


Figure 33 – Timeline of major events in the development of the suspension preheater in the 20th century.

The current standard preheater design applied for new cement plants is a five stage cyclone-based process with an ILC. This process is currently the best compromise between thermal performance, pressure drop, and construction costs. Production rates in each cyclone string can reach up to 6000 TPDc and gas exit temperatures are around 270 – 320 °C. Separation efficiencies of the cyclones range between 0.75 and 0.95.

Alternative heat exchange principles, such as fluidized beds and indirect heat exchange processes have not been applied successfully in cement production due to challenging raw meal powder properties and insufficient heat transfer rates, respectively.

From a process point of view, the combination of riser ducts and cyclones is very suitable for performing the desired heat exchange processes. However, due to a continuous desire to reduce costs and improve performance, some inherent design problems are apparent: (a) The geometry and arrangement of the cyclones and risers makes the tower tall, (b) the cylindrical geometry alone also increases capital costs and (c) makes it difficult to integrate power production processes, (d) the gas velocities inside the cyclones induces a relative high pressure drop, and (e) the design is not easily scalable.

Chapter 3

Preheater Efficiency

"When you can measure what you are speaking about, and express it in numbers, you know something about it. When you can't measure it, your knowledge is meager and unsatisfactory"

– Lord Kelvin, British mathematical physicist and engineer

Thermal evaluation and comparison of preheaters is not easily done due to the varying operation conditions, design specifications, and lack of generalized comparison parameters. Typically, the industry uses the caloric energy consumption per mass unit of clinker or gas exit temperatures for comparisons, but these values depend on all the processes in the pyroprocessing unit, including calciner and kiln, why they for a comparison of preheaters only are not practical.

The purpose of this section is twofold: (a) Suggest and apply generalized comparison parameters, and (b) using these parameters, investigate how the entrainment and separation processes influence the thermal performance of the preheater.

In order to thermally evaluate a preheater, knowledge of the sizes and temperatures of the mass flows is required. These can be estimated by setting up and solving mass and energy balances for gas and particles in the preheater. Such a model and the resulting simulated process conditions are described in the following sections.

3.1 Model Boundaries

The model is set up for an ILC preheater. The model boundaries enclose the cyclone stages above the calciner, leaving the calciner and calciner cyclone out of the model. The temperature in the calciner cyclone is determined by the operation conditions of the calciner and not the heat exchange performance of the preheater, why it is of no interest from a heat exchange point of view. The model contains $N-1$ stages, where N denotes the official number of stages in the

preheater system. A schematic drawing showing the model boundaries on a five stage preheater is given in Figure 34.

There are two inlet particle streams, the cold particle feed and hot dust from the calciner cyclone, and particle outlets from stages $N-1$ and 1, while there is only a single gas in- and outlet.

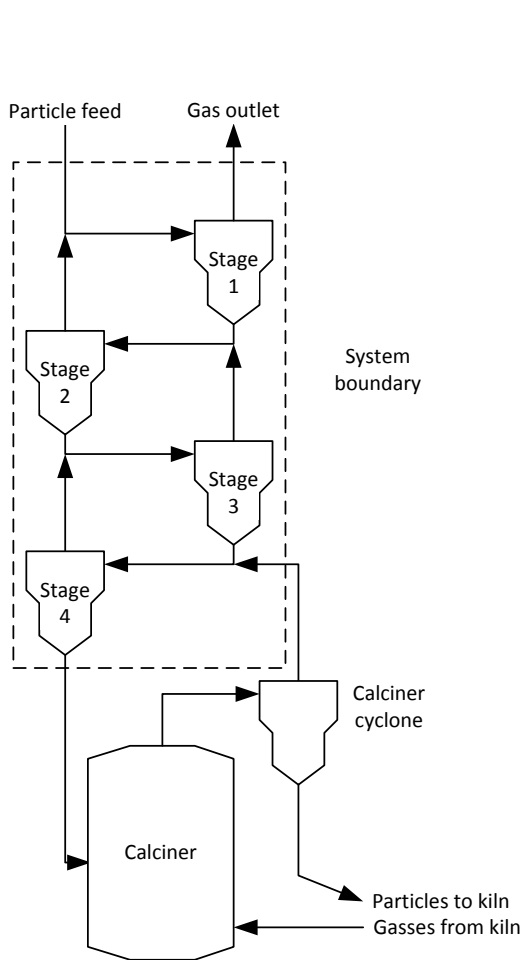


Figure 34 – Model boundaries for the preheater model shown for a five stage system. Dominant flows are depicted.

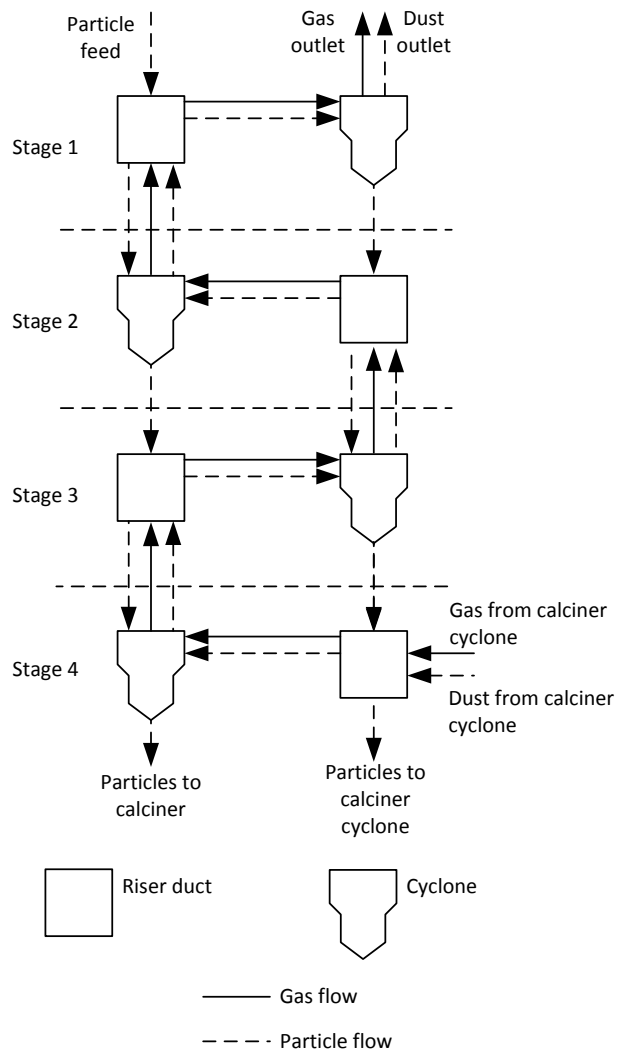


Figure 35 – Modeled gas and particle flows in a five stage preheater.

3.2 Model Set Up

Each stage consists of a riser and a cyclone, as shown in Figure 35. In each riser, particles, which enter from the cyclones above and below, are assumed mixed with the gas. In the riser, a fraction of particles are entrained and fed to the cyclone in the same stage, while the remaining fraction falls through the riser to the cyclone below. Complete entrainment in the risers is assumed under normal operation conditions in cement plants, but for the sake of completeness, an option for not entrained particles is included in the model. In each cyclone, a fraction of the particles entering the cyclones is separated from the gas, and directed to the riser below. The particles not separated follow the gas to the cyclone above as entrained dust. A mixing of particles and gas takes place, as well as a split of the particle streams can occur, in both riser and cyclone. In both types of units ideal heat exchange and instant mixing are assumed.

The model consists of mass and energy balances, generally given as:

$$In + Produced = Out + Accumulated \quad \text{Eq. 19}$$

At steady state, the *Accumulated*-term equals zero. No mass or heat is assumed produced, why the *Produced*-term equals zero as well. A schematic drawing of a single stage, illustrating the nomenclature of the relevant flows, is displayed in Figure 36.

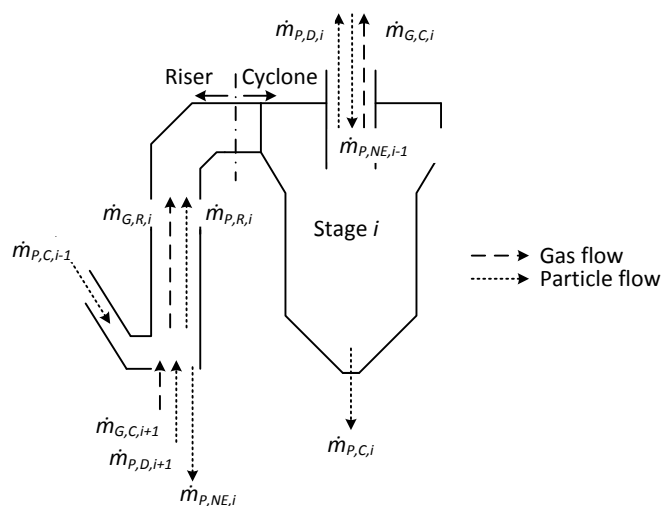


Figure 36 – Schematic drawing of a preheater stage with indication of particle and flows.

\dot{m}_p denotes mass flow of particles, indices R , C , D , and NE , short for *riser*, *cyclone*, *dust*, and *not entrained*, are: Entrained flow in the riser, separated particles in the cyclone, particles not separated in the cyclone, and particles not entrained in the riser, while indices i , $i+1$, and $i-1$ represents the respective stages. \dot{m}_G is the mass flow of gas.

The mass balances for gas and particles in stage i are given as:

$$\text{Particles, riser:} \quad \dot{m}_{P,R,i} = \dot{m}_{P,C,i-1} + \dot{m}_{P,D,i+1} - \dot{m}_{P,NE,i} \quad \text{Eq. 20}$$

$$\text{Particles, cyclone:} \quad \dot{m}_{P,R,i} = \dot{m}_{P,C,i} + \dot{m}_{P,D,i} - \dot{m}_{P,NE,i-1} \quad \text{Eq. 21}$$

$$\text{Gas, riser:} \quad \dot{m}_{G,R,i} = \dot{m}_{G,C,i+1} \quad \text{Eq. 22}$$

$$\text{Gas, cyclone:} \quad \dot{m}_{G,C,i} = \dot{m}_{G,R,i} \quad \text{Eq. 23}$$

Top and bottom stages differ from the above stated, as not all streams are present.

The energy balances for each unit in stage i are given as:

$$\begin{aligned} \text{Cyclone} \quad & (C_{P,P} \cdot (\dot{m}_{P,C,i} + \dot{m}_{P,D,i}) + C_{P,G} \cdot \dot{m}_{G,C,i}) \cdot (T_{C,i} - T_{Ref}) = \\ : \quad & C_{P,P} \cdot (\dot{m}_{P,R,i} \cdot (T_{Riser,i} - T_{Ref}) + \dot{m}_{P,NE,i-1} \cdot (T_{R,i-1} - T_{Ref})) + C_{P,G} \cdot \dot{m}_{G,R,i} \cdot (T_{R,i} - T_{Ref}) \quad \text{Eq. 24} \end{aligned}$$

$$\begin{aligned} \text{Riser:} \quad & (C_{P,P} \cdot (\dot{m}_{P,R,i} + \dot{m}_{P,NE,i}) + C_{P,G} \cdot \dot{m}_{G,R,i}) \cdot (T_{R,i} - T_{Ref}) = \\ & C_{P,P} \cdot (\dot{m}_{P,C,i-1} \cdot (T_{C,i-1} - T_{Ref}) + \dot{m}_{P,D,i+1} \cdot (T_{C,i+1} - T_{Ref})) + \\ & C_{P,G} \cdot \dot{m}_{G,C,i+1} \cdot (T_{C,i+1} - T_{Ref}) \quad \text{Eq. 25} \end{aligned}$$

The reference temperature, T_{Ref} , is set to 25 °C. T_C and T_R are the temperatures of the cyclones and risers, respectively. At full entrainment the temperature in the riser and cyclone will be identical in a given stage.

The split of particles in cyclones and risers are described by two efficiencies; an entrainment efficiency and a separation efficiency. The entrainment efficiency describes how much is entrained in the riser, compared to the amount fed. The separation efficiency describes the amount of separated particles in the cyclone, compared to the amount fed to the cyclone. The entrainment and separation efficiencies are defined as:

Cyclone:

$$\eta_{Sep,i} = \frac{\dot{m}_{P,C,i}}{\dot{m}_{P,R,i} + \dot{m}_{P,NE,i-1}} \quad \text{Eq. 26}$$

Riser:

$$\eta_{Ent,i} = \frac{\dot{m}_{P,R,i}}{\dot{m}_{P,C,i-1} + \dot{m}_{P,D,i+1}} \quad \text{Eq. 27}$$

The two particle streams, particles fed to the calciner and dust from the calciner cyclone, are related as:

$$\dot{m}_{P,D,N} = (1 - \eta_{Sep,N}) \cdot \dot{m}_{P,C,N-1} \quad \text{Eq. 28}$$

For $N \geq 2$, the model computes $6 \cdot (N - 1)$ mass flows and $2 \cdot (N - 1)$ temperatures using $4 \cdot (N - 1)$ mass balances, $2 \cdot (N - 1)$ efficiency expressions and $2 \cdot (N - 1)$ energy balances. Input parameters are inlet temperatures, size of particle feed, solid load, number of stages, specific heat capacities, and separation and entrainment efficiencies for each stage. A total of $8 + 2 \cdot (N - 1)$ input parameters are required.

Using the model as stated above, the simulated temperatures will be the highest possible at the given conditions, as no heat loss is considered.

3.3 Process Efficiency

In order to evaluate the performance of a preheater, it is desired to provide a parameter, which encapsulates the performance. Normally for heat exchangers such numbers are a thermal efficiency or number of transfer units, but designing efficiency parameters for a system such as the preheater is more complicated than for a continuous shell and tube heat exchanger. Considerations regarding the definition of both thermal and particle transport efficiency parameters are provided in the following sections.

3.3.1 Thermal Efficiency

The recirculation of particles, the particle stream from the calciner cyclone, and the stage-based nature of the preheater system complicate matters in terms of determining an efficiency parameter, which can be used to compare different systems and which behaves intuitively correct.

Defining a traditional particle heating efficiency, considering the energy in the heated particle streams and available energy in the inlet streams, yields:

$$\varphi_{Abs} = \frac{\Delta Q_P}{\Delta Q_{Avialable}} = \frac{\dot{m}_{P,C,N-1} \cdot C_{P,P} \cdot (T_{C,N-1} - T_{P,In}) + \dot{m}_{P,NE,N-1} \cdot C_{P,P} \cdot (T_{R,N-1} - T_{P,In})}{\dot{m}_G \cdot C_{P,G} \cdot (T_{G,Inlet} - T_{P,In}) + \dot{m}_{P,Cal} \cdot C_{P,P} \cdot (T_{Cal} - T_{P,In})} \quad \text{Eq. 29}$$

where index *Cal* describes calciner cyclone conditions. Q_P is the energy content of the particle streams. In Eq. 29, the energy content of the two particle flows that leaves the system at stage N-1 constitutes the nominator, while the denominator is the energy content in the gas and particle inlets at the stage N-1. The cold particle feed is being used as reference state, why it is omitted.

The undesirable property of this definition is, despite considering a process with no heat or dust losses and infinitely many stages, φ_{Abs} may never reach unity. This is caused by the difference in the heat capacity of the gas and solid streams. Therefore φ_{Abs} cannot be used to determine how close to ideal operation a given system is, as the maximum achievable efficiency for the given configuration is unknown. However, it summarizes the absolute performance of the system, indicating how much of the inlet energy that is utilized as intended.

Alternatively, the energy in the outlet particle streams could be normalized with the maximum obtainable energy, as computed for a system with similar inlet conditions, full separation and entrainment, and an indefinite number of stages. Intuitively, this would yield values between zero and unity. The normalizing parameter then depends on solid load for the given system, thus this thermal efficiency cannot be used to compare systems operating at different conditions. Instead, it provides a relative thermal performance relating the performance of a given system to the performance of an ideal system with an infinite number of stages, operating under similar conditions. The relative thermal efficiency, φ_{Rel} , is defined as:

$$\varphi_{Rel} = \frac{\Delta Q_P}{\Delta Q_{P,N=\infty}} = \frac{\varphi_{Abs,N \neq \infty}}{\varphi_{Abs,N=\infty}} \quad \text{Eq. 30}$$

Principally, the thermal efficiencies could also be based on the gas stream. This is not advantageous as the cooling of the gas not only reflects performance of the heat exchange with particles but also heat loss and false air sucked into the system. Both of these phenomena would yield a better cooling of the gas, but reduce the amount of energy available for the gas-particle heat exchange.

Summarizing the two suggested efficiency parameters: For evaluating the performance of a given system, the relative efficiency holds information on how efficient the system is compared

to an ideal system, while the absolute efficiency describes how much of the inlet energy that is utilized as intended.

Work found in literature [105,106] considers a thermal efficiency similar to the one given in Eq. 29, considering either a single stage [106] or on tri-string cyclone preheater configuration [105], while neglecting the dust stream from the calciner cyclone.

3.3.2 Transport Efficiency

To describe the internal particle transport in each stage, a stage transport efficiency, $\eta_{Transport,i}$ is applied, defined as the product of the entrainment and separation efficiencies for a given stage i :

$$\eta_{Transport,i} = \eta_{Ent,i} \cdot \eta_{Sep,i} \quad \text{Eq. 31}$$

The transport efficiency describes the ratio between the particles separated in the cyclone and the particles fed to the stage. As stated previously, in a cement plant during normal operation, the entrainment efficiency is close to one, reducing the stage transport efficiency to:

$$\eta_{Transport,i} = \eta_{Sep,i} = \frac{\dot{m}_{P,C,i}}{\dot{m}_{P,C,i-1} + \dot{m}_{P,D,i+1}} \quad \text{Eq. 32}$$

3.4 Assumptions, Parameters, and Physical Properties

To simplify the model, the following assumptions are made:

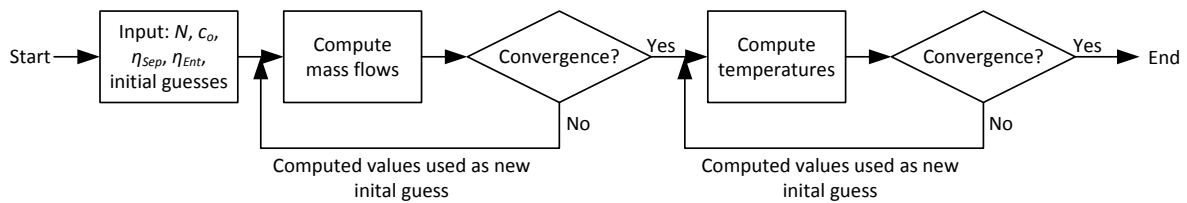
- System is in steady state.
- Ideal, instant heat exchange takes place in both riser and cyclone.
- No heat loss.
- Constant mass of gas (no false air).
- Temperature independent specific heat capacities of gas and particles.
- No chemical reactions or phase transitions.

The operational and physical parameters needed to solve to the model are presented in Table 10.

Table 10 – Parameters needed for preheater efficiency considerations.

Parameters	Value	Source
Gas inlet temperature (operation temperature of calciner), $T_{G,In}$	850 °C	[19]
Particle inlet temperature, $T_{P,In}$	50 °C	[87]
Heat capacity for particles, $C_{P,P}$	900 J/Kg/K	[67]
Heat capacity for gas, $C_{P,G}$	1071 J/Kg/K	[87]
Variables		
Number of stages, N	2 – 6	-
Solid load (feed), c_0	0.6 – 1.0 kg solid/ kg gas	-
$\eta_{Transport,i} = \eta_{Ent,i} \cdot \eta_{Sep,i}$	0.1 – 1.0	-

Due to the recycled particle streams moving upwards in the system, the solution procedure is iterative, both for determining mass flow of particles and temperatures. The computational algorithm is shown in Figure 37.

**Figure 37** – Computational algorithm for cyclone preheater model.

3.5 Model Results

Solving the model yields the temperature profile and mass streams in a cyclone preheater, thereby enabling computation of the efficiency parameters.

To investigate the influence of the solid load and number of stages on ϕ_{Abs} and ϕ_{Rel} , the thermal efficiencies has been computed for systems with solid loads between 0.6 kg/kg and 1.0 kg/kg, two to six stages, inlet temperatures as stated in Table 10, and $\eta_{Transport} = 1.0$ for all stages. The results are provided in Figure 38 and Figure 39.

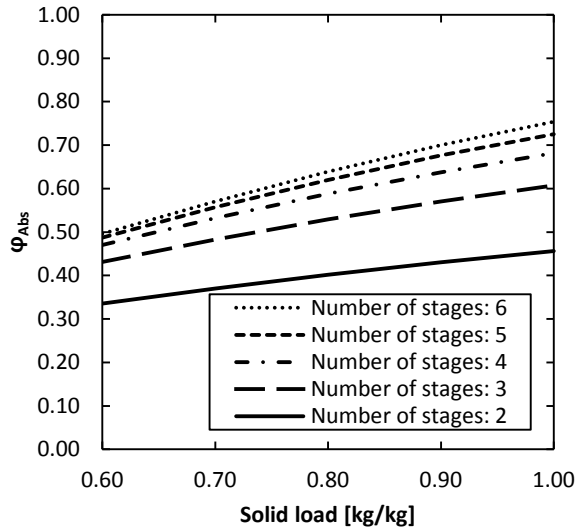


Figure 38 – Absolute efficiencies for systems containing between two and six stages. $\eta_{Transport} = 1.0$.

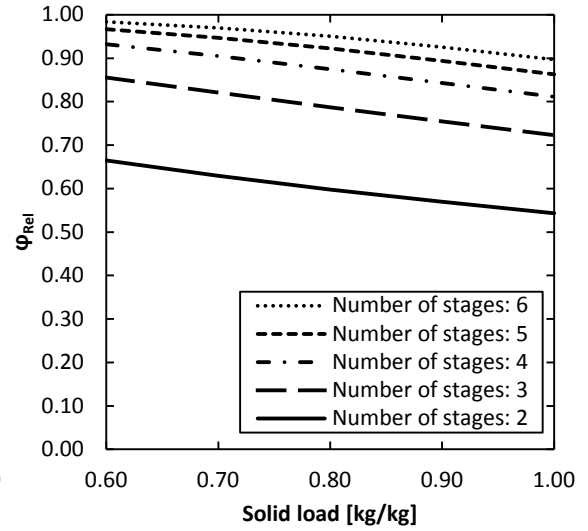


Figure 39 – Relative efficiencies for systems containing between two and six stages. $\eta_{Transport} = 1.0$.

The absolute efficiency, φ_{Abs} , increases with the solid load, indicating that a larger fraction of energy is transferred from the hot gas to the particle outlet streams when more particles are present due to larger heat capacity of the particle streams. The relative efficiency decreases with increasing solid load, indicating that the highest possible efficiency increases more than the absolute efficiency. Furthermore, the influence of the number of stages shows that the more stages, the better thermal performance, and that the gain for each additional stage is reduced as the number of stages increases. At solid loads of 0.6 kg/kg, the relative efficiency of a six stage system is close to unity, indicating that no gain will be achieved if adding more stages. The effect of adding stages is more profound at higher solid loads.

In order to analyze the influence of the transport parameters on the thermal performance, a five stage preheater is considered. Solid load = 1.0 kg/kg and $\eta_{Transport}$ in the form of η_{Ent} and η_{Sep} are varied between zero and unity. The results of analyzing three different series; (a) $\{\eta_{Ent} = \eta_{Sep} = [\sqrt{(0.1)} \dots \sqrt{(1.0)}]\}$, (b) $\{\eta_{Sep} = 1, \eta_{Ent} = [0.1 \dots 1.0]\}$ and (c) $\{\eta_{Ent} = 1, \eta_{Sep} = [0.1 \dots 1.0]\}$ are provided in Figure 40. Only the absolute efficiencies are provided, as the trends of the relative and absolute parameters are identical due to the single value of the normalizing parameter, $\varphi_{Abs, N=\infty} = 0.84$.

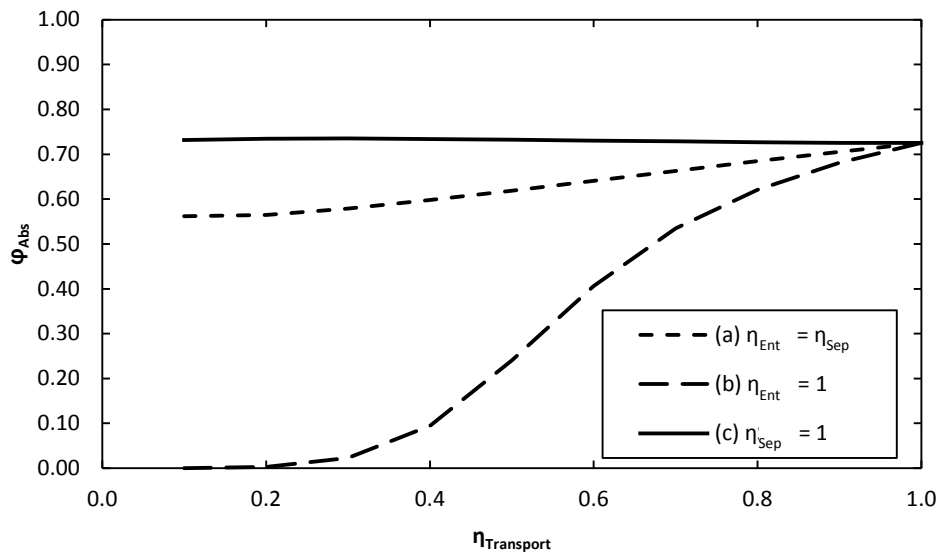


Figure 40 – Absolute thermal efficiency for systems with $N = 5$ as a function of $\eta_{Transport}$. $c_0 = 1.0$ kg/kg.

Values below $\eta_{Transport} = 0.1$ have not been investigated as system performance at these settings becomes highly effected by the large internal recirculation, especially when both η_{Ent} and η_{Sep} are close to zero.

The separation efficiency has the largest impact on the thermal performance, indicted by a thermal performance close to zero for low values of the separation efficiency. The effect of the entrainment efficiency is insignificant, which is the consequence of constant number of heat exchange steps. Varying both η_{Ent} and η_{Sep} (series a) results in a behavior lying between the two extreme conditions.

To further evaluate the usability of the suggested thermal efficiencies, efficiencies are computed for a series of preheater configurations found in literature. The available preheater data is provided in Table 11, where also systems with $\eta_{Transport} = 1.0$ are provided for comparison.

The thermal efficiencies for these configurations are given in Table 12 using both simulated and measured temperatures, principally corresponding to systems with and without heat loss. The inlet gas temperatures for the ideal systems are set to 850 °C.

The absolute thermal efficiencies based on the measured temperatures reveal for all the considered preheater configurations that ϕ_{Abs} are between 61 % and 71 %. According to ϕ_{Abs} , the

best performing system is the six staged Plant A, while Plant C is the poorer. The four staged Plant E performs better than the five staged plant B, due to slightly higher separation efficiencies and a 7 % higher solid load, while the modern standard preheater with five stages at the given conditions performs slightly poorer than the six staged Plant A. The relative thermal efficiencies, φ_{Rel} , indicate that the systems perform between 74 % and 97 % of the maximal heat exchange possible.

Table 11 – Evaluation and comparison of preheater configurations from literature.

Description	N	c_o [kg/kg]	$\eta_{Sep,i}$	Measured temperatures [°C] ^B	Source
Ideal 4	4	1.0^A	{1.0, 1.0, 1.0, 1.0}	-	-
Plant C	4	1.02	{0.90, 0.90, 0.80, 0.85}	{74, 345, 563, 708 ^C , 870}	[59]
Plant D	4	0.92	{0.91, 0.82, 0.69, 0.83}	{60, 336, 521, 709, 817}	[59]
Plant E	4	0.98	{0.92, 0.78, 0.79, 0.66}	{60, 358, 576, 730, 893}	[59]
Ideal 5	5	1.0^A	{1.0, 1.0, 1.0, 1.0, 1.0}	-	-
Modern standard	5	0.94 ^D	{0.96, 0.90, 0.90, 0.85, 0.80}	{60 ^A , 310, 480, 640, 785, 850}	[19]
Plant B	5	0.92	{0.80, 0.75, 0.75, 0.85, 0.60}	{60, 368, 552, 693, 808, 870}	[59]
Ideal 6	6	1.0^A	{1.0, 1.0, 1.0, 1.0, 1.0, 1.0}	-	-
Plant A	6	0.87	{0.92, 0.90, 0.86, 0.82, 0.80, 0.55}	{25, 287, 478, 617, 719, 787, 864}	[59]

^A Chosen value, yielding highest possible φ_{Abs} .

^B Temperatures given as {particle feed, stage 1, ..., stage N (calciner cyclone)}

^C Measured data not available, temperature modeled by [59].

^D Assumed equal to the average of the values found in [59].

Table 12 – Computed thermal efficiencies with and without heat loss.

Description	φ_{Abs}	φ_{Rel}	φ_{Abs}	φ_{Rel}
Computed from	Simulated temperatures (Heat loss not included)		Measured temperatures (Heat loss included)	
Ideal 4	0.68	0.81	-	-
Plant C	0.64	0.78	0.61	0.74
Plant D	0.61	0.79	0.62	0.80
Plant E	0.70	0.82	0.67	0.78
Ideal 5	0.73	0.86	-	-
Modern standard	0.73	0.92	0.71	0.90
Plant B	0.64	0.83	0.63	0.82
Ideal 6	0.75	0.90	-	-
Plant A	0.75	1.02	0.71	0.97

The computed thermal efficiencies, given in Table 12, reveal that efficiencies for the ideal systems can be surpassed, exemplified by the data from Plant A. The reason is that the increased recycled particle stream from calciner cyclone increases both temperature and mass flow in the lower stages of the preheater, and in terms of energy content dominates over the feed stream, why systems with low separation in the calciner cyclone can have a higher thermal efficiency than the desirable ideal systems. These “better-than-ideal” systems are in practice not favorable, due increased pressure drop, higher fuel demand in the calciner, and higher gas exit temperatures, however. These parameters are not included in the definition of the thermal efficiencies, why these unwanted properties are not reflected in the computed values.

The general trend for the actual preheater configurations is that the more stages, the higher relative thermal efficiency, which is similar to the trend shown in Figure 39. The absolute thermal efficiencies based on the simulated temperatures reveal the same ranking as found from the actual temperatures, and also indicates that around 2 – 5 % of the thermal performance is lost due to heat loss, which are close to the typical value of 4 % [55,68]. Note that the inlet temperatures of particles and gas do not influence the thermal efficiencies, but only the temperature profile in the preheater.

An example of the output data for the ideal five stage system is shown in Figure 41. For comparison Figure 42 shows the result of simulating the modern standard plant. Particle recirculation and increased temperatures are the consequences non-ideal particle transport patterns.

Note that for Plant D and the Modern Standard the measured temperatures are higher than the computed temperatures, indicating that the model does not account for all processes contributing to the temperature or site specific conditions. The neglected processes could be combustion of fuel particles or recarbonization of CaO to CaCO₃. Alternatively, the specific heat capacities might be significantly different from the ones considered in the model.

The exothermic recarbonization reaction is potentially significant. Incorporating the recarbonization process into the model requires the risers and cyclones characterized as reactors in terms of residence time and degree of mixing, besides adding component mass balances and temperature specific kinetics, which for a simple evaluation of the preheaters are not relevant.

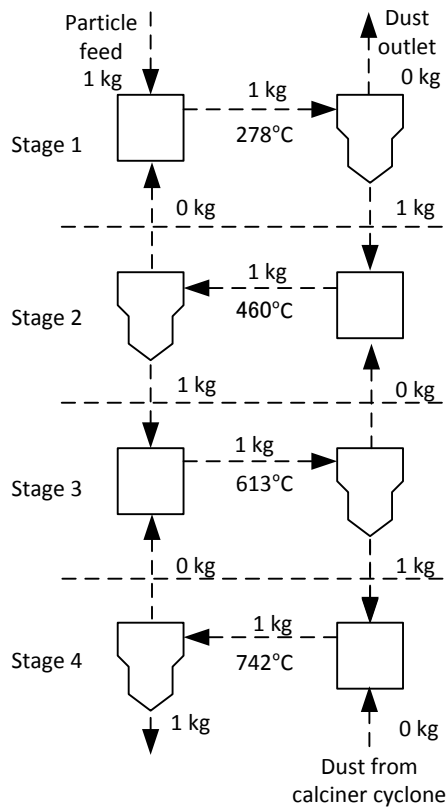


Figure 41 – Modeled temperatures and particle flows in a five stage preheater under ideal conditions, $\eta_{Transport} = 1.0$, $c_0 = 1.0$ kg/kg, $\dot{m}_{P,in} = 1.0$ kg/s, $T_{P,in} = 60$ °C, and $T_{G,in} = 850$ °C.

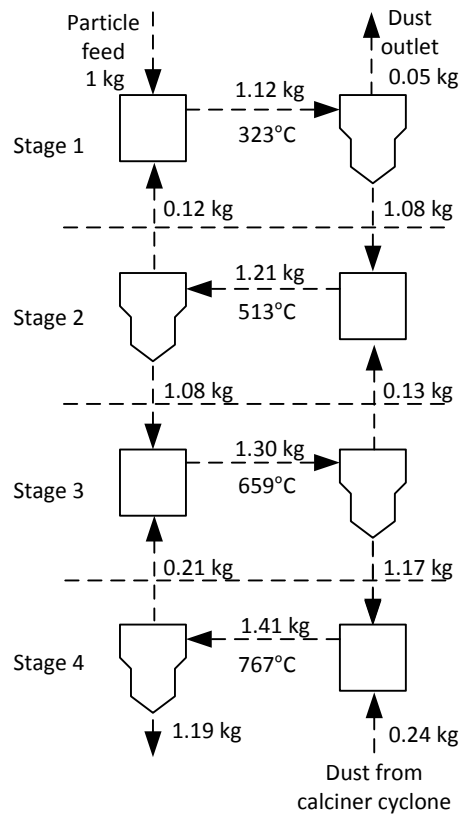


Figure 42 – Modeled temperatures and particle flows in a five stage preheater using separation efficiencies stated by Alsop [19]. $c_0 = 0.94$ kg/kg, $\dot{m}_{P,in} = 1.0$ kg/s, $T_{P,in} = 60$ °C, and $T_{G,in} = 850$ °C.

3.6 Summary

The cyclone preheater model provided a tool for obtaining flows and temperatures in cyclone preheaters, and enabled an analysis of the suggested thermal efficiencies. The analysis of the preheaters in terms of thermal efficiency revealed that the thermal performance can be described by a set of parameters, an absolute and a relative thermal efficiency. Definitions and descriptions are provided in Table 13.

Table 13 – Definition and descriptions of use for the thermal efficiencies.

Name	Expression	Comments
Absolute thermal efficiency	$\varphi_{Abs} = \frac{\Delta Q_P}{\Delta Q_{Avalable}}$	Describes the fraction of energy transferred to the desired particle streams. Does not reach unity even for ideal systems. Rewards large recirculation from calciner cyclone.
Relative thermal efficiency	$\varphi_{Rel} = \frac{\Delta Q_P}{\Delta Q_{P,N=\infty}}$	Describes the performance relative to ideal performance. Cannot be used comparison of systems. Rewards large recirculation from calciner cyclone.

An analysis showed that the absolute efficiency increased with solid load, while the relative thermal efficiency decreased. Both efficiencies increased with number of stages in the preheater, and the additional performance gain for each additional stage became lower and lower. The analysis also showed that the higher solid load, the larger gain for each additional stage, thus the higher the solid load, the larger number of stages might be feasible. The analysis also revealed that the separation efficiency is the major particle transport parameter in terms of achieving high thermal performance, while the entrainment efficiency was insignificant.

Analyzing six actual preheater configurations revealed that φ_{Abs} ranged between 61 % and 71 %, and φ_{Rel} were between 74 % and 97 %. Generally, both thermal efficiencies increased with the number of stages.

The model generalized and simplified the preheater conditions, which in some cases lead to systems that were not described as intended, yielding lower simulated than actual temperatures. This indicated that processes such as recarbonization or combustion of fuel in the lower stages might contribute significantly to the temperature profile in some specific cases. Furthermore, $\varphi_{Rel} > 1$ could be achieved in certain cases when the separation efficiency in the calciner cyclone is low. This was caused by recirculation of hot particles from the calciner cyclone, which dominated both temperature and sizes of mass flows in stage N-1. A value above unity did not mean that such a system performs better than an ideal system, but merely indicates a shortcoming of the definition of the efficiency parameter, which does not include the effects of increased fuel consumption, increased pressure drop, and increased recirculation in the lower parts of the preheater.

Despite these inaccuracies the suggested thermal efficiencies proved useful for evaluating actual preheater performance.

Chapter 4

Design Development

“Better one idea too many, than one too few”

– Klaus Hjuler, research engineer at FLSmidth A/S, supervisor

This project is concerned with the development of a novel preheater concept, which can compete with the cyclone preheaters in terms of performance and feasibility. The reason for not seeking to enhance knowledge and performance of the existing technology, as done over the last 80 years by both companies and researchers, can be found in the outline for this project. From the project objective:

“... the objective of this project is not to further optimize the existing technology, but to rethink the entire preheating process...”

The first generations of this new process may not be directly competitive with the highly optimized industrial standard but should have potential to be at least equally efficient and economical feasible.

This chapter outlines the development of the chosen heat exchanger design from idea generation and selection to evaluation of working mechanisms and identification of critical aspects.

4.1 Desired Properties

Objectives in the early phases of the project included development of a new preheater with improved thermal efficiency and reduced emissions. However, for a new radically different preheater to be accepted by the cement producers, economic aspects weigh heavier than potential emission reductions and marginal thermal improvements. Therefore the main objective of the development described in this work, is focused on developing a design with reduced construction costs, while maintaining similar thermal performance as the current facilities. The

operational cost, consisting mainly of the thermal efficiency and the pressure drop, is also an important comparison parameter, as well as operational stability and acceptable performance for a wide range of operation conditions. This includes resilience to blockages and deposition on internal surfaces. The major desired properties for preheater can be summarized to:

- Lower capital costs than cyclone preheater.
- At least similar thermal efficiency to the cyclone preheater.
- Similar or lower pressure drop than cyclone preheater.
- High operational stability.
- Wide operation range in terms of varying gas velocities and solid load.

Other desired properties include co-generation of power in the preheater. Currently, trends in the cement industry focuses on generating power from waste heat production process, but the power produced does not cover the need of the cement plant. An integrated power and cement plant, self-sustained with power has not been realized, mostly due to difficulties of designing a three way heat exchanger, heating particles and generating steam from the combustion gases created in the calciner and kiln.

Also easy scalability and reduced construction height are desired. The reduced building height is tightly related to the construction costs, but also serves to reduce the visual impact of the cement plant in the landscape. From a practical point of view it is desired to develop a design, which is testable in the available pilot hall facilities. The desired secondary properties can be summarized to:

- Utilization of process gases for steam production.
- Easily scalability.
- Low building height.
- Design testable in available facilities.

4.2 Idea Generation

Idea generation was undertaken in a series of meetings between academia and industry, supported by studies of literature and patents. These studies, which in a condensed and revised form are presented in Chapter 2, revealed a series of preheater designs and highlighted some of the operational issues. For the shaft preheater, especially the disadvantages of the particle saturation driven separation, and uncontrolled gas and particle flow patterns were problematic.

Besides revealing shortcomings of the alternative preheater configurations, the study also served to provide inspiration for the development of new designs.

During the initial period of the project numerous ideas were discussed and evaluated. Two designs were more promising, why they were considered in more detail. These two; (a) a design based on draft tube spouted beds (DTSB) and (b) a design with similar operational principles as the cyclone preheater, called the two dimensional heat exchanger (2D-HX), are described in the following sections.

The latter design proved to be the most promising idea generated, and was selected for experimental investigations. Therefore more details about this concept will be presented, than for the DTSB concept.

4.2.1 Draft Tube Spouted Bed (DTSB) Concept

DTSBs are typically handling particles that do not easily fluidize, such as group D particles as defined by Geldart [102], but can also be used with group C particles, such as raw meal [107]. A jet of gas is introduced at the bottom of the reactor, entraining particles from a moving bed. The jet and entrained particles move up through a central draft tube and, once reaching the freeboard, the entrained particles spout onto the top of the moving bed. An illustration of the principle is given in Figure 43. Preliminary tests carried out in a lab-scale glass DTSB reactor showed that stable operation with raw meal could be achieved.

For application as a preheater the gas should be brought in contact with particles of increasing temperature, which could be achieved in a series of draft tubes units. Combining the individual units into a single rectangular unit, where particles moves sideways due to either gravity or inclined jets, while the gas moves from down and up, could principally establish the desired heat exchange process. The concept is illustrated in Figure 44.

Several issues, including controlling and generating the jets of hot gas and ensuring that the particles do not leave with the gases, has been identified. Furthermore, the behavior of a hot moving raw meal bed is unknown. The advantages of this design would be a very low construction height, simple geometries, and easily scalability. This idea in its original form was proposed by Hjuler [108].

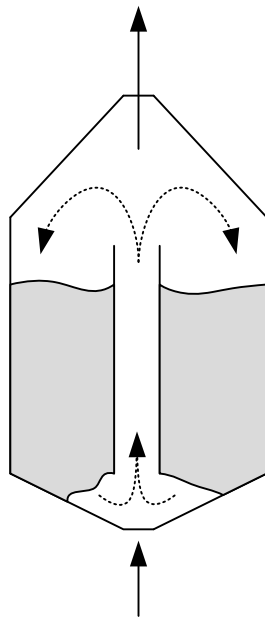


Figure 43 – Illustration of the draft tube spouted bed principle. Dashed lines indicate particle movement, full lines indicate gas movement.

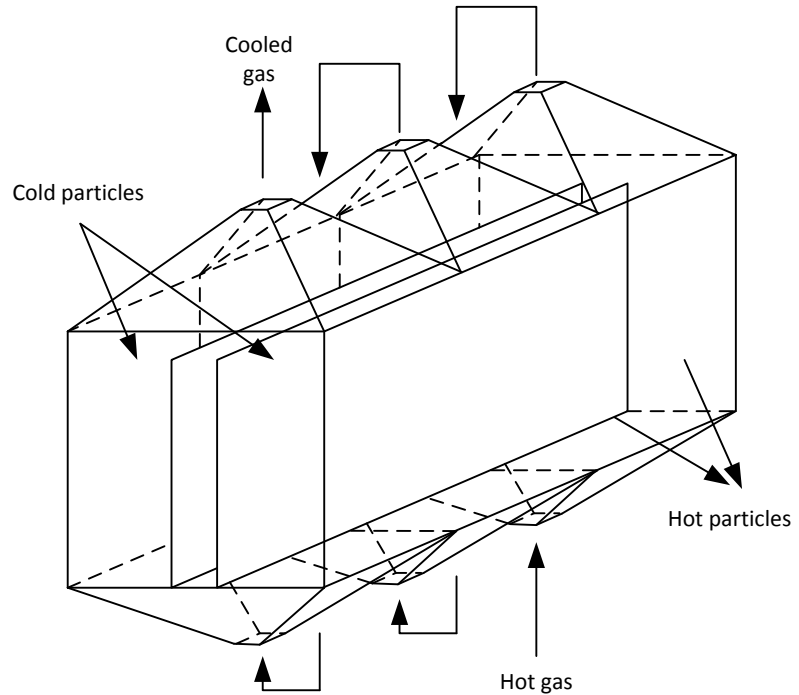


Figure 44 – Conceptual 3-D drawing of the draft tube spouted bed heat exchanger.

4.2.2 Two Dimensional Heat Exchanger (2D-HX) Concept

From desires to produce a shaft preheater with fewer or no of the shortcomings of the previously presented designs, the concept of the two dimensional heat exchanger (2D-HX) were devised. Inspiration the KHD shaft, pneumatic transport systems, and even cyclone preheater designs are identifiable.

The operational principle of the 2D-HX consists of a series of mixing and separation processes carried out in a counter-current pattern. The principle is illustrated in Figure 45. Cold raw meal is fed to the top stage, where a moving particle bed is formed. From the bottom of the moving bed, particles are fed into a fast flowing gas, where they are entrained. Once the particles are transported through a narrow channel, called the transport channel, the particles and gas are separated in a separation chamber, where a second moving particle bed is formed. In the transport channel, the gas and particles heat exchange.

Leaving the separation chamber, the gas moves upwards, while the heated particles moves down, creating the counter-current pattern. These processes are repeated in each stage. The particles leave the system from the lowest stage (not depicted in Figure 45), while gas exits the system from the top stage.

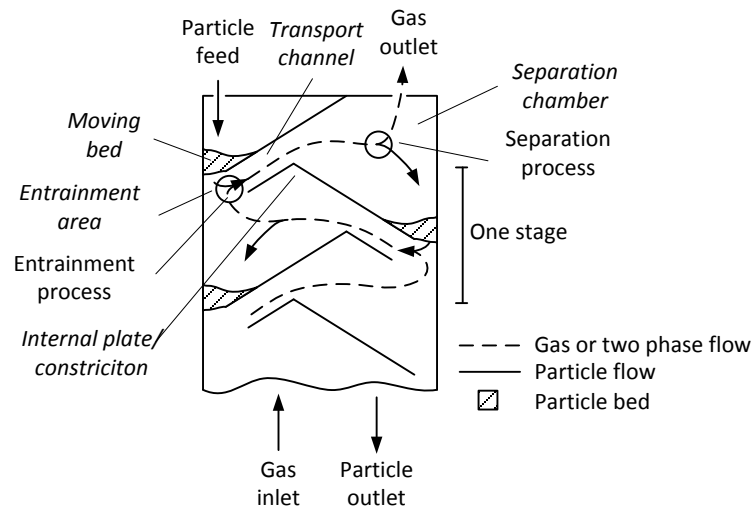


Figure 45 – Schematic drawing of the operation principles and nomenclature of the two-dimensional heat exchanger (2D-HX). Nomenclature is given in *italics*. Only the top part is displayed.

The separation is expected to be driven by two processes; a gravimetric and an inertial driven process. Despite the inertial process only consist of a single turn of the gas flow, the efficiency can be as high as 95 %, as shown by Gartside and Woebcke [109] for 50 μm particles.

The 2D-HX is expected to perform better than the shaft preheaters considered in Chapter 2 due to (a) better control of the process, (b) higher thermal efficiency due to less recirculation, and (c) the physical separation of the two internal processes, entrainment and separation, allows individual optimization of the design in order to improve both processes.

The major problems related to this design are expected to be to (a) ensure a stable particle flow, (b) control the particle flow from each bed, (c) ensure sufficient separation, and (d) maintain two-dimensional operation.

Properties of design

The properties of the 2D-HX are related to the simple design. One of the major advantages is the so-called two-dimensional design. A two-dimensional design can be described as design where the major features can be enclosed in a single vertical cross section of the equipment. To exemplify the two-dimensional concept, a bookshelf as shown in Figure 46 is considered: The bookshelf can be defined in the depth and height dimensions, while the length does not hold any significant design aspects. The length determines the capacity, and can during the design phase be adjusted to suit the requirements. The same principles apply to the 2D-HX, where the major design aspects can be found in the length and height dimensions, while the depth of the system can be adjusted to the desired capacity. The definitions of dimensions can be found in Figure 46 and Figure 47.

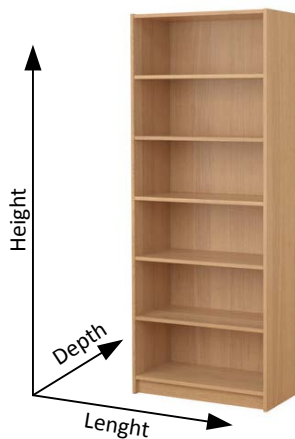


Figure 46 – An example of a two-dimensional design, a bookshelf. Length can be adjusted to suit capacity requirements [110].

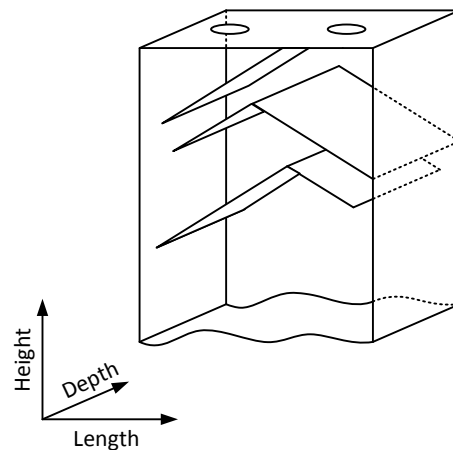


Figure 47 – Definition of dimensions for the 2D-HX. Depth can be adjusted to suit capacity requirements.

The individual stages in the 2D-HX design are identical, which, together with the two-dimensional aspect, makes the design modular. This means that the heat exchanger can be designed with a specific number of stages and capacity from a single basic unit. By increasing the number of stages in a stack, the thermal performance increases to a certain point, and by placing more stacks next to each other, the production rate can be increased. The concept and relevant denominations are illustrated in Figure 48.

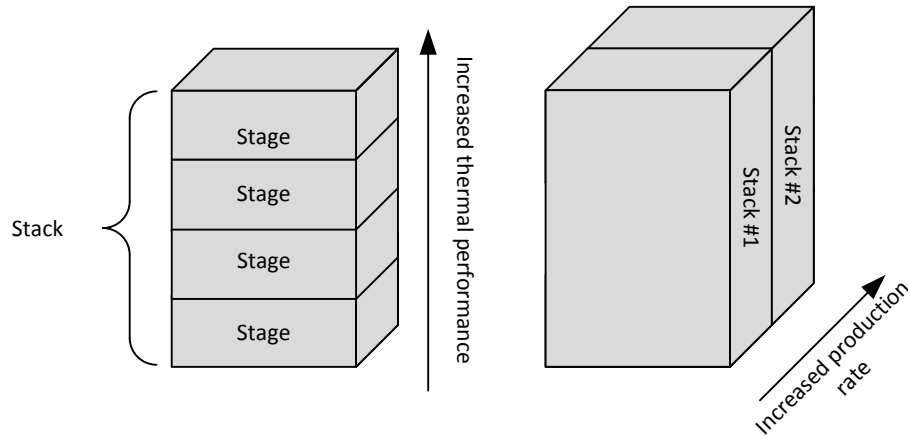


Figure 48 – The modular concept of the 2D-HX.

The geometries of the 2D-HX are mostly planar, which reduces cost and construction complexity. Furthermore, the design allows prefabrication of elements of which to construct the heat exchanger, another similarity to the bookshelf, shown in Figure 46. These elements could preferably be produced on a central factory, and then transported by sea or land to the construction site. This one-design-fits-all reduces further the construction costs. The feature, being a central element of the design, has been patented [111]. This idea is originally proposed by Dam-Johansen [112].

Design considerations

A detail from the first sketch of the 2D-HX design has been provided in Figure 49.

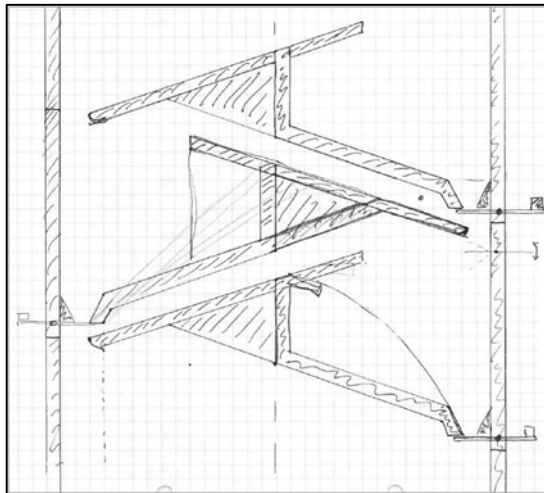


Figure 49 – Original sketch of the 2D-HX principle [112].

The original design, shown in Figure 49, could principally work, but to improve operation with raw meal, several things have been considered and modified. The slope of the internal surfaces were originally around 20° , which could be advantageous for handling free flowing particles, but for operation with raw meal, the slope should be steeper to avoid dead areas or blockages. In the first version for experimental testing, an angle of 45° has been chosen. The disadvantage of increasing the angle is higher construction height.

To increase the entrainment of particles, some internal constrictions have been installed, forcing the gas flow close to the particle bed. The design development is summarized in Figure 50.

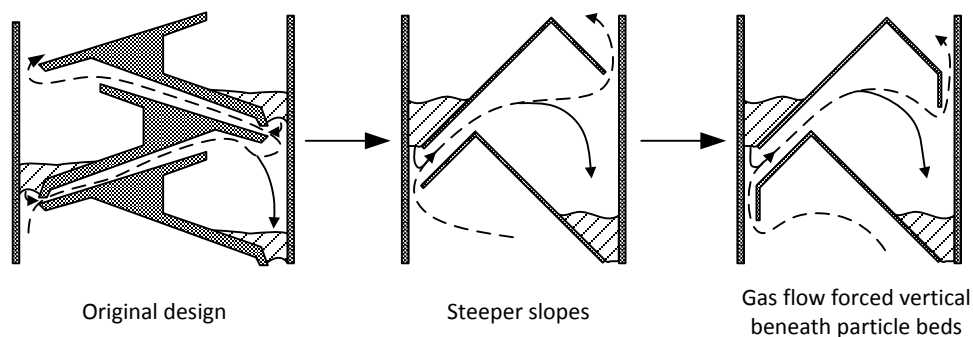


Figure 50 – Design development of 2D-HX before actual testing. Gas and two-phase flow indicated by dashed lines. Solid flows are indicated with full lines.

The particle flow rates from each particle bed should be controlled to ensure stable operation. For this purpose, a simple particle gate, either sliding or tipping should be sufficient. The gate should be operated according to the particle bed level, keeping it constant at a certain level. To ensure flow of particles, air nozzles could be installed in each the particle bed to break up undesired stable particle formations.

4.3 Summary

Through a series of meetings with industry and academia, several ideas for a novel preheater were identified. Of these, two were presented: The DSTB and the 2D-HX. The 2D-HX concept proved the most promising. This concept was chosen for further experimental investigation due to expected low construction costs, similar operational principles to cyclone preheaters, simple geometries, modular construction, and realizable operation. Furthermore, the design could be tested in the pilot facilities available. From the original design, the 2D-HX has been modified for better performance before actual testing.

Chapter 5

Experimental Approach, Set-ups, and Materials

"Getting there is half the fun"

Slogan of Cunard Line

The experimental work of this thesis is focused on documenting the performance of the suggested heat exchanger design. This is done through investigations of (a) particle flow patterns and (b) thermal performance. Observations regarding stability and operability are also of interest for validating the design. An experimentally stepwise approach has been applied, involving three set-ups of increasing complexity. This approach has made it possible to gradually confirm operation principles and gain insight in system performance. The observations made on each set-up have been implemented to improve design and operation of the following. An overview of the aim of each set-up, as well as the obtained types of data are given in Table 14, while operational characteristics can be found in Table 15.

The first two set-ups were semi-continuous systems operating at ambient temperature, developed to investigate the particle transport patterns, and located at DTU. These set-ups were designed to prove the heat exchanger concept in terms of particle transport patterns, before a hot heat exchanger set-up was designed, and not designed for intensive experimental work. The third set-up was a continuous proof of concept (PoC) bench-scale heat exchanger designed to operate at temperatures up to 800 °C in order to evaluate heat exchange performance. This set-up was, due to its size, production rate of hot particles, necessary auxiliary equipment, and the dusty nature of raw meal, located at Dania, FLSmidth's test center, 50 km north of Aarhus, Denmark.

Table 14 – Overview of experimental work and obtained data.

Set-up name	Objective	Session	Obtained data	
			Flow patterns	Thermal
Single-stage	Investigation of transport properties in a single stage.	-	X	-
Multi-stage	Investigation of transport properties in multiple stages, particle bed behavior, and separation process.	-	X ^A	-
Proof of Concept (PoC)	Detailed investigation of transport properties, operational stability using one to four stages. Designed to achieve proof of hot operation.	1 st	(X) ^B	(X) ^B
		2 nd	X	X ^C
		3 rd	X	-

^A Experimental work performed by Andersen [113].

^B Commissioning, reported by Quintero [114].

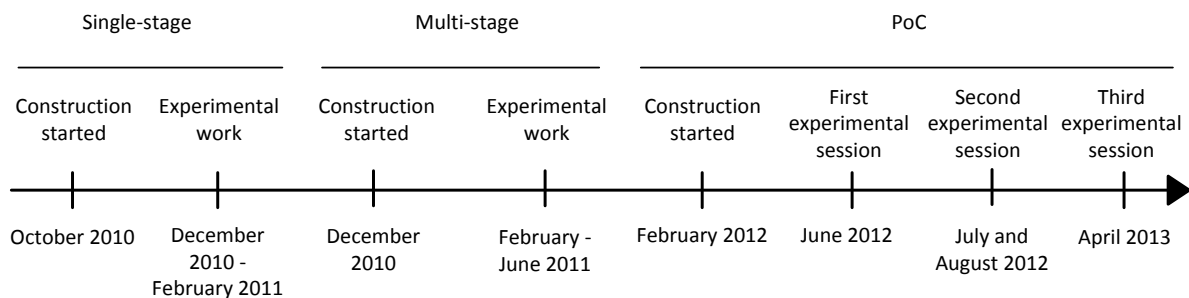
^C Experimental proof of concept.

Table 15 – Overview of operational characteristics of experimental set-ups.

Set-up name	No. of stages	Type of particles	Maximum particle feed rate	Maximum gas temperature	Maximum gas feed rate	Operation modes
Single-stage	1	Sand and raw meal	180 kg/h	Ambient	63 kg/h	Semi-continuous
Multi-stage	4	Raw meal	180 kg/h	Ambient	90 kg/h	Semi-continuous
Proof of Concept (PoC)	1 – 4	Raw meal	200 kg/h	800 °C	200 – 425 kg/h ^A	Continuous

^A Depending on temperature. The lower the temperature, the higher the available gas flow.

Due to time restrictions on use of existing auxiliary equipment and project economy, the experimental work on Dania has been limited to three sessions. A timeline for the experimental work is provided in Figure 51.

**Figure 51** – Timeline of experimental work.

In the following sections, descriptions of each set-up and summarized experimental procedures will be provided, as well as the materials used, will be described. Please refer to Appendix A for detailed experimental procedures.

5.1 Single-stage Set-up

The Single-stage set-up consisted of a single stage of the heat exchange design. It was equipped with an air inlet and outlet, three access points for emptying and cleaning the set-up, nozzles for local fluidization of particles in feed chamber, and a particle gate. Construction materials were wooden panels with a transparent polycarbonate front. A schematic drawing and a photo are provided in Figure 52 and Figure 53, respectively.

An overview of the set-up, including auxiliary equipment, is provided in Figure 54. A rotameter was used as flow meter, and was calibrated using a gas meter. The filter system consisted of an industrial size vacuum cleaner. The maximum air flow rate was around 63 kg/h, limited by the suction capacity of the vacuum cleaner. Sub atmospheric pressure was desired in the system to limit dust emissions.

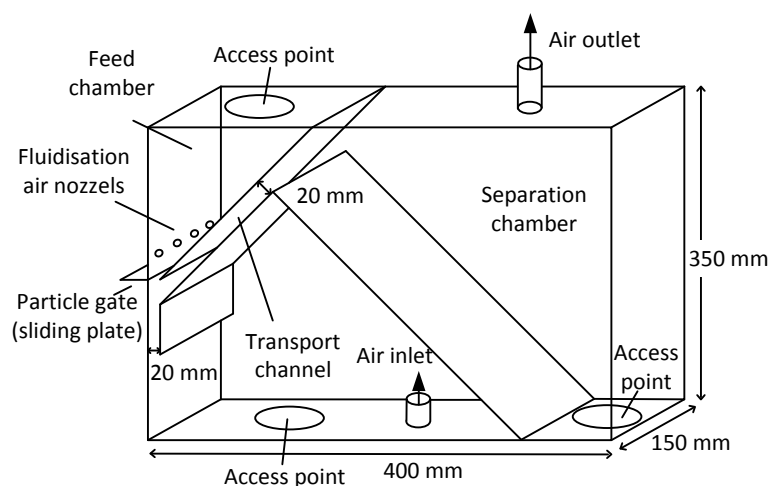


Figure 52 – Schematic drawing of the Single-stage set-up.

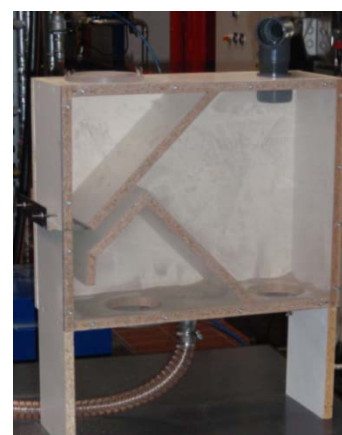


Figure 53 – Photo of the Single-stage set-up. Fluidization nozzles not installed at the time of the photo.

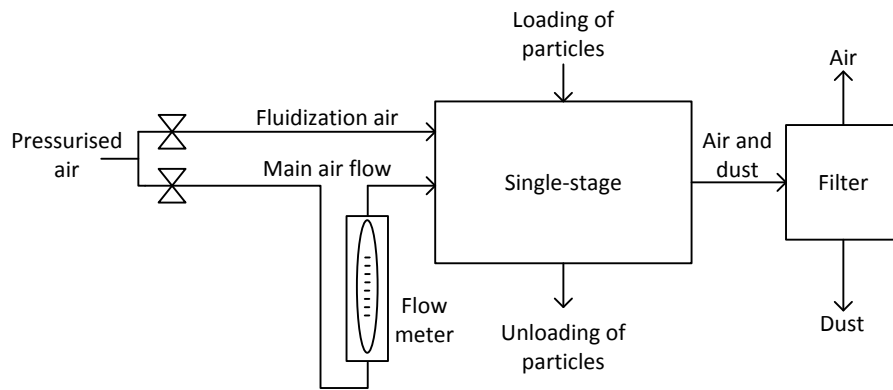


Figure 54 – Process diagram of the Single-stage set-up, including filters, flow meter, and valves.

The system was a semi-continuous system, initially loaded with a known mass of particles in the particle feed chamber. The gas flow was adjusted to the desired level, and the particle gate was opened, allowing a certain mass flow of particles. The system was then run until depletion of particle feedstock. Data was obtained by weight measurements of particles accumulated at the different locations after each experiment, and visual observations made through the transparent front panel.

5.2 Multi-stage set-up

Principally, the Multi-stage set-up was similar to the Single-stage set-up but instead of one stage, it contained four stages. A schematic drawing and a photo of the multistage heat exchanger design can be found in Figure 55 and Figure 56. Construction materials were wooden panels and transparent polycarbonate.

The individual stages were identical to the Single-stage set-up. The total height was approximately 1750 mm. Compared to the single set-up, the most significant changes were: (a) four stages, (b) improved particle gates, constructed as a tilting plate, rotating around an axis, (c) increased capacity for particles at the bottom and top stages for longer operation, and (d) upgraded filter capacity. Flow for both fluidization and main gas was measured by rotameters. A process diagram is shown in Figure 57.

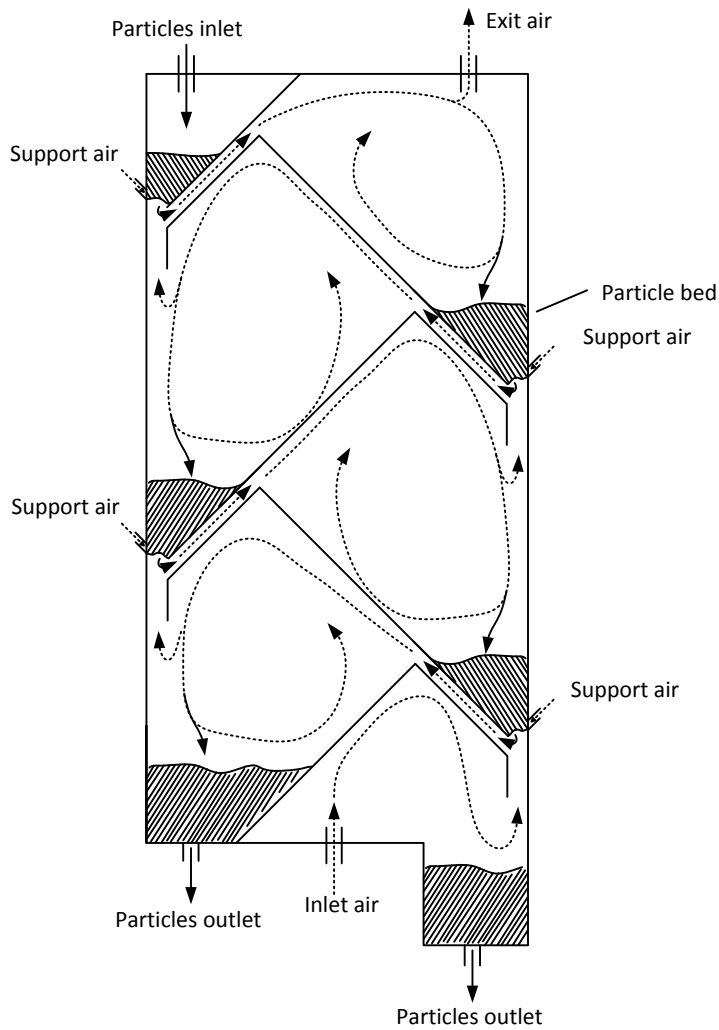


Figure 55 – Schematic drawing of the Multi-stage set-up with expected particle and gas flows.

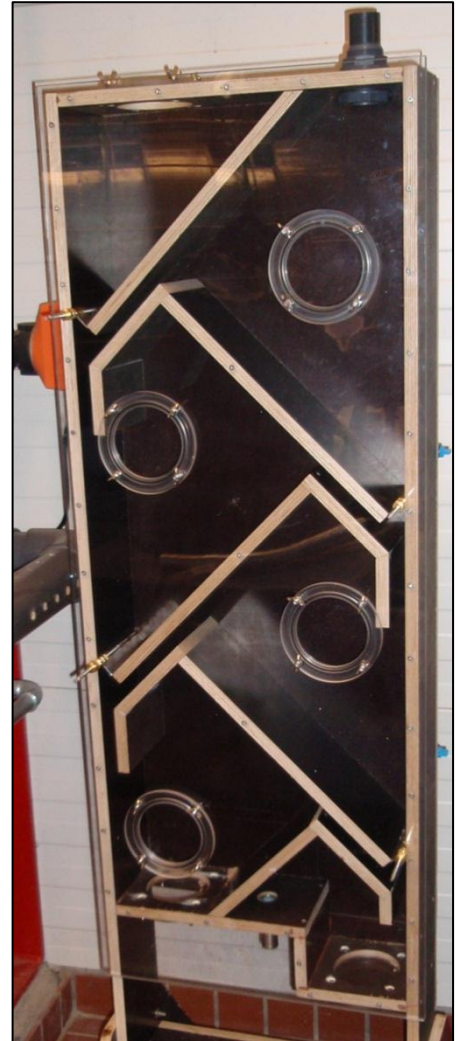


Figure 56 – Photo of the Multi-stage set-up. Fluidization nozzles were not installed at the time of the photo.

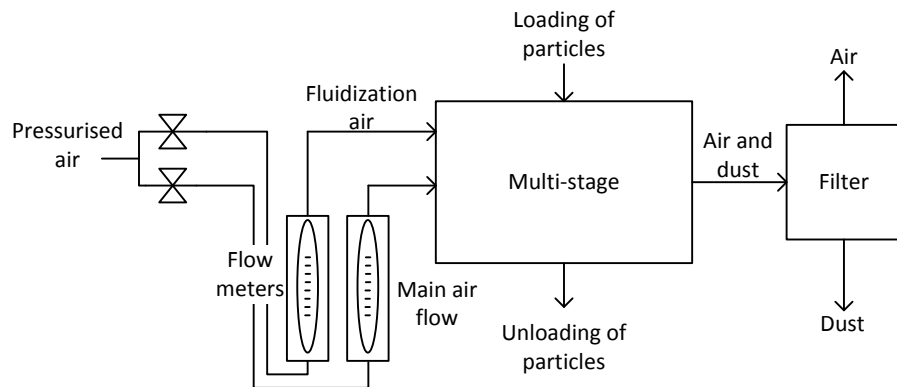


Figure 57 – Process diagram of the Multi-stage set-up, including filters, flow meter, and valves.

The startup and shutdown procedures for the Multi-stage set-up were similar to the Single-stage set-up: Initially all particle gates were closed and the top compartment was filled with a weighted amount of particles. After adjusting the gas flows to the desired levels, the top stage particle gate was opened and particles were transported to the second stage. Once enough particles were present to ensure no gas could pass through the formed particle bed, the gate at the second stage was opened and so on. When not enough particles were present at a given stage, the gate was closed. Depending on the initial mass of particles in the feed stock, not all stages were active simultaneously. Quasi-steady state could be achieved on the individual stages for shorter periods of time when the net transport to the given bed was zero. Data was obtained from weight measurements of particles at each of the final bottom locations and the filter.

5.3 Proof of Concept Set-up

The PoC set-up has been constructed of high temperature resistant steel, equipped with up to twelve thermocouples, and five differential pressure sensors. Due to a modular construction, the system could be reconfigured in terms of number of stages and positioning of sensors, depending on the purpose of the experimental work carried out. This also enabled a stepwise introduction of stages when commissioning the set-up. A schematic drawing of the four stage set-up and standard position of sensors are provided in Figure 58. A process diagram of the entire set-up is provided in Figure 59. The modular construction of the system is evident from the construction drawings, Figure 60, and the photo of the actual set-up, Figure 61.

The depth of the system was 200 mm, and the dimensions of the transport channels were 50 mm by 200 mm. The installed height of the entire set-up was approximately 4000 mm. At each stage, three sight glasses were installed for visual access to the particle bed. The gates were principally similar to the gates in the Multi-stage set-up, but instead of introducing fluidization air in the particle beds, the gates were vibrated to ensure a stable particle flow. The gates were operated manually according to visual observations. The angels of the internal walls were 70°. Feeder and containers collecting heated particles had capacities to run between one and three hours, depending on particle feed rate. During hot operation, the system was isolated with 100 mm isolation material. Hot air was supplied from an electrical gas preheater.

To achieve isothermal conditions, a flow of hot gas was used to heat up the entire set-up. Once thermally stable conditions were achieved, particle flow could be initiated. The particle beds were filled from the top and down. During initial operation with particles, the temperature of the set-up decreased. After a certain period, typically around a half to one hour, an operational

steady state was reached. During this steady state, experimental data was achieved. Data consisted of continuous temperature, pressure and weight data. A description of the data acquisition can be found in section 5.3.1 – *Data Acquisition*.

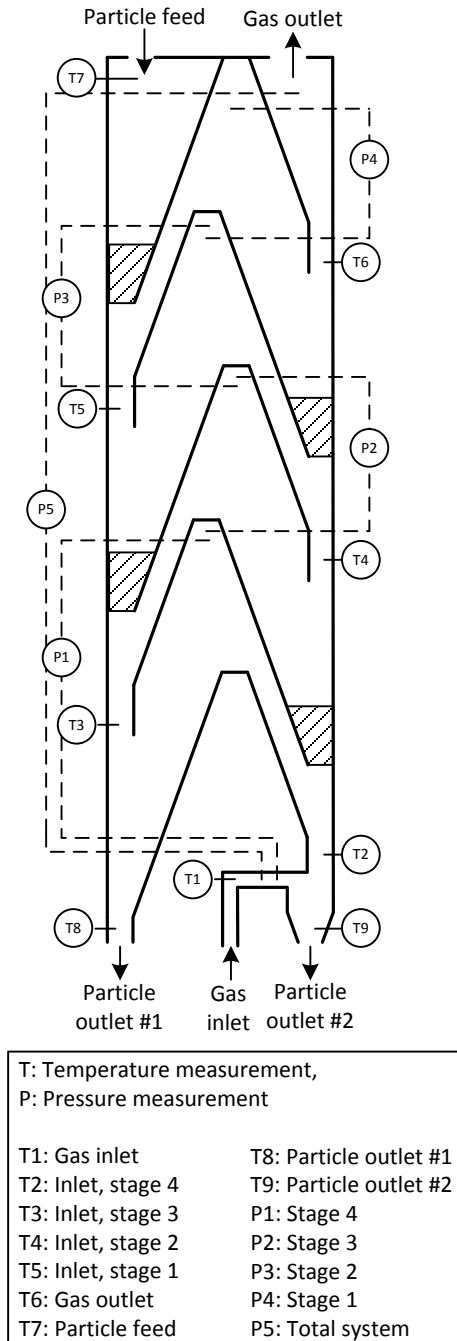


Figure 58 – Configuration of a four stage system during heat exchange experiments. Temperature and pressure sensors are depicted.

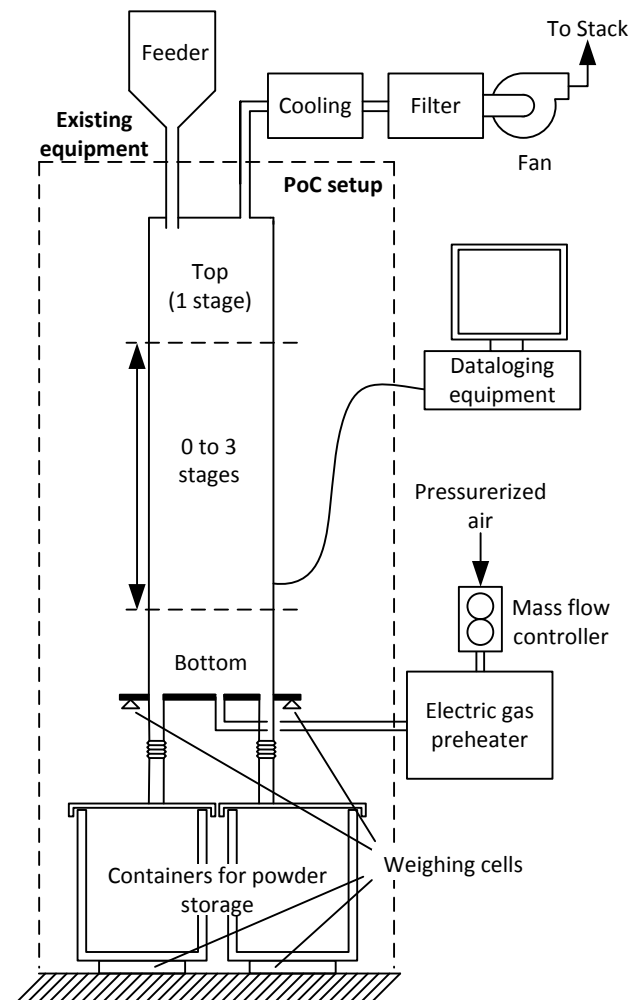


Figure 59 – Process diagram of PoC set-up. Existing equipment at Dania is shown outside the dashed line.

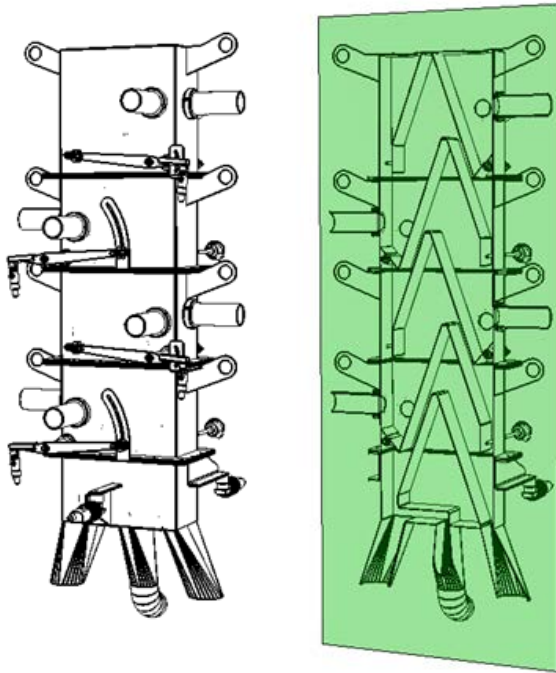


Figure 60 – Solid works drawings of the PoC set-up with four stages. A center cut plane is shown to the right.

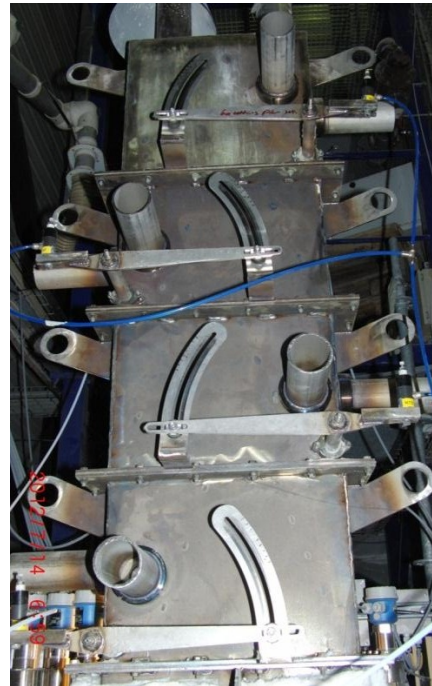


Figure 61 – Photo of set-up without isolation. Visible are the identical three center stages and the top stage.

For visual access to the gas and flow patterns, a special stage for the 2D-HX was designed with transparent sides. Backlit video material were produced at 300 frames per second, capturing the dynamic flow pattern of particles for analysis. The recordings were obtained in the system schematically depicted in Figure 62. Figure 63 shows the actual transparent module with light source installed oppositely.

Due to constructional limitations, the entire process could not be seen through the transparent stage. For example the entire entrainment region could not be viewed and the vertical channel below entrainment area was also difficult to visually access. The system could only be run at ambient temperature, when inclosing the transparent module.

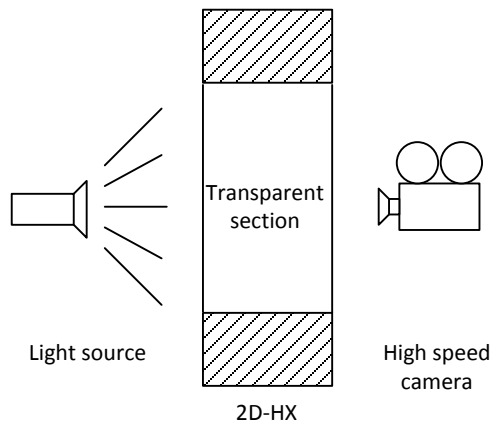


Figure 62 – Set-up for live recording of separation behavior.

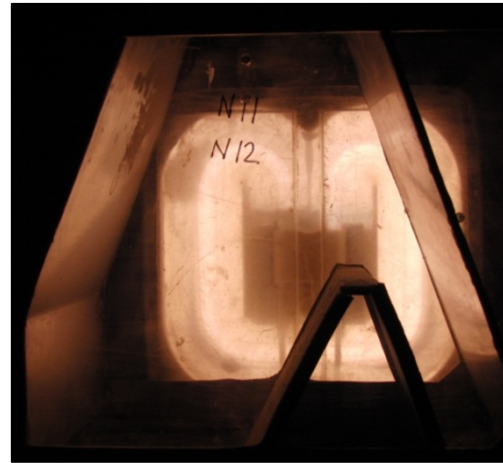


Figure 63 – Internal view of transparent model. Light source installed oppositely.

5.3.1 Data Acquisition

The data from the PoC set-up were recorded using the control and data collection software at Dania, ECS. Data were recorded once per second. A screen dump, showing the tailored configuration for the PoC set-up with a single stage, is given in Figure 64.

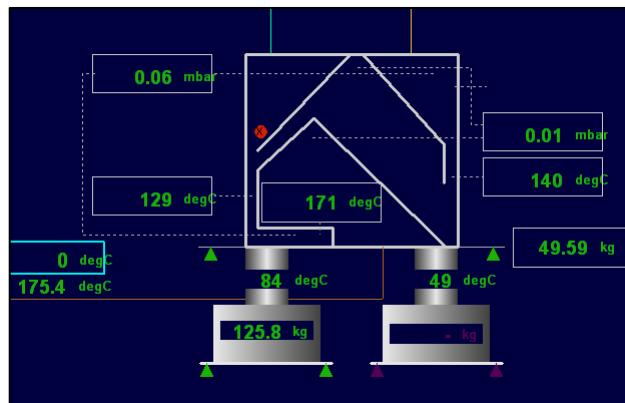


Figure 64 – Screen dump from the data logging software, ECS.

From the continuously recorded data, the operational steady state was identified in each experiment, and the relevant data excerpted. The duration of the steady state was between 10 and 30 minutes, defined by temperature changes of less than 5 % / min. An example of a full data-set is given in Figure 65. The operational steady state is marked by two vertical lines at approximately $t = 6500$ s and $t = 8300$ s. The experimental data from the PoC set-up, presented

in Chapter 6 and 7, are steady state data; average temperatures and collected mass of particles during steady state. The inlet conditions are constant during experiments. A full description of the data treatment is provided in Appendix B.

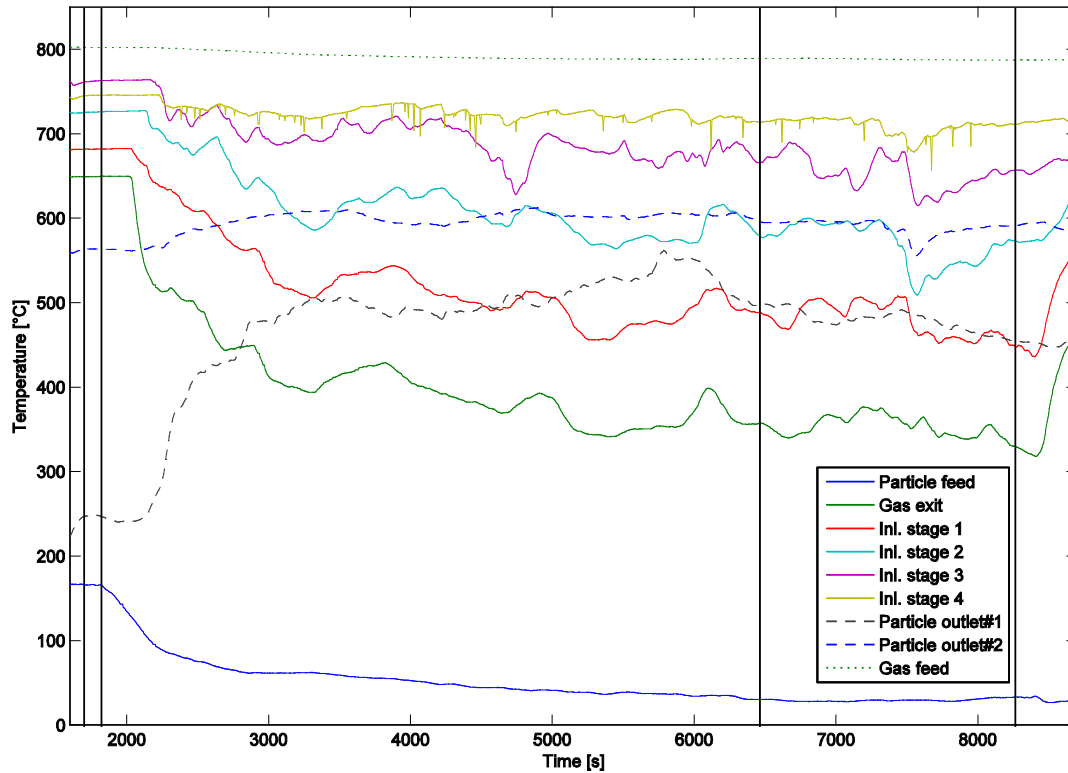


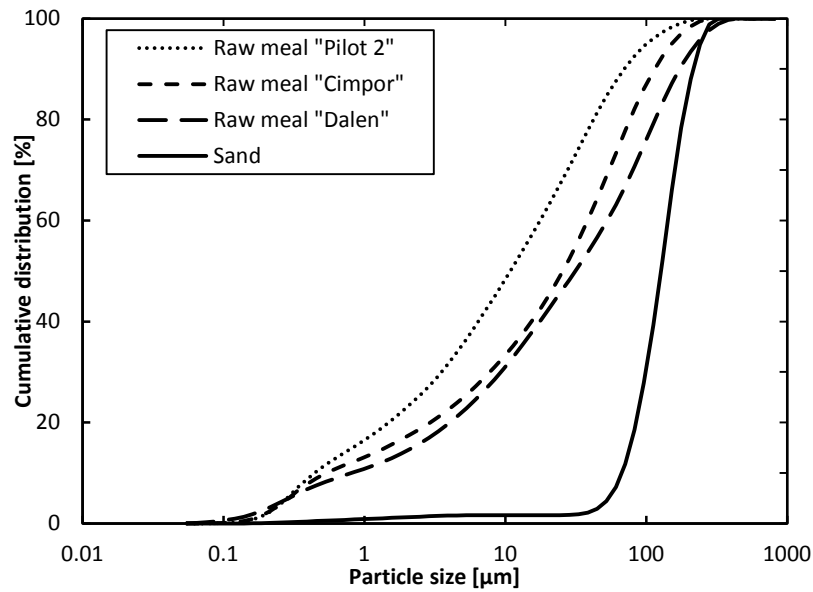
Figure 65 – Temperatures of experiment PoC#2. Vertical lines indicate the two periods of stable operation: Initial and operational steady state, respectively.

5.4 Materials

The relevant properties of particles used in the experimental work, sieved beach sand and three industrial raw meals, are summarized in Table 16. The cumulative size distributions are provided in Figure 66. The particle size data have been obtained by laser diffraction, and the flow ability and density using a Schulze ring shear tester [115]. The particle flowability factor numerically expresses the flowability of powders: The higher the number, the easier flowing powder.

Table 16 – Properties of particulate material used during experimental work.

Particle type	Volumetric mean diameter [μm]	Loose density [kg/m^3]	Particle classification [102]	Particle flow factor	Used in
Sand	137	$1.4 \cdot 10^3$	Group B	17 (free flowing)	Single-stage set-up
Raw meal "Dalen"	30.1	$1.0 \cdot 10^3$	Group C	N/A	Single-stage set-up
Raw meal "Cimpor"	25	$1.2 \cdot 10^3$	Group C	2.8 (cohesive)	Multi-stage set-up
Raw meal "Pilot 2"	12	$1.1 \cdot 10^3$	Group C	1.7 (very cohesive)	PoC set-up

**Figure 66** – Cumulative size distribution for the used particles.

The gas used is air, supplied at either ambient or elevated temperatures and at a pressure around 1 bar, depending on operation conditions and set-up.

Chapter 6

Investigation of Transport Processes

“Felix, qui potuit rerum cognoscere causas” (approximately: Fortunate is he, who is able to know the causes of things)

– Vergil, ancient Roman poet

This chapter presents selected results of the investigation of the transport processes in the 2D-HX, which consists of entrainment and separation processes. The results presented in this section are based all three set-ups, and are presented in chronological order to illustrate the progress in the experimental work, and the development of insight in the performance of the heat exchanger.

Experimental results are given in full details in Appendix C.

6.1 Definition of Efficiencies

Recalling Chapter 3, particle transport in a system similar to the cyclone preheater can be described by a separation and an entrainment efficiency. The overall stage transport efficiency is the product of these two parameters. Considering a single stage, as shown in Figure 67, the efficiencies are defined as:

$$\eta_{Transport} = \eta_{Ent} \cdot \eta_{Sep} = \frac{\dot{m}_B + \dot{m}_D}{\dot{m}_{Feed}} \cdot \frac{\dot{m}_B}{\dot{m}_B + \dot{m}_D} = \frac{\dot{m}_B}{\dot{m}_{Feed}} \quad \text{Eq. 33}$$

In the semi-continuous systems, the efficiencies will not be computed from mass flows, but the masses of particles collected at the relevant positions after each experimental run.

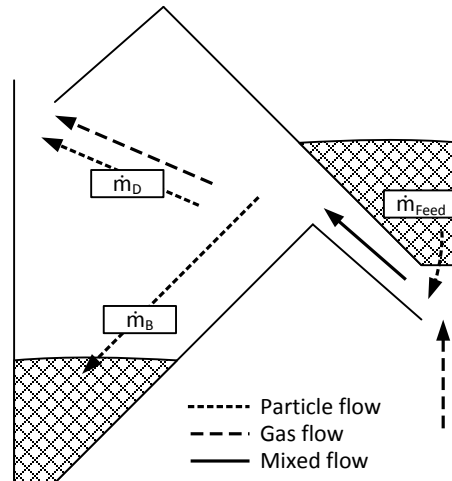


Figure 67 – Schematic drawing of particle flows in a single stage in the 2D-HX.

6.2 Results: Single-stage Set-up

To gain a first insight in the transport performance of the 2D-HX, experiments were carried out on the Single-stage set-up. Initially sand was used due to the easy handling and free flowing properties. The effects of (a) average gas velocity in the transport channel, (b) initial mass of particles in feed stock, and (c) solid load, on the entrainment and separation efficiencies have been investigated by a two level fractional experimental design with four center points, applied on the three experimental parameters; gas flow, particle gate gap, and initial mass of particles in feed stock. An analysis of variance (ANOVA) has been carried out on the resulting conditions. Experimental settings and measured efficiencies are given in Table 17. The gas velocity has been computed from the cross sectional area of the transport channel and the measured volumetric gas flow, while the solid load has been obtained from the initial mass of particles, the duration of each experiment, and the gas flow. The results of the ANOVA are presented in Table 18.

The term *treatment* covers the effects considered. Both single and two-factor effects are investigated to reveal if any interaction is significant. The *F-ratio* is a measurement of the influence of the treatment compared to the experimental uncertainties⁷. The column *Prob. > F* indicates the probability of the treatment not having a significant influence on the investigated parameter (separation or entrainment efficiencies) [116]. Here, an uncertainty level of 5 % ($\alpha = 0.05$) is chosen. Significant effects are marked by bold.

⁷ F-ratio is computed as the mean sum of squares for each treatment divided with the mean square of the error.

Table 17 – Experimental settings and results for used in an ANOVA for sand particles in the Single-stage set-up.

Ex. name	Particle gate opening [mm]	Duration [s]	Initial weight ^A [g]	Velocity ^A [m/s]	Solid load ^A [kg/kg]	η_{Sep}	η_{Ent}
S#1	6	30	30	3.10	3.16	0.97	0.67
S#2	6	34	1010	3.10	2.80	0.96	0.75
S#3	6	36	1001	3.10	2.62	0.96	0.77
S#4	6	30	1000	3.10	3.14	0.96	0.65
S#5	3	56	755	2.52	1.62	0.96	0.50
S#6	3	73	1259	2.52	2.00	0.84	0.57
S#7	9	15	755	2.52	5.84	0.97	0.57
S#8	9	25	1249	2.52	5.80	0.97	0.62
S#9	3	104	751	3.68	0.57	0.96	1.00
S#10	3	108	1256	3.68	0.92	0.97	1.00
S#11	9	22	756	3.68	2.73	0.96	0.79
S#12	9	31	1256	3.68	3.21	0.93	0.91

^A Used for ANOVA

Table 18 – Results of the ANOVA for the Single-stage set-up

Treatment	Separation		Entrainment	
	F Ratio	Prob. > F	F Ratio	Prob. > F
Weight	2.5	0.19	4.2	0.11
Solid load	0.54	0.50	4.4	0.10
Gas velocity	1.2	0.33	51	0.0020
Weight x Solid load	1.8	0.25	0.24	0.65
Weight x Gas velocity	3.1	0.15	0.36	0.58
Solid load x Gas velocity	1.7	0.26	11	0.029
Residual plot	OK – random deviation		OK – random deviation	

The results of the ANOVA for the entrainment efficiencies suggest that only two treatments are significant: The gas velocity and the interaction between solid load and gas velocity. The remaining parameters were reported insignificant. Regarding the separation efficiency, the ANOVA showed that no treatments were significant, indicating that the influence of the treatments on the separation efficiency at the investigated conditions is indistinguishable from the experimental uncertainties. The standard deviations of the entrainment and separation data have been reported to be 0.05 and 0.03, respectively, indicating good reproducibility.

Following the conclusion of the ANOVA, the effect of gas velocity on Dalen raw meal have been investigated. Obtained efficiencies are provided in Figure 68 and Figure 69. Note that both efficiencies are depicted against the characteristic velocity, which is the average gas velocity in the transport channel. The gas velocity in the separation chamber is up to eight times lower, depending on position and gas flow patterns.

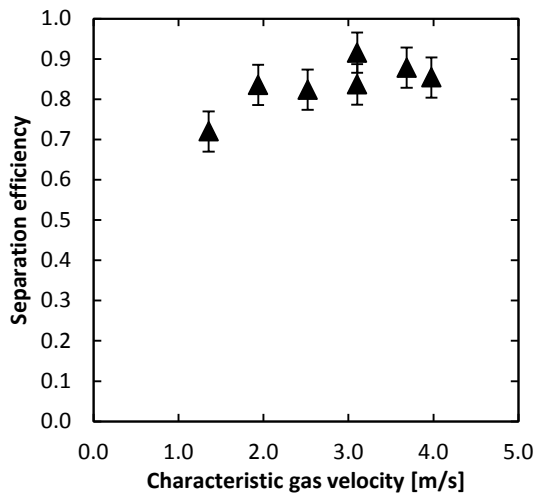


Figure 68 – Measured separation efficiencies for Dalen raw meal in the Single-stage set-up.

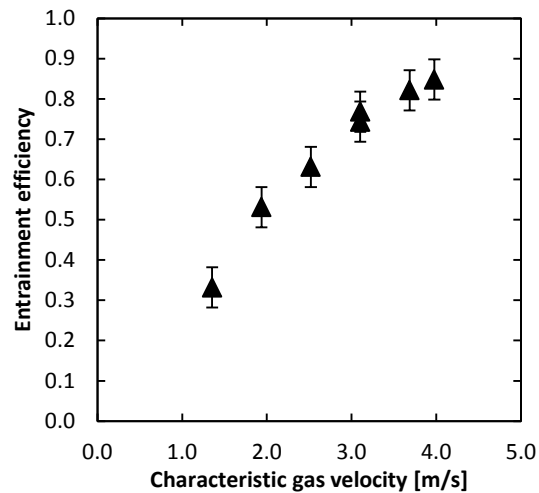


Figure 69 – Measured entrainment efficiencies for Dalen raw meal in the Single-stage set-up.

For increasing gas velocities, the entrainment efficiency increases, while the separation efficiency apparently increases slightly. The data above yield transport efficiencies, as computed by Eq. 31, between 0.24 to 0.72. The highest values are found at the highest gas velocities. Comparing the separation efficiency of the raw meal with the separation efficiency of sand, significantly lower values are found for the raw meal, caused by the smaller particle sizes.

6.3 Results: Multi-stage Set-up

The transport patterns for particles repeatedly entrained and separated in four consecutive stages have been investigated in the Multi-stage set-up. The results of a series of experiments with Cimpor raw meal as particulate matter and gas velocities between 1.8 m/s and 4.4 m/s are provided in Figure 70. Results indicate that increasing the gas velocity increases the entrainment efficiency, as found in the Single-stage set-up, and increases the size of the dust stream leaving the system. Figure 71 provides an explanation of the particle locations mentioned in Figure 70.

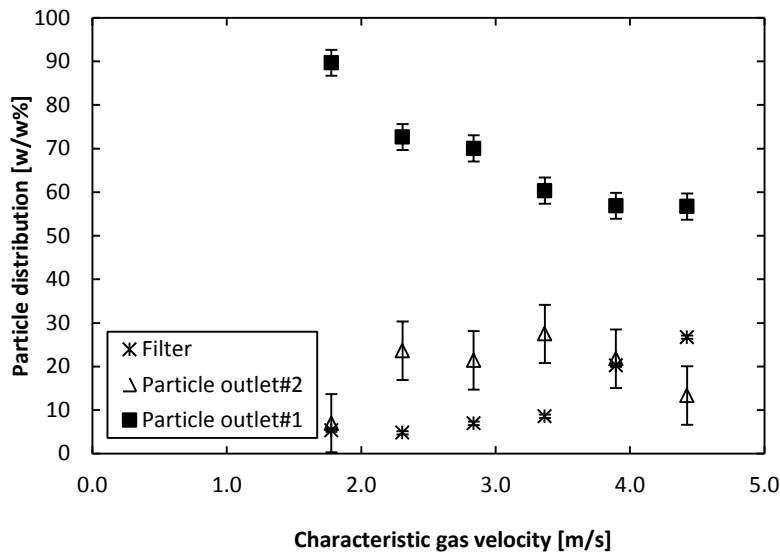


Figure 70 – Final distribution of particles in the Multi-stage set-up.

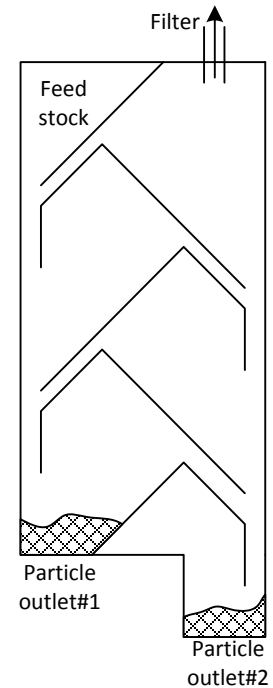


Figure 71 – Position of initial and final positions of particles in the Multi-stage set-up

Entrainment and separation efficiencies are not directly obtainable from the experimental data. To gain information on the internal transport processes on each stage, the overall system behavior is modeled using coupled mass balances for all stages, similar to the cyclone preheater model presented in Chapter 3. Additional information on the model can be found in [113]. Data from the Single-stage set-up indicated that the separation efficiency did not depend on gas velocities in the actual range of gas velocities, and that the entrainment efficiency as a function of the gas velocities yielded an s-shaped curve. Therefore, for simplicity, the entrainment efficiency is assumed to follow a Sigmoid function, while separation is assumed constant, 0.70. The general Sigmoid function is provided in Eq. 34, where C is a fitting parameter.

$$\eta_{Ent} = \frac{1}{1 + e^{-v_g + C}} \quad \text{Eq. 34}$$

By fitting model predictions to the data shown in Figure 70, the fitting parameter $C = 2.9$ is found. The model predictions and experimental data are compared in Figure 72. A depiction of the assumed entrainment and separation efficiencies can be found in Figure 77 and Figure 78.

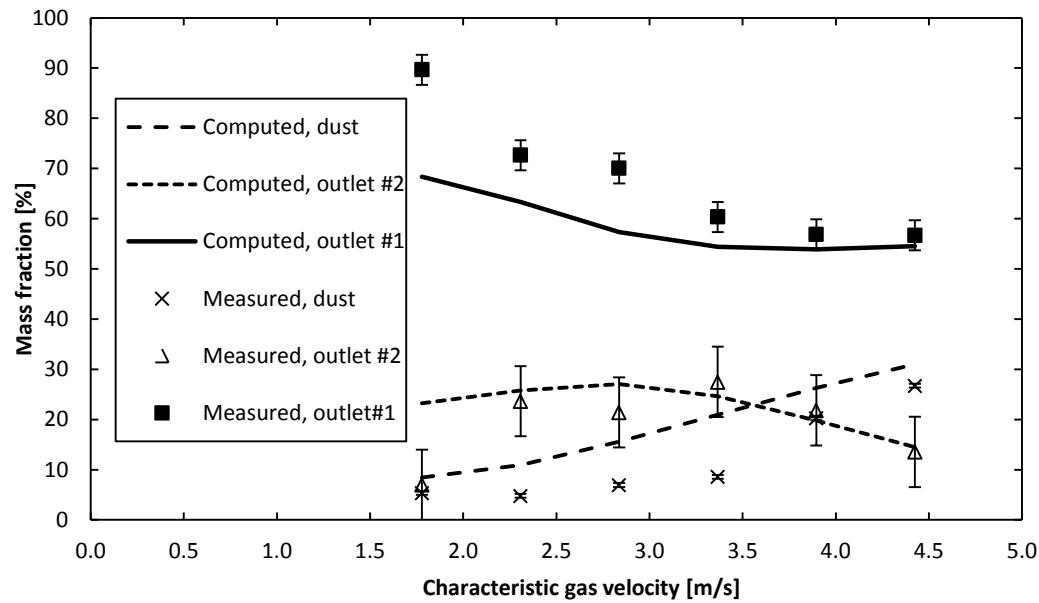


Figure 72 – Comparison between predicted particle distribution and measured data.

The model fits the experimental data reasonably, with deviations of up to 20%, and trends represented correctly. The predicted optimum for the outlet #2 is shifted to the left, compared to the experimental data. Deviations are largest at low gas velocities. The model results indicate that the entrainment and separation efficiencies applied in the model resemble the actual system behavior reasonably, thereby confirming the observations made on the single stage set-up.

6.4 Results: PoC Set-up

A thorough analysis of entrainment and separation efficiencies has been carried out on the PoC set-up. For these experiments, the PoC set-up was configured to contain one stage, and was operated at ambient conditions, enabling shorter time between experiments. Each data set is obtained during a steady state of 10 – 20 minutes, smoothing out operational disturbances. The analysis of entrainment and separation has been investigated in both second and third experimental session (see Table 14, Chapter 5), and three independent data sets exist. All obtained data have been collected in section 6.5 – *Overview and Comparison of Data* as well as provided in Appendix C. In this section, the experiments P3#9 – P3#35 are treated.

Gas velocities in the transport channel between 1.5 and 9.9 m/s have been investigated at 27 different conditions. Experiments were divided into four data series, depending on the solid load, and labeled according to the desired solid load. Actual solid loads were deviating slightly

from the desired values, due to varying gas flow. Solid load was varied between 0.45 and 1.06 kg solid/kg gas. The solid load and the gas velocity could be varied independently within the range of available particle and gas feed rates. Particle feed rates of 60, 100, 140 and 200 kg/h have been applied. Results are presented in Figure 73 and Figure 74.

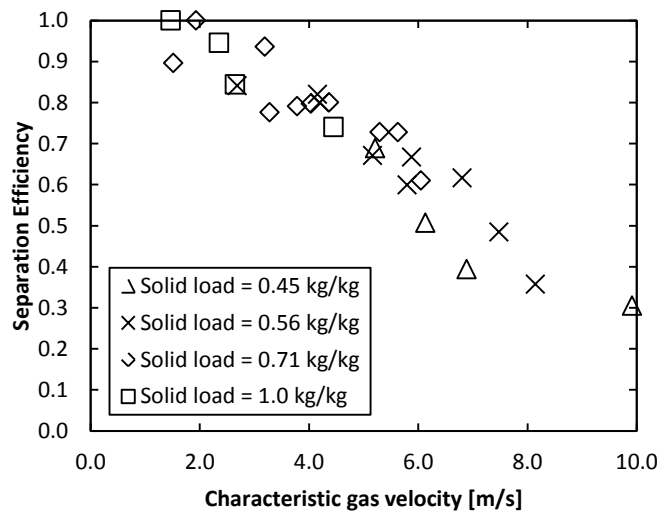


Figure 73 – Separation efficiencies obtained from experiments on the PoC set-up with a single stage. $T_{G, in} = 20\text{ }^{\circ}\text{C}$.

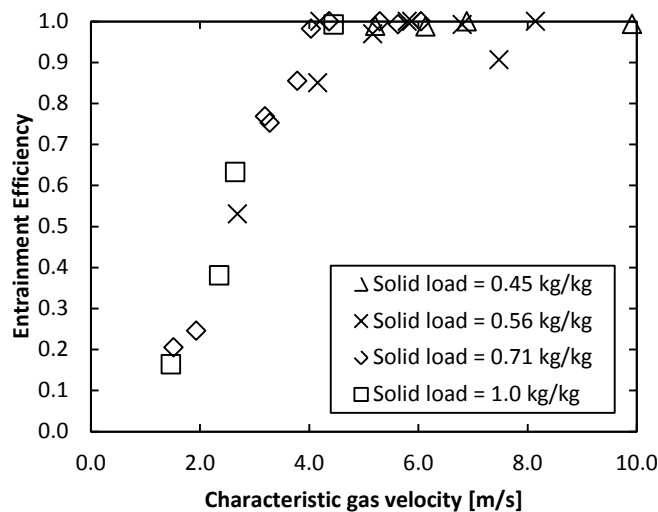


Figure 74 – Entrainment efficiencies obtained from experiments on the PoC set-up with a single stage. $T_{G, in} = 20\text{ }^{\circ}\text{C}$.

The trend shown in Figure 74 is similar to the trend observed in the data from the Single- and Multi-stage set-ups, while the data in Figure 73 show a trend of decreasing separation

efficiencies as gas velocity increases. This has not been seen in the previous data series, likely due to the low gas velocities previously applied, and uncertainties related to the semi-continuous operation.

To identify if solid load influences the efficiencies, the data of Figure 73 and Figure 74 are plotted against solid load in Figure 75 and Figure 76. Indications of gas velocity are provided as dashed lines.

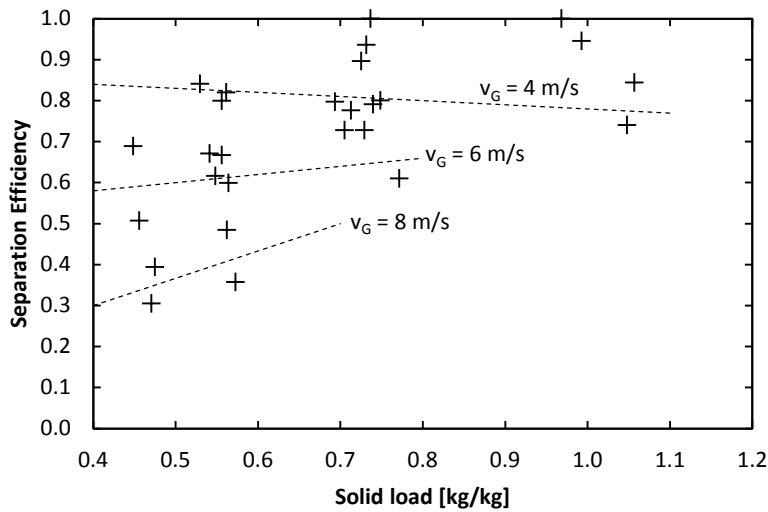


Figure 75 – Separation efficiencies from the PoC set-up with a single stage. Dashed lines indicate gas velocity ranges. $T_{G, \text{in}} = 20 \text{ }^\circ\text{C}$.

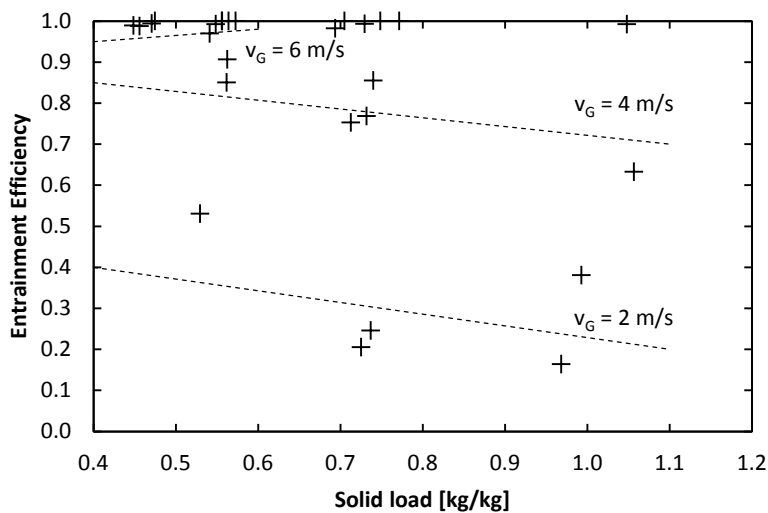


Figure 76 – Entrainment efficiencies obtained from the PoC set-up with a single stage. Dashed lines indicate gas velocity ranges. $T_{G, \text{in}} = 20 \text{ }^\circ\text{C}$.

It is noted that plotting the efficiencies against gas velocity yields more clear trends, while the data, when plotted against solid load, yields a murkier picture with less clear trends. The presented data does not unambiguously indicate the effect of the solid load.

An ANOVA has been performed on both efficiencies. The results of the analysis, provided in Table 19, show that given the actual data, the solid load under the tested conditions neither influences the separation nor the entrainment process. In the investigated operation range, both processes depends only on gas velocity at the given uncertainty level ($\alpha = 0.05$).

Table 19 – Results of ANOVA for entrainment and separation efficiencies

Treatment	Separation		Entrainment ($0.10 < \eta_{\text{Ent}} < 0.90$)	
	F Ratio	Prob. > F	F Ratio	Prob. > F
Solid load	1.53	0.23	1.89	0.21
Gas velocity	109	< 0.0001	142	< 0.0001
Solid load x Gas velocity	1.79	0.19	3.92	0.095
Residual plot	OK – random deviation		OK – random deviation	

The linear fit of parameters in the ANOVA was unable to match the full range of entrainment data satisfactory, yielding a nonrandom distribution of residuals, why $0.10 < \eta_{\text{Ent}} < 0.90$ were used in the analysis. This data range contains the dynamic behavior of the entrainment process. For $\eta_{\text{Ent}} > 0.90$ very little dependency of either gas velocity or solid load is observed.

The ANOVA is only applied to data from the third session (#2). Testing all available data from the PoC set-up yields similar results.

6.5 Overview and Comparison of Data

Plots showing all obtained separation and entrainment data from the PoC set-up are provided in Figure 77 and Figure 78, respectively.

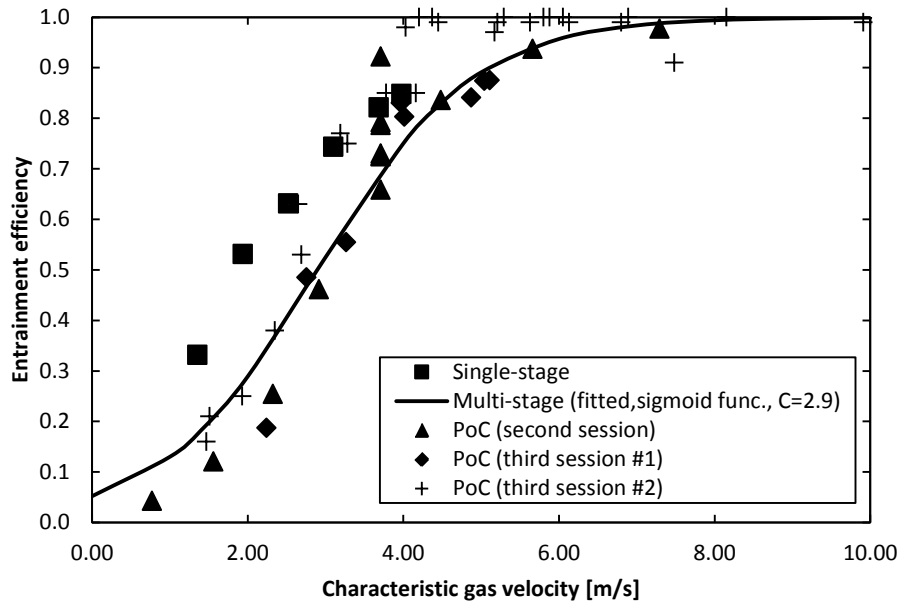


Figure 77 – Collection of all measured entrainment data on the three set-ups as a function of the characteristic gas velocity (the velocity in the transport channel).

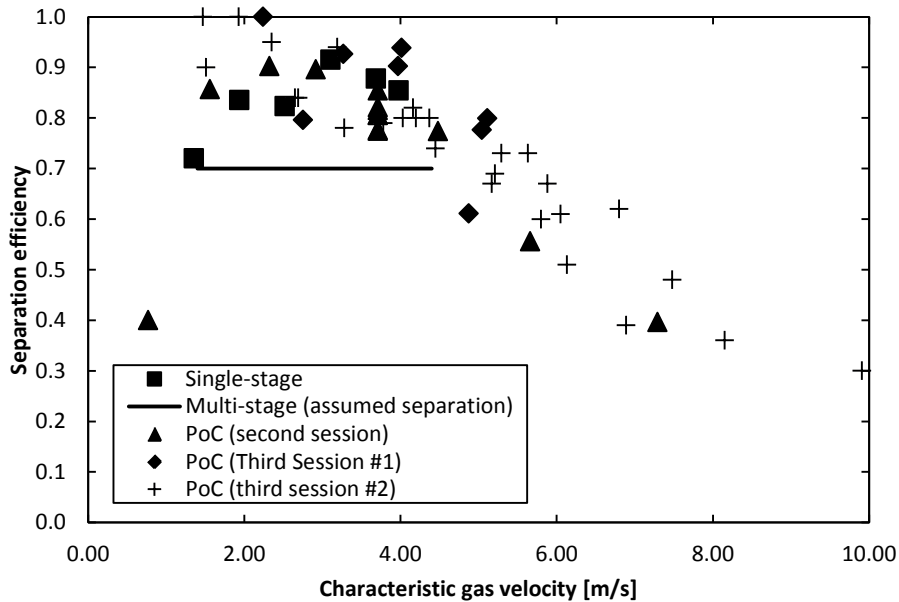


Figure 78 – Collection of all measured separation data on the three set-ups as a function of the characteristic gas velocity (the velocity in the transport channel).

Recall, that in the multistage set-up, the entrainment and separation efficiencies could not be measured directly and were identified by modeling the system. The entrainment efficiencies were assumed to follow a Sigmoid function, and the separation efficiencies were assumed constant.

The data series *PoC (second session)* and *PoC (third session#1)* have not been presented previously, while the remaining data has.

The fitted Sigmoid function from the multistage set-up fits well the entrainment efficiency, while the assumed separation efficiency seem under estimated.

Comparing the data from all experimental sessions, differences of around 20 % are found. These differences are attributed to usage of different raw meal as well as the geometry of the entrainment area differs slightly in the three set-ups. Furthermore, the *data PoC (third session #2)* are obtained during under sub atmospheric conditions, similar to the industrial process, where the *PoC (second session)* and *PoC (third session #1)* are run with small over pressure in the system.

The separation efficiencies are forming a band with a width of approximately 20 % and appears to have an optimum around $v_{\text{Char}} = 3$ m/s. This is discussed in section 6.7.1 – *Separation Process*.

6.6 Visual Observations

In the following, the visual observations during work on the PoC set-up will be presented. These observations are aimed to increase understanding of internal mechanisms.

The visual observations presented here are obtained during experiments with characteristic gas velocities of approximately 2.5 m/s. The expected entrainment efficiency is around 0.5 and the separation around 0.9. The described trends have also been confirmed at $v_G = 5.1$ m/s.

6.6.1 Separation Process

The slow motion videos show that gas and particle flows within the system are very dynamic and pulsating in behaviour. The observed particle trends include (a) formation of ropes or strands of particles in the separation chamber moving downward as a single unit, (b) the position of the particle rope varies dynamically between left and right chamber walls but is most

often found in the center, (c) the main flow of particles are observed in the center of the chamber, moving downward, (d) some particles impinge occasionally on wall opposite of the inlet, (e) the observed vertical particle velocity is approximately 0.5 – 1.5 m/s (average gas velocities in chamber ≈ 0.77 m/s), and (f) instable eddies form at the sloping wall just below the inlet to the chamber, lifting deposited particles into the gas. Examples of the visual data obtained are provided in Figure 79. In the provided photos, the transport channel is visible to the right and the separation chamber to the left. Particles and gas flow from right to left.

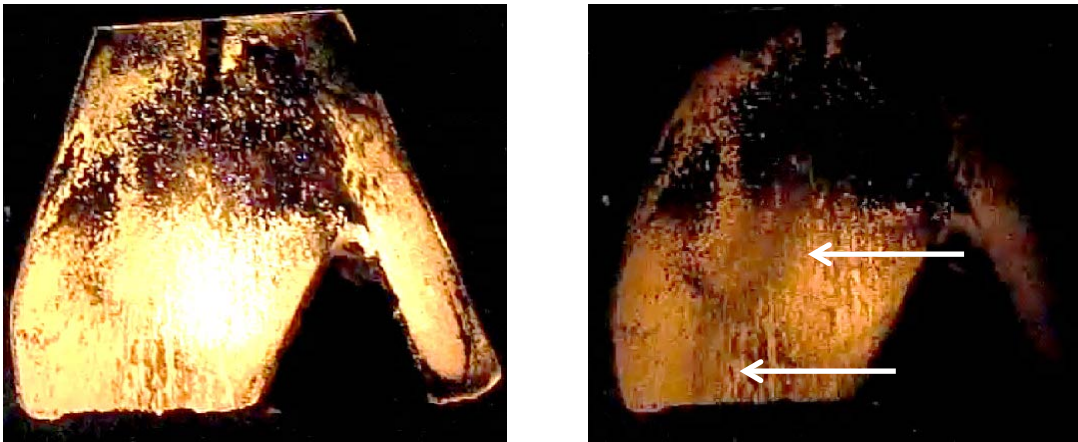


Figure 79 –Selected pictures from high speed recording during experiments. Points of interest marked by arrows.
Left: System before flow of particles is started. Right: Rope of particles visible in the center of the chamber.

The observations are summarized in Figure 80, where the location of (a) the main flow of particles, (b) the temporary eddy, and (c) the occasional impingement of particles on the left wall of the separation chamber are depicted.

In order to gain information on the gas flow patterns in the system, CFD simulations have been performed at conditions similar to the conditions during the video recording. The resulting gas flows are depicted in Figure 81.

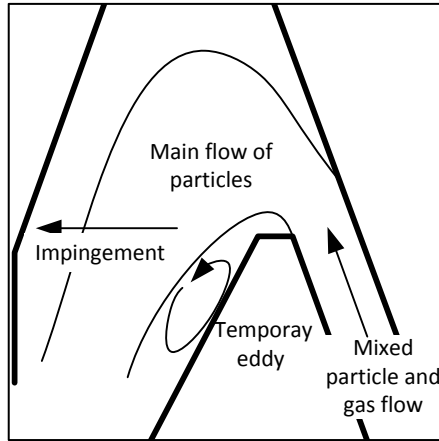


Figure 80 – Summary of visual observations of particle flow influencing the separation process.

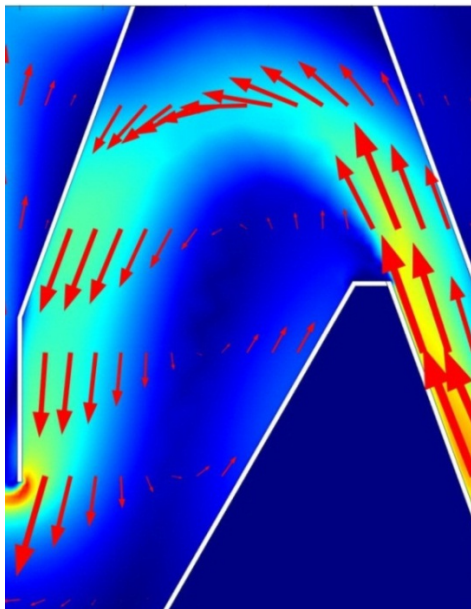


Figure 81 – Gas velocity profiles from CFD simulation. Red = 5 m/s, yellow = 3 m/s, turquoise = 2 m/s. Light blue = 1 m/s.

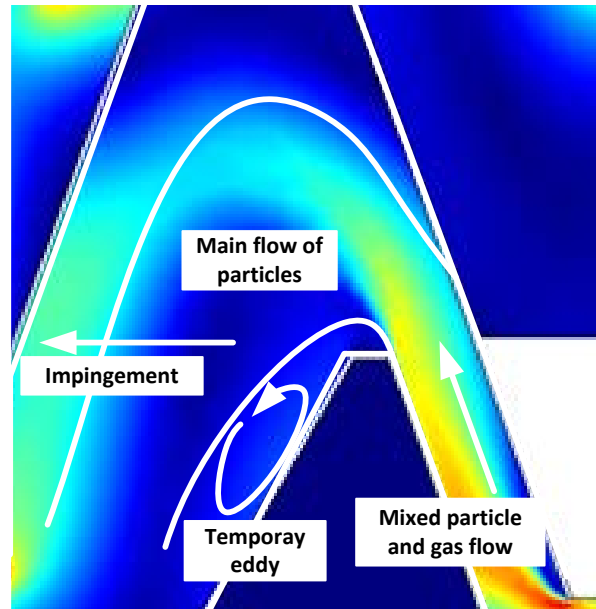


Figure 82 – Combination of simulated gas flow and visual particle flow patterns.

The simulations show that there is a pocket of low gas velocities underneath the band of fast flowing gas. By comparison of the visual observations and the CFD simulations, it is found that the particles move down in the low gas velocity pocket, as seen in Figure 82. Gravity forces the particles to leave the high gas velocity band, and once in the low gas velocity area, the horizontal velocity component is reduced, and the particles have time to settle.

The eddy, also found in Figure 81, is unwanted, as it lifts deposited particles from the wall into flowing gas.

The impingement of particles on the wall opposite the inlet occurs when particles have not been separated from the main gas flow. At the contact with the wall the particles lose momentum, but as the gas is flowing along the left wall, the impinged particles are reentrained into the gas. Thus, the particles separated by impingement do not contribute to the overall separation, as they are most likely re-entrained at a lower point in the system.

6.6.2 Entrainment Process

The visual observations regarding the entrainment process can be summarized to: (a) Entrainment occurs two places: Directly below the particle gate and in the vertical channel at bottom of entrainment area, (b) particle clouds are transported up through the entrainment area, (c) a stable eddy is formed below particle gate, creating an area with low concentration of particles, (d) some particles fall from particle gate directly down on plate below, and slides downwards, inducing the eddy motion, and (e) system pulsates, induced by the entrainment of particles. An example of the visual observations of the entrainment area obtained during operation is provided in Figure 83.



Figure 83 – Particle void with low particle concentration in the entrainment area. Point of interest is marked by arrow.

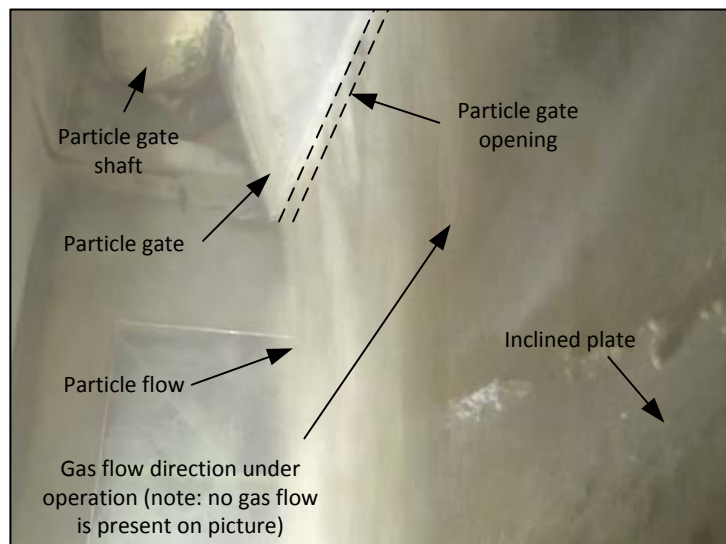


Figure 84 – Picture of the particle flow from the particle gate. No gas flow is present. Particles fall in a curtain-like pattern.

The stable eddy is visible as a light area with low concentration of particles. Gas is flowing vertically, from the bottom and up, while particles are fed from the top. The geometry of the separation chamber can be seen in Figure 84, as well as the curtain like particle flow from the particle bed above. No gas flow is present in this photo.

The observations of the particle flow in the entrainment region are summarized in Figure 85, and compared to the results of the CFD simulation in Figure 86.

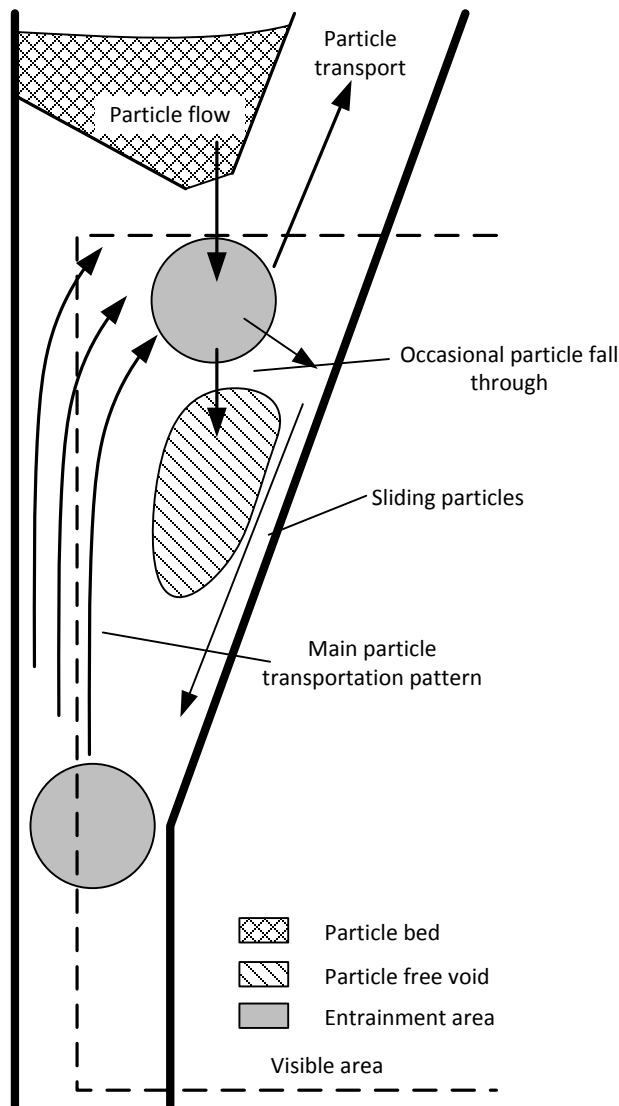


Figure 85 – Summary of observations in the entrainment area. The area visible through the transparent stage is marked by a dashed line.

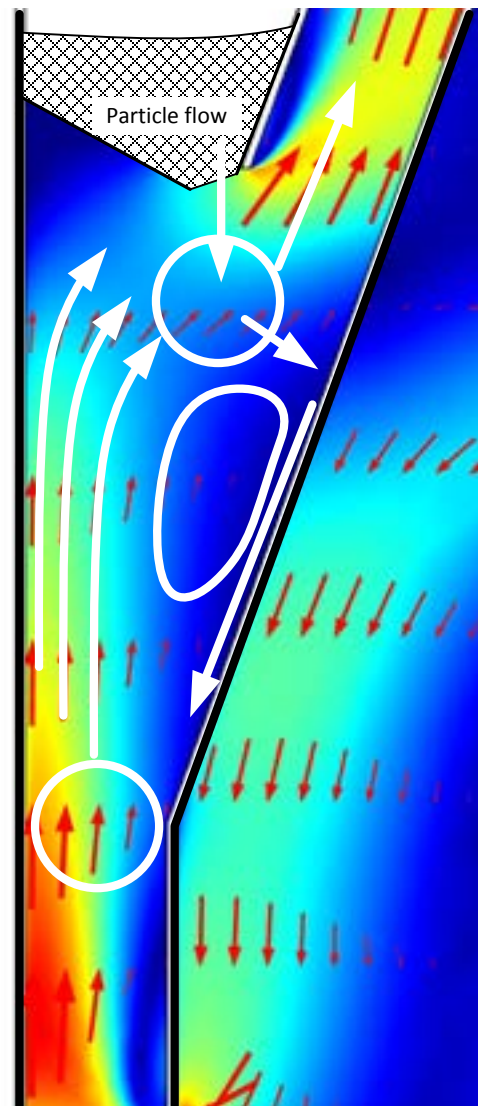


Figure 86 – Comparison between observations and CFD simulations in entrainment area. Gas velocities: Red = 5 m/s, yellow = 3 m/s, turquoise = 2 m/s. Light blue = 1 m/s.

It is noted that directly below the particle gate, the gas velocities are relatively low, 0.5 – 1.5 m/s with average values around 1 m/s, compared to the velocities in the channels. This causes particles to occasionally fall through the gas stream and land on the inclined plate. The majority of the particles are, however, entrained directly below the particle gate at the given conditions.

Once the particles reach the channel on the upside of the particle gate, where the gas velocities are increased, very few particles leave the gas. Furthermore, it should be noted that the formation of the eddy below the particle gate is not predicted by the CFD simulations. As seen in Figure 86, no counter-current flow of gas is expected from the gas flows alone at this position, why the downward gas flow must be generated by the flow of particles.

6.7 Identification of Governing Mechanisms

Based on the observations and measured data, the fundamental mechanisms governing the separation and entrainment processes are sought identified. In the following, a discussion will outline the possible processes.

6.7.1 Separation Process

The separation process was expected to be constituted by partly by an inertial separation, created by the 180° turn of the gas stream at the outlet of the separation chamber, and partly by a gravity-driven process.

Generally, it is considered that the effect of an inertial separation increases with gas velocities as seen for cyclones, but neither observations nor measured data indicate any such trend, why the separation process most likely is not inertial driven.

Therefore the separation process must be gravity driven. However, the observed particle settling velocities were in the order of 0.5 – 1.5 m/s, which is much higher than the terminal settling velocity of single raw meal particles according to Stokes law ($v_{\text{Stokes}} \approx 0.01$ m/s).

Principally, two mechanisms can explain the observed accelerated gravitational settling:

1. When two or more particles moves through an infinite, otherwise empty fluid under influence of gravity, the settling velocity is higher than for individual particles [117,118]. The increased settling velocity is a result of inter-particle forces, which pushes and drags the particles to a faster settling. In the current case, the separation chamber is “empty” from the point-of-view of the particles at the front of each particle strand, suggesting that this phenomenon can occur.

2. Formation of raw meal particle clusters or agglomerates, increasing the effective diameter of the particles to achieve the observed settling velocities. Applying Stokes Law of settling, assuming a cluster density of $1/3 - 1/10$ of the single particle density [119], the cluster size can be estimated to 0.2 mm to 0.5 mm (approximately 20 – 40 times the average single particle diameter).

The findings and discussions regarding the separation process are summarized in Table 20. The two explanations mentioned above are summarized under the term *accelerated gravitational settling*.

Table 20 – Summarization of discussion of separation mechanisms.

Hypothesized separation mechanism	Comments	Effect on separation process
“Normal” gravitational settling	Settling of particles, caused by gravity, transport particles away from the band of moving gas. This increases the residence time, and allows the particle to settle.	Minor effect
Accelerated gravitational settling	<ol style="list-style-type: none"> The particles are observed to move in rope formations. The particles at the front of the particle band initiate a local downward flow of gas as well as enhance the settling of the following particles by dragging them downwards. The particles form agglomerates or clusters, thereby settling faster than the single particles 	Major effect
Impingement on chamber walls	Particles impinge on the wall of the chamber, but re-entrains in the gas on the way down	Little to no overall effect
Inertial separation	The particles in the main gas flow could be forced out of the gas by the 180° turn at the outlet of the separation chamber, but no experimental data indicate an inertial separation process.	Little to no overall effect

In the measured data, decreasing separation efficiencies were observed at increasing gas velocities. This trend corresponds well with a process driven by gravitational settling: When increasing the gas velocity, the residence time is reduced, yielding shorter time for the particles to leave the main gas flow, reducing the separation.

The ANOVA performed on the data from the PoC set-up, revealed that no influence of the solid load on the separation efficiency could be identified, while the separation mechanism suggested above implies that the local particle concentrations are the contributing to the separation. This indicates that in the range of solid loads investigated the effect on the separation efficiency is small, compared to the experimental uncertainties.

Principally, the solid load would be expected to influence the separation process: Increasing solid loads should yield increasing separation and vice versa, which could explain the tendency of low separation efficiency at low gas velocities and the optimum behavior seen in Figure 78. At low gas velocities the solid load in the separation chamber is low as a consequence of a small amount of entrained particles.

6.7.2 Entrainment Process

The entrainment of particles occurs when the drag force, exerted by the gas on the particles, exceeds the gravitational force. Therefore, the entrainment process was expected to depend on the gas velocity, as well as density difference between gas and particles, system geometry, and mass flow of particles.

In the present experimental work, the entrainment process was found to depend on gas velocity. Solid load was not found to significantly influence the entrainment efficiency. Dependencies of geometry and density difference have not been investigated.

The entrainment process has been identified to take place at two locations; directly below the particle gate and in the vertical channel. The entrainment of particles in the vertical channel pulsates. Particles are entrained after a short built up period, where the particle concentration locally increases. When the particles are entrained a lower concentration is left behind and particle concentration builds up again. This pulsation is creating the very dynamic behavior witnessed in the separation chamber.

6.8 Comparison with Industrial Preheater Cyclone

To compare the performance of the 2D-HX with the performance of the industrially available preheater cyclones, the transport efficiencies are computed. The resulting graph is a volcano curve, shown in Figure 87.

To the left of the optimum, the entrainment efficiencies are low, yielding low transport efficiencies, while to the right the separation efficiencies are low. The optimum is located at

characteristic gas velocities of 4 – 5 m/s, with around $\eta_{Transport} = 0.80$. The preheater cyclone transport efficiencies have previously been reported to be in the range of 0.70 – 0.95.

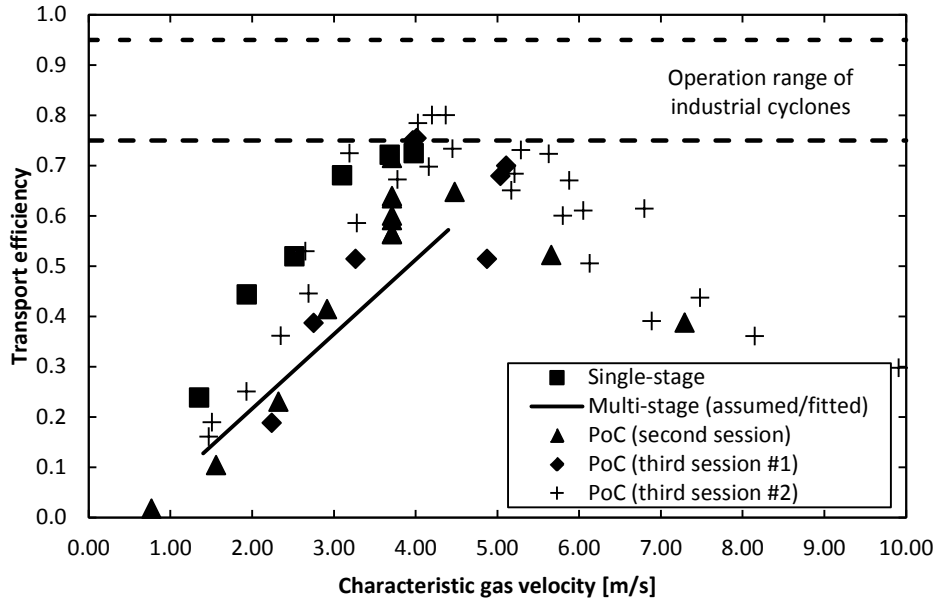


Figure 87 – Experimentally obtained transport efficiencies for the 2D-HX. Typical data range of industrial cyclones is given as an interval marked by horizontal dashed lines.

A summarized comparison of the 2D-HX and the industrial preheater cyclone is provided in Table 21. The major differences are the separation principle and the gas velocities in the system.

Table 21 – Comparison of transport properties of industrial preheater cyclone and 2D-HX design.

	Preheater cyclone	2D-HX
Separation principle	Inertial	Accelerated settling
$\eta_{Transport}$ at optimal conditions	0.70 – 0.95	0.70 – 0.80
$v_{G, entrainment}$	20 – 24 m/s	4 – 5 m/s
$v_{G, sep}$	N/A	1.3 – 1.7 m/s

6.9 Summary

The internal separation and entrainment processes in the 2D-HX have been experimentally investigated.

An analysis of the results from the Single-stage set-up showed that the entrainment process depended on the gas velocity with solid load playing a minor role. The test series performed on the Multi-stage set-up suggested that the entrainment efficiency depended highly on the gas velocity, following approximately a Sigmoid function with the constant = 2.9. The more thorough test series, carried out on the PoC set-up, revealed that the solid load did not influence the entrainment efficiency in the range of solid loads investigated, 0.5 – 1.0 kg/kg.

Visual observations provided additional information on the mechanism of the entrainment mechanism: The entrainment of particles occurs at two locations in the entrainment area of the set-ups; directly below the particle gate and in the vertical channel. The entrainment process generated pulsating gas and particle flow, which was visible in the separation chamber.

The separation efficiency was also investigated in the three set-ups. The results were less clear, compared to the entrainment efficiency, however. The separation data from the Single-stage set-up did not reveal any trends, due to experimental uncertainties. The Multi-stage set-up showed that constant separation efficiency in the investigated range of gas velocities, 1.8 – 3.4 m/s, was reasonable. An ANOVA performed on test data from the PoC set-up indicated that the separation efficiency only depended on the gas velocity, but the identified mechanism, accelerated settling, and the few data points obtained at gas velocities lower than 2 m/s (causing low entrainment and thereby low solid load in the separation chamber) suggested that solid load did influence the separation: The higher solid load, the higher separation efficiency.

In the separation chamber the particles formed ropes, moving downwardly, separating the particles from the gas flow. The operation principle of the separation process was identified to be an accelerated gravitational settling with vertical settling velocities of around 0.5 – 1.5 m/s. Impingement and inertial separation mechanism were found to be insignificant at the operational conditions tested.

Transport efficiencies were found to follow a volcano curve with optimum around characteristic gas velocities at 4 – 5 m/s and maximal values of $\eta_{\text{Transport}} = 0.80$. Outside the optimum, either low entrainment or low separation efficiencies dominated the transport efficiency. Compared to the industrial standard, the optimum values are in the lower range of acceptable values, typically ranging from 0.70 to 0.95.

Several similarities in terms of flow patterns were found by comparing the visual observations and CFD simulations performed for the system, thereby supporting that correct flow patterns are obtained by the CFD. The CFD simulations showed that local gas velocities in both entrainment

area and separation chamber varies significantly, and that the transport processes depends on the gas flow patterns and thereby the system geometry.

The effect of different geometry has not been investigated, as experiments have been limited to the three set-ups described previously.

Chapter 7

Investigation of Heat Exchange Performance

“Chemical Engineers are not gentle people, they like high temperatures and high pressures”

– Steve LeBlanc, professor and reaction engineering textbook author

Selected results of the thermal investigation of the 2D-HX, as well as phenomena observed during high temperature operation of the PoC set-up are presented in this chapter. The data includes information on heat loss, thermal performance, and evaluation of the heat exchange process. In this section also the measured pressure drops will be presented.

Not all available data will be presented in detail in the following sections. Complete datasets are available in Appendix C.

7.1 Results: Thermal Performance

In order to evaluate the performance of the heat exchange process between gas and solids in the 2D-HX, and to identify potential operation related issues, the PoC set-up has been operated at inlet temperatures of up to approximately 800 °C. Seven experiments, called proof of concept (PoC) experiments, testing the design at as close to industrial conditions as possible, will be reported here. The hot experiments can be divided into two categories: (a) Experiments carried out at industrial conditions; gas inlet temperatures above 700 °C and solid loads around one in a four stage heat exchanger (experiments PoC#1 – #3) and (b) experiments carried out at lower temperatures aimed at investigating the heat exchange performance of the system (experiments PoC#4 – #7).

The temperatures have been measured at different locations. In all experiments gas temperatures at inlet to each stage were measured, additionally particle bed temperatures were measured in PoC#4 – #7. In PoC#6 and #7 also the freeboard temperature were also measured. In PoC#6 and #7 the PoC set-up contained one stage. In the remaining experiments reported, four stages were used.

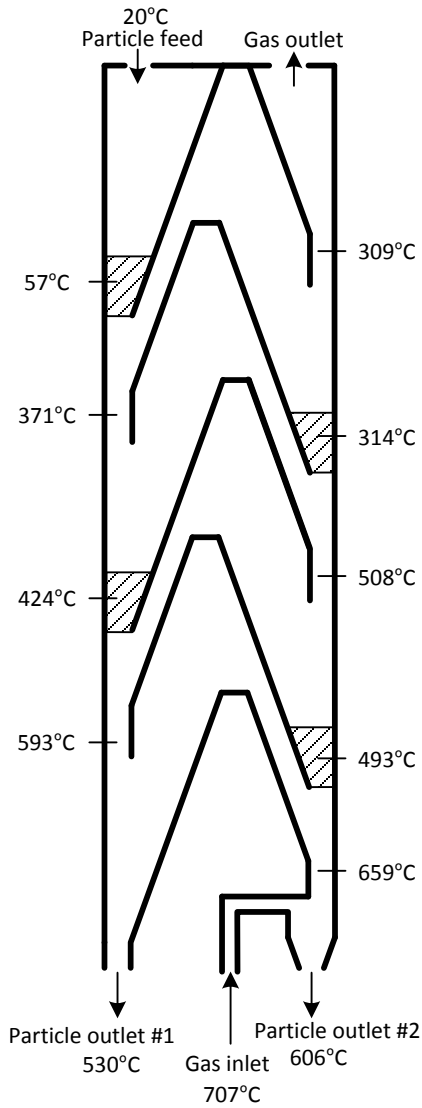


Figure 88 – Results from PoC#5 with indication of position of thermocouples. Temperatures measured in particle beds and at gas inlet to each stage.

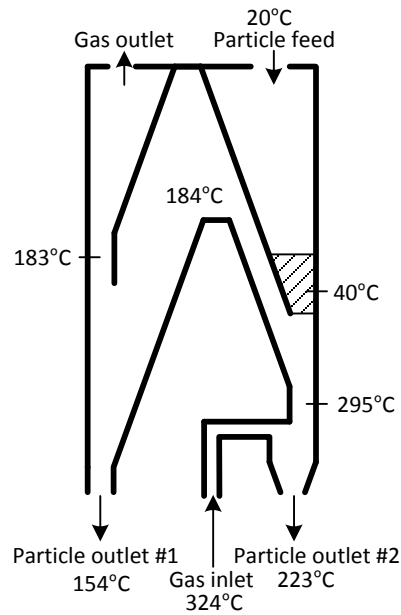


Figure 89 – Results from PoC#6 with indication of position of thermocouples. Temperatures measured in particle bed, the freeboard and at gas inlet to the stage.

Two examples, PoC#5 and #6, highlighting the different configurations investigated, are provided in Figure 88 and Figure 89. The locations of the thermocouples and the measured average values at steady state are shown.

Summarized operational data for all seven PoC experiments are provided in Table 22. Flow rates of gas and particles have been conservatively chosen due to capacity limitations of the gas cooling equipment and the temperature requirements of the bag filter handling the exhaust gases from the set-up.

Table 22 – Summary of PoC experiments.

System configuration	PoC#1	PoC#2	PoC#3	PoC#4	PoC#5	PoC#6	PoC#7
Number of stages, N	4	4	4	4	4	1	1
Location of temperature measurements	Stage inlets	Stage inlets	Stage inlets	As PoC #1 and in particle beds	As PoC #1 and in particle beds	As PoC #4 and in freeboard	As PoC #4 and in freeboard
Experimental settings							
Duration [min]	84	109	36	84	56	60	35
Duration of steady state [min]	30	30	10	17	13	19	8
Gas flow [kg/hr]	80	80	100	90	90	80	146
Particle flow [kg/hr]	78	94	94	61	78	78	78
Characteristic gas velocities							
Top stage [m/s]	3.8	4.0	5.0	4.8	4.1	2.9	5.3
Bottom stage [m/s]	6.8	6.8	6.2	7.1	7.0	N/A	N/A
Distribution of particle							
Particle outlet#1	0.55	0.46	0.39	0.21	0.54	0.77	0.51
Particle outlet#2	0.13	0.13	0.07	0.02	0.07	0.07	0.07
Particles blown out	0.32	0.41	0.54	0.78	0.41	0.15	0.41
In- and outlet temperatures							
$T_{G,inlet}$ [°C]	790	790	707	710	707	324	243
$T_{G,outlet}$ [°C]	321	354	361	398	309	183	180
$T_{P,inlet}$ [°C]	20	20	20	20	20	20	20
$T_{P,outlet,average}$ [°C]	522	505	564	508	541	159	162
Characteristic parameters							
Solid load, c_o [kg/kg]	1.0	1.2	0.9	0.7	0.9	1.0	0.5
Stability [max(%change)/min]	0.24	0.30	1.30	0.7	2.5	0.9	1.0
Absolute thermal efficiency, ϕ_{Abs}	0.30	0.50	0.36	0.08	0.39	0.29	0.18

Initially, it should be noted that operation at close to industrial conditions with raw meal is possible. The particles are heated from 20 °C to 522 – 564 °C in four heat exchange steps. The gas is correspondingly cooled by approximately 350 – 400 °C. The distribution of particles, especially in PoC#3, indicates that the separation efficiency in the top stage is far from unity. Considering the gas velocities in the top stage, and the separation efficiency data presented in Chapter 6, separation efficiencies between 0.6 and 0.8 would be expected.

The absolute thermal efficiencies suggest that under the given settings between 8 % and 50 % of the energy in the hot gas has been utilized for particle heating. The major reason for the low values is the low separation efficiency, reducing the particle flows from the outlets at bottom of the system.

The temperature profiles of PoC#4 and PoC#5, depicted in Figure 90, reveal that the particle are being heated in each stage, and that the temperature gain in each stage decreases as the particles approaches the gas temperature, as expected.

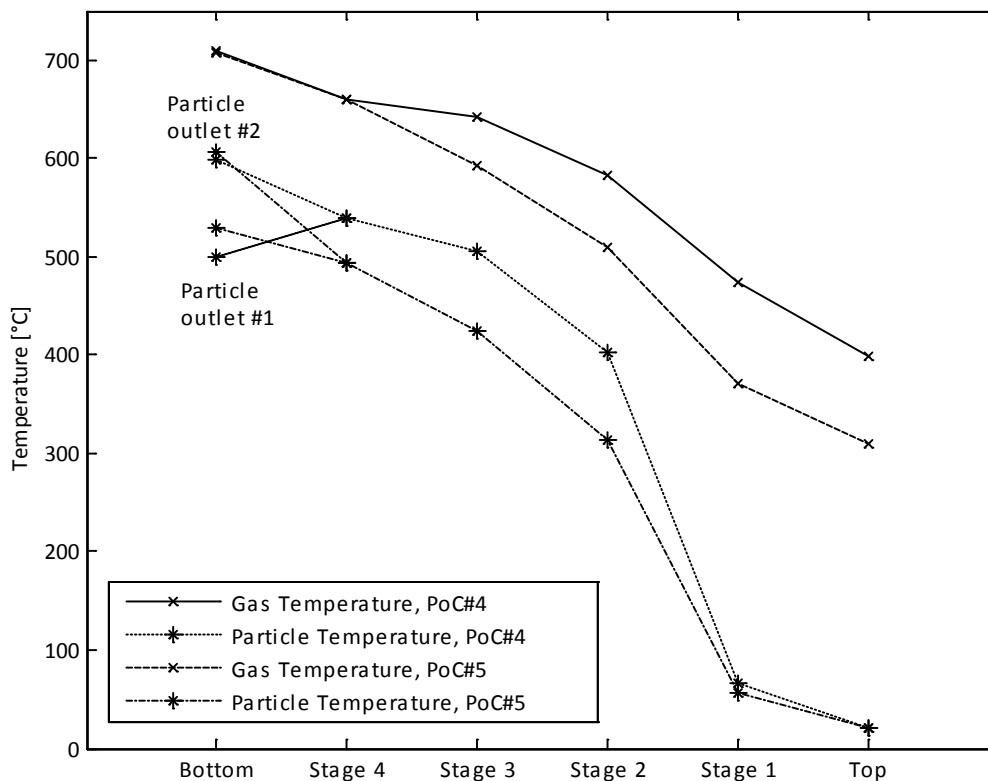


Figure 90 – Steady state temperatures of gas and particles during PoC#4 and PoC #5.

The inlet temperatures of gas and particles to a given stage are plotted at the same x-axis position in Figure 90. After the heat exchange in a given stage, the resulting particle temperatures can be found at a lower stage (higher stage number), while the resulting gas temperatures can be found at a higher stage (lower stage number).

The effect of increased solid load can be seen on Figure 90, where lower temperatures are archived for PoC #5 ($c_o = 0.9$ kg/kg) than PoC #4 ($c_o = 0.7$ kg/kg), due to the higher heat capacity of the particle stream. Remarkably, the temperature of particle outlet #1 during PoC#4 is lower than the temperature measured at the inlet of stage 4. This indicates either (a) an incomplete heat exchange, (b) a fall through of colder particles from stage 3 cooling the thermocouple, or (c) a significant local heat loss.

From the measured particle bed temperatures, several things should be noticed; (a) the particle bed in the top/feed stage is hotter than the particle feed, indicating that the particles in the top/feed stage are heated by conduction through the walls and internal plates of the set-up, (b) some particle beds are hotter than the gas leaving the stage. This could further indicate that thermal conduction in the system is significant, or that fall through of particles from the above stage cools the gas leaving the stage, and (c) the temperature difference between gas and solid after heat exchange is in the range of 20 – 30 °C.

Furthermore, it was found that the heat exchange takes place in the transport channel, as observed from Figure 89, where the freeboard temperature is similar to the outlet gas temperature. In experiments PoC#6 and PoC#7, the residence time of particles and gas in the transport channel is in the range of 80 – 140 ms, theoretically allowing enough time for a full heat exchange to take place, yet the temperature difference between the particle bed and gas outlet indicates that the heat exchange is not complete under the given settings, which is most likely caused by insufficient and/or too slow mixing.

Finally, the evaluation of the steady state periods reveals that the system can be kept stable during operation, indicated by a maximum %-wise temperature change per minute between 0.30 % and 2.5 %. This instability is generated by the manual operation of the particle gates at each stage.

7.2 Results: Heat Loss

The heat loss from the system was measured during periods of operation with no particle flow, typically between PoC experiments, where the set-up and gas preheater needed to reach a new

thermal equilibrium. Summarized data for the heat loss experiments, TEQ#1 – #10, are given in Table 23.

The actual heat losses are found from an energy balance, and estimated to between 0.9 and 4.1 kW. Due to a leak in the electric gas preheater, the precise gas flows are uncertain in some of the experiments, thereby also the actual thermal heat loss.

Table 23 – Comparison of characteristic data for heat loss experiment.

Ex. name	T_{Out} [°C]	T_{In} [°C]	Gas flow [kg/h]	Heat loss, [kW]	φ_{Loss}	$\varphi_{Loss, computed}$
TEQ#1	656	781	80	3.4	0.18	0.20
TEQ#2	655	805	80	4.1	0.21	0.20
TEQ#3	484	534	100	1.6	0.10	0.13
TEQ#4	672	865	75 ^A	3.3	0.24	0.22
TEQ#5	576	690	75 ^A	1.9	0.18	0.17
TEQ#6	392	451	75 ^A	0.9	0.14	0.11
TEQ#7	555	622	60 ^A	0.9	0.12	0.16
TEQ#8	578	728	60 ^A	2.0	0.22	0.18
TEQ#9	377	424	112.5 ^A	1.1	0.12	0.11
TEQ#10	427	510	112.5 ^A	2.0	0.17	0.13

^A Electric gas preheater leaking, estimated gas flow.

The heat loss from the set-up depends on (a) the gas velocities, which determines the convective heat transfer coefficients, (b) the temperatures, determining the driving force, (c) the geometry of the system, (d) the isolation characteristics, and (e) the surface area.

Generally a more or less linear dependency of the temperatures and the heat loss should be expected, but due to the uncertainties of the measured gas flows, the effect of different gas velocities, and the isolation not being uniformly distributed around the set-up, a simplified approach is considered: Defining a heat loss parameter, φ_{Loss} , as:

$$\varphi_{Loss} = \frac{Q_{Loss}}{Q_{In}} = 1 - \frac{C_{P,G} \cdot (T_{G,Out} - T_{Amb})}{C_{P,G} \cdot (T_{G,In} - T_{Amb})} \quad \text{Eq. 35}$$

where Q is energy content, T temperature, indices *Out*, *In* and *Amb* are outlet, inlet and ambient (20 °C) conditions, respectively, and $C_{P,G}$ is the specific heat capacity computed as 20 % O₂ and balance N₂ [104]. The heat loss parameter describes the fraction of the supplied thermal energy

that is converted to energy loss, and is independent of the mass flows, as long as the mass flow through the 2D-HX set-up is constant.

An observed general trend is that the higher the inlet temperature, the higher heat loss. Simplifying the data trend by assuming a linear dependence between heat loss and gas inlet temperatures, a useful, although purely empirical, correlation can be obtained;

$$\varphi_{Loss} = 2.6 \cdot 10^{-4} \cdot T_{in} [^{\circ}C] - 0.0052 \quad \text{Eq. 36}$$

Note that at 20 °C, the heat loss is computed to zero. The unit of the constant, k_{heat} , is [$^{\circ}C^{-1}$] while φ_{Loss} is dimensionless. Absolute deviation between the computed and the measured values are between 1 and 4 %, as seen in Table 23.

This simple equation can be used to predict heat loss from the PoC set-up of a given temperature. However, applying this equation to other systems, significant uncertainties must be expected. As mentioned previously, a more complete model for the heat loss has not been established due to uncertainties regarding gas flows, isolation, and changing temperature differences.

7.3 Results: Observations

The temperature during PoC#1 – #3 were high enough for impurities in the raw meal to ignite. An example of glowing particles during PoC#3 is shown Figure 91. Temperatures between 650 °C and 700 °C were measured at the time of the photo.

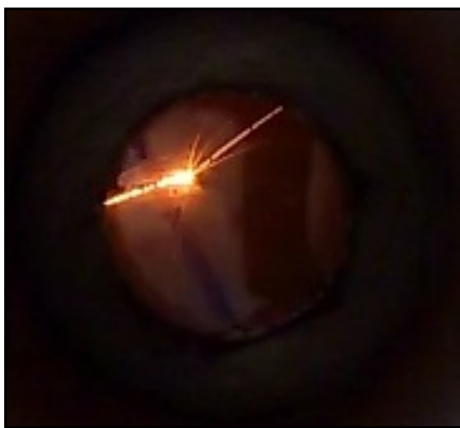


Figure 91 – Photo of an igniting particle observed at stage 3 just before the start of experiment PoC#3.

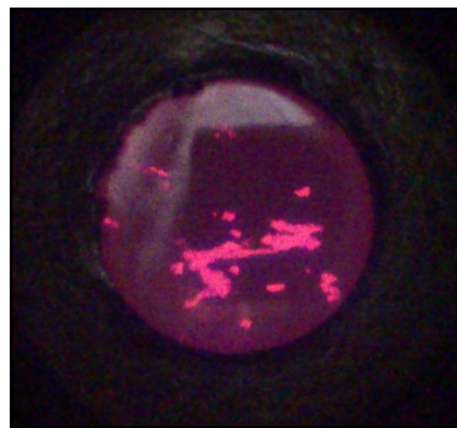


Figure 92 – Red glowing interior at stage 4 before start of experiment PoC#2.

At gas inlet temperature around 790 °C, the interior of the system glowed dark red as shown in Figure 92, displaying the red glow of the interior seen through gaps in the deposited raw meal. Judging from the color of the glowing metal, the temperature is between 700 and 800 °C, which corresponds well with the measured temperatures, 750 – 800 °C.

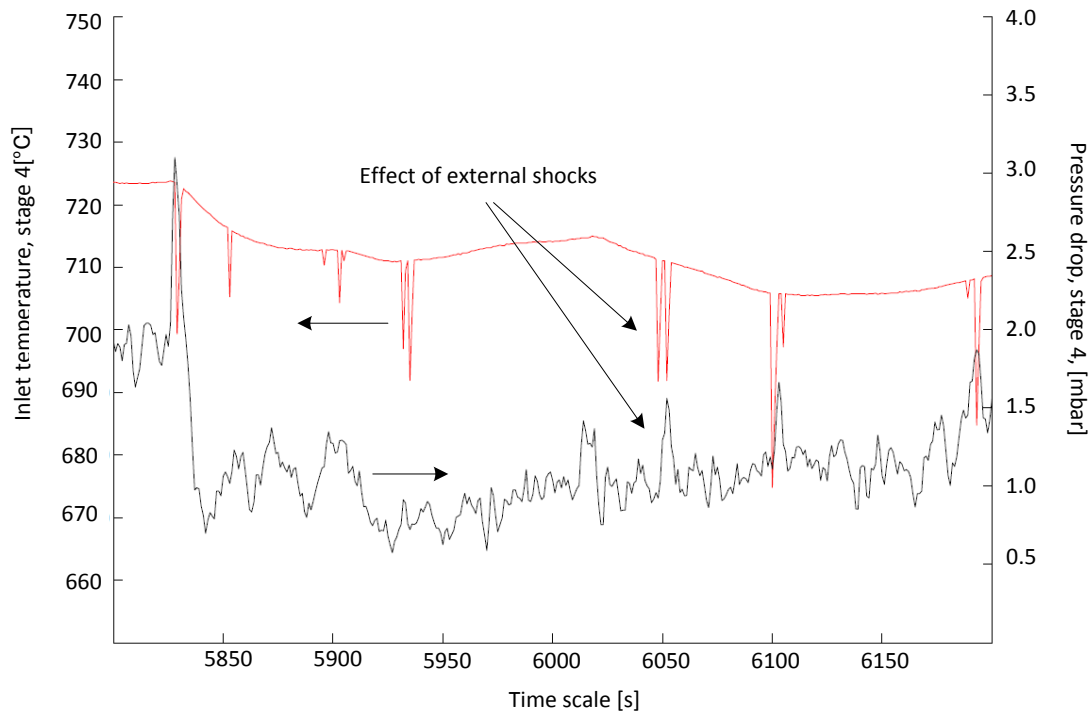


Figure 93 – Indirect effects of externally applied shocks to stage 4 during PoC#1. The time axis relates to the given data file.

The particle flowability was observed to deteriorate at increasing temperatures. Especially above 500 °C particles stuck to internal surfaces, making visual observations difficult and yielding problems ensuring stable particle bed levels. To ensure the flow of particles, external shocks were applied on the system to reinitiate particle flow. As seen in Figure 93, the shocks initiated particle flow, indicated by increased pressure drop of the stage and reduced temperature. Approximately one shock per minute was necessary.

To further investigate the flowability of raw meal at elevated temperatures, a separate study has been carried out in a powder strength measuring monoaxial shear tester. The results indicated that flowability of raw meal is significantly reduced at temperatures above 550°C, caused either

by calcination or belite formation in the raw meal. The reporting of this work has been carried out separately and is provided in appendix G.

Particle deposition on the interior was also observed during disassembling of the set-up. Where gas velocities were low ($v_G < 1 - 2$ m/s) or particles impacted on walls, deposits of up to 2 cm in thickness were found. Photos of the interior are provided in Figure 94 and Figure 95. Deposits were soft and easily removed.



Figure 94 – Side view of the interior of the bottom stage after the PoC experiments, showing particle outlet #1



Figure 95 – Top view of the interior of the bottom stage after the PoC experiments. Two thermocouples are visible: Particle outlet #2 and inlet to bottom stage.

7.4 Results: Pressure drop

During experiments, pressure drop over each stage and the overall set-up were measured. The pressure drops are very dynamic during experiments, depending strongly on (a) particle flow, (b) gas velocity, and (c) blockages of pressure transmission lines. The measured pressure drops are averaged during steady state and over the stages in the set-up. Data can be found in Table 24. The operational characteristics of the experiments can be found in Table 22. For later modeling purposes, both the pressure drop with and without particles have been provided.

The data suggests that the gas friction in the system corresponds to 0.1 – 0.8 mbar/stage, depending on operation conditions. When particles are introduced in the system, the pressure drop increases to around 1 – 2 mbar per stage, accumulating to 4 – 8 mbar for the total system.

Thus, 0.5 – 2.4 mbar per stage are contributed by the particle-wall and particle-gas interaction, which corresponds to between 48 % – 86 % of the total pressure drop.

Table 24 – Measured average pressure drops over a single stage with and without the presence of particles.

Name	ΔP_G [mbar/stage]	ΔP_{G+P} [mbar/stage]
PoC#1	0.1	0.7
PoC#2	0.4	0.9
PoC#3	0.6	2.2
PoC#4	0.3	1.2
PoC#5	0.3	2.7
PoC#6	0.5	0.8
PoC#7	0.8	1.4

7.5 Evaluation of Thermal Performance

Using the thermal efficiencies described in Chapter 3, experiments PoC#1 – #7 have been evaluated. The results are provided in Table 25. Thermal efficiencies, corrected for heat loss in order to enable a truer comparison of the 2D-HX with the cyclone preheater, where heat loss is significantly lower, are also given. The correction is done by assuming the thermal efficiencies are increased with 50 % of the heat loss, thereby suggesting that some of the energy, instead of being lost, is used for higher particle and gas temperatures.

Table 25 – Summary of thermal efficiency for PoC#1 – #7.

System configuration	PoC#1	PoC#2	PoC#3	PoC#4	PoC#5	PoC#6	PoC#7
Number of stages, N	4	4	4	4	4	1	1
Estimated heat loss, φ_{Loss}	0.20	0.20	0.18	0.18	0.18	0.08	0.06
Thermal efficiencies							
Absolute thermal efficiency, φ_{Abs}	0.50	0.30	0.36	0.08	0.39	0.29	0.18
Relative thermal efficiency, φ_{rel}	0.69	0.37	0.53	0.14	0.58	0.64	0.61
Corrected thermal parameters							
Corrected heat loss, $\varphi_{Loss, corrected}$	0.10	0.10	0.09	0.09	0.09	0.04	0.03
Corrected absolute thermal efficiency, $\varphi_{Abs, corrected}$	0.60	0.40	0.45	0.17	0.48	0.33	0.21
Corrected relative thermal efficiency, $\varphi_{rel, corrected}$	0.83	0.50	0.67	0.31	0.71	0.72	0.71

The measured absolute thermal efficiencies are between 0.08 and 0.50, corresponding to relative efficiencies between 0.14 and 0.69. The normalization values used to compute the relative thermal efficiencies are computed using the model described in Chapter 3, which under ideal conditions (full entrainment and separation) is applicable for the 2D-HX. The heat losses are estimated using Eq. 36. The relative thermal efficiency allows comparison of the experiments with a single stage and four stage, and indicates that the single stage systems perform reasonable well, with corrected relative thermal efficiencies around 0.71. For PoC#6 – #7, the absolute efficiencies are low as a consequence of only one heat exchange process.

7.6 Comparison of Heat Exchanger Design with Industrial Standard

The thermal performance parameters of the 2D-HX are summarized and compared with the corresponding parameters for the cyclone preheater in Table 26. Only the data from PoC#1 – #3 are reported, as gas inlet temperatures should be comparable. The cyclone preheater properties have been given previously in Chapters 2 and 3.

Table 26 – Comparison of thermal properties of industrial cyclone preheater and the 2D-HX.

	Preheater cyclone	2D-HX
Gas inlet temperature	817 – 893 °C	707 – 790 °C
Particle inlet temperature	50 – 60 °C	20 °C
Particle outlet temperatures	700 – 800 °C	505 – 564 °C
φ_{Abs}	0.61 – 0.71	0.36 – 0.50
φ_{Rel}	0.74 – 0.97	0.37 – 0.69
φ_{Loss}	~ 0.04	0.18 – 0.20
$\varphi_{Loss, corrected}$	N/A	0.09 – 0.10
$\varphi_{Abs, corrected}$	N/A	0.45 – 0.60
$\varphi_{Rel, corrected}$	N/A	0.50 – 0.83
Temperature difference	20 – 30 °C	20 – 30 °C

The gas and particle inlet temperatures are up to 100 °C and 50°C lower in the experiments, respectively, causing lower particle outlet temperatures. This aspect, combined with the higher heat loss, accounts for the lower particle outlet temperatures of the PoC set-up.

Comparing the thermal efficiencies, it is found that the industrial system performs about 25 % better than bench-scale 2D-HX. When correcting for the heat loss, the difference is around 20 %. The temperature differences between gas and particles after heat exchange in a given stage are similar in the two preheaters. Both processes are limited by insufficient mixing or time for full heat exchange. Note that despite the residence time in the riser ducts of the cyclone preheaters is around 200 ms – 400 ms, this time is insufficient due to the large amount of particles that needs to be entrained, mixed and then heat exchange. The amounts handled in the 2D-HX are significantly lower, so is the residence time, 80 – 140 ms.

The measured pressure drop data is closely related to the actual set-up, and a comparison between the industrial cyclone preheater and the 2D-HX is not relevant, why it has been omitted from Table 26. The pressure drops will at a later point be used for estimating large-scale facility performance.

7.7 Summary

The thermal performance of the 2D-HX has been investigated using the PoC set-up. Results from experiments with conditions similar to the industrial process confirmed that stable operation is possible. In experiments PoC #1 – #5 the particles were heated to above 500 °C in four heat exchange steps with a gas at inlet temperatures between 707 and 790 °C. Thermal efficiencies between 0.08 and 0.50 were measured, while heat loss was estimated to 18 % to 20 % of the available energy for the high temperature experiments.

The comparison of heat loss-corrected thermal efficiencies for the 2D-HX and corresponding data for the industrial preheater showed that the industrial process thermally performs around 20 % better, mostly caused by lower dust loss.

The heat exchange process in 2D-HX was found to take place in the transport channel.

The hot experiments revealed several issues, which might be of interest: (a) Particle flowability deteriorates at temperatures above 500 °C, (b) deposits build up internally where gas velocities are low, (c) manual operation of the system induces disturbances, and (d) batch-wise collection and feeding of particles limits continuous operation on the PoC set-up time to 1 – 3 hours.

During disassembling and reconfiguration of the set-up soft and easily removed build-ups were observed.

The deteriorating particle flowability was confirmed in a separated investigation, using a monoaxial shear tester.

Temperatures were high enough for impurities in the raw meal feed to ignite, possibly affecting temperature and gas composition. The consequences of this have not been investigated.

The pressure drops were measured to 4 – 8 mbar for a four stage system. Without particles, the pressure drops were in the range of 1 – 2 mbar for a four stage systems. The friction created by the particles thus contributed with the major part of the pressure drop. The pressure drops were not compared to the industrial cyclone preheater, as the parameters are not comparable due to differences in production capacity.

Chapter 8

Modeling of 2D-HX

“Everything must be made as simple as possible. But not simpler”

– Albert Einstein, German theoretical physicist

To predict the performance of the 2D-HX concept at conditions different from the experimental settings, and the capacity of full-scale facilities, a model describing mass and energy flows is required. Similar to the model for the cyclone preheater described in Chapter 3, the 2D-HX model will be founded on energy and mass balances, while additional mathematical descriptions of the two internal processes, entrainment and separation, are needed to describe system behavior.

The pressure drop will also be included, as it is a major comparison parameter describing preheater performance.

In this chapter, a model describing the 2D-HX will be set up. To illustrate the validity of the model, computed results will be compared with experimentally obtained data.

8.1 Modeling of the Internal Processes

The development of models describing the internal processes is based on the experimental data and observations presented in Chapter 6. The turbulent and pulsating behavior of the gas and particle flows, and the uncertainty related to the measured data do not allow detailed mechanistic models that consider individual particles and local gas flow patterns, why macro models, depending on geometry and process conditions, are desired. Generic models for this type of processes are not available in literature, but the likeness between the 2D-HX and both cyclones and pneumatic transport systems provides inspiration for the model set up.

8.1.1 Separation Process

The separation mechanism was in Chapter 6 found to depend on the gas velocity, while influence from the solid load could not be directly identified. Yet evidence of solid load influencing separation was found, and as literature describing particle-gas separators often reports of solid load having an effect on separation [20,120], solid load will be included in the modeling of the separation process.

To illustrate the considerations regarding modeling the separation process, three models will be presented and evaluated according to their capabilities of describing the measured data, and dependencies of operational and geometric parameters. The models are based on different particle-related phenomena.

Model #1: Froude number

In literature describing processes where the particle-gas interaction is influenced gravity the Froude number, Fr , is often encountered [34,120–122]. The Froude number is the ratio between inertia of a body, and the gravitational forces on the same body.

$$Fr = \frac{v_G^2}{g \cdot L} \quad \text{Eq. 37}$$

where g is gravitational acceleration, v_G is gas velocity and L is the characteristic length of the considered system. Applying the dimension of the separation chamber and the gas velocity, $v_{G, Sep}$:

$$L_{Sep} = 0.18m \quad \text{Eq. 38}$$

$$v_{G, Sep} = v_{G, Channel} \cdot \frac{L_{Channel}}{L_{Sep}} = v_{G, Channel} \cdot \frac{0.05m}{0.18m} \quad \text{Eq. 39}$$

Plotting the measured separation efficiencies against the Froude number divided by the solid load is shown Figure 96. A decreasing trend is observed, which can be approximated by an exponential function that has the correct limiting behavior.

The exponential model is given as:

$$\eta_{Sep} = \exp\left(-k_1 \cdot \frac{Fr}{c_o}\right) \quad \text{Eq. 40}$$

where k_j is a fitting parameter, equal of 0.164. The fit of the model is illustrated in Figure 97. The majority of the computed data points fits the measured within 10 %, and only one data point is represented with more than 25 % deviation.

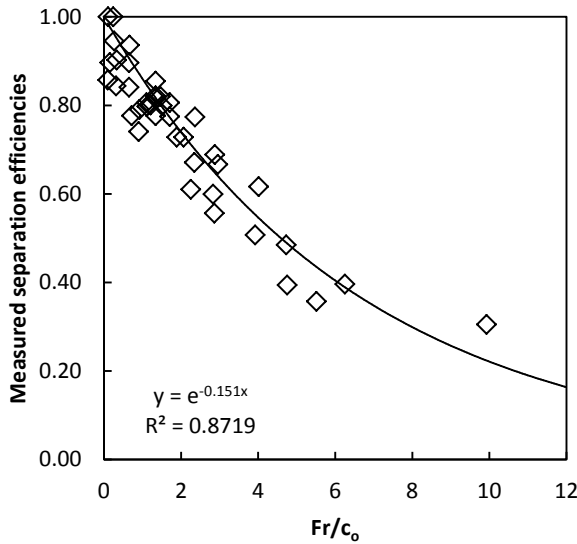


Figure 96 – Measured separation efficiencies depicted against Fr/c_o . An exponential declining function has been fitted to data.

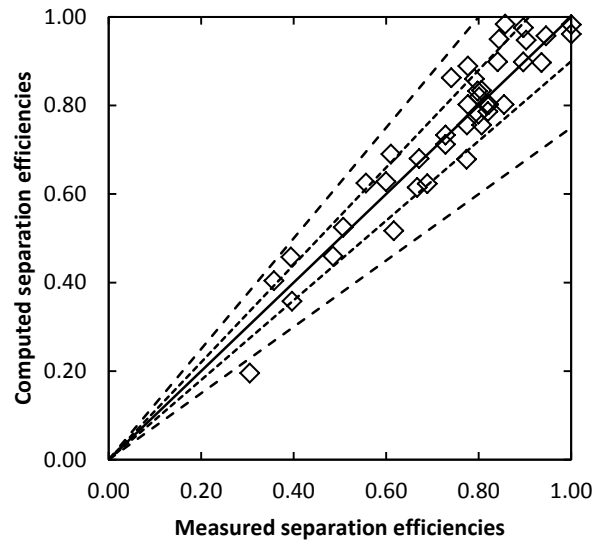


Figure 97 – Measured separation efficiencies depicted against computed ($\eta_{Sep} = \exp(-0.164 \cdot Fr/c_o)$). Deviations of 10 and 25 % are shown.

Model #2: Pneumatic transport analog

Model #2 assumes that the gas and particle behavior in the separation chamber behaves similar to a horizontal pneumatic transport pipe, enabling the saltation velocity to be computed. The saltation velocity is the gas velocity where particles start to leave the gas flow and deposit on the bottom of a pipe [120]:

$$c_{o,Sal} = \frac{Fr^{1100 \cdot d_p + 2.5}}{10^{1440 \cdot d_p + 1.96}} \Rightarrow \tag{Eq. 41}$$

$$\frac{\dot{m}_{p,Sal}}{\rho_G \cdot v_{Sal} \cdot A} = \left(\frac{1}{10^{1440 \cdot d_p + 1.96}} \right) \cdot \left(\frac{v_{Sal}}{\sqrt{g \cdot L_{system}}} \right)^{1100 \cdot d_p + 2.5} \tag{Eq. 42}$$

$\dot{m}_{p,Sal}$ is the mass flow of particles entering the separation process, ρ_G is the gas density, A is the cross sectional area, and d_p is the mean particle diameter. To transform the computed saltation velocity to a separation efficiency, an efficiency expression, with desirable limiting behavior from the cyclone theory, is modified and applied:

$$\eta_{Sep} = \frac{\left(k_2 \cdot \frac{v_{Sal}}{v_G} \right)^{m_2}}{1 + \left(k_2 \cdot \frac{v_{Sal}}{v_G} \right)^{m_2}} \quad \text{Eq. 43}$$

To compensate for the geometry and process being different from a pneumatic transport pipe, the saltation velocity is corrected by a constant, k_2 . The exponent m is the slope of the efficiency curve. At $k_2 = 0.44$ and $m_2 = 4$, the data points are represented as illustrated in Figure 98. As $k_2 < 1$ the actual saltation velocity is lower than in a pneumatic transport pipe as expected. Reasonable accuracy is achieved and data is represented with less than 25 % deviation.

Model #3 – Accelerated settling

Assuming that in the separation chamber, the gas flows in a band with a similar width as the transport channel, and that the particles that leave this band of fast flowing gas are separated, it is possible to utilize the vertical settling velocity of the particles to obtain an expression for the separation. The relation between the length travelled by the particles, and the width of the transport channel is given as:

$$\eta_{Sep} = \frac{\left(\frac{L_V}{L_{Channel}/2} \right)^{m_3}}{1 + \left(\frac{L_V}{L_{Channel}/2} \right)^{m_3}} \quad \text{Eq. 44}$$

Thus, particles which travelled a distance equal to the half the width of the transport channel have a 50 % chance of being separated. The distance travelled, L_V , is found from the residence time, τ , and vertical velocity, v_v :

$$L_V = \tau \cdot v_v \quad \text{Eq. 45}$$

The vertical velocity, v_v can be described by Stokes law of settling particles at low (<1) particle Reynolds numbers:

$$v_{Stokes} = \sqrt{\frac{4}{3} \cdot \frac{d_p \cdot (\rho_p - \rho_G) \cdot g}{3 \cdot f_p \cdot \rho_G}} \quad \text{Eq. 46}$$

where f_p is the friction factor, normally determined graphically from the particle sphericity and Re_p [35]. In Chapter 6, it was observed that the settling velocities of the particles exceeded the theoretical terminal velocity of single particles due to the formation of particle strands. In these strands, the average particle has a lower friction factor than a single particle, resulting in higher

velocities. The effective particle friction can be found by fitting the model to the measured data. The computed efficiencies are shown in Figure 99.

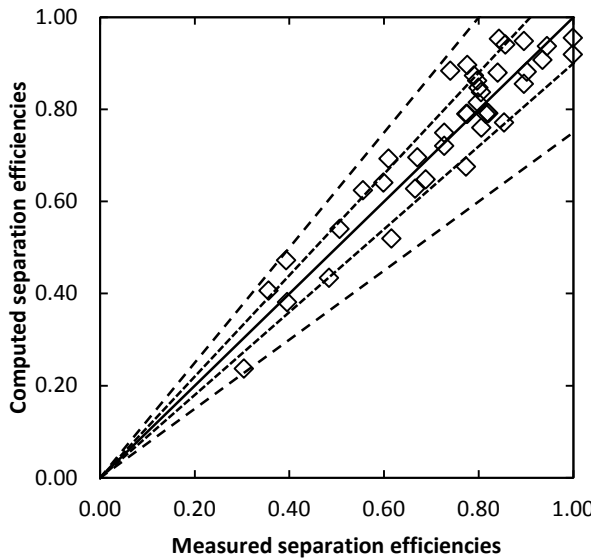


Figure 98 – Measured separation efficiencies depicted against computed (Model #2). Deviations of 10 and 25 % are shown.

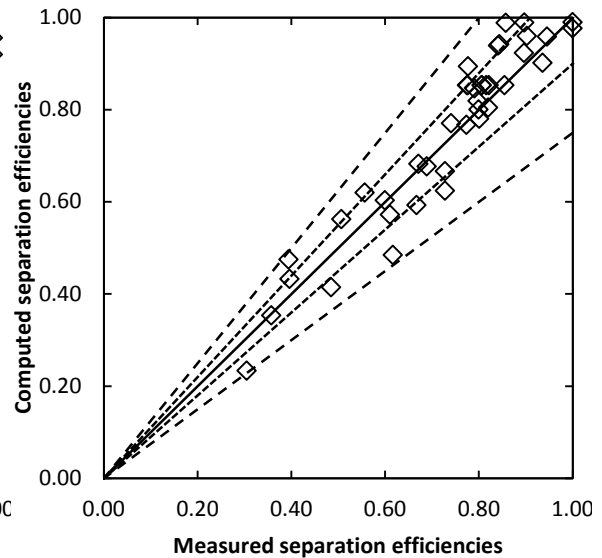


Figure 99 – Measured separation efficiencies depicted against computed (Model #3). Deviations of 10 and 25 % are shown.

The effective friction factor, $f_{p,eff}$, is determined to 3.9, which is approximately four to five times lower than for single particles in an empty fluid at similar Reynolds number. The effective friction factor may also cover over a downward moving gas flow in the particle strand, induced by the particles. The resulting terminal velocity is around 0.30 m/s, which is in the same order of magnitude as the observed particle velocities. The exponent, m_3 , in the efficiency expression is found to 3.

Discussion

In the modeling work, several approaches, besides the ones presented here, have been investigated, including models based on the critical load limit, as suggested by Muschelknautz [27] or Wang et al. [123]. These models performed in terms of fit and parameter dependencies poorer than the models presented here. Considering the separation chamber as a settling tank yielded even poorer results.

The models have varying degrees of theoretical foundation, all contain experimentally fitted constants, consider gravity as the driving force, and the inertia of the gas as the counteracting force. The separation models are compared in Table 27.

Table 27 – Summary of separation process Models #1 – #3.

	Model #1 – Froude no.	Model #2 – Pneu. Trans.	Model #3 – Acc. Settling	
Fitting parameters	$k_1 = 0.12$	$k_2 = 0.44, m_2 = 4$	$f_{p,eff} = 3.9, m_3 = 3$	
Sum of errors ^A	0.14	0.15	0.15	
Parameters	v_G, L_{Sep} and c_o	v_G, L_{Sep}, c_o, d_p and ρ_{gas}	$v_G, L_{Sep}, d_p, \rho_G$ and $L_{channel}$	
Major assumptions	Separation process can be described by Froude number	System is analogous to pneumatic transport systems	Particles move as a single particles with reduced friction	
Limiting behavior	v_G	$v_G \rightarrow \infty: \eta_{Sep} \rightarrow 0$ $v_G \rightarrow 0: \eta_{Sep} \rightarrow 1$	$v_G \rightarrow \infty: \eta_{Sep} \rightarrow 0$ $v_G \rightarrow 0: \eta_{Sep} \rightarrow 1$	$v_G \rightarrow \infty: \eta_{Sep} \rightarrow 0$ $v_G \rightarrow 0: \eta_{Sep} \rightarrow 1$
	L_{Sep}	$L_{Sep} \rightarrow \infty: \eta_{Sep} \rightarrow 0$ $L_{Sep} \rightarrow 0: \eta_{Sep} \rightarrow 1$	$L_{Sep} \rightarrow \infty: \eta_{Sep} \rightarrow 1$ $L_{Sep} \rightarrow 0: \eta_{Sep} \rightarrow 0$	$L_{Sep} \rightarrow \infty: \eta_{Sep} \rightarrow 1$ $L_{Sep} \rightarrow 0: \eta_{Sep} \rightarrow 0$
	c_o	$c_o \rightarrow \infty: \eta_{Sep} \rightarrow 1$ $c_o \rightarrow 0: \eta_{Sep} \rightarrow 0$	$c_o \rightarrow \infty: \eta_{Sep} \rightarrow 1$ $c_o \rightarrow 0: \eta_{Sep} \rightarrow 0$	-
	d_p	-	$d_p \rightarrow \infty: \eta_{Sep} \rightarrow 1$ $d_p \rightarrow 0: \eta_{Sep} \rightarrow 0$	$d_p \rightarrow \infty: \eta_{Sep} \rightarrow 1$ $d_p \rightarrow 0: \eta_{Sep} \rightarrow 0$
	ρ_G	-	$\rho_G \rightarrow \infty: \eta_{Sep} \rightarrow 0$ $\rho_G \rightarrow 0: \eta_{Sep} \rightarrow 1$	$\rho_G \rightarrow \infty: \eta_{Sep} \rightarrow 0$ $\rho_G \rightarrow 0: \eta_{Sep} \rightarrow 1$
	$L_{channel}$	-	-	$L_{channel} \rightarrow \infty: \eta_{Sep} \rightarrow 0$ $L_{channel} \rightarrow 0: \eta_{Sep} \rightarrow 1$

$$^A SoE = (\eta_{Measured} - \eta_{computed})^2$$

Overall, the models show similar limiting behavior and accuracy. From a process modeling point of view, Model #3 is less interesting, as it does not consider the effect of the solid load. Model #1 has a slightly better fit than Model #2, while Model #2 includes on the gas density, which is expected to be significant when modeling systems at temperatures different from ambient.

Due to the accuracy and the origin in pneumatic transport regimes, which legitimates the parameter dependencies, Model #2 will be applied to illustrate the methodology of the model implementation and solution in the following. Principally Model #1 and #3 might have served equally well.

8.1.2 Entrainment

Two models for the entrainment process will be suggested, and the better model identified. To reduce confusion, the models of the entrainment process will be named models #4 and #5.

According to the findings of Chapter 6, the entrainment process depends solely on the gas velocities in the entrainment area.

Model #4: Pneumatic transport analog

Similar to Model #2, the system is considered as a pneumatic transport system, and assuming that the particle pickup velocity can be used to describe the entrainment of particles, a model can be set up [120]:

$$Fr_{Pickup} = 0.0428 \cdot Re_{P, Pickup}^{0.175} \cdot \left(\frac{L_{Ent}}{d_p} \right)^{0.25} \cdot \left(\frac{\rho_P}{\rho} \right)^{0.75} \Rightarrow \quad \text{Eq. 47}$$

$$\frac{v_{Pickup}}{\sqrt{g \cdot d_p}} = 0.0428 \cdot \left(\frac{L_{Ent} \cdot \rho \cdot v_{Pickup}}{\mu} \right)^{0.175} \cdot \left(\frac{L_{Ent}}{d_p} \right)^{0.25} \cdot \left(\frac{\rho_P}{\rho} \right)^{0.75} \Rightarrow \quad \text{Eq. 48}$$

$$v_{Pickup} = \left(0.0428 \cdot \left(\frac{L_{Ent} \cdot \rho}{\mu} \right)^{0.175} \cdot \left(\frac{L_{Ent}}{d_p} \right)^{0.25} \cdot \left(\frac{\rho_P}{\rho} \right)^{0.75} \cdot (g \cdot d_p)^{0.5} \right)^{\frac{1}{0.825}} \quad \text{Eq. 49}$$

where v_{Pickup} is the velocity where particles are entrained from a horizontal surface. $Re_{P, Pickup}$ is the particle Reynolds number at the pickup velocity. In the entrainment area $L_{Ent} = 0.05$ m, and the gas velocity is equal the characteristic gas velocity.

The pickup velocity is combined with an efficiency expression and a constant, k_4 :

$$\eta_{Ent} = \frac{\left(\frac{v_{gas}}{k_4 \cdot v_{Pickup}} \right)^{m_4}}{1 + \left(\frac{v_{gas}}{k_4 \cdot v_{Pickup}} \right)^{m_4}} \quad \text{Eq. 50}$$

The predicted results are shown in Figure 100 and Figure 101. The parameters have been estimated to $m_4 = 4$ and $k_4 = 2.57$. As $k_4 > 1$, the gas velocity needed to entrain the particle is larger than the gas velocity needed to suspend particles from the walls of horizontal transport pipes. This is caused by the particles shadowing each other from the gas flow, and by the particles having downward inertia at the feeding point to the gas. The geometry of the

entrainment area is important for the entrainment process, why the factor k_4 most likely is highly geometry dependent.

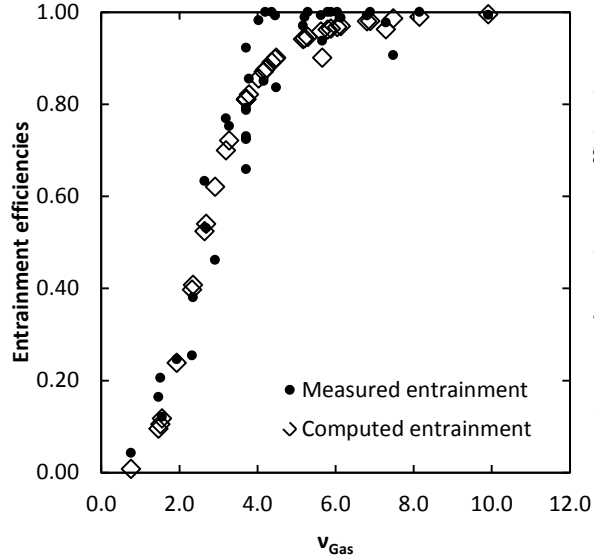


Figure 100 – Measured and computed entrainment efficiencies (Model #4) depicted as a function of gas velocity in the transport channel.

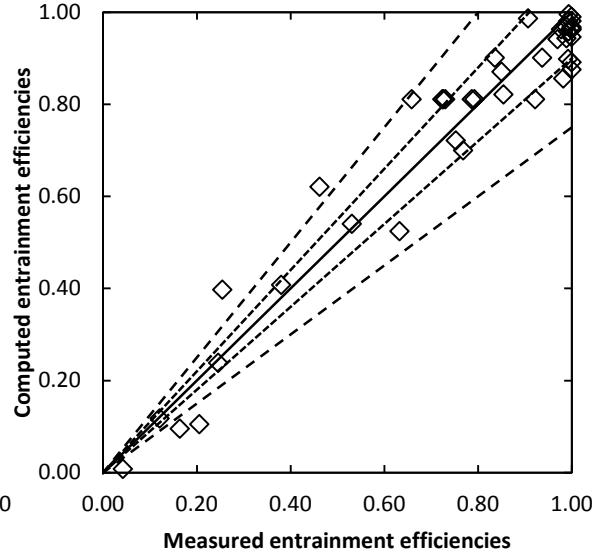


Figure 101 – Computed entrainment efficiencies (Model #4) depicted against the measured entrainment efficiencies. Deviations of 10 and 25 % are shown.

Generally, the entrainment efficiency is reasonable represented, but the model underestimates the majority of the data sets at entrainment efficiencies close to one. This is caused by the model not being capable of predicting the sharp rise to full entrainment around $v_G = 4$ m/s. The computed trend, shown in Figure 100, appears reasonable, compared to the experimental data.

Model #5: Force balance

Applying a similar approach as in Model #3, using Stokes law, as stated in Eq. 46, to describe the vertical velocity of the particles in the entrainment area, while fitting an effective friction coefficient, yields an applicable model of the entrainment. The applied efficiency expression is different from that of Model #3 due to the direction of the gas flows.

$$\eta_{Ent} = \frac{\left(\frac{v_{gas}}{v_{Terminal}} \right)^{m_5}}{1 + \left(\frac{v_{gas}}{v_{Terminal}} \right)^{m_5}} \quad \text{Eq. 51}$$

The friction factor, $f_{p,eff}$ is found to be 0.04, approximately 200 – 300 times lower than expected for a single settling sphere. The computed results are shown in Figure 102 and Figure 103.

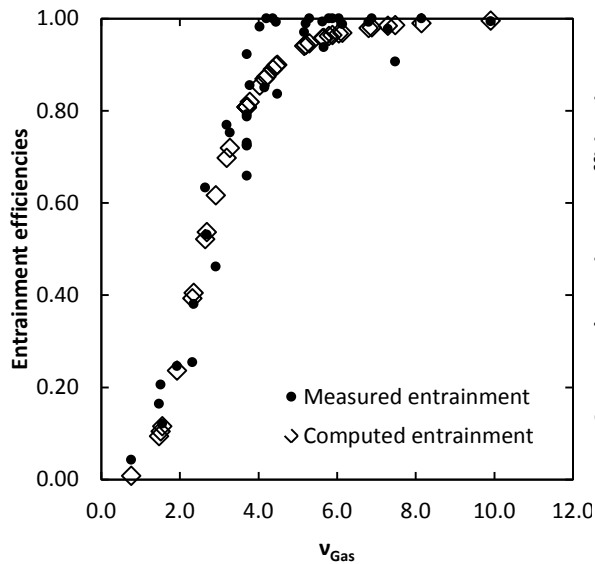


Figure 102 – Measured and computed entrainment efficiencies (Model #5) depicted as a function of gas velocity in the transport channel.

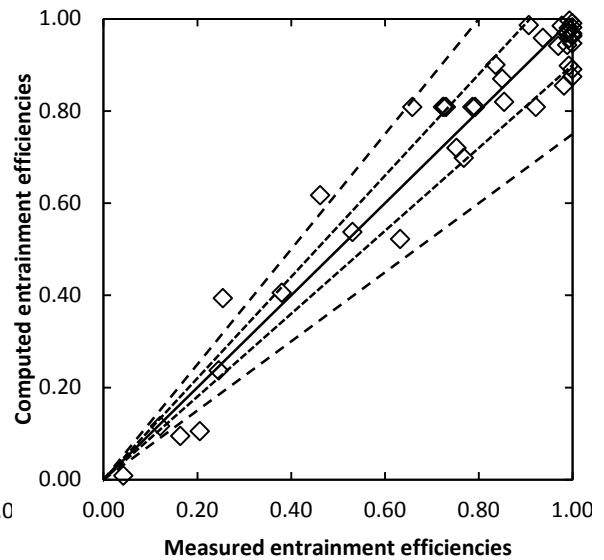


Figure 103 – Computed entrainment efficiencies depicted against the measured entrainment efficiencies using Model #5. Deviations of 10 and 25 % are shown.

Similar to Model #4, the sharp rise of entrainment efficiencies is difficult described by model #5. Both trend, Figure 102, and fit, Figure 103, appear reasonable. Deviations of up to 30 % have been found.

Discussion

For the entrainment, it has not been possible to identify a model of similar simplicity as Model #1, as the sharp rise of the entrainment efficiency at velocities at 3 – 4 m/s is difficult modeled by the use of dimensionless groups alone.

The two models describing the entrainment process are compared in Table 28.

Table 28 – Summary of entrainment process models#4 and #5.

		Model #4 – Pneumatic Transport	Model #5 – Force balance
Fitting parameters		$k_4 = 2.57, m_4 = 4$	$f_{p,eff} = 0.04, m_4 = 4$
Sum of errors ^A		0.22	0.21
Dependence of		$v_G, l_{system}, d_p, \rho_G$ and μ	v_G, d_p and ρ_G
Major assumptions		System is analogous to pneumatic transport systems	Particles move as a single particles with reduced friction
Limiting behavior	v_G	$v_G \rightarrow \infty: \eta_{Ent} \rightarrow 1$	$v_G \rightarrow \infty: \eta_{Ent} \rightarrow 1$
		$v_G \rightarrow 0: \eta_{Ent} \rightarrow 0$	$v_G \rightarrow 0: \eta_{Ent} \rightarrow 0$
	l_{system}	$l_{system} \rightarrow \infty: \eta_{Ent} \rightarrow 0$	-
		$l_{system} \rightarrow 0: \eta_{Ent} \rightarrow 1$	-
	ρ_G	$\rho_G \rightarrow \infty: \eta_{Ent} \rightarrow 1$	$\rho_G \rightarrow \infty: \eta_{Ent} \rightarrow 1$
		$\rho_G \rightarrow 0: \eta_{Ent} \rightarrow 0$	$\rho_G \rightarrow 0: \eta_{Ent} \rightarrow 0$
	d_p	$d_p \rightarrow \infty: \eta_{Ent} \rightarrow 0$	$d_p \rightarrow \infty: \eta_{Ent} \rightarrow 0$
		$d_p \rightarrow 0: \eta_{Ent} \rightarrow 1$	$d_p \rightarrow 0: \eta_{Ent} \rightarrow 1$
	μ	$\mu \rightarrow \infty: \eta_{Ent} \rightarrow 1$	-
		$\mu \rightarrow 0: \eta_{Ent} \rightarrow 0$	-

$$^A SoE = \left(\eta_{Measured} - \eta_{computed} \right)^2$$

When comparing Model #4 and #5, two aspects are of identified: (a) The temperature dependence of Model #4 is expected to be better than Model #5 as both fluid density and viscosity is present. Both parameters of importance for evaluating drag and lift forces on an object. Secondly (b), the models predict the entrainment with similar precision and identical efficiency parameters, m_4 and m_5 .

As accuracies are similar, Model #4 is selected for modeling of the 2D-HX due to the relationship with the chosen separation model and the dependencies of several parameters, reported by literature, to be significant for drag and lift forces on particles [35,124].

8.2 Pressure Drop

Modeling of the pressure drop is not directly relevant for establishment of the 2D-HX model, but from a process evaluation and comparison point of view, the pressure drop is of interest. Two approaches for modeling the pressure drop will be described; a (a) pneumatic transport analog and (b) CFD simulation.

The numeration of the models will be continued from the previous sections to avoid confusion.

Model #6: Pneumatic transport analog

Rhodes [120] describes a method for determining the pressure drop in a pneumatic transport system founded on a momentum balance. The overall pressure drop can be attributed pressure drop generated by friction, acceleration and elevation for both gas and particles:

$$\Delta P_{Stage} = \underbrace{\Delta P_{G,Fric}}_{(1)} + \underbrace{\Delta P_{G,Acc}}_{(2)} + \underbrace{\Delta P_{G,Elv}}_{(3)} + \underbrace{\Delta P_{P,Fric}}_{(4)} + \underbrace{\Delta P_{P,Acc}}_{(5)} + \underbrace{\Delta P_{P,Elv}}_{(6)} \quad \text{Eq. 52}$$

which can be approximated by:

$$\Delta P_{Stage} = \underbrace{F_{W,P}}_{(1)} \cdot L + \underbrace{\frac{\rho_G \cdot \varepsilon \cdot v_G^2}{2}}_{(2)} + \underbrace{\rho_P \cdot (1 - \varepsilon) \cdot L \cdot g \cdot \sin \theta}_{(3)} + \underbrace{F_{W,G}}_{(4)} \cdot L + \underbrace{\frac{\rho_P \cdot (1 - \varepsilon) \cdot v_P^2}{2}}_{(5)} + \underbrace{\rho_G \cdot \varepsilon \cdot L \cdot g \cdot \sin \theta}_{(6)} \quad \text{Eq. 53}$$

where $F_{W,G}$ and $F_{W,P}$ is the wall friction force between gas, particles and wall, respectively, ε is the void fraction, θ is the angle of the pipe section, while L is the length. The numbers in parentheses identifies the terms from Eq. 52 to Eq. 53

It is assumed that the gas pathway can be approximated by series of pipe sections, as illustrated in Figure 104, while the particle pathway is simply assumed to consist of a horizontal and vertical transport, as shown in Figure 105. Upon reaching the separation chamber, the particles are assumed to not influence the pressure drop.

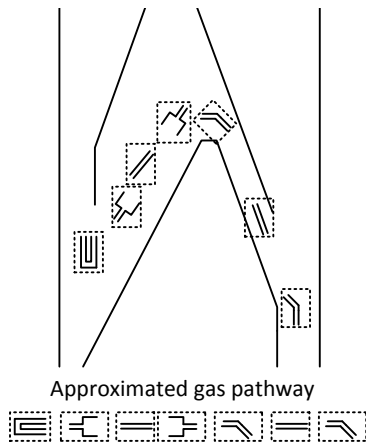


Figure 104 – Approximated gas pathway in a single stage of the 2D-HX.

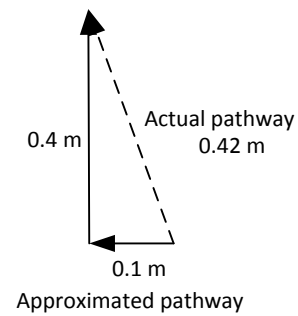


Figure 105 – Approximated particle pathway in a single stage

The evaluation of the Model #6, Eq. 53, is described in Appendix D, where also it is shown that the resistance in the gas pathway is equivalent to 110 m of pipe with $D = 0.1$ m. The results of the pressure drop computations are given in Figure 106.

Model #6 over predicts the pressure drop by up to 200 %, while absolute deviations are less than 2 mbar. The gas friction term (term 1 in Eq. 52), is responsible for between 60 % and 80 % of the computed pressure drop, indicating that the equivalent pipe length has possibly been estimated too high. The particle friction term (term 4) contributes with between 10 % and 30 % of the total pressure drop. The model will not be attempted improved as the measurements of the pressure drop are related to large deviations and uncertainties. Especially the fluctuation of the measured pressures induces large uncertainties, and the occasional blockage of pressure transmission lines reduces usability of the data. The results of this model should be used with additional caution, yet the computed results indicate the order of magnitude of the pressure drop correctly.

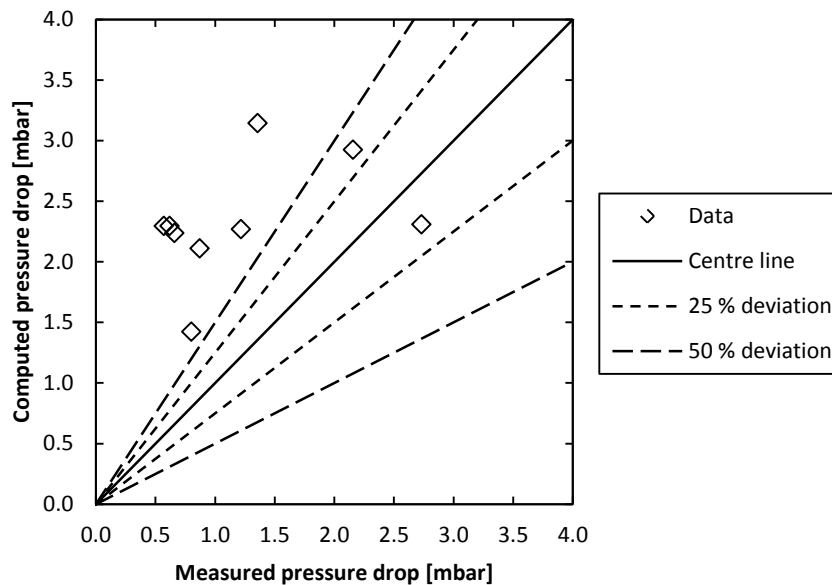


Figure 106 – Comparison of measured and computed pressure (Model #6). Deviations of 25 % and 50 % are indicated.

Model #7: CFD simulation

The CFD model used to investigate the internal flow patterns, described in Chapter 6, can also be used to determine the pressure drop of the system when no particles present. The pressure difference over a stage is obtained as the difference between the absolute pressures at the

entrance and the exit of a stage in an isothermal system, as illustrated in Figure 107. As isothermal conditions are assumed, the pressure drops over all stages are identical. The temperature is set to the average temperature of the system.

The deviation between the measured and computed pressure drops are up to 60 %, while the absolute deviations are below 0.35 mbar.

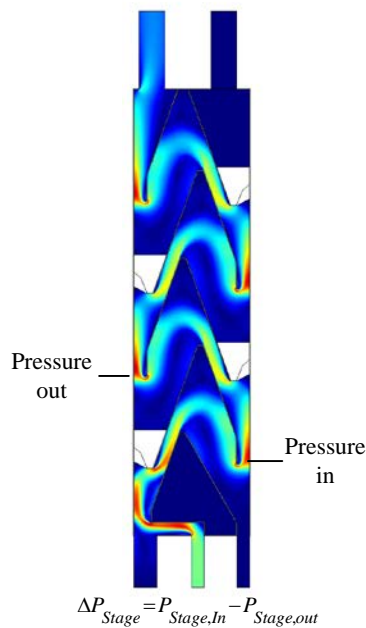


Figure 107 – Velocity profile for PoC#1 with indications of measurement points for pressure.

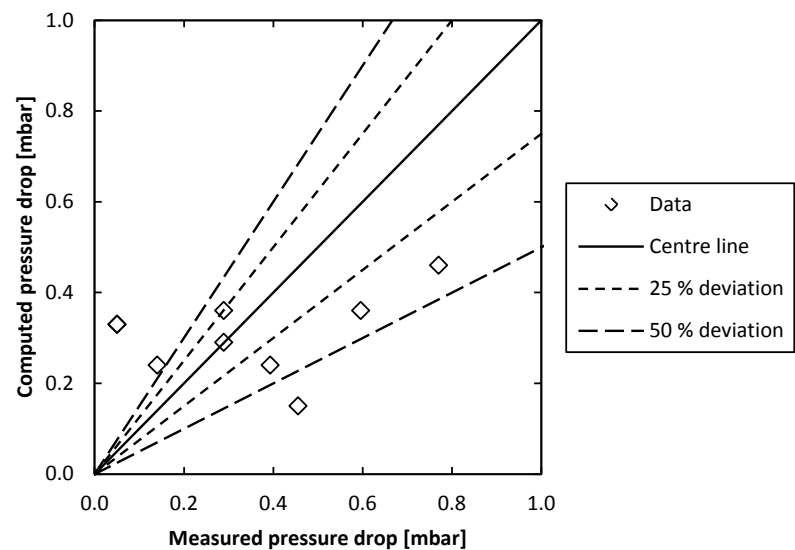


Figure 108 – Comparison of measured and computed pressure drops for pure gas flows (Model #7). Deviations of 25 % and 50 % are indicated.

Discussion

The order of magnitude of the pressure drop over a single stage can be approximated by both a pneumatic transport model (Model #6) and a CFD model (Model #7) with absolute deviations of less than 2 mbar. The CFD model predicts more accurately the particle free pressure drop, but cannot account for any significant amount of particles.

An analysis of the pressure loss computations shows that the friction of the gas and the friction of the particles are the major contributors to the pressure loss, contribution with more than 90 % of the total pressure. The acceleration and elevation terms are in comparison neglectable.

For the modeling of the 2D-HX, the pneumatic transport model, Model #6, will be used, as this model is capable of predicting the pressure drop of the system with particles, which is a cardinal point. Furthermore, Model #6 can be incorporated in the model of the 2D-HX, which is not an option with the CFD computations. Upon implementation, Model #6 will be simplified by neglecting the acceleration and elevation terms. Uncertainties, in same order of magnitude as the computed pressure drops, must be expected.

8.3 Modeling of 2D-HX

A model covering the 2D-HX is set up and described in the following. An outline of the relevant internal gas and particle flows, assumptions, and solution procedure is given, before the model and estimated parameters are verified against experientially obtained data.

8.3.1 Mass and Energy Balances

The mass and energy balances represent the flows and internal processes in the 2D-HX. An illustration of the considered flows and sub-stage processes in a given stage is provided in Figure 109.

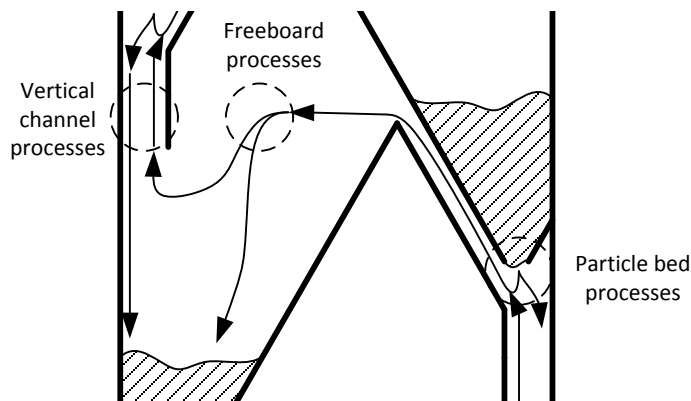


Figure 109 – Drawing of the simulated particle flows and processes in a single stage. Gas flow is not depicted.

Three processes are considered: (a) The freeboard, (b) the vertical channel, and (c) the particle bed. The gas, not depicted in Figure 109, flows up through the vertical channel, below the particle bed, into the freeboard, and out through the vertical channel, etc. Schematically, the particle flows depicted in Figure 109, translates to the box diagram shown in Figure 110.

The major heat exchange is assumed to take place in the freeboard, wherefrom the particles are directed to either the particle bed or the dust flow. Secondary heat exchange processes are assumed to take place in both the vertical channel and the particle bed. In the vertical channel, the mass flows of the entering particles steams are assumed constant. The heat loss is assumed to only affect the freeboard.

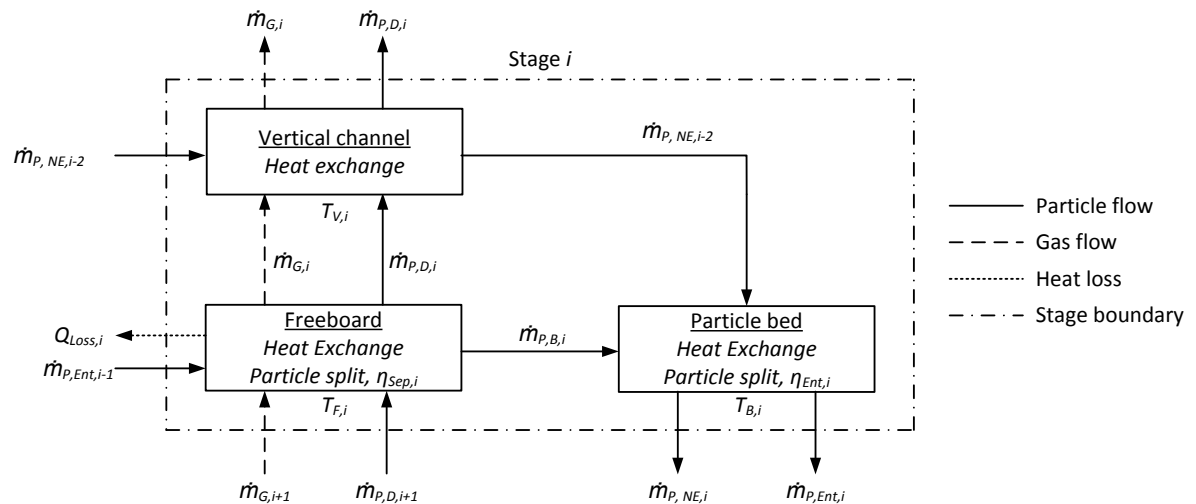


Figure 110 – Stage boundary and internal processes considered in the 2D-HX model.

The entrainment efficiency used to determine the flows $\dot{m}_{P,NE,i}$ and $\dot{m}_{P,Ent,i}$ are dictated by the flows and temperatures entering from the vertical channel of stage $i+2$. Combining the individual stages yields a model covering the entire system, as shown in Figure 111 for a system with of N stages.

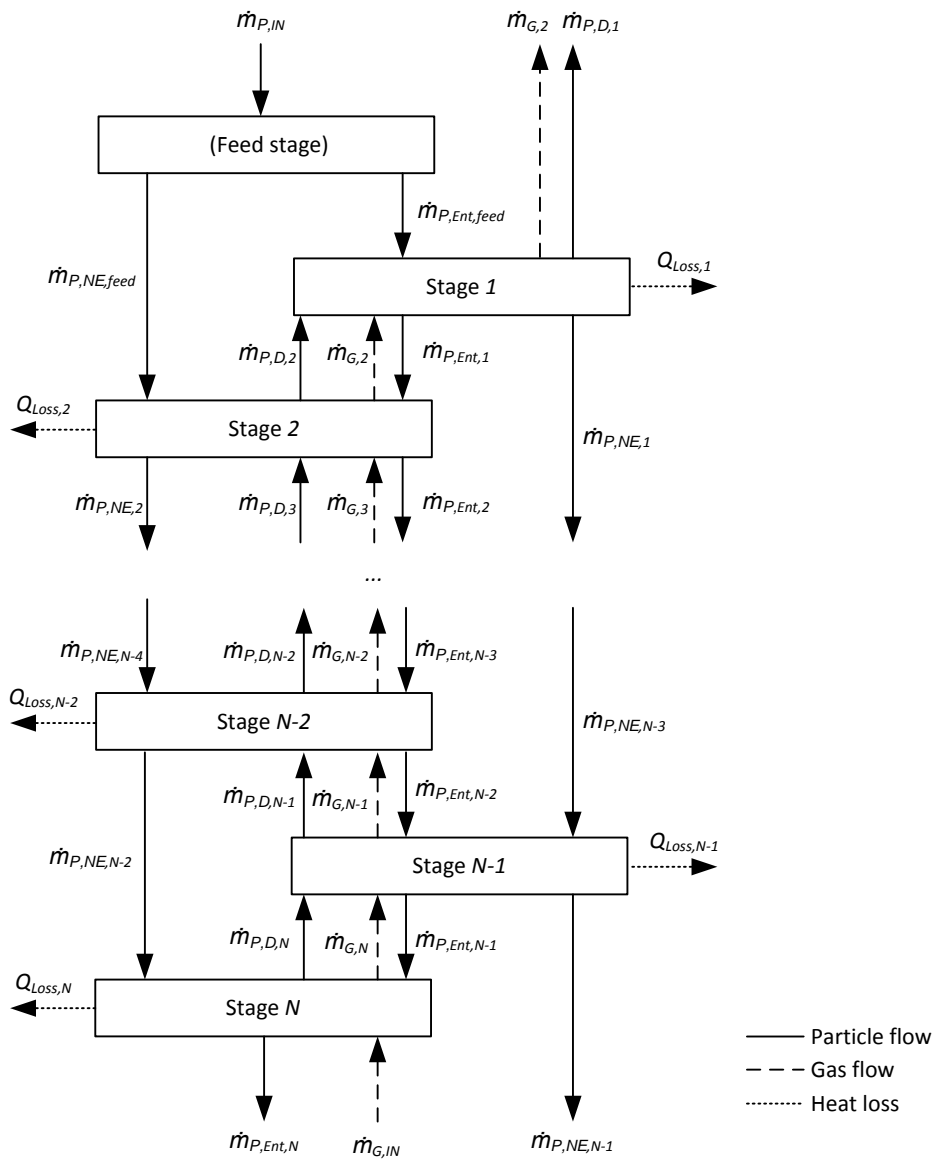


Figure 111 – Schematic overview of mass and energy balances for the 2D-HX concept.

The feed stage shown in Figure 111 is not a heat exchange stage, why it has not been numerated. The feed stage is the top chamber, into which the particles are fed. The major difference between the modelling of the cyclone preheater and the 2D-HX is that the streams $\dot{m}_{P,NE}$ skips a stage, thus these streams experience fewer heat exchange steps than the $\dot{m}_{P,Ent}$ streams.

The implemented mass and energy balance equations can be found in Appendix E.

8.3.2 Assumptions

The following assumptions are made to simplify the model:

- The system is in steady stage.
- Heat exchange takes place in the freeboard, the vertical channel, and the particle bed.
- Each stage sub-process is considered isothermal and the heat exchange is instant.
- The flows $\dot{m}_{P,Dust}$ and $\dot{m}_{P,NE}$ only exchanges heat in the vertical channel.
- The gas stream is constant, neglecting calcination and false air.
- Heat capacity of gas and particles are independent of temperature. The used values are: $C_{P,P} = 900$ J/kg/K and $C_{P,G} = 1071$ J/kg/K.
- The heat loss is described as a linear function of the stage temperatures, as derived in Chapter 7. The slope of the linear function is k_{heat} .

8.3.3 Solution Method

The mass and energy balances and entrainment and separation models have been implemented in MatLab. The computational algorithm is depicted in Figure 112. The solution procedure is iterative with two nested loops computing mass flows and temperatures.

The main script, *main2DHX.m*, contains the energy and mass balances, while the entrainment and separation models are constructed as functions, *n_S.m* and *n_E.m*, requiring gas velocities, geometry and particle properties as input. The input to the model, including experimental data, is given in a separate input file.

As seen in Figure 111, top and bottom stages are different from the middle stages in terms of mass flows. In the model, they are computed similar to the middle stages, but irrelevant streams are set to zero, why generic expressions can be used for all stages but the feed stage, which has been specified separately. Details on the implementation in MatLab can be found in Appendix E.

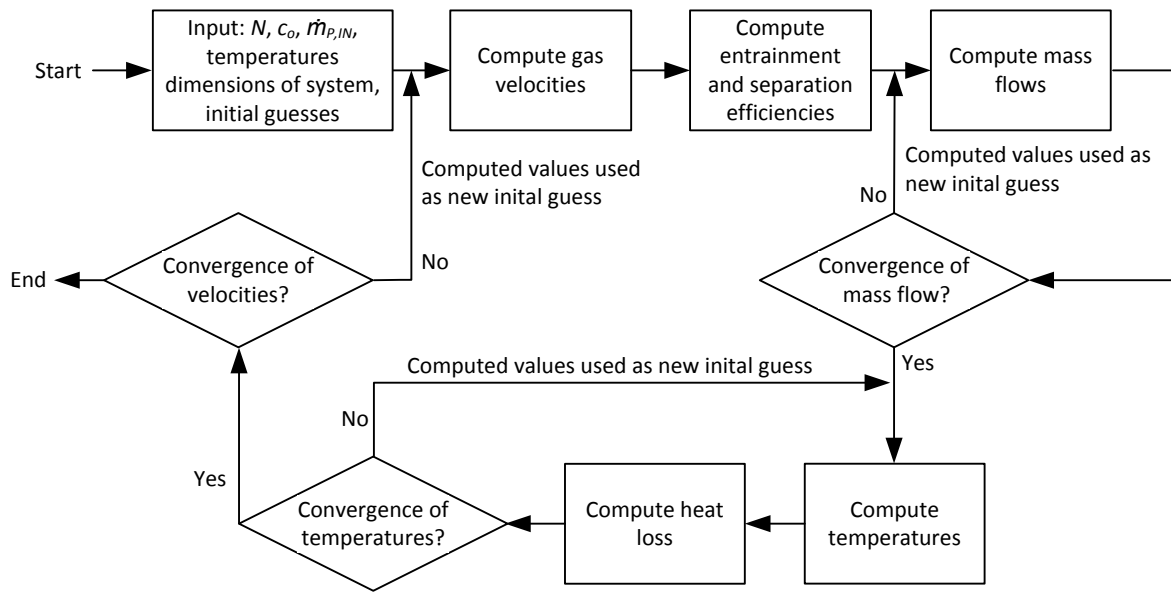


Figure 112 – Algorithm for the 2D-HX model.

8.3.4 Verification

To verify the model applicability, modeled results have been compared with experimental data. Two comparison parameters are used: (a) The dust fraction, given as the amount of dust leaving the system divided by the particle feed, and (b) the temperatures measured at each stage and at the gas outlet. The model contains four empirically fitted parameters: (a) k_2 , relevant for the separation process, (b) k_4 , relevant for the entrainment process, (c) k_{heat} , relevant for the heat loss, and (d) $m = m_2 = m_4$, the slope of the efficiency curve. These parameters have in section 8.1 – *Modeling of the Internal Processes* and Chapter 6 been determined to $k_2 = 0.44$, $k_4 = 2.57$, $k_{heat} = 2.6 \cdot 10^{-4} \text{ } ^\circ\text{C}^{-1}$, and $m = 4$, respectively.

A comparison between the predicted performance and measured values from the PoC set-up experiments P3#9 – #35 and PoC #6 and #7 are given in Figure 113 and Figure 114. Experiments PoC#6 and #7 are carried out at elevated temperatures, while the data remaining data is obtained at ambient temperatures. Therefore, when comparing the estimated and computed temperatures, only four data points are available.

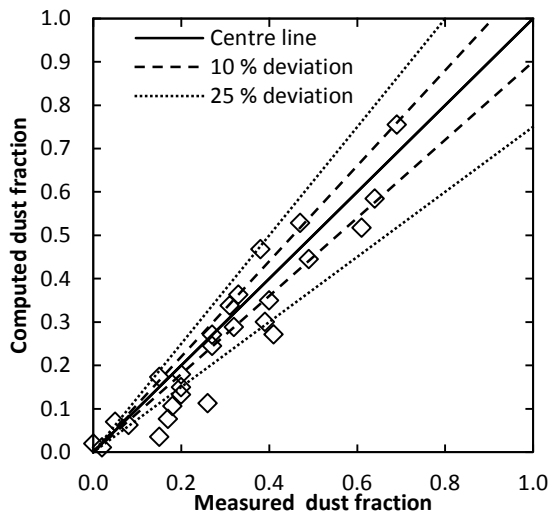


Figure 113 – Comparison between measured and computed dust fractions for PoC single stage experiments. $k_2 = 0.44$, $k_4 = 2.09$ and $k_{heat} = 2.6 \cdot 10^{-4} \text{ } ^\circ\text{C}^{-1}$

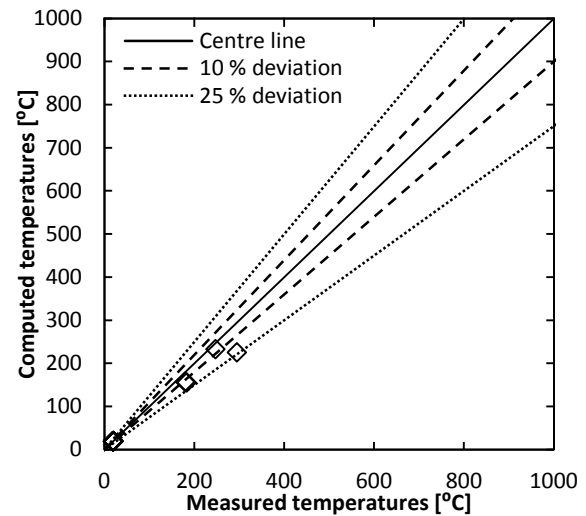


Figure 114 – Comparison between measured and computed temperatures for PoC single stage experiments. $k_2 = 0.44$, $k_4 = 2.09$ and $k_{heat} = 2.6 \cdot 10^{-4} \text{ } ^\circ\text{C}^{-1}$

The model is capable of predicting the majority of the measured dust fractions with less than 25 % deviation and absolute deviations below 0.10. The temperatures are predicted up to 70 °C too low. Considering the uncertainty of the original data, the model performs acceptably.

The results of applying the model to the PoC experiments with four stages, PoC #1 – #5, are provided in Figure 115 and Figure 116.

The major difference between the PoC single stage and PoC four stage experiments are, besides the number of stages, the temperature range. The poor fit, illustrated in Figure 115 and Figure 116, indicates that either the temperature dependence of the internal processes is wrongly represented, or that the individual stages in the four stage set-up do not behave similar to set-up containing only a single stage.

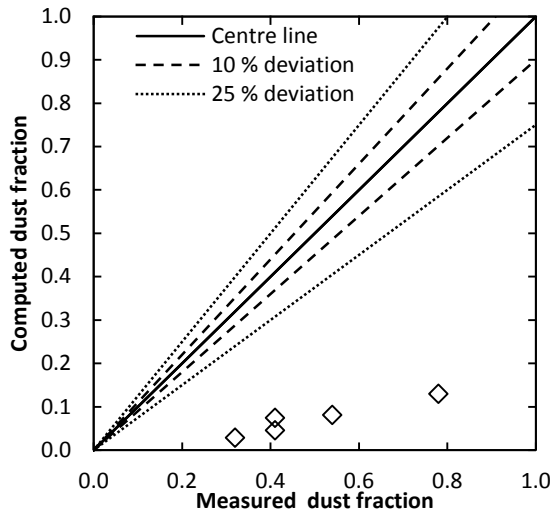


Figure 115 – Comparison between measured and computed dust fractions for four stage experiments. $k_2 = 0.44$, $k_4 = 2.09$ and $k_{heat} = 2.6 \cdot 10^{-4} \text{ } ^\circ\text{C}^{-1}$.

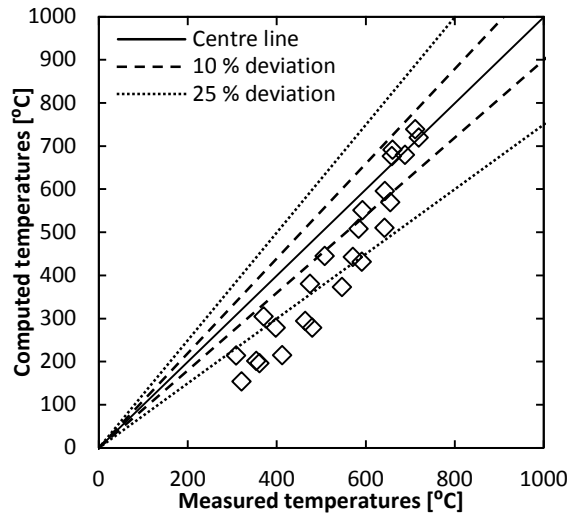


Figure 116 – Comparison between measured and computed temperatures for four stage experiments. $k_2 = 0.44$, $k_4 = 2.09$ and $k_{heat} = 2.6 \cdot 10^{-4} \text{ } ^\circ\text{C}^{-1}$.

To better represent the multi stage behavior, the empirical fitted parameters k_2 , k_4 , and k_{Heat} , have been adjusted to optimize the model performance, using the MatLab function *fminsearchbnd.m*. The cost-function, needed for the optimization, contains the average temperature deviation, average dust fraction deviation, and a penalty for low values of k_4 . Each term is weighted in order for the gradients to be approximately of similar order of magnitude. The penalty is necessary to ensure the physical resemblances of the resulting optimized parameters. The cost function is given by Eq. 54

$$Cost = \frac{\sum_{i=1}^{n_T} |T_{Meas} - T_{Com}|}{n_T} \cdot w_T + \frac{\sum_{i=1}^{n_D} |D_{Meas} - D_{Com}|}{n_D} \cdot w_D + (k_{4,original} - k_{4,opt}) \cdot w_{k_4} \quad \text{Eq. 54}$$

where n is the number of data points for temperature and dust fractions, while w_T , w_D w_{k_4} are weights used to ensure equal weighting of the gradients of each. Here $w_T = 1$, $w_D = 500$ and $w_{k_4} = 5$ is used. The resulting optimized parameters are: $k_2 = 0.29$, $k_4 = 1.52$ and $k_{heat} = 1.5 \cdot 10^{-4} \text{ } ^\circ\text{C}^{-1}$.

The optimized parameters indicate that the separation process is performing poorer than expected, while the entrainment process performs better. The heat loss parameter is found to be significantly lower than initially expected. The resulting data is plotted in Figure 117 and Figure 118. The model, using the optimized parameters, is capable of predicting the dust fractions with up to 30 % deviation and absolute deviations below 0.1, while deviations for the temperatures

are up to 80°C. Comparing the fit of the model using the optimized parameters and the original values, significant improvements have been achieved, especially in the prediction of the dust fraction.

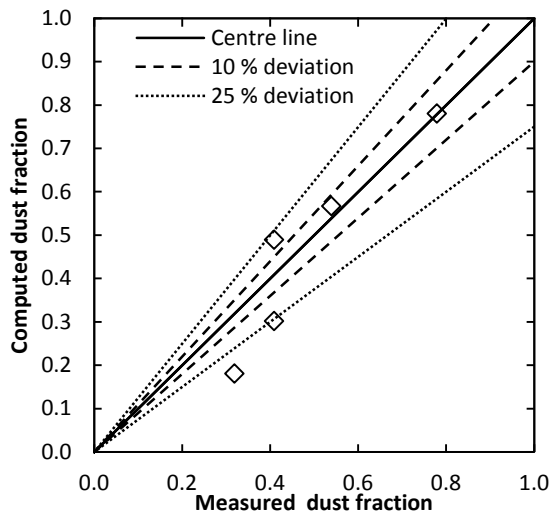


Figure 117 – Comparison between measured and computed dust fractions for four stage experiments. $K_2 = 0.29$, $k_4 = 1.52$ and $k_{heat} = 1.5 \cdot 10^{-4} \text{ } ^\circ\text{C}^{-1}$.

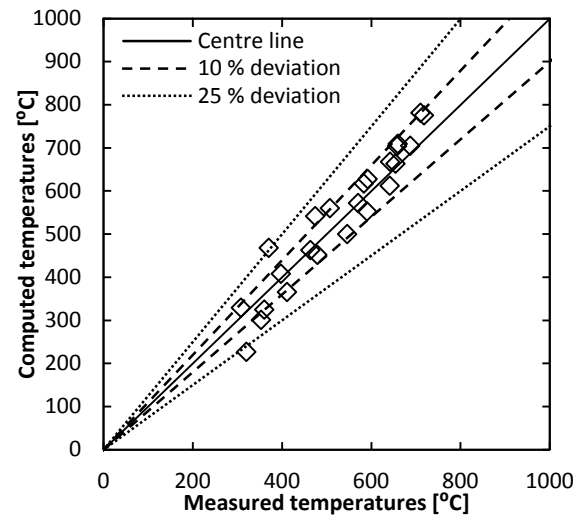


Figure 118 – Comparison between measured and computed temperatures for four stage experiments. $K_2 = 0.29$, $k_4 = 1.52$ and $k_{heat} = 1.5 \cdot 10^{-4} \text{ } ^\circ\text{C}^{-1}$.

Besides being capable of predicting the system behavior, the 2D-HX model can be used to gain information on the internal processes, especially the transport efficiency, which is a major comparison parameter for cement plant preheaters. Furthermore, the transport efficiency can be used to ensure that the system performance using the optimized parameters is reasonable.

Transport efficiencies for the top stage of a four stage cold system ($T_{in} = 20 \text{ } ^\circ\text{C}$) and a hot system ($T_{in} = 790 \text{ } ^\circ\text{C}$) have been computed as a function of the characteristic velocity, using both the original and the optimized parameter sets. The results are shown in Figure 119.

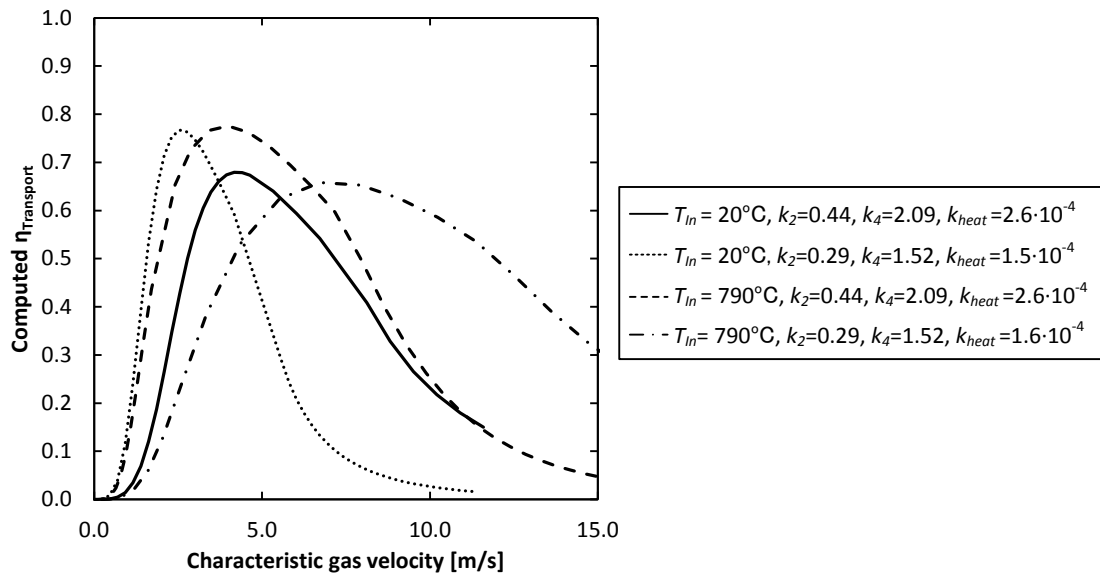


Figure 119 – Computed top stage transport efficiencies for a $N = 4$ system using both original and optimized empirical parameters. Particle feed rate is set to 0.028 kg/s and gas feed rate is varied between $2.8 \cdot 10^{-3}$ and 0.13 kg/s .

The transport efficiencies computed using the optimized parameters resemble the data computed with the original parameters in trends, but with the optima shifted toward lower gas velocities, still indicating that the optimized parameters yields reasonable values for the transport efficiencies.

Furthermore, the difference between the two data series, suggests that either the empiric values have a temperature dependence, or more likely that the developed models lacks some temperature dependency.

The model is intended to model high temperature processes, why the optimized parameters will be used.

8.4 Summary

From the experimental data obtained on the PoC set-up with a single stage, the entrainment and separation processes were modeled. Several models for each process have been proposed and evaluated. The chosen model considers the system as a pneumatic transport and combines velocity expressions with a cyclone efficiency expression, thereby yielding a satisfactory

mathematical description. Both the entrainment and the separation models contained a correction factor and an efficiency parameter, all empirically fitted. The values were found to $k_2 = 0.44$, $k_4 = 2.57$. The constant used for heat loss, as described in Chapter 7, was found to $k_{heat} = 2.6 \cdot 10^{-4} \text{ }^\circ\text{C}^{-1}$.

Combining the models of the entrainment and separation processes, the heat loss estimation, and energy and mass balances for the individual stages, resulted in a model describing the entire set-up. The model have been implemented and solved in MatLab, and the results verified against the experimentally obtained data. The model fitted well the dust fraction and temperatures measured on PoC single stage experiments. Deviation for the dust fractions were less than 25 % with absolute deviations below 0.10. The representation of PoC experiments with four stages was poor with deviations in the order to 200% - 400 % for the dust fractions.

Parameters optimized to fit experimental data, $k_2 = 0.29$, $k_4 = 1.52$ and $k_{heat} = 1.5 \cdot 10^{-4} \text{ }^\circ\text{C}^{-1}$, resulted in an improved model fit, with deviations lower than 80 °C for the temperatures and 0.1 for the dust fractions. The optimized parameters indicated higher entrainment, lower separation and heat loss in the four stage configuration, compared to system with a single stage.

Transport efficiencies computed using the optimized parameters were found to lie within the expected range, and with reasonable gas velocity dependence, thereby confirming the model yielded physical realistic results.

The difference in behavior between the experiments with a single stage and four stages could be related to the absence of a particle bed in the bottom stage and dust in the fed gas flow. Another reason might be that the temperature dependence of the internal processes was not properly represented in the model.

A model of the pressure drop has also been developed: Considering a stage as a pneumatic transport system consisting of a series of bends and pipe sections yielded values in similar order of magnitude as the measured data. The model was not capable of precisely predicting the pressure drop. A CFD model performed better, predicting only gas flows.

Generally, an exact fit between model and data have not be expected due to the uncertainty of the data, including deviations from stable operation. Despite this, the developed models predict performance reasonable.

The developed model will be used to predict the performance of 2D-HX systems during upscaling and optimization. These topics are covered in Chapters 9 and 10.

Chapter 9

Determination of Upscaling Principle

”Scale-up is still not an exact science, but is rather that mix of physics, mathematics, witchcraft, history, and common sense that we call engineering”

– J. M. Matsen, engineer and researcher

To evaluate the operation characteristics of an industrial-scale 2D-HX facility, and thereby the commercial potential of the 2D-HX design, upscaling from the bench-scale experiments is necessary. The 2D-HX model, developed and verified in Chapter 8, principally describes a system of any size and could be used for scaling purposes. However, the model contains fitted elements, and has not been verified against data from equipment of other sizes than the PoC set-up, and using the model for scaling can be questionable. Another method to gain insight in the performance of the full-scale facility is to apply classic upscaling theory, thereby generating a basis for validation of the model performance.

In the following an introduction to classic upscaling strategies is provided. To uncover the scaling parameters relevant for the 2D-HX, inspiration from upscaling of systems with particle-gas interaction, such as fluidized and spouted beds will be considered. The identified scaling parameters will be evaluated, and the resulting equipment dimensions and performance presented. The results will be compared with data obtained from the model.

A thorough study of the full-scale performance of the 2D-HX can be found in Chapter 10, while in present chapter, only the upscaling principles are determined.

9.1 Upscaling Strategies

Scaling-up equipment from laboratory-scale is necessary for any chemical production at industrial-scale. A typical upscaling pathway includes, according to Knowlton et al. [125], who developed a roadmap for scale-up of fluidized beds; (a) Selection of appropriate operation

regime in the reactor, (b) construction of a continuous pilot plant, (c) construction of demonstration plant, and finally (d) construction of commercial plant.

As stated by Knowlton et al., a typical upscaling strategy involves several intermediate steps between lab- and full-scale, including testing in bench- and pilot-scale facilities, before designing the commercial-scale facility.

An overview of the different categories of equipment used in the scale-up procedures of the cement industry, as well as standard production rates and scale ratios are provided in Table 29.

Table 29 – Typical scale-up ratios between different equipment categories in the cement industry.

Equipment category	Typical daily production rates ^A	Scale-up ratios
Laboratory-scale	~ 1 TPDc	>1:5
Bench-scale	~ 5 TPDc	>1:10
Pilot-scale	~50 TPDc	>1:20 – 120
Commercial-scale	1000 – 6000 TPDc	

^A Bench- and laboratory-scale units normally does not run continuously. The daily production rates are theoretically estimated from the production rates during operation.

The total scale ratio between laboratory- and full-scale is typically around 1:1000 – 6000, indicating a very large span between the two types of equipment. This range is not rare in upscaling problems [126], however.

Upscaling is not unproblematic as a variety of issues arise from the larger dimensions and higher flows in upscaled equipment. Typical issues relate to reduced heat and mass transfer rates, incomplete mixing, reduced wall effects, and possibly change of operation regimes. Furthermore, impurities in the full-scale raw materials or undesirable local conditions may cause unexpected problems.

A successful scale-up maintains similarity between the two scales of the process in terms of dynamic, kinematic, geometric, thermal, and chemical behavior. Scale-up literature, here exemplified by processes with a significant gas-solid contact [127–134], is focused on the use of dimensionless groups to describe process relevant phenomena. Keeping these groups constant during scale-up ensures similarity. Other researchers, such as Datta and Ratnayaka [135],

develop semi-theoretical or empirical correlations for description of process parameters across different scales.

An overview of selected dimensionless scaling parameters presented in literature for a variety of particle-gas systems has been collected in Table 30. For a comprehensive comparison of fluidized bed scaling parameters, Rüdissüll et al. [134] made a summarizing review.

Table 30 – Overview of scaling parameters reported in literature for particle-gas systems. The nomenclature of this work has been applied, and the dimensionless groups have been standardized.

Author	Scaling ratio ^A	Unit	Scaling parameters
Weinell [127]	19:1	Circulation fluidized bed combustor	$\frac{v^2}{g \cdot d_p}, \frac{\rho_g}{\rho_p}, \frac{L}{d_p}, \frac{D}{d_p}, \Phi, PSD, geometry$
Glicksman [128] (viscous limit set, Re < 4)	16:1	Fluidized bed	$\frac{v^2}{g \cdot d_p}, \frac{\rho_p \cdot v \cdot d_p}{\mu}, \frac{\rho_g}{\rho_p}, \Phi, PSD, geometry$
Glicksman [128] (inertial limit set, Re > 1000)	16:1	Fluidized bed	$\frac{v^2}{g \cdot d_p}, \frac{\rho_g}{\rho_p}, \Phi, PSD, geometry$
Glicksman et al. [129] (full set)	256:1	Fluidized bed	$\frac{\rho_p \cdot \rho_g \cdot d_p^3 \cdot g}{\mu^2}, \frac{v^2}{g \cdot d_p}, \frac{\rho_g}{\rho_p}, \frac{\rho_g \cdot L \cdot v}{\mu}, \frac{\dot{m}_p}{\rho_p \cdot v}, \Phi, PSD, geometry$
Glicksman et al. [129] (simplified set)	256:1	Fluidized bed	$\frac{v^2}{g \cdot d_p}, \frac{\rho_g}{\rho_p}, \frac{v}{v_{mf}}, \Phi, PSD, geometry$
He et al. [130]	1:4	Spouted bed	$\frac{\rho_g \cdot d_p \cdot v}{\mu}, \frac{v^2}{g \cdot d_p}, \frac{\rho_g}{\rho_p}, \frac{L}{d_p}, \frac{D}{d_p}, \phi, \Phi, \varepsilon, PSD, geometry$
Béttega et al. [131]	1:16	Spouted bed	$\frac{\rho_g \cdot d_p \cdot v}{\mu}, \frac{v^2}{g \cdot d_p}, \frac{v^2}{g \cdot D}, \frac{\rho_g}{\rho_p}, \frac{H}{d_p}, \frac{D}{d_p}, \Phi, \varepsilon, PSD, geometry$
Du et al. [132]	1:2	Spouted bed	$\frac{\rho_p \cdot d_p \cdot v}{\mu}, \frac{v^2}{g \cdot d_p}, \frac{\rho_g}{\rho_p}, \frac{H}{d_p}, \frac{D}{d_p}, \phi, \Phi, \varepsilon, PSD, geometry$
Datta and Ratnayaka [135]	1:2	Pneumatic conveying system	$\Delta P = \frac{K \cdot \rho_{sus} \cdot v_{Entry}}{2}$

^A Given as ratios of characteristic areas of scaled equipment

Nomenclature: v = characteristic gas velocity, g = gravitational acceleration, ρ = density, D = characteristic diameter, L = characteristic length, d_p = mean particle size, Φ = particle sphericity, μ = fluid viscosity, ϕ = internal angle of friction, ε = void in bulk, PSD = non dimensional particle size distribution. Index mf = minimum fluidization.

Parameters such as the Archimedes number, Ar , Froude number, Fr , Reynolds number for both gas and particles, Re and Re_p , and Stokes number, Stk , appear frequently. The mentioned dimensionless groups and their typical definitions are presented in Table 31. Other parameters such as the term *geometry* and the non-dimensional particle size distribution (*PSD*) are present in all but the last of the given sets of scaling parameters shown in Table 30. The term *geometry* contains non-dimensional parameters describing the geometry of the given unit, e.g. height to diameter ratios.

Table 31 – Often encountered dimensionless groups in particle-gas systems.

Name	Symbol	Definition
Archimedes number	Ar	$\frac{d_p^3 \cdot g \cdot \rho_g \cdot (\rho_p - \rho_g)}{\mu^2}$
Euler number	Eu	$\frac{\Delta p}{v^2 \cdot \rho_p}$
Froude number	Fr	$\frac{v^2}{g \cdot d_p}$
Reynolds number	Re	$\frac{\rho_g \cdot D \cdot v}{\mu}$
Reynolds particle number	Re_p	$\frac{\rho_p \cdot d_p \cdot v}{\mu}$
Stokes number ($Re_p < 1$)	Stk	$\frac{\rho_p \cdot v \cdot d_p^2}{18 \cdot \mu \cdot l}$

For scaling of fluidized beds, the full parameter set developed by Glicksman et al. leaves few degrees of freedom for the design of the scaled fluidized bed, which may result in either impractical dimensions of the scaled model or unachievable operation conditions, why the simplified parameter set is often applied instead [134,136]. Validation of the scaling parameters have reported by several authors, among others [137–139], with varying success. Fitzgerald et al. [137] built a 0.4 x 0.4 m scale model of an industrial 1.8 x 1.8 m combustor, considering Re_p , Fr , L/d_p , and the density ratio as scaling parameters. Comparison of full-scale and down-scaled model showed similar hydrodynamic behavior, but a statistical analysis showed that coincident results could not be confirmed with 95 % statistical significance, however. Nicastro and

Glicksman [138] validated the use of the full parameter set with success on a downscaled version of a 0.61 x 0.61 m hot combustor.

The sets of scaling parameters, provided in Table 30, have been obtained by either inspectional analysis of the governing equations or by dimensional analysis.

9.2 Selection of Upscaling Parameters

In the 2D-HX, the heat exchange efficiency is the major performance parameter, but as indicated for the cyclone preheaters in Chapter 3, the transport efficiency dominates the heat exchange process, and as shown in Chapters 6 and 7, the separation process is the most critical internal process. The separation process will therefore be the focus for the scaling-up procedure.

Two approaches: Inspectional analysis and dimensional analysis have been applied to identify the parameters relevant for scaling of the separation process in the 2D-HX. The analyses are provided in Appendix F, while the identified parameters are given in Table 32. The parameter sets are homogenized when possible. This is done by combination of the parameters, e.g. combining Re and L_{Sep}/d_p yields a parameter proportional to the Stokes number. L_{Sep} is the length of the separation chamber, as shown in Figure 120.

Table 32 – Summary of identified scaling parameters.

Method	Scaling parameters as found	Scaling parameters homogenized
Inspectional analysis	$\frac{\rho_G}{\rho_p}, Eu, Re, Fr, \frac{L_{Sep}}{d_p}, \frac{L_D}{d_p}$	$\frac{\rho_G}{\rho_p}, \frac{L_D}{L_{Sep}}, Eu, Re, Fr, Stk$
Dimensional analysis	$\frac{(\rho_p - \rho_G)}{\rho_G}, \frac{L_D}{L_{Sep}}, Stk, Re, Fr, Eu, PSD, c_0$	$\frac{\rho_G}{\rho_p}, \frac{L_D}{L_{Sep}}, Eu, Re, Fr, Stk, PSD, c_0$

The parameters; Re , Fr , Eu , Stk , and ρ_g/ρ_p are found in both analyses, while intuitively important parameters such as PSD and c_0 has not been identified by the inspectional analysis.

The Euler number contains the differential pressure of the process, and thereby indirectly the dimensions of the equipment. However, as neither a detailed model for neither the pressure nor detailed pressure measurements of the separation process are available, Eu is disregarded as scaling parameter.

The density ratio cannot be applied as scaling parameter, as it depends on the gas temperatures, composition and the particle density, and thus not the dimension of the design itself. However, the ratio is relevant in order to ensure similar hydrodynamical behavior. The same applies for PSD and c_0 .

This reduces the list of relevant scaling parameters to: L_D/L_{Sep} , Re , Fr , and Stk .

9.3 Parametric Design and Reference Cases

The selected design parameters contain constrains for the dimension L_{Sep} , which is the length of the separation chamber, and the ratio L_D/L_{Sep} . To this point the remaining design has not be specified.

Assuming a geometrically similar system, a parametric design can be constructed from a characteristic dimensions, here chosen to be $L_{Channel}$. All the relevant dimensions and their measures in the PoC set-up can be found in Figure 120 and Table 33.

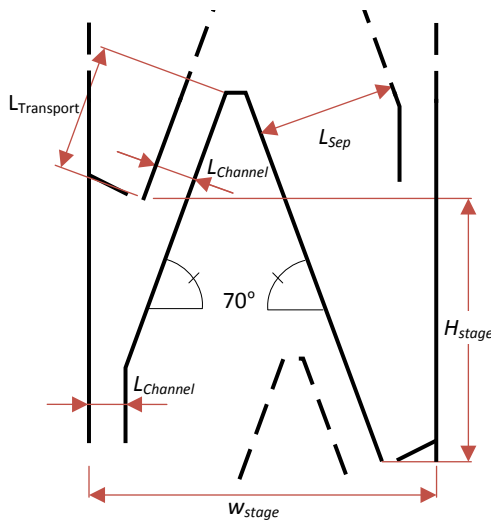


Table 33 – Actual and normal dimensions of PoC set-up.

Parameter	Length in PoC setup	Normalized length
$L_{Channel}$	50 mm	1
$L_{Transport}$	160 mm	3.2
L_{Sep}	175 mm	3.5
H_{Stage}	325 mm	6.5
W_{Stage}	450 mm	9
L_D – depth of system, not depicted in Figure 120.	200 mm	4

Figure 120 – Generic design for intermediate stages of the PoC set-up.

For a given L_{Sep} and the desired number of stages, the remaining design can be determined. The total height of the system, H_{Total} is computed as:

$$H_{Tot} = H_{Stage} \cdot (N + 1) \tag{Eq. 55}$$

The $+I$ accounts for additional height needed for the top and bottom stages respectively. The width of the system is equal to the stage width, W_{stage} , while the depth of the system can be found as:

$$L_{D,Tot} = L_D \cdot \frac{\dot{m}_{P,Tot}}{\dot{m}_{P,Module}} \quad \text{Eq. 56}$$

Where $\dot{m}_{P,Tot}$ is the total desired production capacity, and $\dot{m}_{P,Module}$ is the production rate of the designed module. For more information of the modularity and overall design of the 2D-HX, refer to Chapter 4.

Table 34 – Characteristic parameters of the reference cases used for upscaling.

Parameter	P3#32	PoC#2
Relevant Process and material properties		
Estimated daily production rate	3.2 TPDc	1.5 TPDc
T_{in}	20 °C	790 °C
$v_{Channel}^A$	4.5 m/s	6.6 m/s
ρ_G	1.21 kg/m ³	0.33 kg/m ³
L_{Sep}	0.18 m	0.18 m
Scaling parameters		
L_D/L_{Sep}	1.33	1.33
PSD	Particle size distribution as shown in Chapter 5.	
c_0	1.05	1.2
Re^A	$1.46 \cdot 10^4$	$2.47 \cdot 10^3$
$Stk^{A,B}$	$6.99 \cdot 10^{-3}$	$4.30 \cdot 10^{-3}$
Fr^A	0.9	2.0
Process key parameters		
Number of stages, N	1	4
η_{Ent}	1.0 ^C	0.93 ^D
η_{Sep}	0.74 ^C	0.72 ^D
Dust loss	0.26 ^C	0.32 ^C
^A Computed at inlet conditions in the lowest separation chamber.		
^B Computed as stated in Table 31. $Re_p > 1$ in all cases.		
^C Measured values		
^D Average values estimated using the model developed in Chapter 8.		

When applying classic upscaling theory a reference case is used as a starting point, from where the system performance is extrapolated. To illustrate the influence of the reference case, two cases have been selected for scale-up. These selections are made to ensure best possible performance of the scaled-up system, why high transport efficiency and feed rates are desired. The characteristic performance and scaling parameters for the two reference cases are presented in Table 34.

9.4 Screening of Upscaling Parameters

As the design can be specified from L_{Sep} and L_D , only two degrees of freedom exist. L_D is determined by the ratio L_D/L_{Sep} , leaving a single degree of freedom for determining L_{Sep} . Therefore only one of the parameters Re , Stk , and Fr can be used. Principally, experiments at a different scale should be carried out to determine which of the parameters that represents the performance of the scaled process. To identify the influence, if any, of Re , Stk and Fr , experiments should be planned to keep one of the parameters constant while varying the other. Performing this for each parameter, the scaling parameter or scaling function could be identified. This has not been possible due to limitations in time and resources. Instead, an analysis will be carried out to evaluate the effect of the different parameters on the upscaled design, and a single parameter selected for upscaling purposes.

To identify the effect of each scaling parameter, v_G have been evaluated as function of the scaling ratio. The results are given in Figure 121. As temperatures and particle size are predetermined, keeping Re constant requires that the term $L \cdot v_G$ is kept constant results in a hyperbola function, while keeping Stk constant requires the term v/L constant results in a straight line. Constant Froude number requires that v_G^2/L is constant, yielding a function of the form $v_G \propto \sqrt{L}$.

The gas velocities in the up-scaled systems are much too low in the case of the Reynolds number and much too high in the case of the Stokes number. Application of Re and Stk would yield either too large and thereby expensive equipment or too high velocities resulting in high wear, high pressure drop, and poor separation performance, while the velocities dictated by Fr appears reasonable. Furthermore, in Chapter 8, the Froude number appeared to be closely related to the performance of the separation process.

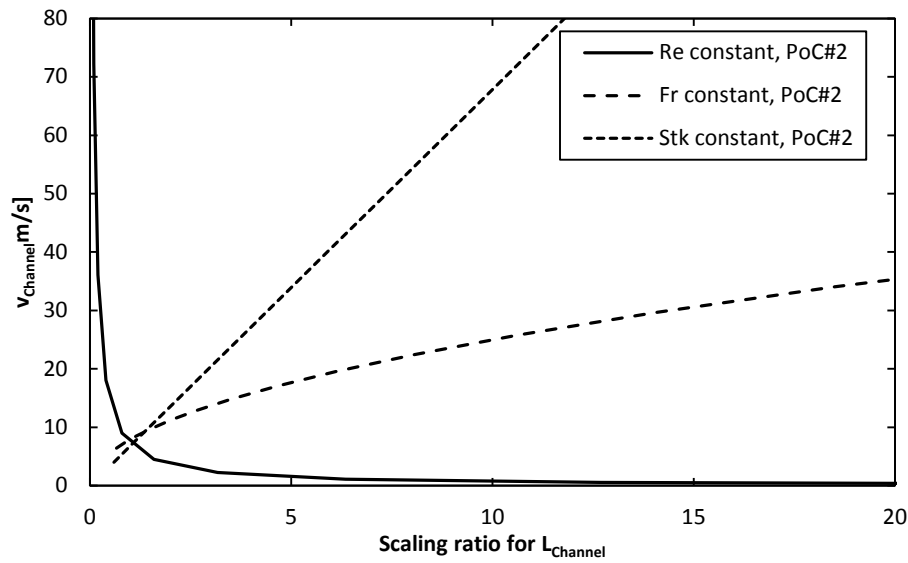


Figure 121 –Velocity in the lower most transport channel as a function of scaling ratio and different scaling parameters, using PoC#2 as reference case.

In short it must be concluded, if the Froude number is not capable of describing the upscaling process, the potential of the 2D-HX is naught.

Thus, the selected scaling parameters related to the design of the 2D-HX are:

$$Fr \text{ and } \frac{L_D}{L_{Sep}}$$

while the parameters:

$$\frac{(\rho_p - \rho_G)}{\rho_G}, c_0, PSD$$

should be kept constant to ensure similar hydrodynamic behavior.

To illustrate the effect of different reference cases, a comparison of estimated particle feed rates and velocities are given in Figure 122 for up-scaled systems based on PoC#2 and P3#32, respectively.

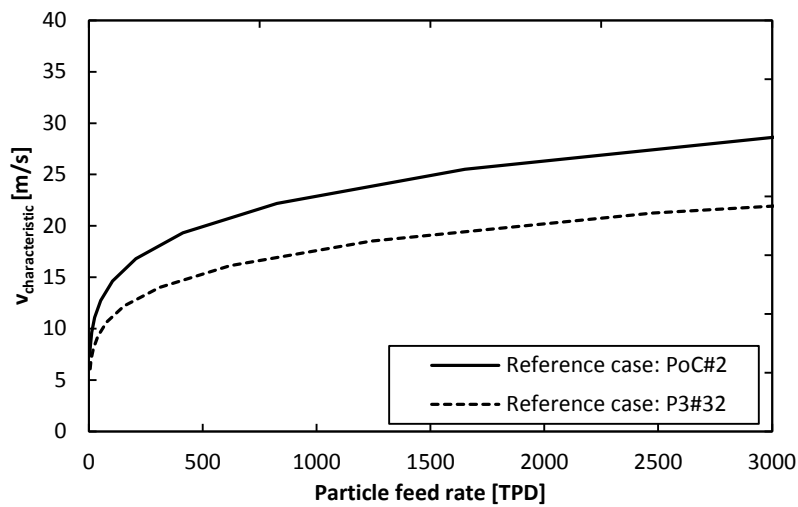


Figure 122 – Characteristic gas velocities as a function of particle feed rate for up-scaled equipment using Fr , c_0 , L/L_D , and PSD as scaling parameters. Two series representing the two reference cases are shown.

The reference case influences the gas velocity, as shown, but also the transport efficiency, particle feed rate, and overall size of the equipment. Comparing the two reference cases, 20 – 30 % higher gas velocities are expected using PoC#2, resulting in smaller dimensions of the equipment.

9.5 Comparison of Classic and Model-based Upscaling

To compare the estimations obtained from classic and model-based upscaling, a system with a 1000 TPD particle feed rate is considered. The classic upscaling process is applied on each of the two reference cases. The model-based upscaled system is based on a characteristic length equal to the average of the values determined by the classic upscaling process. This forces the computed Fr to be in the same range as the values found in the reference cases, and enables a comparison of the two methods. Selected parameters for the reference cases and the upscaled systems are provided in Table 35.

Initially, the similarity of the predicted entrainment and separation efficiencies between the model-based scale-up and the classic upscaling should be noticed. This indicates that the model-based scale-up is equally well suited for scaling purposes as the classic scale-up process. Furthermore, the model provides a more detailed estimate, as it is capable of predicting stagewise efficiencies and temperatures as well as allows optimizations. For these reasons, model-based upscaling will be applied to evaluate the full-scale performance of the 2D-HX.

The estimated production rates for the upscaled processes are around 50 % of the feed. These rates are given as production of clinker, and the low values are caused by dust loss and mass loss of CO₂, released in the calcination process, which takes place after the preheating process. The LOI of raw meal is around 34 %- 38 % [3]. For comparison, the maximum production rate possible for a 1000 TPD feed is around 650 TPDc, while a modern cyclone preheater would produce up to 616 TPDc.

The estimated sizes of the upscaled equipment are 20 – 24 meters in height, 6 – 7 meters wide, and 3 meters in depth. A detailed analysis of predicted sizes and performances of the 2D-HX concept is given in Chapter 10.

Table 35 – Comparison of characteristic parameters for a 1000 TPD particle feed rate system obtained from different scaling methods.

Parameter	Reference case		Classic upscaling		Model-based upscaling
	P3#32	PoC #2	P3#32	PoC #2	
$T_{G,in}$ [°C]	20	790	850	850	850
$\dot{m}_{P,in}$ [TPD]	4.8 ^A	2.7 ^A	1000	1000	1000
$L_{Channel}$ [m]	0.05	0.05	0.72	0.62	0.67 ^B
$v_{Channel}$ [m/s]	4.42	7.9	17	23	20
N	1	4	4	4	4
Dimensions (H x W x D) [m]	0.7 x 0.5 x 0.2	1.6 x 0.5 x 0.2	23.5 x 6.5 x 2.9	20.1 x 5.6 x 2.5	21.8 x 6.0 x 2.7
η_{Ent}	1.0 ^C	0.93 ^D	1.0 ^E	≥ 0.93 ^E	0.97 ^F
η_{Sep}	0.74 ^C	0.72 ^D	0.79	0.72 ^E	0.80 ^F
Fr (lowest stage)	0.9	2.0	0.9	2.0	1.41
Dust loss	0.26 ^C	0.32 ^C	0.26 ^G	0.35 ^G	0.11 ^F
$\dot{m}_{Clinker}$ [TPDc] ^H	2.3	1.0	481	423	578

^A Estimated from production rate during semi-continuous operation.

^B Chosen as the average value of the two lengths found using the classic upscaling approach.

^C Measured values

^D Average values estimated using the model developed in Chapter 8.

^E Assumed to be similar or better than in reference cases due to increased gas velocities.

^F Average values found using the model under upscaled conditions

^G Obtained by simulation assuming constant η_{Ent} and η_{Sep} in all stages.

^H LOI = 0.35 assumed.

9.6 Summary

Both inspectional and dimensional analyses, based on maintaining the similarity of the separation process during upscaling, revealed that ρ_G/ρ_p , L_D/L_{Sep} , Eu , Re , Fr , and Stk were the relevant scaling parameters. The dimensional analysis furthermore suggested c_0 and PSD as important parameters.

The parametric design of the 2D-HX left only one degree of freedom for determining L_{Sep} . A screening of Re , Fr , and Stk showed that only Fr produced reasonable gas velocities in the up-scaled systems.

For this reason, and as Fr and the separation process were in Chapter 6 found tightly related, Fr was chosen as scaling parameter determining L_{Sep} .

The list of chosen scaling parameters has been identified to:

$$Fr, \frac{L_D}{L_{Sep}}, \frac{(\rho_p - \rho_G)}{\rho_G}, c_0, PSD$$

Principally no guarantee for the performance of the scaled-up equipment can be made when the scaling parameter is selected by preference. The choice made here is, from a process understanding point of view, reasonable, though.

A comparison between classic and model-based upscaling showed that the estimations are similar, why the model will be applied for upscaling purposes. In the evaluation of the upscaling methods, it was found that a four stage 2D-HX preheater, with an clinker production capacity of around 400 – 600 TPD would be around 20 – 24 meters in height, 6 – 7 meters wide, and 3 meters in depth.

Chapter 10

Full-scale Application of the 2D-HX

Concept

“The science of today is the technology of tomorrow”

– Edward Teller, Hungarian theoretical physicist

In this chapter the full-scale characteristics of a raw meal preheater based on the 2D-HX concept are evaluated, and compared with corresponding cyclone preheater data. The 2D-HX model, developed in Chapter 8 and selected for upscaling purposes in Chapter 9, is used to predict the full-scale performance.

Recalling the scaling principles of the 2D-HX, described in Chapter 4, the scaling is based on designing stacks, which consists of a number of stages. The stacks can be combined to increase the production capacity to the desired rate, as illustrated for a four stage system in Figure 123.

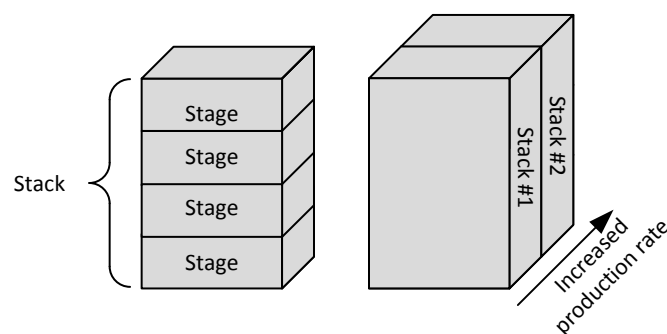


Figure 123 – Upscaling principles of the 2D-HX: Predefined stacks consisting of a number of stages are combined horizontally to achieve the desired production rate.

The capacity of the single stacks influences the characteristics of the full-scale facilities. Stacks with particle feed rates of 2000 TPD, 4000 TPD, and 6000 TPD will be evaluated. Besides the

full-scale facilities, an estimate for a pilot-scale facility is also generated, providing information on a possible next phase in the development of the 2D-HX technology.

This section also contains suggestions for design improvements and alternative applications for a modified 2D-HX. Finally, the identified design and operation related issues are presented.

10.1 Determination of Operation Conditions

The 2D-HX model predicts the operational conditions using dimensions, particle-, and gas feed rates as input. The model is applied on a range of values for the characteristic length, $L_{Channel}$. In order to determine the best combination of conditions, the resulting performance is analyzed. This analysis is described in the following, exemplified by a four stage 2D-HX stack with a particle feed rate of 2000 TPD. The parameters applied in the upscaling process are similar to the operation conditions of the cyclone preheater and given in Table 36.

Table 36 – Parameters used for prediction of full-scale 2D-HX performance.

Parameter	Symbol	Value
Gas inlet temperature	$T_{G,In}$	850 °C
Particle inlet temperature	$T_{P,In}$	60 °C
Number of heat exchange stages	N	4
Particle feed rate	$\dot{m}_{P,Feed}$	23.1 kg/s / 2000 TPD
Solid load	c_0	1.0 kg/kg
Particle diameter	d_p	$12 \cdot 10^{-6}$ m
Specific gas heat capacity	$C_{P,G}$	1071 J/Kg/K
Specific particle heat capacity	$C_{P,P}$	900 J/Kg/K
Absolute pressure	P	98045 Pa ^A
Loss on ignition	LOI	35 %
$L_D / L_{Channel}$	-	4
$L_{Sep} / L_{Channel}$	-	3.5

^A Pressure in the computations assumed constant, equal to the average absolute pressure in the preheater.

To identify the optimal value of $L_{Channel}$, several process relevant parameters must be considered, including (a) gas velocity, (b) transport efficiency, (c) dust loss, and (d) equipment volume.

The computed relationship between $L_{Channel}$ and the maximal gas velocity, found in the transport channel in the lowest stage in the system, is shown in Figure 124. The velocity is dictated by the

temperatures in each stage and the cross sectional area. As expected, the larger the dimensions, the lower the gas velocity.

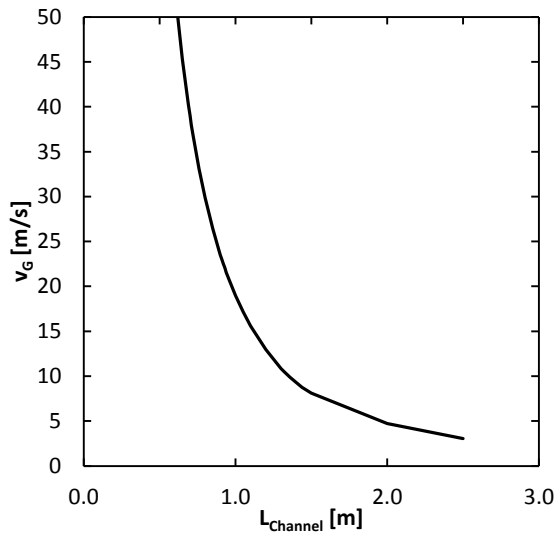


Figure 124 – Gas velocity in the transport channel at the lowest stage as a function of the characteristic length of the system, $L_{Channel}$. $T_{G,In} = 850$ °C, $T_{P,In} = 60$ °C, $\dot{m}_{P,Feed} = 2000$ TPD, $c_0 = 1.0$, $N = 4$.

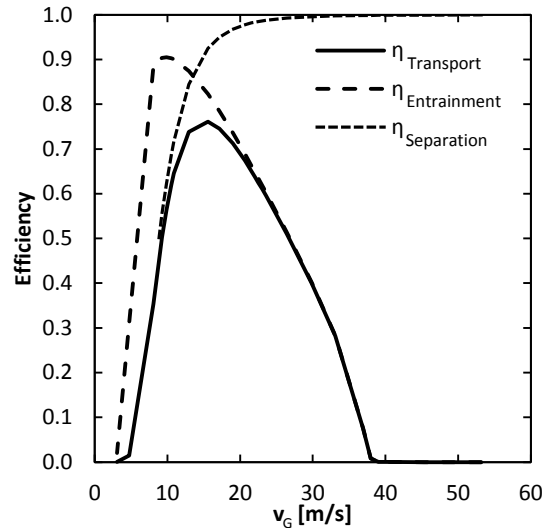


Figure 125 – Entrainment, separation, and transport efficiency at the lowest stage of the four stage preheater as a function of the gas velocity in the transport channel at the lowest stage. $T_{G,In} = 850$ °C, $T_{P,In} = 60$ °C, $\dot{m}_{P,Feed} = 2000$ TPD, $c_0 = 1.0$, $N = 4$.

The gas velocity affects the internal processes, such as the separation efficiency, which, as illustrated in Figure 125, has a peak around $v_G = 10$ m/s. At higher velocities the separation efficiency drops due to high gas velocity, while at lower velocities, the reason is low solid load (due to reduced entrainment). The transport efficiency has an optimum around 15 m/s. The dust loss and production rate, depicted in Figure 126, show that the higher the gas velocity, the higher the dust loss, which reduces the production rate. The maximal production rate is dictated by the LOI of the raw meal and is equal 1300 TPDc for the 2000 TPD stack. Finally, the thermal efficiencies for the upscaled system, displayed in Figure 127, indicate that the optimal velocity is around 12 – 15 m/s.

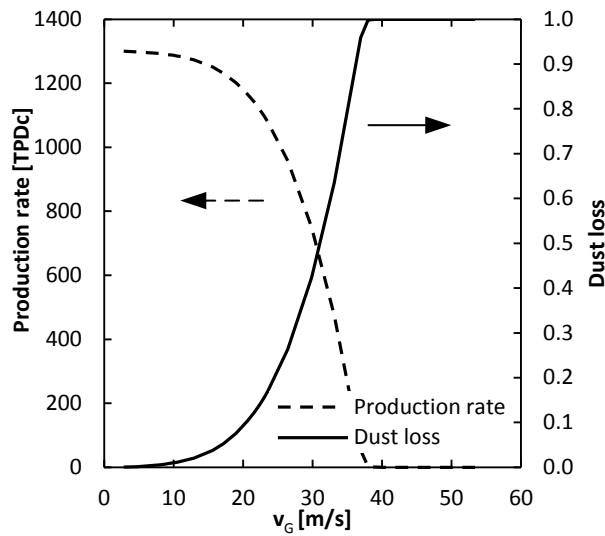


Figure 126 – Dust loss and production rate in tons clinker per day [TPDc] for an upscaled system as a function of the gas velocity in the transport channel at the lowest stage. $T_{G,in} = 850\text{ °C}$, $T_{P,in} = 60\text{ °C}$, $\dot{m}_{P,Feed} = 2000\text{ TPD}$, $c_0 = 1.0$, $N = 4$.

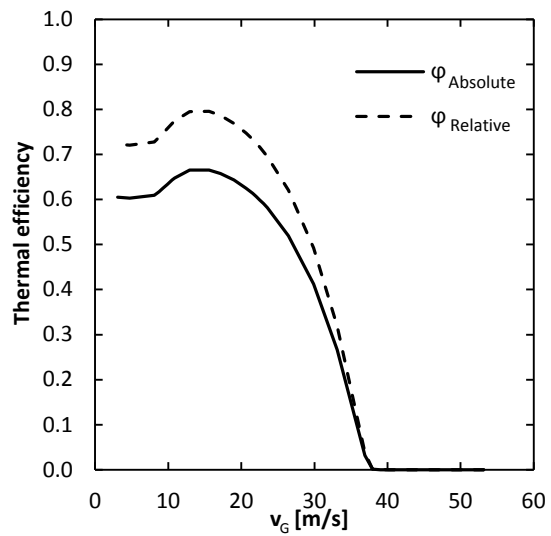


Figure 127 – Thermal efficiencies as a function of gas velocities in the lowest transport channel. $T_{G,in} = 850\text{ °C}$, $T_{P,in} = 60\text{ °C}$, $\dot{m}_{P,Feed} = 2000\text{ TPD}$, $c_0 = 1.0$, $N = 4$.

Instead of designing the system according to the performance of the internal processes, the system could be designed to have the highest production rate in the smallest equipment volume.

The approximate volume of the 2D-HX can be found from $L_{Channel}$.

$$V_{Stack} = H \cdot W \cdot D = (6.5 \cdot L_{Channel} \cdot (N+1)) \cdot (9 \cdot L_{Channel}) \cdot (4 \cdot L_{Channel}) = 19.5 \cdot (N+1) \cdot L_{Channel}^3 \quad \text{Eq. 57}$$

Considering the production rate per equipment volume as a function of the gas velocity yields a selection criterion, as shown in Figure 128 for the 2000 TPD system.

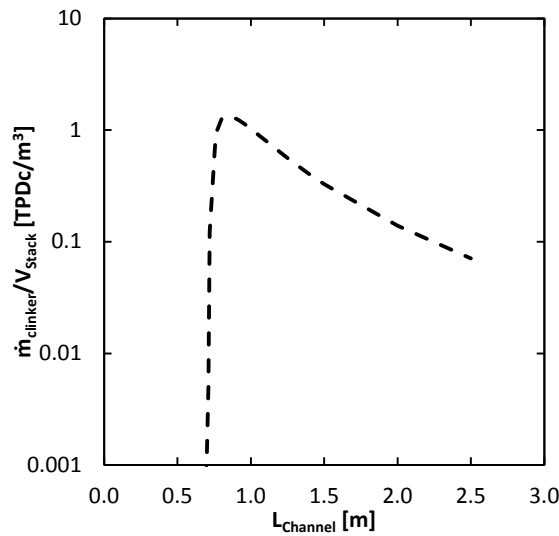


Figure 128 – Clinker production rate per equipment volume as a function of the characteristic length, L_{Channel} . The maximum represents the optimal length for the given conditions in terms of equipment size.

The 2D-HX should be designed to match the optimum of the curve given in Figure 128. However, in some cases, this selection criterion would select systems with dust fractions higher than 15 % – 20 %, which is unacceptable. Therefore the determining criterion will be that the dust fraction should be below 15 %, with as high as possible volumetric production rate. In practice this results in dust losses around 15 %. For the 2000 TPD stack, this leads to $L_{\text{Channel}} = 0.92$ m.

The predicted temperatures and mass flows for a 2000 TPD four stage stack are provided in Figure 129. Table 37 summarizes the operational and design related data.

The particles are heated to around 710 °C, while the exhaust gas leaves at 300 °C. The relative thermal efficiency is 0.72 and the dust loss 14 %. The heat loss is according to the predictions around 6 %. The size of the stack is found to be 30 meters tall, eight meters wide and four meters deep.

The estimated pressure drop is around 41 mbar per stage. For comparison, the cyclone preheater has a pressure drop of 30 – 40 mbar for the entire preheater [3,19]. The estimated pressure drop in the 2D-HX is significantly higher than expected, as gas velocities in the system described here are lower than in the cyclone preheater, why lower pressure drops are expected. This indicates that either the considered geometry induces a significantly higher pressure drop than anticipated, or that the empirical equations used to predict the pressure drop are applied outside their validated range of application, yielding wrong estimations. The latter being the most

likely. Despite the apparent inaccuracy of the pressure drop model, the model will be evaluated for the remaining estimations as well.

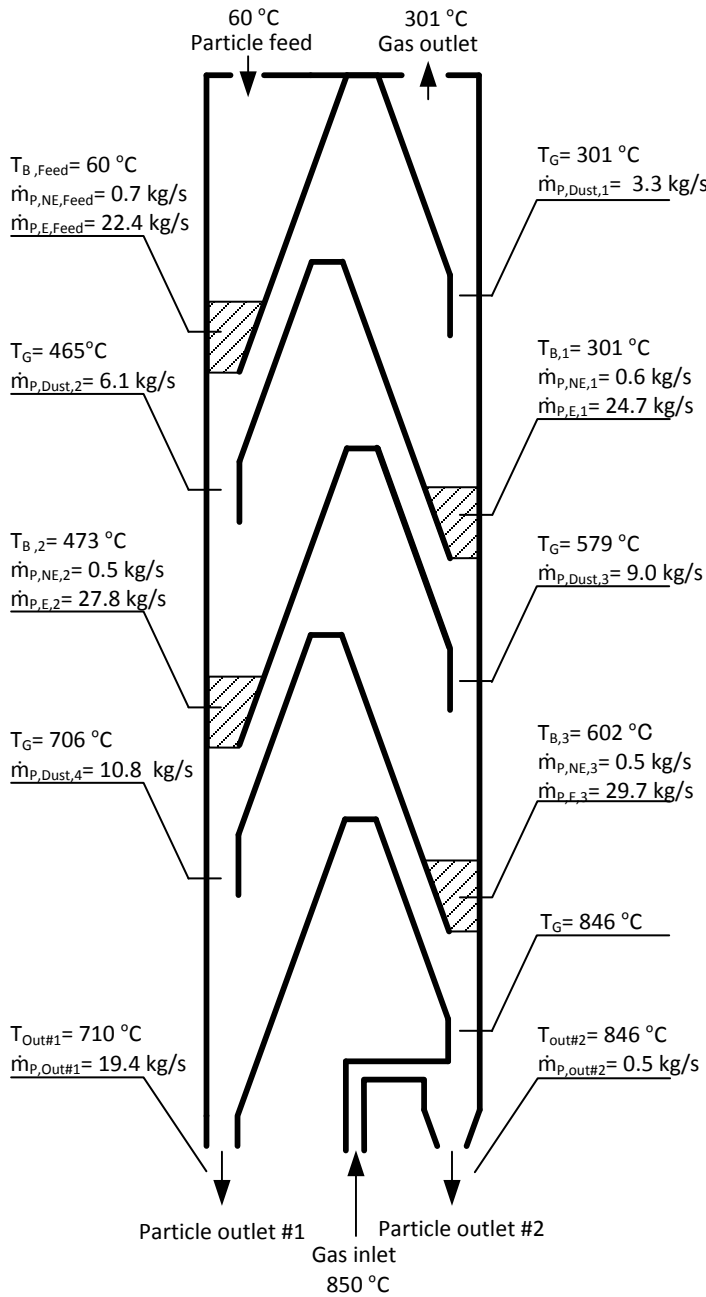


Table 37 – Summarized operational parameters for an upscaled 2000 TPD 2D-HX.

Parameter	Value
$\dot{m}_{P,Feed}$	23.1 kg/s / 2000 TPD
N	4
c_o	1.0
φ_{Abs}	0.60
φ_{Rel}	0.72
φ_{Loss}	5.8 %
$\dot{m}_{P,Clinker}$	12.9 kg/s / 1114 TPD
$v_{g, Channel}$	15 – 23 m/s
Size (H x W x D)	30 m x 8 m x 4 m
Dust loss	14 %
Pressure drop/stage ^A	41 mbar

^A Computed assuming a temperature of 600 °C

Figure 129 – Predicted temperatures and mass flow for a stack with four stages and a particle feed rate of 2000 TPD.

10.2 Full-scale 2D-HX Facilities

The evaluation of full-scale facilities is based on stacks with particle feed rates of 2000 TPD, 4000 TPD, and 6000 TPD. As illustrated in Figure 123, these stacks are the starting point for achieving the desired production capacities. Each stack is designed as described in the previous section. Data for the upscaled 2D-HX facilities are summarized in Table 38.

Table 38 – Predicted operational data for three 2D-HX stack sizes.

Parameter	2000 TPD	4000 TPD	6000 TPD
$\dot{m}_{P,Feed}$	23.1 kg/s / 2000 TPD	46.6 kg/s / 4000 TPD	64.4 kg/s / 6000 TPD
N	4	4	4
c_o	1.0	1.0	1.0
φ_{Abs}	0.60	0.61	0.60
φ_{Rel}	0.72	0.73	0.72
φ_{Loss}	5.8 %	5.9 %	5.8 %
$\dot{m}_{P,Clinker}$	12.9 kg/s / 1114 TPDc	26.2 kg/s / 2262 TPDc	38.7 kg/s / 3347 TPDc
$L_{Channel}$	0.92 m	1.21 m	1.43 m
$T_{P,Out}$	710 °C	710 °C	709 °C
Size (H x W x D)	30 m x 8 m x 4 m	39 m x 11 m x 5 m	46 m x 13 m x 6 m
Dust loss	14 %	15 %	14 %
Pressure drop/stage ^A	41 mbar	60 mbar	77 mbar

^A Computed assuming a temperature of 600 °C. Pressure drop most likely overestimated.

Thus, a facility capable of producing 6000 TPD clinker would consist of approximately five 2000 TPD units, three 4000 TPD units, or two 6000 TPD units.

10.3 Comparison of the Upscaled 2D-HX and Cyclone Preheaters

As highlighted in Chapter 6, one of the major performance parameters for the cyclone preheaters is the transport efficiency. Using the 2D-HX model, the transport efficiencies for the 2000 TPD and the 6000 TPD facilities are predicted. In Figure 130, the data is compared with typical cyclone preheater data.

The performance of the lowest stages is similar in the cyclone preheater and 2D-HX, indicated by a $\eta_{Transport}$ around 0.75 – 0.80, while the top cyclones perform better than the top stages in the

2D-HX, which has maxima around 0.90. Note that the maximum values of $\eta_{Transport}$ for the 6000 TPD facility are around 0.05 higher than for the 2000 TPD stack. The maxima are located around 12 – 15 m/s for the 2000 TPD stack and around 15 – 18 m/s for the 6000 TPD stack.

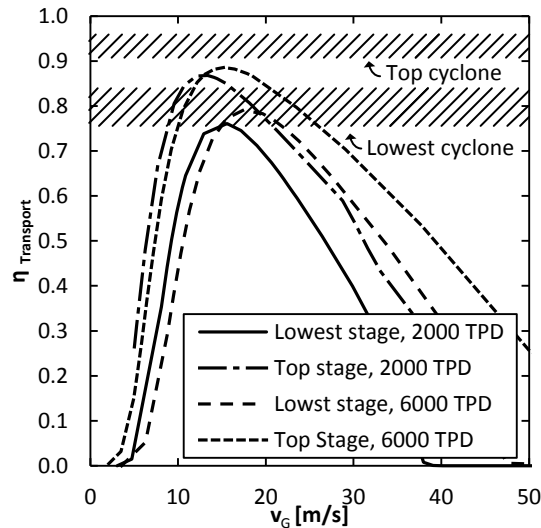


Figure 130 – Comparison of transport efficiencies in two different 2D-HX stacks and cyclone preheaters. 2000 TPD and 6000 TPD particle feed stacks are shown.

Another comparison parameter is the construction height. A graphical comparison of the height of the 2D-HX and the cyclone preheaters are given in Figure 131, displaying a standard tower, a very tall six stage facility, described by Dembla and Mersmann [54], and two 2D-HX facilities. To compensate for the height of the auxiliary equipment an extra height of 15 meters have been added in Figure 131. The 2D-HX preheater is between 40 and 60 % lower. Note that the cyclone preheater structure also contains the calciner, which in some cases is up to 100 meters tall [54], thus the preheating facility is not the only unit dictating the preheater structure height.

To compare the capital costs of the 2D-HX and the cyclone preheaters, the volume of the equipment is used as a quantity proportional to the capital costs. The cyclones are assumed cylindrical with height equal to twice the diameter, which is in line with the findings for cement cyclones as stated in Chapter 2. Ducts and structural support is not included in the cyclone volume estimated. The 2D-HX volume is computed by Eq. 57. The 2D-HX volumes are compared with cyclone data from various sources [8,14,52–55] in Figure 132.

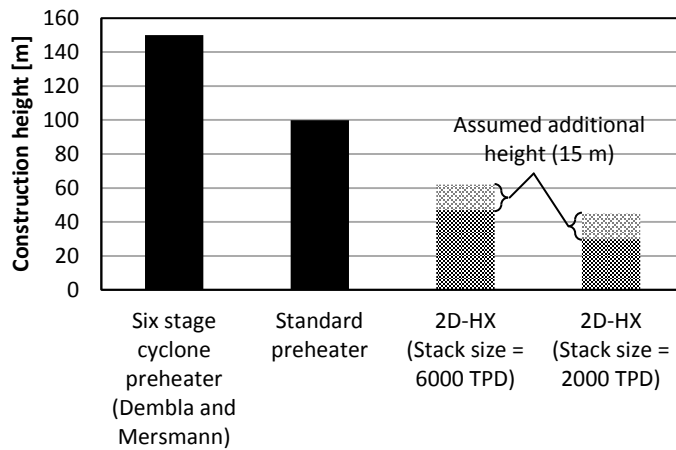


Figure 131 – Comparison of preheater heights. Required additional height for auxiliary equipment for the 2D-HX is assumed to be 15 m. Data from Dembla and Mersmann [54] shown.

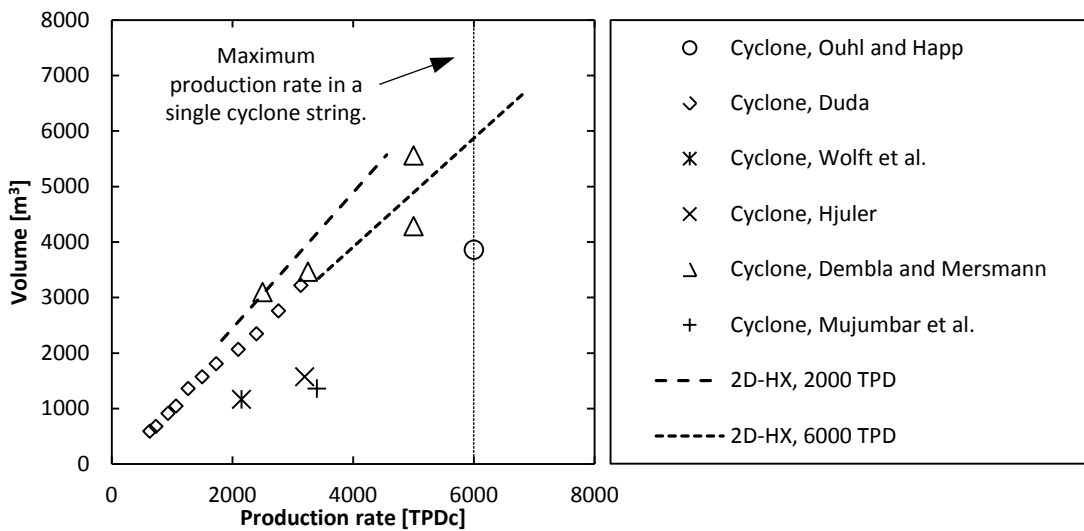


Figure 132 – Comparison of inner volumes for four stage 2D-HX and cyclone preheaters. Two stack sizes are considered for the 2D-HX concept: 2000 TPD and 6000 TPD particle feed rate. Cyclone volumes are estimated from diameters, assuming cylindrical geometry. No ducts are included in the estimates. The maximal single cyclone preheater string production rate is indicated by a vertical line. Cyclone data from Duda [8], Ouhl and Happ [14], Wolff et al.[52], Hjuler [53], Dembla and Mersmann [54], and Mujumbar et al. [55] is provided for comparison.

The variations in the computed cyclone volumes are related to site specific conditions and the cyclone technology at the time of publication. The data of Duda [8] is approximately 30 years old, and the data of Dembla and Mersmann [54] describes a high altitude facility, where low pressure drop and low environmental impact is required. The remaining data indicates smaller volumes of the cyclones.

The two 2D-HX facilities yield different volumes: The lower stack capacity has the higher volume, indicating that the 6000 TPD stack is more feasible than the 2000 TPD. Comparing the 2D-HX and the cyclone volume, the 2000 TPD facility is in the upper range of cyclone sizes, while the 6000 TPD facility is slightly lower than the data of Duda [8] and Dembla and Mersmann [54]. The modern cyclones have smaller volumes than both the 2D-HX facilities considered here, but the volume of the two different technologies is in the same order of magnitude under the given assumptions.

A more detailed cost estimate of both the cyclone preheater and the 2D-HX concept has not been made for several reasons. Especially challenging is the cost of the cyclone preheater support structure, the influence of the calciner on the support structure and cyclone preheater layout, and the detailed design of the 2D-HX: Material thickness, size, and requirements for auxiliary support structure, and connection segments with the remaining of the pyroprocessing system.

Considering clinker production rates of 3000 and 6000 TPDc, a comparison of all relevant parameters between the cyclone preheater and two different preheaters utilizing the 2D-HX concept is given in Table 39. Stack sizes of 2000 TPD and 6000 TPD is considered.

The thermal efficiencies, φ_{Abs} and φ_{Rel} of the 2D-HX are similar to the values for the cyclone preheater, around 0.61 and 0.72, respectively, but are in the lower end of the reported range for the cyclone preheater. The transport efficiencies around 0.10 percentage point lower for the 2D-HX, resulting in a larger dust loss. The gas velocity range, thermal loss, and expected volumes are of similar values, while the height is significantly reduced for the 2D-HX.

As the construction height of the 2D-HX is significantly lower than the cyclone preheaters, it may be feasible to consider adding more stages to the preheater, thereby improving the thermal efficiency and raising particle outlet temperatures. A stack size of 6000 TPD with four to seven stages has been evaluated. The data can be found in Table 40. As the number of stages increases, the both thermal efficiencies increases, averagely 2 % per additional stage caused by increasing particle outlet temperatures and reduced dust loss. On the contrary, the volume and the pressure drop of the system increases proportional to the number of stages.

Table 39 – Comparison of properties of cyclone preheaters and 2D-HX designs.

	Preheater cyclone	Stack size = 2000 TPD	Stack size = 6000 TPD
Number of stacks (3000 TPDc/6000 TPDc)	-	3/5	1/2
φ_{Abs}	0.61 – 0.71	0.60	0.61
φ_{Rel}	0.74 – 0.97	0.72	0.73
Heat loss	~ 4 %	6 %	6 %
$\eta_{Transport}$ at optimal conditions	0.75 – 0.95	0.75 – 0.85	0.66 – 0.88
Dust Loss	5 – 11 %	14 %	14 %
Pressure drop / stage ^A	~ 10 mbar	41 mbar	77 mbar
$v_{g, ent}$	20 – 24 m/s	15 – 23 m/s	18 – 28 m/s
Overall size (H x W x D) (3000 TPDc/6000 TPDc) [m]	80 – 120 m x 10 m x 10 m ^B	30 m x 8 m x 12 m / 30 m x 8 m x 20 m	46 m x 13 m x 6 m / 46 m x 13 m x 12 m
Estimated equipment volume (3000 TPDc/6000 TPDc) ^C	1500 – 3500 m ³ / 3900 – 4300 m ³	2733 m ³ / 4555 m ³	3421 m ³ / 6842 m ³

^A Computed at 600 °C. Model most likely overestimating the pressure drop.

^B The size estimate for entire preheater structure does not depend on production capacity. Specific estimates have not been possible to obtain. The given size also encompasses other process equipment.

^C Volume of cyclones approximated by assumption of cylindrical geometry and a height of 2·D and identical cyclones in all stages.

Table 40 – Overview of the performance of a 6000 TPD stack size for different number of heat exchange stages.

	4 stages	5 stages	6 stage	7 stages	7 stages
Absolute thermal efficiency	0.60	0.63	0.66	0.67	0.66
Relative thermal efficiency	0.72	0.76	0.78	0.81	0.78
Particle outlet temperature	709 °C	735 °C	754 °C	767 °C	768 °C
$L_{Channel}$	1.43 m	1.43 m	1.43 m	1.43 m	1.38 m
Height	47 m	56 m	65 m	74 m	72 m
Volume, approximately	3400 m ³	4100 m ³	4900 m ³	5700 m ³	4900 m ³
Dust loss	14 %	13 %	12 %	11 %	15 %

The last column of Table 40 shows the characteristic of a system designed as a seven stage system, where the other configurations are designed as four stages facilities. It is observed that height can be reduced by a couple of meters, without sacrificing particle outlet temperature.

As stated in Chapter 4, another property of the 2D-HX design is the modular or piecewise construction. This concept is illustrated in the patent application [111] and shown in Figure 133.

The production of the elements of which to construct the 2D-HX can be standardized, thereby obtaining construction cost reductions by series production. Two options exist: Either (a) the elements are produced centrally and thereafter transported to the construction site by ship and/or truck or (b) the elements are produced near the construction site. Principally the simple geometry of the majority of the elements means lower capital cost per equipment volume than for the more complexly shaped cyclones.

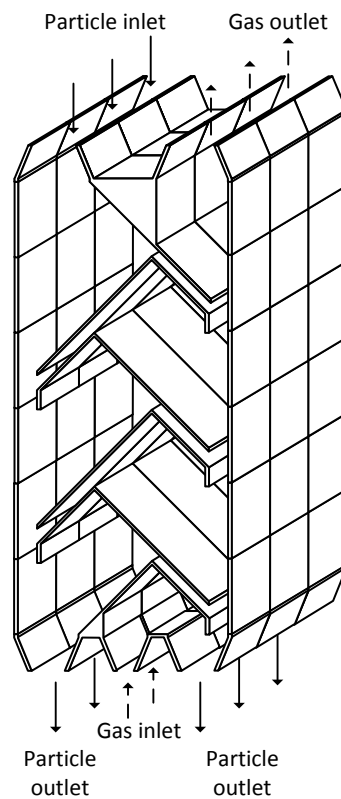


Figure 133 – Example of a piecewise construction of a four stage 2D-HX preheater [111].

10.4 Implementation in a Cement Plant

Implementing the 2D-HX concept into a cement plant requires the plant layout of the pyroprocessing unit to be re-done to incorporate the requirements of the 2D-HX. The layout must be optimized to improve stability and robustness of the process and reduce capital costs. An illustration of the plant layout with a 2D-HX is given in Figure 134. The units are drawn approximately to scale for a 3000 TPD plant with a five stage preheater. Only the major components and ducts are displayed.

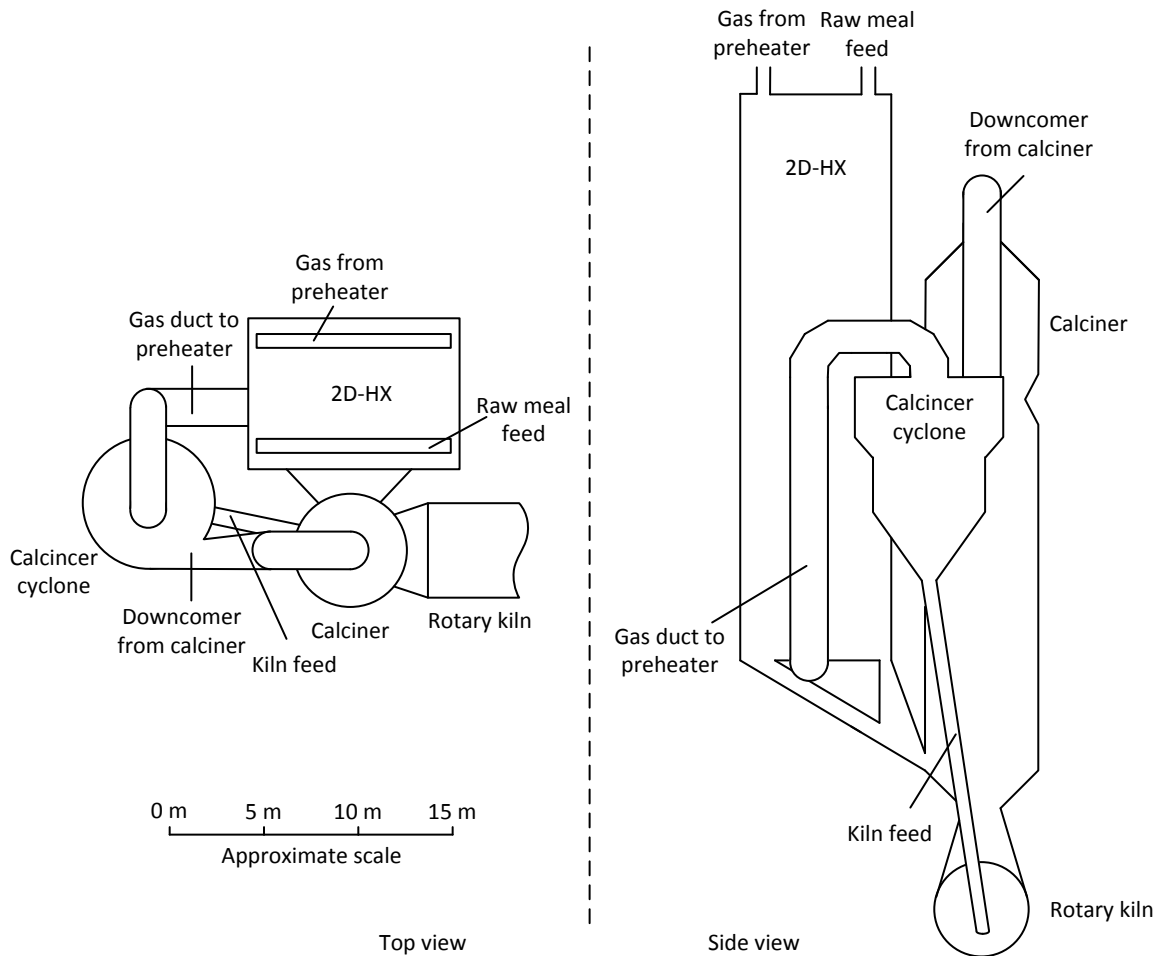


Figure 134 – Schematic drawing showing the integration of the 2D-HX in an 3000TPDc ILC cement plant replacing the cyclone preheater stages. Top and side views are shown. Scale is approximate.

The combustion gases from the kiln are led into the calciner from the cold end of the rotary kiln. From the calciner, gas and particles are led to the calciner cyclone via the calciner downcomer. The gas from the calciner cyclone is then led to the 2D-HX preheater, while the particles are fed to the rotary kiln. Raw meal is fed to the preheater and after preheating into the calciner. The cooled gas from the preheater is typically utilized for drying or heating of raw materials or utilized in a waste heat recovery facility for power production (not depicted in Figure 134).

The illustration given in Figure 134 serves only to provide a starting point for layout discussions, and can undoubtedly be improved by industrial designers and cement plant experts.

10.5 Pilot-Scale Facility

The next phase in the development of the 2D-HX could be to establish a pilot-scale facility. This would allow testing in larger scale and for longer periods of time. To improve the basis for decision, a pilot-scale facility is presented here. The designed pilot-scale facility consists of four stages. The particle feed rate is set to 48 TPD. The predicted operational parameters are given in Table 41.

Table 41 – Predicted operational data for a four stage pilot-scale 2D-HX.

Parameter	Pilot-scale
$\dot{m}_{P,Feed}$	0.56 kg/s / 48 TPD
c_o	1.0 kg/kg
N	4
ϕ_{Abs}	0.61
ϕ_{Rel}	0.73
ϕ_{Loss}	6 %
$\dot{m}_{P,Clinker}$	0.32 kg/s / 27 TPDc
$L_{Chammel}$	0.21 m
$T_{P,Out}$	702 °C
Size (H x W x D) (rounded up)	7 m x 2 m x 1 m
Dust loss	12 %
Pressure drop/stage ^A	6 mbar

^A Computed assuming a temperature of 600 °C. Pressure drop most likely overestimated

An illustration of the size of the existing four stage cyclone pilot-scale preheater at the test center of FLSmidth A/S, Dania, and a 2D-HX with similar performance characteristics are given in Figure 135.

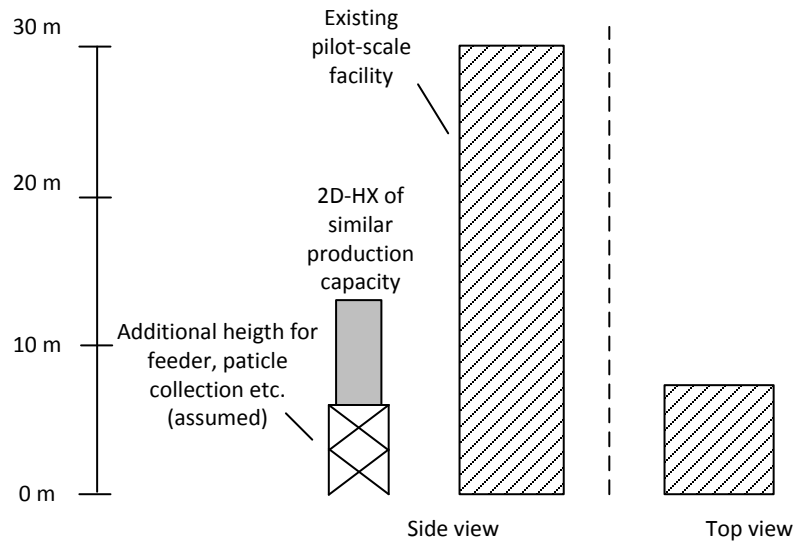


Figure 135 – Comparison of a 2D-HX pilot-scale and the existing pilot-scale facility at FLSmidth.

The existing pilot-scale facility is around 30 – 35 m tall with a foot print of around seven by seven meters and includes four heat exchange cyclones. The structure furthermore includes calciner and exhaust gas stack. These units are included in the structure shown in Figure 135. A structure below the pilot-scale 2D-HX has been added to indicate that additional auxiliary equipment is necessary for the 2D-HX to be operational. The size of the structure displayed is six by four meters and should include feeder, particle handling equipment and structural support.

10.6 Optimization of 2D-HX Design

The 2D-HX design considered and described until this point has been developed conservatively to ensure a successful proof of concept. The design can be optimized in several ways, thereby improving the potential of the 2D-HX. Based on the 2D-HX model and visual observations during the experimental sessions three ways to improve the operation of the 2D-HX is described and evaluated in the following section. The aim of the design changes is to reduce the size of the full-scale facilities by improving the performance.

10.6.1 Alternative Parametric Design

The size of the full-scale facility is obtained from the parametric design, presented in Chapter 9. From the chosen $L_{Channel}$, the equipment height and volume is determined, including the length of the separation chamber, L_{Sep} . The ratio $L_{Sep} / L_{Channel} = 3.5$ used in the experimental work was

determined from the available gas and flow rates. It is expected that the design can be improved by changing this ratio.

To obtain the most compact equipment, the highest gas flow rates possible should be used, and to ensure the best possible separation, L_{Sep} should be highest possible, leading to the conclusion that the higher $L_{Sep} / L_{Channel}$ ratio, the better, with a limitation to the gas velocities in the system, chosen to be similar to the velocities in the cyclone preheater, around 25 m/s. For a 2000 TPD facility, a ratio, $L_{Sep} / L_{Channel} = 4$ and a $L_{Channel} = 0.87$ yields the best performing system. A comparison between the original 2000 TPD facility and the optimized is given in Table 42.

Table 42 – Comparison of original 2000 TPD facility and a facility optimized with respect to the ratio $L_{Sep} / L_{Channel}$.

Parameter	Original	Optimized
$\dot{m}_{P,Feed}$	23.1 kg/s / 2000TPD	23.1 kg/s / 2000 TPD
N	4	4
$L_{Sep} / L_{Channel}$	3.5	4
c_o	1.0	1.0
$\eta_{Transport, bottom stage}$	0.64	0.66
φ_{Abs}	0.60	0.62
φ_{Rel}	0.72	0.74
φ_{Loss}	6.1 %	6.1 %
$\dot{m}_{P,Clinker}$	12.9 kg/s / 1114 TPDc	13.3 kg/s / 1145 TPDc
$L_{Channel}$	0.92	0.87
Size (H x W x D)	30 m x 8 m x 4 m	32 m x 8 m x 3 m
Volume	911 m ³	900 m ³
Dust Loss	15 %	12 %

The optimized 2000 TPD unit has a significantly lower dust loss, higher thermal efficiency, and approximately 1 % smaller volume. The maximum gas velocity in the optimized 2000 TPD facility is 25 m/s.

10.6.2 Addition of Exit Cyclone

To reduce the dust loss, a traditional top cyclone can be installed at the gas outlet of the 2D-HX. The collected dust can be recycled back to the 2D-HX. To reduce the dust loss to desired levels, 5 – 11 %, the top cyclone should have a collection efficiency of 30 – 70 %.

The effect of adding a cyclone is shown in Table 43 assuming that the collected dust is recycled to the bed of stage 1, and collection efficiency of the cyclone is 70 %

Table 43 – Effect of top cyclone mounted on gas exit. Both the optimized and original 2000 TPD facilities are considered.

Parameter	Original		Optimized	
	Standard	With cyclone	Standard	With cyclone
$\dot{m}_{P,Feed}$	23.1 kg/ s / 2000 TPD	23.1 kg/ s / 2000 TPD	23.1 kg/ s / 2000 TPD	23.1 kg/ s / 2000 TPD
N	4	4	4	4
$L_{Separation} / L_{Channel}$	3.5	3.5	4	4
c_o	1.0	1.0	1.0	1.0
$\dot{m}_{P,Clinker}$	12.9 kg/s / 1114 TPDc	14.3 kg/s / 1234 TPDc	13.3 kg/s / 1145 TPDc	14.3 kg/s / 1234 TPDc
$L_{Channel}$	0.92 m	0.88 m	0.87 m	0.81 m
2D-HX Size (H x W x D)	30 m x 8 m x 4 m	29 m x 8 m x 4 m	32 m x 8 m x 3 m	30 m x 8 m x 3 m
Volume	911 m ³	907 m ³ ^A	900 m ³	846 m ³ ^A
Dust loss	15 %	5 %	12 %	5 %
$\eta_{cyclone}$	-	70	-	70

^A Top cyclone with D = 3.6 m and H = 10.8 m assumed [8]. V = 110 m³.

The cyclone reduces the dust loss to 5 %, at the cost of increased pressure drop (not computed), and increases process complexity. The volume reduction achieved by reducing the 2D-HX size is counteracted by the additional cyclone volume, and the final reductions are between one and four percentage. The reduced dust loss enables an increased production capacity of 10 % of the stacks. The gas velocities in the systems are unaffected by the additional cyclone and in the case of the optimized system with cyclone where $L_{Channel}$ has been lowered to 0.81 m, the gas velocities are up to 29 m/s, exceeding the limit of 25 m/s.

A system operating at the maximum velocity limit cannot be reduced in size without violating the velocity criterion. Dust loss can still be reduced, though. The solid load in the stream fed to the cyclones is in the order of 0.1 – 0.2 kg/kg at 300 °C.

10.6.3 Alternative Separation Geometry

As previously mentioned the geometry of the separation chamber in the experimental set-up was determined by the available flow rates, and the angles (70°) of the internal plates were

conservatively chosen to ensure particle flow. Significant height, and thereby volume reductions, can be achieved if these angles can be lowered. The geometric relation between angles of the internal plates and height reductions are given in Figure 136. The reference case is the 70° design.

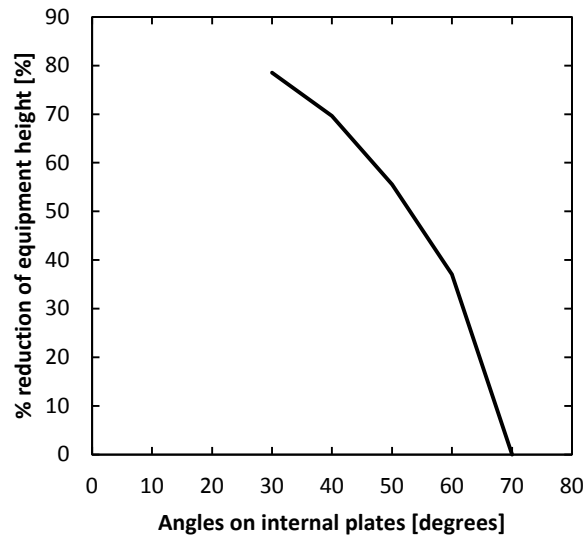


Figure 136 – Height reductions as a function of the angles on the internal plates. The 70° case is used as reference.

If the angles can be lowered to 60°, the height can be reduced with up to 35 % without affecting the gas flow significantly.

In the early experimental versions of the 2D-HX, an angle of 45° was used. This angle was insufficient for raw meal operation, but more than adequate for easier flowing particles, such as sand.

Angles between 55° and 70° should be investigated for raw meal operation as even minor reductions of angles yields significant volume reductions.

Changing the geometry of the plates, not just the angles, may additionally improve operation in terms of lower pressure drop and/or improved separation efficiency. The experimental work, described in Chapter 6, revealed that an inertia driven separation did not take place in the separation chamber with the current design of the internal plates. It was also shown that full

entrainment was readily obtainable at full-scale relevant gas velocities. Therefore a design modification as shown in Figure 137 might be beneficial.

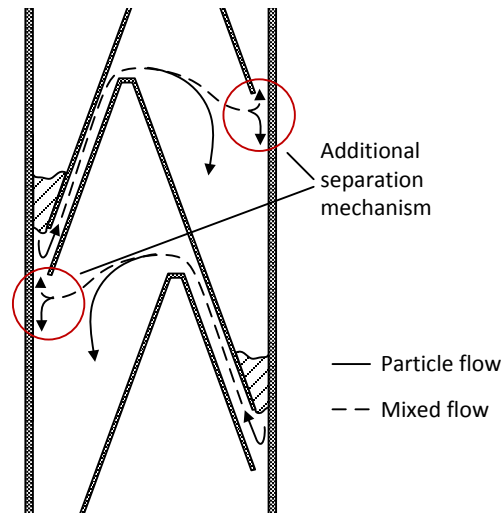


Figure 137 – Suggested design for improved separation efficiency.

The removal of the vertical part of the internal plates will cause the gas and carried particles to impact on the side wall instead of the vertical plate. The gas is forced upward and the particles downward. No crossing of the separated particles and gas flow occurs, contrary to the current design. This is expected to improve separation efficiency, especially at higher gas velocities, while possibly reducing the entrainment efficiency. This design resembles an intermediate design presented in Chapter 4. It was opted out of to increase entrainment efficiency, which, as it turns out, is most likely not necessary.

Other designs of the internal plates can be designed. In order not to deteriorate the separation process, the following criteria should be fulfilled: (a) A sharp edge at the entrance to the separation chamber should be present (the edge creates an eddy with moves particles downward), (b) no obstructions to the gas flow forcing the gas downward when the majority of the particles are still entrained should be installed, and (c) the gas flow should not be forced to cross a flow of already separated particles.

Attention should also be given to horizontal surfaces, where particles will collect. The collected particles will form a pile corresponding to the nearby gas flows, but in a full-scale facility the weight of the pile can be in order of tons on each stage, requiring additional structural strength and possess a safety hazard both during production and maintenance operations.

10.6.4 Summary of Optimizations

The effects of the suggested optimizations on the size of the 2D-HX are quantitatively summarized in Table 44. A reduction of the internal angles of both 5° and 10° has been considered.

Table 44 – Summarization of optimization suggestions.

Suggestion	Estimated volume/cost reduction compared to original design
Addition of cyclone	10 %
Reduction of angle from 70° to 65°/ 60°	20% / 35 %
Optimization of L_D/L_{Sep}	1 – 2 %

The combined effect of the suggested optimizations yields a 30 – 45 % volume reduction of the original design, thereby making the 2D-HX concept significantly more feasible, as estimated volumes of full-scale designs are slightly smaller than the comparable cyclone processes.

Not included in these estimates are the potential savings from series production, simple and planar geometry, and reduced preheating support structure, which further enhances the potential of the 2D-HX concept.

10.7 Identified Issues

In the course of the development and testing of the 2D-HX, and in discussions with relevant people from both industry and academia, potential issues have been identified. In the following, the major issues mentioned during the discussions are described.

Maintaining two dimensional operation

The concept of the 2D-HX requires continuous two dimensional operation, which, as the depth becomes larger, becomes increasingly difficult to maintain. If two dimensional operation cannot be maintained, the flow patterns of gas and particles can pass each other without heat exchanging. Another issue of the two dimensional operation is the operation of the particle gates over a length of several meters. The particle gates should be capable of dosing the same amount of particles per meter of the equipment, taking into consideration local conditions, such as differences in temperature, gas velocity, particle deposition, and particle flowability. The gates

are one of the most critical elements of the 2D-HX technology. Each particle gate should consist of a series of sections, each allowed to move independently of the adjacent sections.

It must be expected that a maximum depth of the system exists, why the two dimensional concept cannot be expanded indefinitely. The exact value for the maximum depth must be determined experimentally, simultaneously evaluating the performance and design of the particle gates. If the desired production rate requires a larger depth than allowable, the stacks must be separated physically.

Inlets and outlets

Another aspect of the two dimensional operation is the design of the inlets and outlets. The gas inlet and outlets should be constructed with manifolds, ensuring an equal gas flow over the entire depth of the heat exchanger. A more pressing issue is the feeding and collection of particles. Designing the feed stage properly, the particles can most likely be fed from few feeding points. The bottom of the piles of raw meal created in the top stage spreads out over the depth of the equipment, thus a particle feeding manifold is not required in the same way as for gas. The collection of the hot particles from the bottom of the 2D-HX is more problematic. The particles should preferably move without mechanical aid into the calciner. To accommodate this, the angle of the particle pipes should be in the range of $60^\circ - 70^\circ$. This means that for each meter the particles need to move sideways, approximately 1.5 – 2.5 meters of height is required. Furthermore, these ducts require additional materials, raising the cost of the 2D-HX. These criteria are also setting a maximum depth for the 2D-HX.

Particle flowability

The operation of the 2D-HX depends highly on the continuous flow of particles in each particle bed. The experiences gathered in present experimental work suggest that the flowability of raw meal is acceptable, and particle flow can be ensured at high temperatures with external means such as vibration.

The experiments carried out did not simulate the presence of neither carbonating nor re-carbonating particles, nor was the temperature high enough for belite formation to start. These reactions influence the flowability of the raw meal, and at temperatures higher than 550°C flowability is deteriorated [140] (see appendix G).

Another aspect not considered is the presence and recirculation of alkali sulfate, typically originating from alternative fuels. The alkali sulfates evaporate in the kiln and condensate at

temperatures below 800 [3]. Between 600 °C and 800 °C a melt is formed, which condensates on the raw meal, thereby reducing the flowability. To ensure a stable particle flow, even during severe deposition, air blasters should be installed, and the dimensions of the design should allow some deposition without blocking.

Thermal resistance of internal plates

The final issue mentioned here is a lifetime issue of the internal surfaces in the 2D-HX. The internal plates separating the chambers are exposed to high temperatures without the possibility for external cooling. Thus, despite isolation protecting the structural elements, the temperatures might reach critical levels. Similar aspects are found for the rotary kilns, where too high shell temperatures are problematic. For the cyclones the heat loss to the surroundings from the outer surface areas protects the structure from overheating.

Normally a layer of refractory lining is installed in the pyroprocessing equipment for thermal and wear protection of the steel structure. The refractory should be installed on all internal surfaces in the 2D-HX, including the undersides of all chamber and channel lofts. On these planar horizontal surfaces, the refractory lining are especially difficult to install and keep in position, according to the industry [53].

10.8 Other Applications

The 2D-HX concept has been developed for heat exchanging the hot combustion gases and cold raw meal particles in the cement industry, but during the development, modifications and additional areas of application have been identified.

In the following some of these are briefly described. The ideas mentioned are not designed in detail, but serves to illustrate potential applications of the 2D-HX given further development.

10.8.1 Co-generation of Power

As stated in Chapter 4, one of the secondary objectives for the 2D-HX is integration of a steam generating circuit for power production with higher efficiency than is obtainable using the exhaust gases from the preheater. The planar geometry of the walls and internal plates are well suited for integration with heating surfaces for steam production, turning the 2D-HX preheater into a three-way heat exchanger.

The steam could be produced counter-current to the gas flow, ensuring maximal outlet temperature and, if needed, additional heating surfaces could be installed at the gas inlet to the 2D-HX. A conceptual drawing is shown in Figure 138.

For a four stage 6000 TPD stack producing 3350 TPDc with $L_{Channel} = 1.43$ m, the area available for heating of a working fluid, including the additional heating surfaces at the gas inlet, is at least 600 m^2 . Additional heating surfaces could be installed in vertical wall elements as well. Installing heating surfaces on the upward facing surfaces should be avoided as deposits will form and reduce the energy transfer significantly.

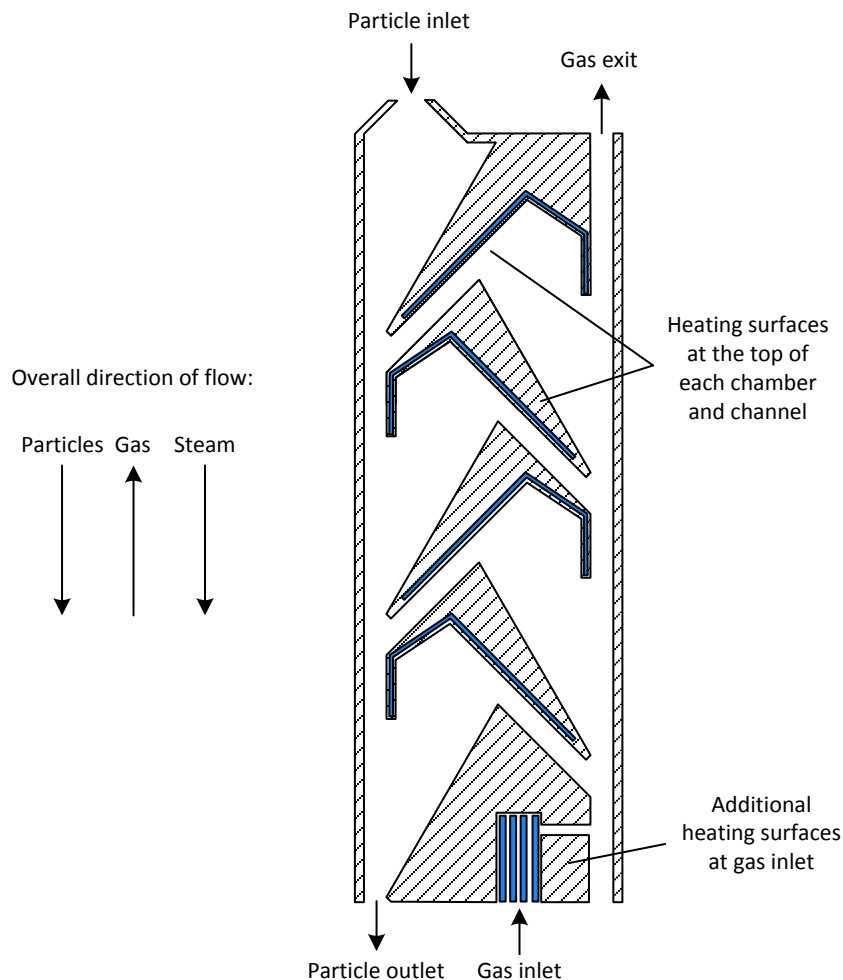


Figure 138 – Schematic drawing of the 2D-HX concept with integrated heating surfaces for steam production.

Estimations show that the overall heat transfer coefficient from the process gas to the steam is in the range of $12 - 16 \text{ W/m}^2/\text{K}$ without significant depositions and neglecting any radiation

contribution, leading to an energy transfer of around 1 MW from the process gas to the steam. For comparison, the gas at the inlet to the preheater contains more than 40 MW of thermal energy. The energy transferred to the stream is not in itself sufficient to produce any significant amounts of power. Instead the 2D-HX in this configuration should work as a superheater, heating the steam used in a WHR system, thereby increasing the efficiency of power generation cycle.

Assuming an inlet temperature to the 2D-HX superheater of 315 °C, a steam flow of 10 kg/s [141], and an energy transfer in the 2D-HX superheater of 1 MW to the steam, the steam can be heated to approximately to 365 °C. Comparing theoretical Carnot efficiencies, assuming a cold reservoir temperature of 40 °C, the efficiency of converting the thermal energy to electricity can be increased from 47 % to 51 %. The additional energy in the stream would also yield an additional increase in power production.

Deposits will form on the heating surfaces, lowering the heat transfer coefficient. Effective values of the overall heat transfer coefficient down to 1 – 5 W/m²/K must be expected during severe deposition. The deposits should periodically be removed, either by air blasters or thermal shedding.

The thermal energy for superheating the working fluid might not be present in adequate quantities at the current conditions in the preheater and additional thermal energy must be supplied. Assuming this additional fuel is alternative fuels, cheap power can be made available, and a larger fraction of the power requirements of the cement plant can be covered, thereby reducing operation costs.

An advantage besides generating power is the temperature reduction of the internal surfaces, which reduces the thermal wear and increases lifetime, as well as eliminates the requirement of refractory lining on some of the downward facing surfaces. Some of the drawbacks of integrating steam and power production are increased process complexity and capital costs. Another issue to consider is conservatism of the cement producers towards integrated processes and radically different technologies.

10.8.2 Integration of Calciner/Combustion Chamber

The 2D-HX can be equipped with a combustion chamber below the lowest heat exchange stage. This combustion chamber can either supply additional thermal energy for heat exchange purposes, including steam generation mentioned previously or act a calciner, thereby replacing the separate calciner and calciner cyclone. The expected advantages of the integrated calciner

include increased fuel particle residence time, reduced construction costs, and simpler plant layout.

The particles combust in the freeboard under suspension fired conditions, similar to the current calciner.

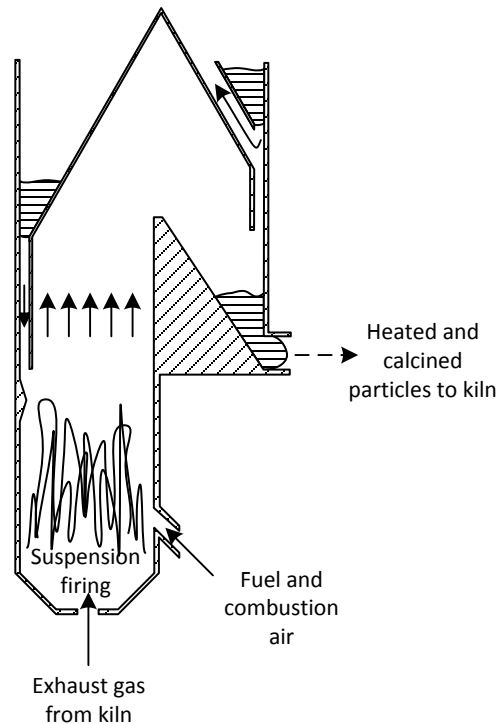


Figure 139 – Illustration of the 2D-HX preheater with a combustion chamber integrated in the bottom of the preheater stack.

10.8.3 Application for drying purposes

The 2D-HX concept might also be adapted for drying purposes in a simplified smaller version, providing a simple, low cost solution for drying of e.g. grain and malt.

Typical drying times for wheat are under fluidized bed conditions in the range of milliseconds to seconds [142], while drying in drying chambers are in the range of minutes [143]. The time scale for larger fixed bed in the range of hours [144,145].

Large scale drying is typically performed in large fixed bed, resulting in poor drying performance, and occasional spoiled crops due to insufficient and too slow drying. The safe moisture content in the kernels is 15 wt% on a dry basis [142].

In the 2D-HX, the drying process would create a co-current heat exchange under transport conditions in each stage, enabling a fast and efficient drying process. During the drying process the gas cools, and water content increases, resulting in the dew point might be reached. This is undesirable as drying cannot be undertaken under such conditions, thus from a process point of view, a maximal number of stages exists.

The process should be driven by a compressor, thus operating above atmosphere pressure for simplicity. The heat can be supplied by combustion of natural gas or from an electrical heater.

When drying malt, a dual operation can be achieved, both drying the kernels and separating the rootlets from the kernels.

10.9 Industry Remarks

The comments from the industry regarding the commercial aspects of the 2D-HX preheater are summarized in a strength-weaknesses-opportunities-threats (SWOT) diagram shown in Table 45 [53].

Table 45 – SWOT table summarizing the commercial aspects of the 2D-HX preheater [53].

Technical (internal)	
Strengths	Weaknesses
<ul style="list-style-type: none"> – More compact than cyclone preheater – Self-sustained construction – Pre-cast/pre-manufactured construction elements – Capacities can be increased by adding stacks – Low pressure drop – Lower heat loss due to compact structure – Lower false air entrainment – Easier access for maintenance – Integrated membrane walls for superheating of steam 	<ul style="list-style-type: none"> – Large area of internal flow divider plates – Thermal stresses in square design – Subject to material build-ups – Operation of mechanical valves required – Exit gas cyclone required – Process control more complicated – Split of material feed to 2D HX stacks – Layout of piping to calciner/kiln
Customers/Competition (external)	
Opportunities	Threats
<ul style="list-style-type: none"> – Lower building height of preheater – Lower civil construction costs – Lower power consumption – Easy retrofit of preheater capacity – Higher steam temperature for higher electricity generation efficiency 	<ul style="list-style-type: none"> – Further development of cyclone preheater design – “Shaft preheater design” conceived as outdated

Generally the positive aspects focus on reduced capital costs, lower construction height, and possibility for superheating of steam, while the negative aspects are related to the construction of the internal plates, mechanically operated particle gate, and layout of piping and ducts.

10.10 Summary

The full-scale 2D-HX for application in a cement plant as a preheater was evaluated. Based on three different particle feed rates (2000 TPD, 4000 TPD, and 4000 TPD), three stacks were designed. The design criterion, determining the characteristic width of the transport channel, was chosen to ensure dust fraction lower than 15 %, with as high production rate per equipment volume as possible. Applying these criteria, a $L_{Channel}$ for the 2000 TPD facility were determined to be 0.93 m, yielding a 30 m tall structure. The 6000 TPD facility was found to be 47 meters tall and $L_{Channel} = 1.45$ m.

A comparison between a full-scale 2D-HX for application in a cement plant and the standard cyclone preheater revealed that the 2D-HX have (a) 4 – 10 percentage point higher dust loss, (b) similar thermal efficiencies, (c) 40 – 60 % lower construction height, (d) around 10 percentage point lower transport efficiency, and (e) comparable equipment volume. Taking the equipment volume as a measure of the capital costs, the capital costs of the two types of heat exchangers have thus been found to in the same order of magnitude.

The pressure drop was computed for the 2D-HX facilities using the model developed in Chapter 8, and found to be in the range of 41 – 77 mbar per stage, which were higher than anticipated. The gas velocities in the 2D-HX are lower than the in cyclone preheater, but the computed pressure drops of the 2D-HX is multiple times larger, which indicates that the applied model might not represent the actual pressure drop correctly.

Suggestions for optimization of the separation chamber geometry were provided. The most significant height and volume reductions could be obtained by reducing the angle of the internal plates. As example, a reduction from 70° to 60° yielded a height and volume reduction of up to 35 %. Other suggestions included varying the parametric design, especially the ratio $L_{Sep} / L_{Channel}$, which yielded improvements in the order of 1 – 3 %, both for thermal performance and for volume. Larger improvement could be made, but gas velocities increased to values above 25 m/s, which were evaluated as too high in terms of wear and pressure drop.

Adding a top cyclone at the gas stream from the 2D-HX was also considered. This reduced the dust fraction significantly, and increased the production rate about 10 % without, while the volume was not reduced. The cyclone increases pressure drop and process complexity.

Applying the suggested optimizations to a full-scale 2D-HX preheater, volume reductions of between 30 and 45 % were found, thereby making the full-scale 2D-HX smaller than the cyclone preheaters with similar dust loss, thermal performance, and lower construction height. In this estimate, the possible cost reductions of reduced preheater support structure, simple geometry, and series production of the 2D-HX have not been included.

Generally, the current estimates show that overall the 2D-HX and a modern cyclone preheater are more or less comparable in thermal performance and dust loss, while the 2D-HX is expected to be more complicated to control but significantly lower.

The estimates given in the present chapter illustrate the expected behavior of the 2D-HX at the current level of process understanding. The 2D-HX model has been used to predict the full-scale facility mass and temperature flows. As stated in Chapter 9, this assumes that the model can be used across a scale ratio of 1000.

Chapter 11

Conclusions and Outlook

“Discussion is just a tool. You have to aim; the final goal must be a decision”

– Harri Holkeri, former Prime Minister of Finland

The main objective of present work has been to develop and test a gas/solid heat exchanger, which could be used as a preheater in the cement industry replacing the cyclone-based processes used today.

The work has been initiated by a review of previous and current preheating technologies, which revealed that the cyclone-based preheaters in terms of operational efficiency and stability are the other suspension preheating processes superior. During the development of the cyclone preheater technology in the 1950s – 1970s, several alternative concepts including shaft preheaters were investigated, and opted out of due to too high energy consumption. For the shaft preheater, the major issue identified was the large internal recycling of particles and poor separation.

The standard preheating facility today consists of a five stage preheater facility with an inline calciner (ILC). The operational parameters of interest are the thermal energy consumption, pressure drop, lifetime, and capital costs.

Using a model, based on mass- and energy balances for the cyclone-based preheating process, it has been found for five actual preheater configurations that between 61 and 71 % of the thermal energy in the inlet gases were transferred to the raw meal particles before being fed to the calciner, and that this corresponded to between 74 and 97 % of the maximal energy transfer possible.

Following the literature review and analysis of the cyclone preheaters, several design suggestions for an alternative to the cyclone preheater have been made. Of these, the most

promising was the two-dimensional heat exchanger (2D-HX), which performed the heat exchange between gas and particles in a similar process as the cyclone preheaters but in a more compact structure, and using a different particle-gas separation technique. The major design features of the 2D-HX were a modular construction, planar geometries, compact structure, easy scaling, and a two-dimensional design.

The 2D-HX has been tested in three different set-ups: Single-stage set-up, Multi-stage set-up, and proof of concept (PoC) set-up. The experimental work was aimed at three targets: (a) Investigating the two internal processes, the separation and the entrainment, (b) achieving a proof of concept at industrial conditions, and (c) providing data for modeling purposes.

The experimental data indicated that the separation process is determined by a mechanism described as accelerated settling, where particles settled in ropes or clusters thereby allowing a higher settling velocity (0.5 – 1.5 m/s), than anticipated from the settling velocities given by Stokes Law of settling (< 0.01 m/s).

Applying an analysis of variance (ANOVA) on the separation data, only the gas velocity has been found to influence the process, but evidence, in form of visual observations and a few data points obtained as low gas velocities ($v_G < 2$ m/s), indicated that solid load also influenced the separation process. The separation efficiency decreased with increasing gas velocities.

Analyses of the data describing the entrainment process showed that the entrainment is improved by increasing gas velocities.

Separation and entrainment efficiencies have been found comparable in all three set-ups, despite powder and operational conditions were slightly different. Compared to the cyclone preheater, the transport efficiency, defined as the product of the separation and entrainment efficiencies, were 10 – 20 % lower in the 2D-HX.

During experiments with inlet gas temperatures around 800 °C, it has been showed, that the system could be operated satisfactorily, heating particles to around 500 °C – 550 °C in a four stage heat exchange process. Heat loss, pressure drop, and thermal efficiencies have been evaluated. The thermal efficiencies were around 20 % lower than found for the cyclone preheaters, caused by larger dust losses, slightly lower inlet temperature difference, and larger heat loss.

The flowability of the raw meal has been investigated both in situ during hot operation of the PoC set-up and in a separate monoaxial shear tester. Results from both set-ups indicated that

flowability deteriorated at temperatures from around 500 °C and up, probably due to the sintering the raw meal caused by the initiating belite formation.

The internal processes in the 2D-HX have been modeled by considering the system analogous to a pneumatic transport system. The separation mechanism has been modeled by salting out mechanisms, and the entrainment using pick-up mechanisms. This has been chosen after a screening of several relevant model suggestions. Each internal process model contained two fitting parameters. The overall system has been modeled using mass- and energy balances.

To estimate full-scale parameters, the relevant scaling parameters have been identified using inspectional analysis and dimensional analysis. The resulting parameters were Re , Stk , Fr , PSD , L_{sep}/L_D , ρ_G/ρ_p , and c_0 , of which only one of the parameters Re , Stk , Fr could be chosen. A screening showed that only using Fr , competitive full-scale parameters could be achieved. Therefore Fr , PSD , L_{sep}/L_D , ρ_G/ρ_p , and c_0 have been assumed applicable as scaling parameters.

Using the model, predictions of full-scale 2D-HX-based preheaters indicated that the capital cost, estimated as the equipment volume, is in the same order of magnitude as the cyclone-based preheaters. The most modern cyclone-based preheaters have according to a direct comparison up to 30 – 40 % smaller volumes, however. Furthermore, the comparison has revealed that dust loss was higher in the 2D-HX, the thermal efficiencies comparable, and the height of the 2D-HX is 40 – 60 % lower than the cyclone-based preheater facilities. The overall size of a 3000 TPDc 2D-HX preheater was 46 x 13 m x 6 m.

Suggestions for optimizing the 2D-HX have been provided, potentially reducing the volume of the full-scale 2D-HX with between 30 and 45%, thereby making the 2D-HX smaller than the cyclone preheater facility, and reducing dust loss to 5 %.

Possible additional reductions of capital costs associated to the reduced preheater structural support structure, the simple planar geometry of the 2D-HX, and the series production have not been quantified.

Furthermore, the 2D-HX may be integrated with other processes in the cement plant, such as waste heat recovery and the calciner, thereby providing alternatives, which are not possible with the current cyclone design.

11.1 Outlook and Future work

A significant work before commercialization of the 2D-HX can be achieved, still lies ahead. Future investigation and development of the 2D-HX concept could progress as follows:

1. Application of computational particle fluid dynamic (CPFD) models such as Barracuda®. The experimental data should be used to verify model predictions, where after full-scale facilities can be investigated. The model could also be used to verify the selection of scaling parameters chosen in present work.
2. Based on model results and present work, a pilot-scale 2D-HX facility should be constructed. Subsequently continuous testing of process performance, stability, and control should be performed. Overall design and operational parameters have been suggested in section *10.5 – Pilot-Scale Facility*.
3. Installation of 2D-HX on a side-stream in a cement plant for testing under actual plant conditions.

This author recommends that at least the 2D-HX is sought described using CPFD, and full-scale characteristic and performance are re-evaluated before any further decisions are taken regarding the application of this technology. The overall evaluation of whether or not the 2D-HX is competitive with the cyclone preheater should not be made at current time.

Academically, the following are suggested as follow-ups on the present work:

- Establishment of flexible particle-gas equipment test facility, containing particle feed and dust handling systems, which would allow test of alternative geometries of the internal plates for use in the 2D-HX, thereby optimizing the performance and reducing costs.
- Development of a more suitable powder flowability evaluation method, as very little work has been made on the topic of temperature dependent powder flow properties. The influence of alkali condensation, raw meal size distribution, and CO₂ content in the gas are obvious subjects for investigation.
- Identification of other areas of application of the 2D-HX, and execution of detailed evaluations, including modeling and experimental work, for the application in other industries, such as drying of grain or malt.

Cited Literature

- [1] European IPPC Bureau, Reference Document on Best Available Techniques in Cement, Lime, and Magnesium Oxide Manufacturing Industries, 2013.
- [2] TensorCrete, Environmental Impact of Cement Production (<http://tensorcrete.com/>), Accessed August, 2013.
- [3] J.I. Bhatti, Innovations in Portland Cement Manufacturing, Portland Cement Association, ISBN: 9780893122713, 2004.
- [4] FLSmidth A/S, Dry Process Kiln Systems, Sales Material, 2009.
- [5] P. Hewlett, Lea's Chemistry of Cement and Concrete, 4th ed., John Wiley & Sons Inc, New York, ISBN: 9780750662567, 2003.
- [6] A. Nielsen, Combustion of Large Solid Fuels in Cement Rotary Kilns, Ph.D. thesis, Technical University of Denmark, Kgs. Lyngby, ISBN: 9788792481665, 2012.
- [7] S. Telschow, Clinker Burning Kinetics and Mechanism, Ph.D. thesis, Department of Chemical and Biochemical Engineering, Technical University of Denmark, ISBN: 9788792481788, 2013.
- [8] W.H. Duda, Cement Data Book, 3rd ed., Bauverlag GmbH, Weisbaden und Berlin, ISBN: 9783762501800, 1985.
- [9] World Coal Association, Coal & Cement (<http://www.worldcoal.org/coal/uses-of-coal/coal-cement/>), Accessed August, 2013.
- [10] Cement Engineering Design, Cement Engineering Design (<http://en.sinoma.cn/>), Accessed September, 2013.
- [11] Cement Sustainable Initiative, GNR Project Reporting CO2 (<http://www.wbcscement.org/>), Accessed August, 2013.
- [12] ICR Research, Welcome to the new Builds (1), International Cement Review, 1, 2013.
- [13] E. Worrell, L. Price, N. Martin, Carbon Dioxide Emissions from the Global Cement Industry, Annual Review of Energy and the Environment, 2001.
- [14] J. Ouhl, K. Happ, Building the World's Largest Kiln Line, in: IEEE Tech. Conf., 2007: pp. 103–113.

- [15] The European Cement Association, Cement industry - Main Characteristics (<http://www.cembureau.be/>), Accessed August, 2013.
- [16] FLSmidth A/S, Company Announcements (www.FLSmidth.com), Accessed September, 2013.
- [17] O.G. Lellep, Process of and Apparatus for Treating Cement and Similar Materials, Patent no. US1992704, 1929.
- [18] N.A. Madlool, R. Saidur, M.S. Hossain, N.A. Rahim, A critical review on energy use and savings in the cement industries, *Renewable and Sustainable Energy Reviews*, 15, 2042–2060, 2011.
- [19] P.A. Alsop, *The Cement Plant Operations Handbook*, Fifth edit, Emirates Printing Press, 2007.
- [20] A.C. Hoffmann, L.E. Stein, *Gas Cyclones and Swirl Tubes*, 2.Edition ed., ISBN: 9873540746942, 2007.
- [21] D. Leith, D. Mehta, Cyclone Performance and Design, *Atmospheric Environment*, 7, 527–549, 1973.
- [22] C.J. Stairmand, The Design and Performance of Cyclone Separators, *Transactions of the Institution of Chemical Engineers*, 29, 356–383, 1951.
- [23] P. Swift, Dust Control in Industry, *Steam and Heating Engineer*, 38, 453–456, 1969.
- [24] C.E. Lapple, Processes use many Collector Types, *Chemical Engineering*, 58, 144–151, 1951.
- [25] W. Barth, Berechnung und Auslegung von Zyklonabscheidern auf Grund Neuerer Untersuchungen, *Brennstoff-Wärme-Kraft*, 8, 1956.
- [26] R.M. Alexander, *Fundamentals of Cyclone Design and Operation*, Australian Institute of Mining and Metallurgy, 203–228, 1949.
- [27] M. Trefz, E. Muschelknautz, Extended Cyclone Theory for Gas Flows with High solids Concentrations, *Chemical Engineering & Technology*, 16, 153–160, 1993.
- [28] E. Muschelknautz, Die Berechnung von Zyklonabscheidern für Gase, *Chemie Ingenieur Technik*, 63–71, 1972.
- [29] C. Lapple, Gravity and Centrifugal Separation, *American Industrial Hygiene Association Quarterly*, 37–41, 1950.

-
- [30] D. Leith, W. Licht, The Collection Efficiency of Cyclone Type Particle Collectors - a New Theoretical Approach, *AIChE Symposium Series* 68, 196–206, 1972.
- [31] C. Cortes, A. Gil, Modeling the Gas and Particle Flow Inside Cyclone Separators, *Progress in Energy and Combustion Science*, 33, 409–452, 2007.
- [32] J.R. Grace, A.A. Avidan, T.M. Knowlton, *Circulating Fluidized Beds*, Blackie Academic & Professional, Chapman & Hall, London, 1997.
- [33] E. Muschelknautz, W. Krambrock, *Aerodynamische Beiwerte des Zyklonabscheiders aufgrund neuer und verbesserter Messungen*, Chemie Ingenieur Technik, 1970.
- [34] E. Muschelknautz, K. Brunner, *Untersuchungen an Zyklonen*, Chemie Ingenieur Technik, 1967.
- [35] K.H. Clement, P. Fangel, A.D. Jensen, K. Thomsen, *Kemiske enhedsoperationer*, Polyteknisk forlag, ISBN: 9788750209416, 2004.
- [36] R. Dewil, J. Baeyens, B. Caerts, CFB cyclones at High Temperature: Operational Results and Design Assessment, *Particuology*, 6, 149–156, 2008.
- [37] A.C. Hoffmann, A. Van Santen, R.W.K. Allen, R. Clift, Effects of Geometry and Solid Loading on the Performance of Gas Cyclones, *Powder Technology*, 70, 83–91, 1992.
- [38] A. C. Hoffmann, H. Arends, H. Sie, An Experimental Investigation Elucidating the Nature of the Effect of Solids Loading, *Proceedings of the Filtration Society*, 188–193, 1991.
- [39] F.L. Fassani, L. Goldstein Jr., A Study of the Effect of High Inlet Solids Loading on a Cyclone Separator Pressure Drop and Collection Efficiency, *Powder Technology*, 60–65, 2000.
- [40] K.W. Chu, B. Wang, D.L. Xu, Y.X. Chen, A.B. Yu, CFD–DEM Simulation of the Gas–Solid Flow in a Cyclone Separator, *Chemical Engineering Science*, 66, 834–847, 2011.
- [41] V. Bricout, M.Y. Louge, Measurements of Cyclone Performance under Conditions Analogous to Pressurized Circulating Fluidization, *Chemical Engineering Science*, 59, 3059–3070, 2004.
- [42] B. Wang, D. Xu, K. Chu, A. Yu, Numerical Study of Gas–Solid Flow in a Cyclone Separator, *Applied Mathematical Modelling*, 30, 1326–1342, 2006.
- [43] T. Tawari, F. Zenz, *Evaluating Cyclone Efficiencies From Stream Compositions*, Chemical Engineering, 1984.
-

- [44] F.A. Zenz, *Manual on Refinery Wastes: Volume on Atmospheric Emissions*, API Publication, Madison, 1975.
- [45] K. Tuzla, J. Chen, *Performance of a Cyclone Under High Solid Loadings*, AIChE Symposium Series, 1992.
- [46] R. Wolff, S. Alesi, S. Miller, *Applying Modern Technology in a Step by Step Approach to Improve the Capacity and Efficiency of a Preheater/calcliner Kiln System*, Cement Industry Technical Conference, 1995. XXXVII, 1995.
- [47] H.P. Elkjaer (FLSmidth A/S), *Cyclone*, Patent No. US4848993, 1987.
- [48] M.K. Hansen (FLSmidth A/S), *Cyclone Separator*, Patent No: US7841477B2, 2006.
- [49] KHD Humboldt Wedag, *Burning Technology Preheater*, Sales Material, 2012.
- [50] F. Colaiacovo, *First Successful Installation of Hurriclon in Preheater*, International Cement and Lime Journal, 2000.
- [51] ATec, *World Leader in Cement Pyroprocess Technology*, 2012.
- [52] R. Wolff, S. Alesi, S. Miller, *Improved Preheater/calcliner Efficiency and Capacity*, World Cement Conference, 26, 2–15, 1995.
- [53] K. Hjuler, *Personal contact*, FLSmidth A/S, 2012.
- [54] A. Dembla, M. Mersmann, *Experiences with the Design of Large Size Cement Plants - Process and Layout Considerations in Pyroprocess Systems*, Cement Industry Technical Conference, 2007.
- [55] K. Mujumdar, K. Ganesh, S. Kulkarni, V. Ranade, *Rotary Cement Kiln Simulator (RoCKS): Integrated modeling of pre-heater, calciner, kiln and clinker cooler*, Chemical Engineering Science, 62, 2590–2607, 2007.
- [56] S. Bernardo, M. Mori, A.P. Peres, R.P. Dionísio, *3-D computational Fluid Dynamics for Gas and Gas-particle Flows in a Cyclone with Different Inlet Section Angles*, Powder Technology, 162, 190–200, 2006.
- [57] J.P. Hansen, *SO₂ Emissions from Cement Production*, Ph.D. thesis, Technical University of Denmark, Kgs. Lyngby, ISBN: 8790142969, 2003.
- [58] X. Delong, H. Daohe, *Characteristics of Momentum and Heat Transfer between Gas and Particles in a Transport Bed*, Fluidization '85: Science and Technology, 445–455, 1985.
- [59] M.H. Rasmussen, *Low SO₂ Emission Preheater for Cement Production*, Technical University of Denmark, 2011.

-
- [60] A.W. F. Strauss, E. Steinbiss, Measurement of Retention Times in Cement Burning Systems with the Aid of Radionuclides, *ZEMENT-KALK-GIPS*, 40, 441–446, 1987.
- [61] European IPPC Bureau, Reference Document on Best Available Techniques in the Cement, Lime and Magnesium Oxide Manufacturing Industries, 2010.
- [62] E.S. Jøns, Personal contact, FLSmidth A/S, 2011.
- [63] B. Klotz, New Developments in Precalciners and Preheaters, in: *IEEE Cem. Ind. Conf.*, Ieee, ISBN: 0-7803-3962-2, 1997: pp. 255–280.
- [64] M. Mirolli, The Kalina Cycle for Cement Kiln Waste Heat Recovery Power Plants, *Cement Industry Technical Conference*, 330–336, 2005.
- [65] J. Harder, Latest Waste Heat Utilization Trends in Cement Plants, *ZKG INTERNATIONAL*, 2013.
- [66] ThyssenKrupp Polysius, DOPOL '90 Preheater and PREPOL Calcining System, Sales Material, 2013.
- [67] S. Khurana, Energy Balance and Cogeneration for a Cement Plant, *Applied Thermal Engineering*, 22, 485–494, 2002.
- [68] G. Kabir, A.I. Abubakar, U.A. El-Nafaty, Energy Audit and Conservation Opportunities for Pyroprocessing Unit of a Typical Dry Process Cement Plant, *Energy*, 35, 1237–1243, 2010.
- [69] T. Mukherjee, The Efficiency Improvement in Cement Production by Kiln Production Upgrades, Modernization and thus Optimizing Productiity - A step by Step Approach, *International Congress on the Cement Chemistry*, 2003.
- [70] K. Duong, S. Sheikh, F. Vecchio, Seismic Behavior of Shear-critical Reinforced Concrete Frame: Experimental Investigation, *ACI Structural Journal*, 2007.
- [71] ISC Consulting Enginners, Competances - Cement plants, 2013.
- [72] C. Maarup, Personal observation, 2011.
- [73] W. Alexander, Dust Separator, Patent No. US2542634, 1934.
- [74] H.D. Evans (Shell Development Company), Horizontal Centrifugal Separator, Patent no. US2888096, 1955.
- [75] O. Heinemann (Ennigerloh), H.-H. Schmits (Rheda Wiedenbrück), Apparatus for Heat Exchange between Gas and Fine-grained Material, Patent no. US4756093A, 1988.
-

- [76] F. Kraus (Voest-Alpine Aktiengesellschaft), Wärmetauschereinheit zum Vorwärmen von Zementrohmehl, Patent no. EP0038314, 1981.
- [77] T. Hyppanen, R. Kuivalainen (both of Karhula), H. Ollila (Kaunianien), Centrifugal Separator, US Patent 4,647,279, 1994.
- [78] S.W. Miller, Environmental Considerations for Preheater Design, Cement Industry Technical Conference, 169–186, 2002.
- [79] J. Salmento, R. Shenk, Accurately Predicting Cement Plant Emissions, IEEE Cement Industry Technical Conference, 333–344, 2004.
- [80] J. Horton, A. Linero, F. Miller, Use of SNCR to Control Emissions of Oxides of Nitrogen from Cement Plants, Cement Industry Technical Conference, 316–344, 2006.
- [81] FLSmidth, Preheater Calciner Systems, Sales Material, 2013.
- [82] Y.-J. Zhang, Y.-M. Wei, An Overview of Current Research on EU ETS: Evidence from its Operating Mechanism and Economic Effect, *Applied Energy*, 87, 1804–1814, 2010.
- [83] L.H. Gulbrandsen, C. Stenqvist, The Limited Effect of EU Emissions Trading on Corporate Climate Strategies: Comparison of a Swedish and a Norwegian Pulp and Paper Company, *Energy Policy*, 56, 516–525, 2013.
- [84] S.K. Pathi, CO₂ Capture by Carbonate Looping Process, PhD Thesis, Technical University of Denmark, 2013.
- [85] FLSmidth A/S, Course Material - Alternative fuels, 2011.
- [86] FLSmidth A/S, Maintaining a Competitive Edge, Sales Material, 2013.
- [87] T. Engin, V. Ari, Energy Auditing and Recovery for Dry Type Cement Rotary Kiln Systems – A Case Study, *Energy Conversion and Management*, 46, 551–562, 2005.
- [88] D.S. Hansen, Heat Exchanger, Patent no. GB1249632A, FLSmidth A/S, 1968.
- [89] K.J. Sylvest, Apparatus for Heating or Cooling Granular or Powdered Material, Patent no. GB1251572A, FLSmidth A/S, 1969.
- [90] A.W. McClaine, R.W. Breault, A.F. Litka, F.E. Becker (Thermo Power Corporation), Raining Bed Heat Exchanger and Method of Use, Patent no. US5992041A, 1997.

- [91] W. Zimmermann (Metallgesellschaft Aktiengesellschaft, Frankfurt/M), J. Röder (Carl Schenck Maschinenfabrik), Vorrichtung zum Kühlen von heißem, kleinstückigem Gut, Patent no. DE1082607, Germany, 1956.
- [92] H. Dorst, Contra-flow Direct Heat-exchanger Preheating Fine Granular Material, Patent no. DE4300011A1, 1994.
- [93] G. Albertus, Method of and Apparatus for Exchanging Heat Between Solid Particles and Gases, Patent no. GB1039470A, FLSmidth A/S, 1963.
- [94] G. Albertus, Method of and Apparatus for Exchanging Heat Between Solid Particles and Gases, Patent no. GB1038965, FLSmidth A/S, 1963.
- [95] FLSmidth, Internal report: Area of Focus for Alternative Preheater Design, Unpublished, 1983.
- [96] V.R. Bohman, Neuere Rohmehlvorwärmer für Drehöfen, ZEMENT-KALK-GIPS, 12, 1965.
- [97] H. Dauha, G. Dagong, L. Changyong, Research on Working Principle of Krupp (Shaft) Preheater, Journal of The Chinese Ceramic Society, 1987.
- [98] H. Deussner, Apparatus for Conduction Physical and-or Chemical Reactions between Gases and Fine-grained Solids, Patent no. AU2109870A, Klockner-Humboldt-Deutz, 1969.
- [99] H. Deussner, Einrichtung zur Durchführung physikalischer und/oder chemischer reaktionen zwischen Gasen und feinkörnigen Feststoffen, insbesondere zur Vorerhitzung von Zementrohmehl, Patent no. DE2040667A1, Klockner-Humboldt-Deutz, 1970.
- [100] J. Schuler, Apparatus for Effecting a Direct Heat Exchange between a Fine-grained or Pulverulent Material and a Hot Gas, Patent no. GB1224638A, Polysius, 1968.
- [101] J. Mamok, Apparatus for Contacting a Finely divided Material with a Hot Gas, Patent no. GB1297185A, Wedag Westfalia Dinnendahl, 1969.
- [102] D. Geldart, Types of Gas Fluidization, Powder Technology, 7, 285–292, 1973.
- [103] N. Jordison (Bulk-Flow Technologies), Indirect-heat Thermal Processing of Particulate Material, Patent no: WO128104A1, 2007.
- [104] R.H. Perry, D. Green, Perry's Chemical Engineers' Handbook, Eight Ed., McGraw-Hill, ISBN: 9780071422949, 2008.

- [105] Y. Chen, Y. Hu, D. Xu, F. Zhao, The Theoretical Investigation on the Thermal Efficiency of Tri-strings Suspension Preheater System, *Journal of Xi'an University of Arch & Tech*, 2007.
- [106] P. Yang, N. Liu, Study and Analysis of Cyclone Preheater Thermal Efficiency, *Sichuan Building Materials*, 2010.
- [107] Y. Zhou, L. Ma, Y. Shi, Solids Circulation Rate of Ultra-fine Powders in Spouted Bed with Draft Tube, *Journal of Chemical Industry and Engineering*, 2004.
- [108] K. Hjuler, Personal contact, FLSmidth A/S, 2010.
- [109] R. Gartside, H. Woebcke, Low Residence Time Solid-gas Separation Device and System, Patent no. US4433984, Stone & Webster Engineering Corp., USA, 1984.
- [110] BILLY, IKEA (<http://www.ikea.com>), Accessed August, 2013.
- [111] K. Dam-Johansen, C.M. Rasmussen, An Apparatus for Conduction Physical, Chemical, or Biological Interaction between Gases and Solid Particles, Patent No. WO2013053890, 2013.
- [112] K. Dam-Johansen, Personal contact, DTU Chemical Engineering, 2010.
- [113] S.H. Andersen, Undersøgelse og modellering af ny forvarmerproces til anvendelse i cementproduktionen, Bachelor thesis, DTU, 2011.
- [114] J. Quintero, Operation and Data Treatment of a Proof of Concept Heat Exchange Design, Master thesis, Kgs. Lyngby, 2012.
- [115] D. Schulze, *Powders and Bulk Solids*, Springer Berlin Heidelberg, ISBN: 9783540737674, 2008.
- [116] D.C. Montgomery, *Design and Analysis of Experiments*, 7th Ed., John Wiley & Sons Inc, Hoboken, ISBN: 9780470398821, 2009.
- [117] K. Gotoh, H. Masuda, K. Higashitani, *Powder Technology Handbook*, 3rd ed., Marcel Dekker, New York, ISBN: 1574447823, 2006.
- [118] M. Han, D.L. Lawer, Interaction of Two Settling Spheres: Settling Rates and Collision Efficiency, *Journal of Hydraulic Engineering*, 117, 1269–1289, 1991.
- [119] T. Zhou, H. Li, Estimation of agglomerate size for cohesive particles during fluidization, *Powder Technology*, 57–62, 1999.
- [120] M. Rhodes, *Introduction to Particle Technology*, 1st ed., Wiley, ISBN: 0471984825, 1998.

- [121] F. Cabrejos, G. Klinzing, Pickup and Saltation Mechanisms of Solid Particles in Horizontal Pneumatic Transport, *Powder Technology*, 79, 173–186, 1994.
- [122] E. Muschelknautz, W. Krambrock, Vereinfachte Berechnung horizontaler pneumatischer Förderleitungen bei hoher Gutbeladung mit feinkörnigen Produkten, *Chemie Ingenieur Technik*, 1969.
- [123] S. Wang, M. Fang, Z. Luo, X. Li, M. Ni, K. Cen, Instantaneous Separation Model of a Square Cyclone, *Powder Technology*, 102, 65–70, 1999.
- [124] F. Zenz, N. Weil, A Theoretical-empirical Approach to the Mechanism of Particle Entrainment from Fluidized Beds, *AIChE Journal*, 472–479, 2004.
- [125] T.M. Knowlton, S.B.R. Karri, A. Issangya, Scale-up of Fluidized-bed Hydrodynamics, *Powder Technology*, 150, 72–77, 2005.
- [126] A. Bisio, R.L. Kabel, *Upscale of Chemical Processes*, John Wiley & Sons Inc, ISBN: 0471057479, 1985.
- [127] C.E. Weinell, *Single Particle Behaviour in Circulating Fluidized Bed Combustors*, Ph.D. thesis, Technical University of Denmark, ISBN: 8790142020, 1994.
- [128] L. Glicksman, Scaling Relationships for Fluidized Beds, *Chemical Engineering Science*, 1373–1379, 1984.
- [129] L.R. Glicksman, M.R. Hyre, P.A. Farrell, Dynamic Similarity in Fluidization, *International Journal of Multiphase Flow*, 20, 331–386, 1994.
- [130] Y. He, C. Lim, J. Grace, Scale-up Studies of Spouted Beds, *Chemical Engineering Science*, 52, 329 – 339, 1997.
- [131] R. Béttega, R.G. Corrêa, J.T. Freire, Scale-up study of spouted beds using computational fluid dynamics, *The Canadian Journal of Chemical Engineering*, 87, 193–203, 2009.
- [132] W. Du, J. Xu, Y. Ji, W. Wei, X. Bao, Scale-up relationships of spouted beds by solid stress analyses, *Powder Technology*, 192, 273–278, 2009.
- [133] M. Zlokarnik, *Scale-up in Chemical Engineering*, 2nd ed., Wiley-VCH, ISBN: 9783527314218, 2006.
- [134] M. Rüdüsüli, T.J. Schildhauer, S.M.A. Biollaz, J.R. van Ommen, Scale-up of Bubbling Fluidized Bed Reactors — A Review, *Powder Technology*, 217, 21–38, 2012.
- [135] B.K. Datta, C. Ratnayaka, A Simple Technique for Scaling Up Pneumatic Conveying Systems, *Particulate Science and Technology*, 21, 227–236, 2003.

- [136] L.R. Glicksman, M. Hyre, K. Woloshun, Simplified Scaling Relationships for Fluidized Beds, *Powder Technology*, 77, 177–199, 1993.
- [137] T. Fitzgerald, D. Bushnell, S. Crane, Y. Shieh, Testing of Cold Scaled Bed Modeling for Fluidized-bed Combustors, *Powder Technology*, 35, 107–110, 1984.
- [138] M. Nicastro, L. Glicksman, Experimental Verification of Scaling Relationships for Fluidized Bed, *Chemical Engineering Science*, 39, 1381–1391, 1984.
- [139] M. Horio, A. Nonaka, Y. Sawa, I. Muchi, A New Similarity Rule for Fluidized Bed Scale-up, *AIChE Journal*, 32, 1466–1482, 1986.
- [140] C. Maarup, K. Hjuler, Investigation of Raw Meal Flowability at Temperatures up to 850°C using a Monoaxial Shear Tester, Submitted to *Powder Technology*, 2013.
- [141] Y. Wei-hua, X. Tao, J. Li-yue, Waste Heat Recovery and Power Generation in Cement Works, 2nd International Conference on Power Electronics and Intelligent Transportation System (PEITS), 223–226, 2009.
- [142] S. Giner, A. Calvelo, Modelling of Wheat Drying in Fluidized Beds, *Journal of Food Science*, 1–6, 1987.
- [143] J.R. Barrett, Heat and Mass Transfer Analysis of Intra-kernel Wheat Drying and Rewetting, 109–125, 1981.
- [144] N.H. Abu-Hamdeh, a. M. Othman, An Experimental Study and Mathematical Simulation of Wheat Drying, *Drying Technology*, 22, 491–506, 2004.
- [145] V.K. Srivastava, J. John, Deep bBed Grain Drying Modeling, *Energy Conversion and Management*, 43, 1689–1708, 2002.
- [146] Engineering Toolbox (<http://www.engineeringtoolbox.com/>), Accessed February, 2011.
- [147] E.S. Andersen, P. Jespersgaard, O.G. Østergaard, *Databog Fysik Kemi*, 10th ed., F&K Forlaget, ISBN: 9788787229593, 2003.
- [148] B.L. Hinkle, *Acceleration of Particles and Pressure Drops Encountered in Horizontal Pneumatic Conveying*, 1953.
- [149] R.B. Montgomery, Viscosity and Thermal Conductivity of Air and Diffusivity of Water Vapour in Air, *Journal of Meteorology*, 4, 1949.
- [150] MathWorks, MatLab Central, <Http://www.mathworks.com/matlabcentral/fileexchange>, 2013.

- [151] J.L. Sinclair, R. Jackson, Gas-particle Flow in a Vertical Pipe with Particle-particle Interactions, *AIChE Journal*, 35, 1473–1486, 1989.
- [152] T.B. Anderson, R. Jackson, A Fluid Mechanical Description of Fluidized Beds, *I&EC Fundamentals*, 6, 527–539, 1965.

List of Symbol and Abbreviations

Symbols

Symbol	Description	Unit
A	Area	[m ²]
a	Inlet height of a cyclone	[m]
b	Inlet width of a cyclone	[m]
c ₀	Solid load	[kg/kg]
c _{0L}	Limiting solid load	[kg/kg]
C _p	Specific heat capacity	[J/kg/K]
d _p	Particle diameter	[m]
D	Diameter	[m]
ΔMF _i	I th mass fraction of a certain particle size	[kg]
f	Friction factor	-
g	gravity	[m/s ²]
H	Height	[m]
H _C	Height of cyclone cone	[m]
k _s	Roughness of wall	[m]
k	Fitting parameter	-
L	Length	[m]
ṁ	Mass flow	[kg/s] / [kg/hr]
m	Slope of efficiency curve	-
n	Number of data points	-
N	Number of stages	-
P	Pressure	[Pa] / [Bar]
R	Radius	[m]
Q	Energy content	[J]
S	Height of vortex finder	[m]
T	Temperature	[°C]
w	Weight for cost function	-
<i>Greek letters</i>		
α	Constriction factor	-
β	Geometric ratio, a/R	-

Symbol	Description	Unit
Δ	Difference	-
ε	Void in bulk	-
ρ	Density	[kg/m ³]
η	Particle transport related efficiency	-
φ	Thermal related efficiency	-
Φ	Particle sphericity	-
ϕ	Internal angle of friction	-
θ	Angle of pipe section	[°]
v	Velocity	[m/s]
μ	Viscosity	[kg/m/s]

Indices

<i>1 – 7</i>	Model number	-
50	Cut size	-
Abs	Absolute	-
Acc	Acceleration	-
amb	Ambient	-
B	Bed	-
C	Cyclone	-
Channel	Transport channel	-
Cal	Calciner conditions	-
Com	Computed	-
<i>cs</i>	Control surface	-
D	Dust	-
Body	Cyclone body	-
Eff	Effective	-
Elv	Elevation	-
Ent	Entrainment	-
F	Freeboard	-
Fric	Friction	-
G	Gas	-
H	Horizontal	-
Heat	Parameter describing heat loss	-

Symbol	Description	Unit
i	Stage/interval reference	-
In	Inlet conditions	-
Loss	Loss	-
mf	Minimum fluidization	-
NE	Not entrained	-
Opt	Optimized	-
Out	Outlet	-
P	Particles	-
Pickup	Pickup conditions	-
R	Riser	-
Re	Reynolds number	-
Ref	Reference condition	-
Rel	Relative	-
m	mean	-
Meas	Measured	-
med	median	-
Module	Module specific	-
Sal	Saltation conditions	-
Sep	Separation	-
Stokes	Stokes terminal settling velocity	-
Str	Particle strand/rope	-
T	Temperature	-
Tot	Total	-
v	Vertical channel/Vertical	-
w	wall	-
x	vortex	-
z	Axial	-
θ	tangential	-

Abbreviations

2D-HX – Two dimensional heat exchanger

AF – Alternative fuel

ANOVA – Analysis of variance

CS – Control surface

CC – Carbon capture

CFB – Circulating fluidized bed

CFD – Computational Fluid dynamics

DTSB – Draft tube spouted bed

ECT – Emission trade system

ILC – Inline Calciner

L/D – Length/Diameter ratio

LP – Low pressure drop

MM – Muschelknautz's method

PM – Particulate matter

PoC – Proof of concept

SoE – Sum of Errors

SWOT – Strength, Weaknesses, Opportunities, and Threats

TPD – Tons per day [Ton/day]

TPDc – Tons per day of clinker [Ton/day]

Appendix A

Experimental Procedures

In this appendix, experimental procedures for the three set-ups are provided.

Single-stage set-up

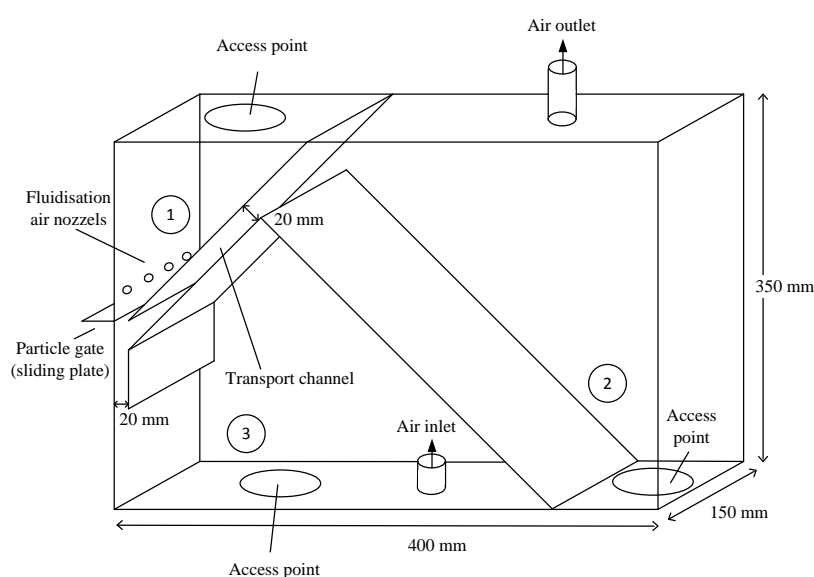


Figure 140 – Schematic drawing of the 1-stage, cold set-up. Numbered indications are: (1) Initial particle location, (2) Final location of entrainment particles, (3) final location of particles not entrained.

Initially the set-up was loaded with a weighted amount of particles into the feed chamber, (1) in Figure 140. The mass of the filter bag was noted. Vacuum cleaners were turned on, followed by setting of desired gas flow. The particle gate was opened at the desired gap and particles start pouring out into the gas. If necessary fluidization air could be applied. Once the particle stock has been depleted, the system was shut down in reverse sequence. The particles collected at (2) and (3) were weighed for data on the particle distribution at the given settings. Weight of particles collected in filter bag could be used for controlling the mass balance. The particle feed rate was obtained from initial mass loaded particles and the time between particle gate opening and particle stock depletion.

Multi-stage set-up

Startup procedure was similar to Single-stage procedure. At initiation of experiments, all particle gates must be closed. Top stage particle gate was moved to the desired opening and particles started to move to stage number 2. Once appropriate layer of particles (2-3 cm) was present in stage number 2, the particle gate of stage 2 was opened. The procedure is repeated for all stages. Once the particle layer was below 2-3 cm or if gas was penetrating the particle layer, the gates opening was reduced or closed. Once all particles were transported to the bottom stage, system was shut down. Collected particles at the two bottom locations were weighed, as well as the particles collected in the filter system.

For further details, please see Andersen [113].

Proof of concept set-up

When system is configured as desired (number of stages and instrumentation), the gas flow at the desired temperature was started. At steady state conditions in the system, the particle feed and vibration was started. Particles were collected at top stage until layer of particles were visible through sight glasses. Particle gate was opened and controlled, ensuring stable particle level. This procedure is repeated for each stage, while controlling level at all active stages. System run until new steady state has been reached.

At shutdown, the particle feed was stopped and each particle bed emptied. The gas preheater was turned off, while maintaining a gas flow of 30 kg/hr. When system is colder than 100 °C, gas flow could be stopped. Data was automatically collected at all times.

Detailed procedure has been provided by Quintero [114].

Appendix B

Data Treatment

The following exemplifies the data acquisition and treatment yielding the data for the PoC set-up. The experiment selected as example for the following descriptions is called PoC #2. The dynamic data for this experiment is provided in Figure 141, Figure 142 and Figure 147. Not all experiments are similar to PoC#2 in operation characteristic, but overall trends are similar. The example also serves for understanding the steady state data presented in the main text.

For the used example, the experiment were started at time = 1800 s and terminated at time = 8500 s. The time scale is independent for each experiment and only relates to the start of the data file for that given experiment.

During PoC #2, the gas inlet temperature was approximately 795 °C – 810 °C and the particle inlet temperature around 20 °C. The measurement of the particle feed temperature is done in the upper part of the set-up, why the temperature is affected by the temperature of the hot gas.

Initially the stable temperatures of the system shown at the initiation of the experiment in Figure 141, should be noticed. This indicates that the system, including the gas preheater, was in thermal equilibrium. At time = 1800 s, the particle flow was initiated to stage 1, which can be seen as a drop in the particle feed temperature. The starting point of the experiment can also be identified from the feeder setting (Figure 142). At approximately time = 2100 s, the gate of stage 1 was opened. The result was a temperature drop in the gas exit temperature, caused by the heat exchange process taking place in stage 1. Afterwards the gates of stages 2, 3 and 4 were opened, resulting in temperature drops in the entire system. The temperature of the inlet to stage 4 was not lowered, indicating that very little heat exchange takes place in the inlet to stage 4. This indicates that only a minor portion of the particles are present in the part of the system, as expected.

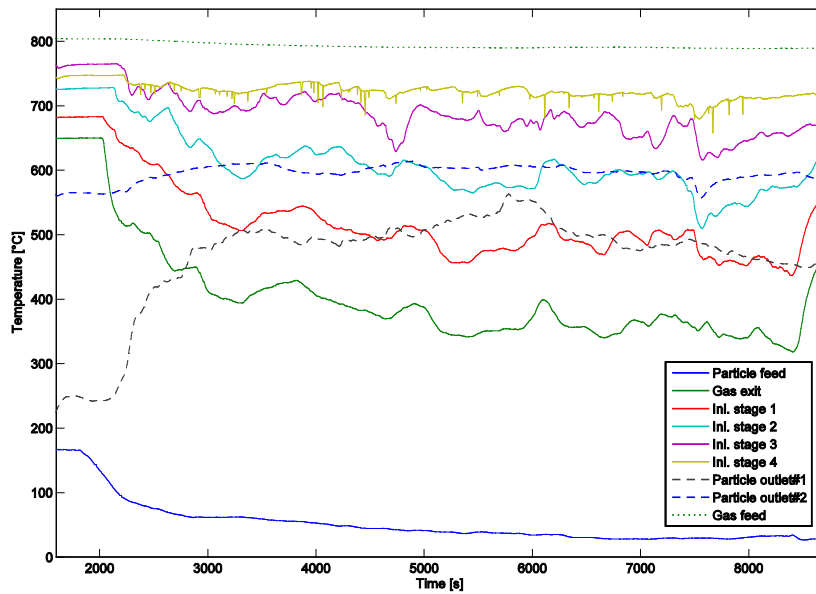


Figure 141 – Temperatures during PoC #2.

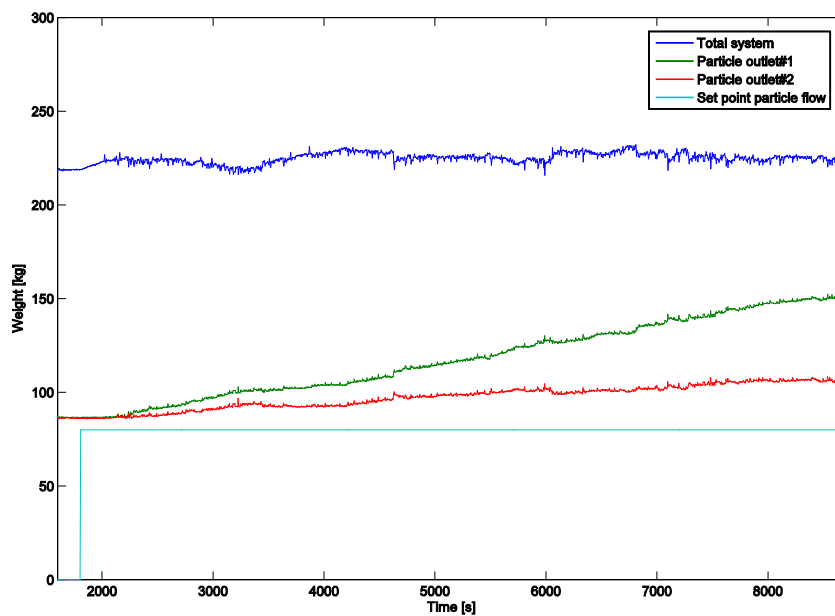


Figure 142 – Dynamic weight data during PoC #2.

The set-up cooled down until a new operational steady state at a lower temperature was reached. The slow cooling of the system was caused by a relatively large thermal mass of the set-up.

The fluctuations observed in the temperatures during the experiments are mainly a consequence of the control and position of each particle gate: If a gate was opened more, more particles were

transported to the stage below, cooling this area more than before and vice versa when the gates were closed. Furthermore, if the position of a lower level gate (stage 2, 3, or 4) was changed, this influenced temperature in all the above stages. This was the main reason for the smaller fluctuations. The larger fluctuations seen in Figure 141 were caused by a stage running low of particles, which resulted in the particle gate being closed with a large temperature increase in the entire system as a consequence. This was the case at the peak around 6000 s.

Steady state considerations

To evaluate the overall performance of the system it is useful to consider temperatures and weights at the initial conditions and at the start and end of the operational steady state.

In Figure 143, the temperatures of the system are depicted together with the selected periods used for computing the initial and steady state conditions. The marked intervals are a period of 120 seconds and 1800 seconds respectively. Note that the position and length of the two stable periods depends on each experiment and are chosen to represent the data as well as possible. The steady state period at the end of the experiment are shown separately in Figure 144.

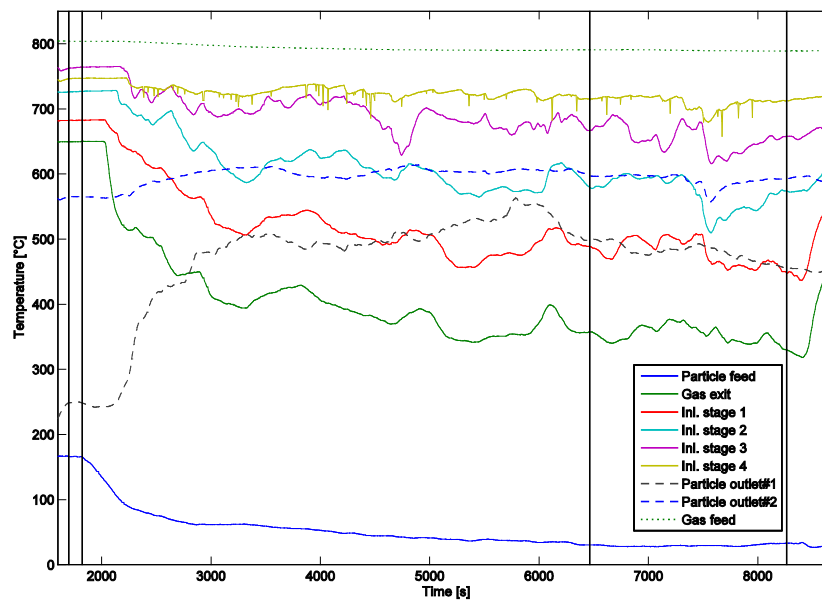


Figure 143 – Temperatures of PoC#2 with indication of start and end conditions.

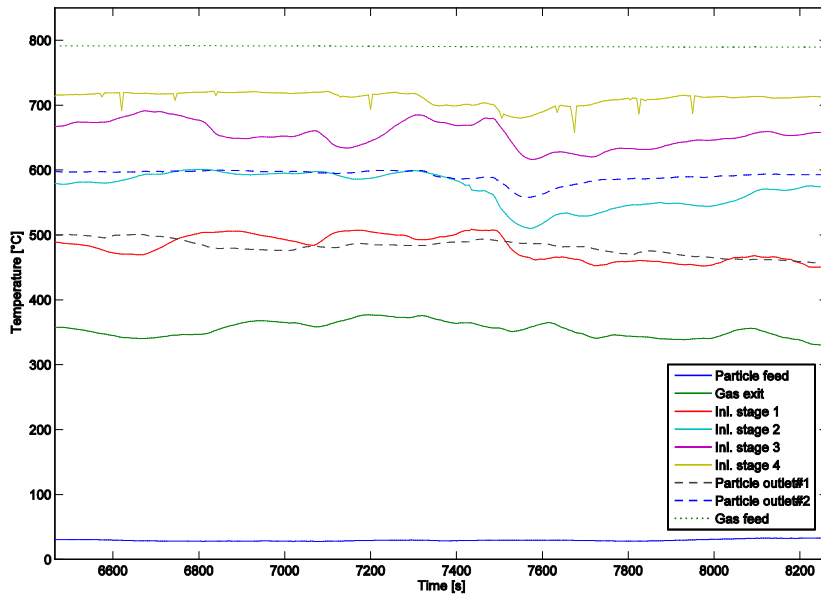


Figure 144 – Dynamic temperature data of PoC #2 in the steady state period.

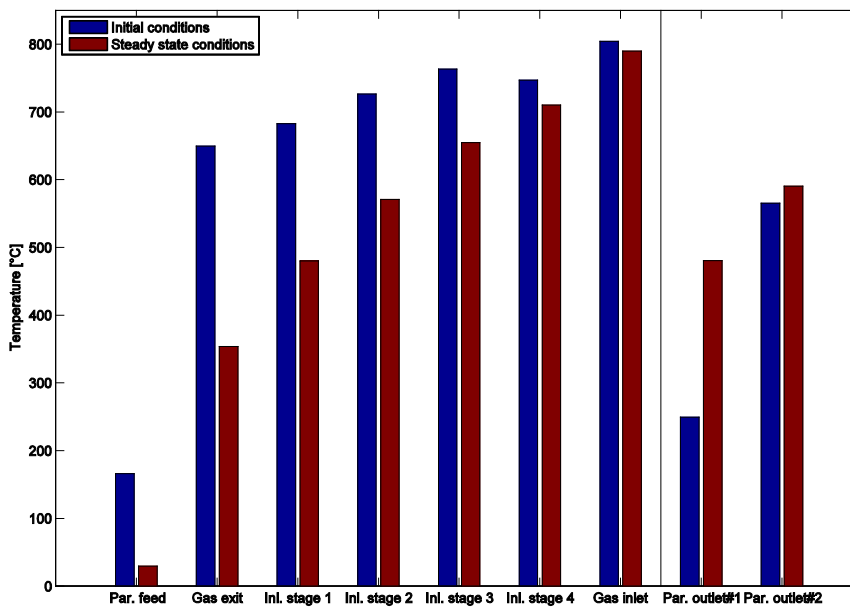


Figure 145 – Temperatures of the system at steady state before and during the experiment, POC #2

The temperature averages for each measurement point at the initial and steady state are plotted in Figure 145. This figure summarizes the thermal performance of the system during the stable operation. From the initial conditions, it was found that there was an energy loss in the empty set-up corresponding to 150 °C in this experiment. This is the temperature difference between the gas inlet and the gas exit. The red bars, indicating average temperatures during the

operational steady state show that the temperatures were lowered during the experiment, and that the exit gas temperature of was lowered from approximately 650 °C to 325 °C. Also the temperature increased for both particle outlets. The temperature difference at the initial conditions between the two particle outlets was caused by their physical location: Particle outlet 2 was close to the gas inlet causing high temperature in that part of the system. Oppositely where no gas movement was present during the initial period, the temperatures were lower.

The steady state data indicates that heat exchange occurs at all four stages. The temperature profile in the system shows that the temperature change over each stage is around 100 °C per stage, with the largest difference over stage 1 and smallest over stage 4. This is in agreement with the expected behavior of the system.

The inlet gas temperatures were fairly constant during the experiment, which is also evident from Figure 145.

During operational steady state, the particle exit temperatures were highest at particle exit #2 as expected as this was where the hottest gas is present. As described previously, not much material ended in particle outlet #2 during operational steady state.

The measured weights during the steady state are depicted in Figure 146. The blue bars indicate the mass at the start of steady state and the red bars the mass at the end of the operational stable period. Thus, the weight data depicted are not averages, but data points at the beginning and end of the stable period, marked by the third and fourth vertical black line from left on Figure 143. The weight gain of the system was neglectable during steady state. The amount of particles collected in particle outlet #1 was approximately 18 kg and for particle outlet #2 the amount was approximately 5 kg. The total amount of particle fed during the experiment was, according to Figure 142, 40 kg.

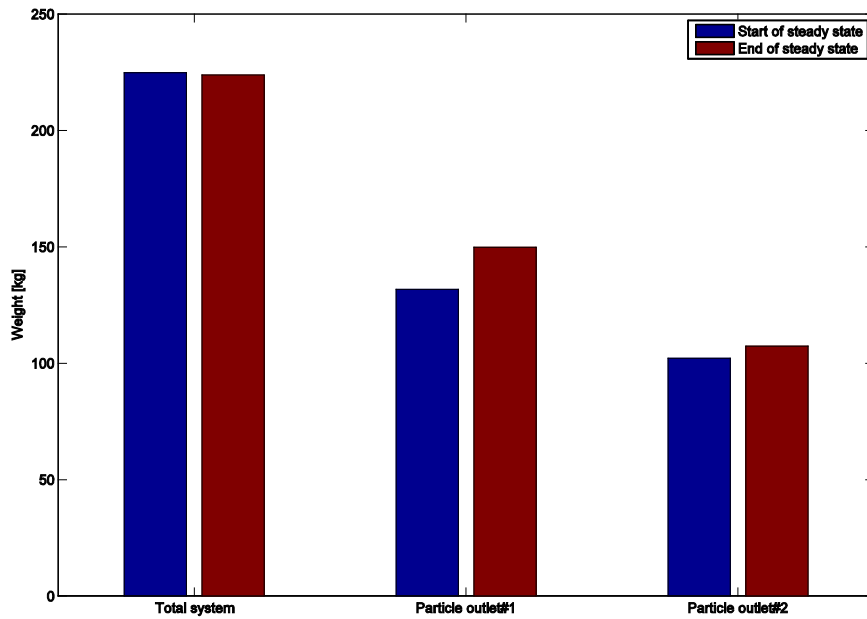


Figure 146 – Weights of the system at steady state before and during the experiment, POC #2

Pressure drop

The pressure drop over each stage and the total system was monitored by five differential pressure sensors. The obtained data is provided in Figure 147.

The maximum total pressure drop over the entire set-up reached around 12 mbar during the experiment, but was typically in the range of 4 – 6 mbar. The pressure drop over each stage depended on the gas velocity, amount of particle transported and possibly also the amount of build-up in pressure transmission lines. Note that the exact pressure drops over each stage should be compared with care as the pressure sensors were prone to build-up in the pressure transmission lines and measurement points. The absolute values were therefore not completely reliable. This was also the reason for some of the pressure drop being negative. However, in terms of trends and order of magnitude of the pressure drop, the data is trustworthy. Figure 148 contains a zoom of the data presented in Figure 147, where the initial period of the experiment can be studied.

From the data in Figure 148 it is evident that the gates are opened in the sequence 1, 2, 3 and 4 as previously described. This can be seen from the increases in pressure drop over each stage at the beginning of the experiment.

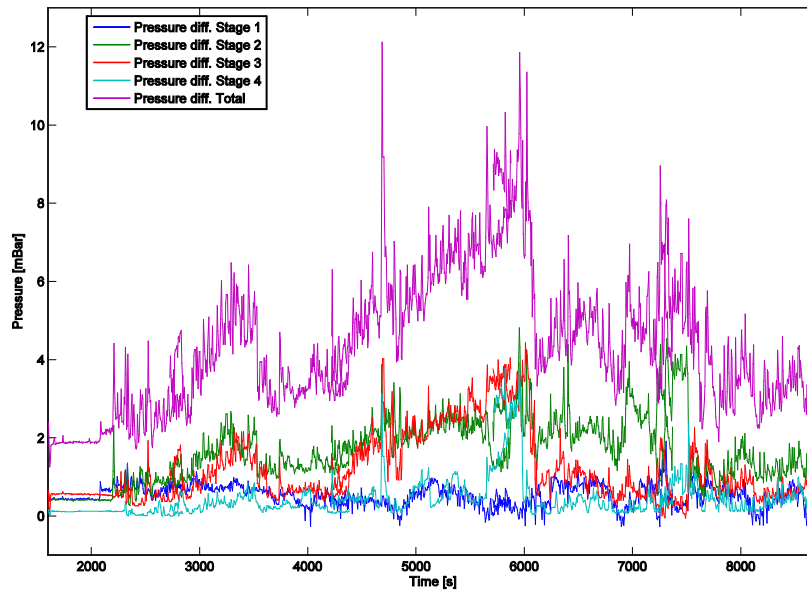


Figure 147 – Dynamic pressure drop data during PoC #2.

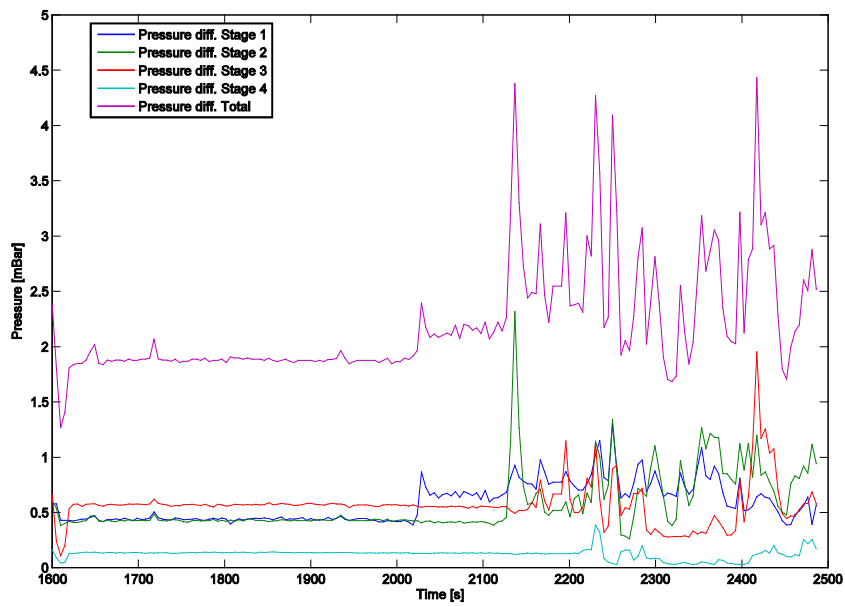


Figure 148 – Pressure drop of PoC #2 at the start of the experiment.

Appendix C

Experimental Data

Investigation of Transport Processes

Table 46 – Experimental settings and results for used in an ANOVA for sand particles in the Single-stage set-up.
Experiments carried out at ambient temperature

Ex. name	Particle gate opening [mm]	Duration [s]	Initial Weight ^A [g]	Velocity ^A [m/s]	Solid load ^A [kg/kg]	η_{Sep}	η_{Ent}
S#1	6	30	1006	3.10	3.16	0.97	0.67
S#2	6	34	1010	3.10	2.80	0.96	0.75
S#3	6	36	1001	3.10	2.62	0.96	0.77
S#4	6	30	1000	3.10	3.14	0.96	0.65
S#5	3	56	755	2.52	1.62	0.96	0.50
S#6	3	73	1259	2.52	2.00	0.84	0.57
S#7	9	15	755	2.52	5.84	0.97	0.57
S#8	9	25	1249	2.52	5.80	0.97	0.62
S#9	3	104	751	3.68	0.57	0.96	1.00
S#10	3	108	1256	3.68	0.92	0.97	1.00
S#11	9	22	756	3.68	2.73	0.96	0.79
S#12	9	31	1256	3.68	3.21	0.93	0.91

^A Used for ANOVA

Table 47 – Experimental settings and results from the Single-stage set-up using Dalen raw meal particles.
Experiments carried out at ambient temperature

Ex. name	Particle gate opening [mm]	Duration [s]	Initial Weight [g]	Velocity [m/s]	Solid load [kg/kg]	η_{Sep}	η_{Ent}
R#1	6	84	1579	3.10	1.77	0.83	0.77
R#2	6	N/A	1118	3.98	N/A	0.84	0.85
R#3	6	50	984.2	3.68	1.56	0.85	0.82
R#4	6	21	1020	3.10	4.58	0.88	0.74
R#5	6	23	704.9	2.52	3.56	0.92	0.63
R#6	6	18	640	1.94	5.37	0.82	0.53
R#7	6	18	603	1.35	7.24	0.84	0.33

Table 48 – Experimental settings and results from the Multi-stage set-up using Cimpor raw meal particles.
Experiments carried out at ambient temperature

Ex. name	Velocity [m/s]	Initial Weight [g]	Collected filter	Collected particle outlet #1	Collected particle outlet #2
M#1	1.8	2788	150	2500	195
M#2	2.3	2918	140	2120	690
M#3	2.8	3450	240	2421	723
M#4	3.4	3439	295	2075	945
M#5	2.8	4523	697	1955	750
M#6	2.8	3454	811	1720	405

Table 49 – Experimental settings and results from the PoC set-up using Pilot 2 raw meal particles. Second session, the number of stages is one.

Ex. name	Velocity [m/s]	Temperature [°C]	Particle flow [kg/hr]	Solid load [kg/kg]	η_{Sep}	η_{Ent}
P2#1	2.32	20	78	0.78	0.90	0.25
P2#2	4.48	20	78	0.40	0.77	0.84
P2#3	2.92	20	78	0.62	0.90	0.46
P2#4	3.71	20	78	0.49	0.85	0.66
P2#5	3.71	20	78	0.49	0.82	0.73
P2#6	1.56	20	78	1.16	0.86	0.12
P2#7	3.71	20	78	0.49	0.82	0.72
P2#8	0.77	20	78	2.37	0.40	0.04
P2#9	3.71	20	78	0.49	0.78	0.73
P2#10	3.71	20	61	0.38	0.81	0.79
P2#11	3.71	20	94	0.59	0.81	0.79
P2#12	3.71	20	61	0.38	0.77	0.92
P2#13	5.66	214	78	0.53	0.56	0.94
P2#14	7.29	204	78	0.40	0.40	0.98

Table 50 – Experimental settings and results from the PoC set-up using Pilot 2 raw meal particles. Third session #1, pressure above atmospheric. Experiments carried out at ambient temperature, and the number of stages is one.

Ex. name	Velocity [m/s]	Particle flow [kg/hr]	Solid load [kg/kg]	η_{Sep}	η_{Ent}
P3#1	4.87	140	0.67	0.61	0.84
P3#2	5.04	100	0.46	0.78	0.87
P3#3	5.11	140	0.64	0.80	0.88
P3#4	2.24	100	1.04	1.00	0.19
P3#5	3.27	100	0.71	0.93	0.55
P3#6	4.01	100	0.58	0.94	0.80
P3#7	2.75	120	1.02	0.80	0.49
P3#8	3.97	180	1.06	0.90	0.83

Table 51 – Experimental settings and results from the PoC set-up using Pilot 2 raw meal particles. Third session #2, pressure below atmospheric. Experiments carried out at ambient temperature, and the number of stages is one.

Ex. name	Velocity[m/s]	Particle flow [kg/hr]	Solid load [kg/kg]	η_{Sep}	η_{Ent}
P3#9	4.37	140	0.75	0.80	1.00
P3#10	5.29	160	0.71	0.73	1.00
P3#11	5.63	176	0.73	0.73	0.99
P3#12	6.05	200	0.77	0.61	1.00
P3#13	1.51	47	0.73	0.90	0.21
P3#14	1.93	61	0.74	1.00	0.25
P3#15	3.28	100	0.71	0.78	0.75
P3#16	3.78	120	0.74	0.79	0.85
P3#17	3.19	100	0.73	0.94	0.77
P3#18	4.03	120	0.69	0.80	0.98
P3#19	5.21	100	0.45	0.69	0.99
P3#20	6.89	140	0.47	0.39	1.00
P3#21	6.13	120	0.46	0.51	0.99
P3#22	9.91	200	0.47	0.30	0.99
P3#23	4.2	100	0.56	0.80	1.00
P3#24	5.17	120	0.54	0.67	0.97
P3#25	5.8	140	0.56	0.60	1.00
P3#26	6.8	160	0.55	0.62	0.99
P3#27	7.48	180	0.56	0.48	0.91
P3#28	8.15	200	0.57	0.36	1.00
P3#29	2.69	61	0.53	0.84	0.53
P3#30	5.88	140	0.56	0.67	1.00
P3#31	4.16	100	0.56	0.82	0.85
P3#32	4.45	200	1.05	0.74	0.99
P3#33	1.47	61	0.97	1.00	0.16
P3#34	2.35	100	0.99	0.95	0.38
P3#35	2.65	120	1.06	0.84	0.63

Investigation of thermal performance

A complete summary of experimental for PoC and TEQ data are provided in the following tables.

Table 52 – Summary of PoC experiments: Overview of experimental settings.

System configuration	PoC #1	PoC #2	PoC #3	PoC #4	PoC #5	PoC #6	PoC #7
Number of stages, N	4	4	4	4	4	1	1
Location of temperature measurements	Stage inlets	Stage inlets	Stage inlets	As PoC #1 and in particle beds	As PoC #1 and in particle beds	As PoC #4 and in freeboard	As PoC #4 and in freeboard
Experimental settings							
Duration [min]	84	109	36	84	56	60	35
Duration of steady state [min]	30	30	10	17	13	19	8
Gas flow [kg/hr]	80	80	100	90	90	80	146
Particle flow [kg/hr]	78	94	94	61	78	78	78

Table 53 – Summary of PoC experiments: Particle distribution.

Particle distribution	PoC #1	PoC #2	PoC #3	PoC #4	PoC #5	PoC #6	PoC #7
Particles fed during steady state [kg]	47.1	38.9	15.7	21.2	16.2	24.3	10.8
Particle outlet #1, steady state [kg]	30.6	18.2	8.1	4.1	10.8	17.9	6.1
Particle outlet #2, steady state [kg]	7.5	5.3	1.5	0.3	1.5	1.6	0.9
System weight change ^A [kg]	-8.8 ^B	-0.9	-5.3 ^B	1.8	-3.9 ^B	1.2	-1.3
Particle, blown out ^C [kg]	17.8	16.4	11.4	15.1	7.8	3.6	5.0
Particle distribution outlet#1	0.55	0.46	0.39	0.21	0.54	0.77	0.51
Particle distribution outlet#2	0.13	0.13	0.07	0.02	0.07	0.07	0.07
Particles distribution blown out	0.41	0.32	0.54	0.78	0.41	0.15	0.41

^A The weight change of the system is used to correct the particles fed, when computing the mass balance and particle distributions.

^B System weight not stable as this prolongs the operational period at the end of each experiment (emptying of top stage)

^C Computed from a total mass balance at steady state

Table 54 - Summary of PoC experiments: Temperatures.

Average temperatures	PoC #1	PoC #2	PoC #3	PoC #4	PoC #5	PoC #6	PoC #7
$T_{G,in}$ [°C]	790	790	707	710	707	324	243
$T_{G,stage 4}$ [°C]	711	717	688	660	659	N/A	N/A
$T_{G,stage 3}$ [°C]	655	642	565	643	593	N/A	N/A
$T_{G,stage 2}$ [°C]	571	547	591	584	508	N/A	N/A
$T_{G,stage 1}$ [°C]	480	412	464	475	371	295	247
$T_{G,outlet}$ [°C]	354	321	361	398	309	183	180
$T_{G,freeboard,stage 1}$ [°C]	N/A	N/A	N/A	N/A	N/A	184	176
$T_{P,in}$ [°C]	20	20	20	20	20	20	20
$T_{P,stage 1}$ [°C]	N/A	N/A	N/A	65	57	40	57
$T_{P,stage 2}$ [°C]	N/A	N/A	N/A	402	314	N/A	N/A
$T_{P,stage 3}$ [°C]	N/A	N/A	N/A	505	424	N/A	N/A
$T_{P,stage 4}$ [°C]	N/A	N/A	N/A	539	493	N/A	N/A
$T_{P,outlet \#1}$ [°C]	481	505	562	500	530	154	156
$T_{P,outlet \#2}$ [°C]	591	596	573	599	606	223	206
$T_{P,outlet,average}$ [°C]	505	522	564	508	541	159	162

Table 55 - Summary of PoC experiments: Computed relevant parameters.

Characteristic parameters	PoC #1	PoC #2	PoC #3	PoC #4	PoC #5	PoC #6	PoC #7
Solid load, c_o [kg/kg]	1.0	1.2	0.9	0.7	0.9	1.0	0.5
Stability [max(%change)/min]	0.24	0.30	1.30	0.7	2.5	0.9	1.0
Absolute thermal efficiency, φ_{Abs}	0.30	0.50	0.36	0.08	0.39	0.29	0.18
Relative thermal efficiency, φ_{Rel}	0.69	0.37	0.53	0.14	0.58	0.64	0.61

Table 56 – Summary of TEQ experiments: Temperatures.

Ex. name	Avg. temp. gas exit	Avg. gas feed	Avg. inl. stage 1	Avg. inl. stage 2	Avg. inl. stage 3	Avg. inl. stage 4	Avg. particle outlet#1	Avg. particle outlet#2
TEQ#1	656	781	679	723	741	723	338	591
TEQ#2	655	805	674	729	755	736	255	600
TEQ#3	484	534	499	510	520	512	379	435
TEQ#4	672	865	715	770	807	787	574	670
TEQ#5	576	690	603	635	656	632	382	541
TEQ#6	392	451	408	425	430	420	243	357
TEQ#7	555	622	577	595	607	594	440	510
TEQ#8	578	728	607	656	679	675	296	526
TEQ#9	377	424	393	407	412	396	282	345
TEQ#10	427	510	447	472	481	473	271	406

Table 57 – Summary of TEQ experiments: Gas flow and computed parameters.

Ex name	Gas flow [kg/h]	Steady state [max(%change)/min]	Actual heat loss, [kW]	Loss
TEQ#1	80	0.00	3.4	0.18
TEQ#2	80	0.05	4.1	0.21
TEQ#3	100	0.00	1.6	0.10
TEQ#4	75 ^A	0.06	3.3	0.24
TEQ#5	75 ^A	0.00	1.9	0.18
TEQ#6	75 ^A	0.01	0.9	0.14
TEQ#7	60 ^A	0.05	0.9	0.12
TEQ#8	60 ^A	0.64	2.0	0.22
TEQ#9	112.5 ^A	0.08	1.1	0.12
TEQ#10	112.5 ^A	0.15	2.0	0.17

^A Electric gas preheater leaking, estimated gas flow.

Appendix D

Pressure Drop Model

Pneumatic transport pressure drop model, as described by Rhodes [120].

The pressure drop over a given stage consists of a contribution from the gas and a contribution from the particles.

$$\Delta P_{Stage} = \Delta P_G + \Delta P_P \tag{Eq. 58}$$

Each contribution can be divided in three terms: Friction, acceleration and elevation:

$$\Delta P_{Stage} = \underbrace{\Delta P_{G,Friction}}_{(1)} + \underbrace{\Delta P_{G,Acc}}_{(2)} + \underbrace{\Delta P_{G,Elev}}_{(3)} + \underbrace{\Delta P_{P,Friction}}_{(4)} + \underbrace{\Delta P_{P,Acc}}_{(5)} + \underbrace{\Delta P_{P,Elev}}_{(6)} \tag{Eq. 59}$$

These values can be mathematically evaluated by considering a momentum balance. A schematic drawing used for setting up a momentum balance is presented in Figure 149.

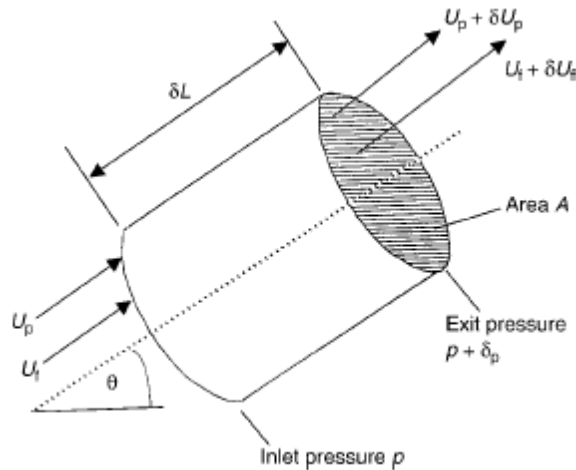


Figure 149 – Schematic drawing of a section of pneumatic transport pipe.

Setting up a momentum balance and integrating, assuming constant density of air, yields:

$$\Delta P_{Stage} = \underbrace{F_{W,G} \cdot L}_{(1)} + \underbrace{\frac{\rho_G \cdot \varepsilon \cdot v_G^2}{2}}_{(2)} + \underbrace{\rho_P \cdot (1 - \varepsilon) \cdot L \cdot g \cdot \sin \theta}_{(3)} + \underbrace{F_{W,P} \cdot L}_{(4)} + \underbrace{\frac{\rho_P \cdot (1 - \varepsilon) \cdot v_P^2}{2}}_{(5)} + \underbrace{\rho_G \cdot \varepsilon \cdot L \cdot g \cdot \sin \theta}_{(6)} \quad \text{Eq. 60}$$

Where, F is the wall friction force between gas and wall (subscript W,G) and particles and wall (subscript W,P). ε is the void fraction.

A priori none of the above terms can be neglected, and each of the terms must be evaluated at the desired conditions and relevant geometries.

Approximated system

For evaluation of the momentum balance, the system is represented by a simplified system. Assumed particle and gas trajectories in a single stage are provided in Figure 150.

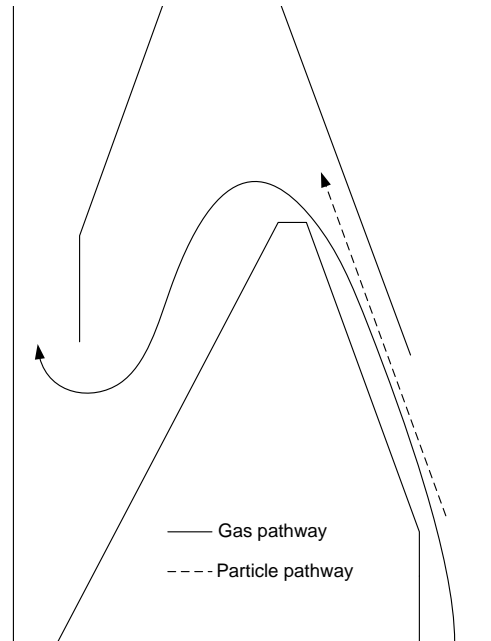


Figure 150 – Schematic drawing of particle and gas pathways.

To simplify the computations and enable the use of the pneumatic transport equations, both particle and gas pathways are simplified:

- The particle pathway will be considered as shown in Figure 152. The particles are assumed to leave the gas flow at the entrance to the separation chamber. The path of the particles is assumed to consist of a horizontal and a vertical part.

- The gas pathway will be described as a series of pipe sections, bends and diameter changes, as shown in Figure 151, which will yield an equivalent length of pipe that offers the same friction as the geometries considered.

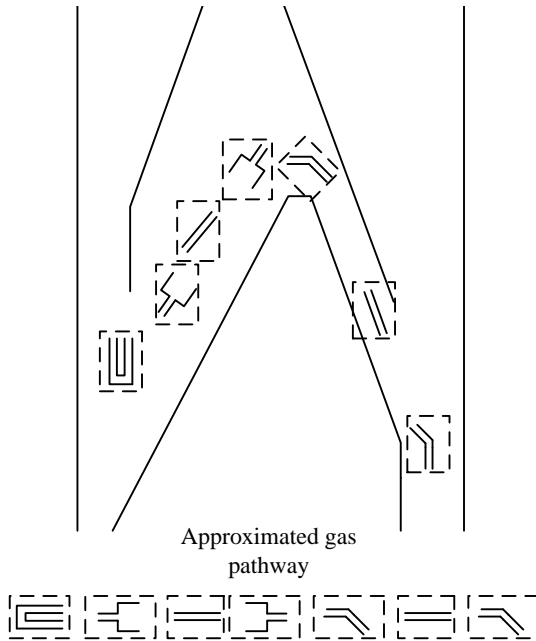


Figure 151– Approximated gas pathway in a single stage of the 2D-HX.

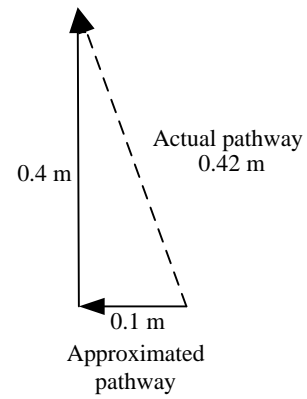



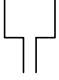

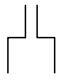



Figure 152 – Approximated particle pathway in a single stage.

The friction of each of the geometries shown in Figure 151 corresponds to a length of pipe providing the same friction, called the equivalent length, $L_{equivalent}$. These are provided in Table 58.

Table 58 – Overview of gas pathway geometries.

Geometry	Dimensions	Friction loss (equivalent pipe length) [35]
45 ° bend	 $D_{mean} = 0.10 \text{ m}$	15 m
Straight section	 $D_{mean} = 0.10 \text{ m}$	0.42 m
45 ° bend	 $D_{mean} = 0.10 \text{ m}$	15 m
Expansion	 $D_{mean} = 0.10 \text{ m} \rightarrow$ $D_{mean} = 0.17 \text{ m}$	10 m
Straight section	 $D_{mean} = 0.17 \text{ m}$	0.30 m
Contraction	 $D_{mean} = 0.17 \text{ m} \rightarrow$ $D_{mean} = 0.10 \text{ m}$	20 m
180° Bend	 $D_{mean} = 0.10 \text{ m}$	50 m
		$\Sigma = 110.72 \text{ m}$

Note that the straight sections only contribute with a very minor part of the pressure loss, why they could in this case be neglected. However, they are included for the sake of completion.

Pressure Model Setup

In the horizontal part, the elevation terms are zero. The acceleration is also assumed to take place in the horizontal part, why in the vertical part, the acceleration terms are zero.

Thus the model consists of the following expressions:

Horizontal pressure drop:

$$\Delta P_H = \frac{\rho_G \cdot \varepsilon_H \cdot v_{G,H}^2}{2} + \frac{\rho_P \cdot (1 - \varepsilon_H) \cdot v_{P,H}^2}{2} + F_{W,P} \cdot L_H + F_{W,G} \cdot L_{H,equivalent} \quad \text{Eq. 61}$$

Vertical pressure drop:

$$\Delta P_H = F_{W,P} \cdot L_V + F_{W,G} \cdot L_V + \rho_P \cdot (1 - \varepsilon_V) \cdot L_V \cdot g + \rho_G \cdot \varepsilon_V \cdot L_V \cdot g \quad \text{Eq. 62}$$

Where indices H and V refers to horizontal and vertical, respectively. Indices P and G refers to particles and gas, respectively. $L_{H,equivalent}$ is the equivalent of pipe which corresponds to the

friction created by the gas flowing through the various geometries in the system. v is the superficial gas. v_G and v_H are actual velocities of gas and particles respectively.

Parameters

The particle and gas specific data used for computing the pressure drop as well as the relevant geometries are provided in Table 60, while operation conditions of selected experiments for investigation of the pressure drop model is provided in Table 59.

Table 59 – Operating conditions for selected experiments.

Name	Particle flow [kg/hr]	Gas flow[kg/hr]	Average temperature [°C]
PoC #2	77.681	80	572
PoC #1	94.247	80	556
EX #1	94.247	100	534
PT#3	61.115	90	554
PT#4	77.681	90	508
PT#1	77.7	80	254
PT#2	77.7	146	211

Table 60 – Parameters for computing pressure drop.

Parameter	Value	Reference
Particle density	2300 kg/m ³	[104]
Particle diameter	12 μm	Measured volumetric diameter
Gas density	Given by: $P \cdot V = n \cdot R \cdot T$ and $M = 29$ g/mol	-
Gas viscosity	$\mu = f(T)$	[146]
Gravitational acceleration	9.82 m/s ²	[147]
L_H	0.10 m	Approximated horizontal length
$L_{H, equivalent}$	110 m	Equivalent horizontal length
L_V	0.40 m	Vertical lifting height
D_{Mean}	0.10 m	$D = \sqrt{L_{Depth} \cdot L_{Channel}}$

Evaluation of Acceleration terms

The acceleration terms, given as a standard kinetic energy expression can be evaluated once the void and actual gas and particle velocities are computed. For the horizontal sections, a semi-theoretical expression derived by Hinkle[148] can be applied:

$$v_{P,H} = v_G \left(1 - 0.0638 \cdot d_P^{0.3} \cdot \rho_P^{0.5} \right) \quad \text{Eq. 63}$$

From continuity:

$$\dot{m}_p = \rho_p \cdot (1 - \varepsilon_H) \cdot v_{p,H} \cdot A \Rightarrow \varepsilon_H = 1 - \frac{\dot{m}_p}{\rho_p \cdot v_{p,H} \cdot A} \quad \text{Eq. 64}$$

Where \dot{m}_p is mass flow [kg/s], A is cross sectional area, and ε is void. \dot{m}_p/A [kg/s/m²] can advantageously be computed as a single parameter.

$$v_{G,H} = \frac{V}{\varepsilon_H} \quad \text{Eq. 65}$$

For the vertical section the relevant equations are:

$$v_{p,v} = \frac{V}{\varepsilon_v} - v_{Stokes} \quad \text{Eq. 66}$$

Where v_{Stokes} is the terminal velocity, computed by Stokes settling law and

$$\dot{m}_p = \rho_p \cdot (1 - \varepsilon_v) \cdot v_{p,v} \cdot A \quad \text{Eq. 67}$$

Wall friction terms

The wall friction terms, terms (3) and (4) is given by Fannings friction factor [120]. For the horizontal sections:

$$F_{w,p} \cdot L_H = \frac{2 \cdot f_p \cdot \rho_p \cdot (1 - \varepsilon_H) \cdot v_{p,H}^2 \cdot L_H}{D_{mean}} \quad \text{Eq. 68}$$

And

$$F_{w,g} \cdot L_H = \frac{2 \cdot f_g \cdot \rho_g \cdot v^2 \cdot L_{H,equivalent}}{D_{mean}} \quad \text{Eq. 69}$$

The particle friction factor, f_p , is determined as:

$$f_p = \frac{3}{8} \cdot \frac{\rho_g}{\rho_p} \cdot \frac{D_{mean}}{d_p} \cdot C_D \cdot \left(\frac{v_{G,H} - v_{p,H}}{v_{p,H}} \right)^2 \quad \text{Eq. 70}$$

Where:

$$Re_p = \frac{\rho_F \cdot (U_{FH} - U_{PH}) \cdot d_p}{\mu} \quad \text{Eq. 71}$$

For $Re_p < 1$:

$$C_D = \frac{24}{Re_p} \quad \text{Eq. 72}$$

The gas friction factor, f_G , depends on Re and the relative roughness of the pipe. A value of 0.005 is assumed here. For the vertical section and expression is available for $F_{W,P} \cdot L_V$

$$F_{WP} \cdot L_V = 0.057 \cdot \frac{\dot{m}_P}{A} \cdot L_V \sqrt{\frac{g}{D_{mean}}} \quad \text{Eq. 73}$$

The gas friction factor is similar to the horizontal expression:

$$F_{W,P} \cdot L_V = \frac{2 \cdot f_P \cdot \rho_P (1 - \varepsilon_V) \cdot v_{P,V}^2 \cdot L_V}{D_{mean}} \quad \text{Eq. 74}$$

Where f_P again is assumed to 0.005.

Elevation terms

The elevation terms are evaluated as presented in the equations with the relevant lengths, voids and velocities.

Appendix E

2D-HX model and Implementation

The implemented mass and energy balances are given in the following.

The entrained flow from the particle bed:

$$\dot{m}_{P,E,i} = (\dot{m}_{P,B,i} + \dot{m}_{P,NE,i-2}) \cdot \eta_{Ent} \quad \text{Eq. 75}$$

The not entrained flow from the particle bed:

$$\dot{m}_{P,NE,i} = (\dot{m}_{P,B,i} + \dot{m}_{P,NE,i-2}) \cdot (1 - \eta_{Ent}) \quad \text{Eq. 76}$$

The dust from the freeboard:

$$\dot{m}_{P,D,i} = (\dot{m}_{P,D,i+1} + \dot{m}_{P,E,i-1}) \cdot (1 - \eta_{Sep}) \quad \text{Eq. 77}$$

The particle flow from freeboard to bed

$$\dot{m}_{P,B,i} = (\dot{m}_{P,D,i+1} + \dot{m}_{P,E,i-1}) \cdot \eta_{Sep} \quad \text{Eq. 78}$$

Energy balance for the i'th freeboard

$$\begin{aligned} (\dot{m}_{P,E,i-1} \cdot (T_{B,i-1} - T_R) + \dot{m}_{P,D,i+1} \cdot (T_{v,i-1} - T_R)) \cdot C_{P,P} + \dot{m}_{G,i+1} \cdot C_{P,G} \cdot (T_{v,i+1} - T_R) = \\ (T_{F,i} - T_R) \cdot (C_{P,P} \cdot (P_{B,i} + P_{D,i}) + \dot{m}_{G,i} \cdot C_{P,G}) \end{aligned} \quad \text{Eq. 79}$$

Energy balance for the i'th vertical channel:

$$\begin{aligned} (\dot{m}_{P,NE,i-2} \cdot (T_{B,i} - T_R) + \dot{m}_{P,D,i} \cdot (T_{f,i} - T_R)) \cdot C_{P,P} + \dot{m}_{G,i} \cdot C_{P,G} + \dot{m}_{P,D,i} \cdot (T_{f,i} - T_R) = \\ (T_{v,i} - T_R) \cdot (C_{P,P} \cdot (\dot{m}_{P,NE,i-2} + \dot{m}_{P,D,i}) + \dot{m}_{G,i} \cdot C_{P,P}) \end{aligned} \quad \text{Eq. 80}$$

Energy balance for the i'th particle bed:

$$(\dot{m}_{P,NE,i-2} \cdot (T_{v,i} - T_R) + \dot{m}_{P,B,i} \cdot (T_{f,i} - T_R)) = (T_{B,i} - T_R) \cdot (\dot{m}_{P,NE,i} + \dot{m}_{P,E,i}) \quad \text{Eq. 81}$$

Abbreviation has been used: Index *R* for *Reference*.

The model has been implemented in MatLab. The main script is Main2DHX.m, which calls the remaining functions and generates the results. In order to use the mass and energy balances stated above for all stages, all data vectors, including vectors with mass flow and temperatures have length $N+4$, where N is the number of stages modelled. The generally positions 3: $N-2$ contains the computed data, while the remain positions are set equal zero. The inlet gas temperature is set in $T_{v,N+4}$ and the particle feed in $\dot{m}_{p,E,1}$.

An overview of all used functions and scripts are given in Table 61. Some generic functions not developed during this work have been utilized as well for simpler and faster solution procedures.

Table 61 – Overview of scripts and functions used to solve the model of the 2D-HX.

Name	Description	Input
<i>Main2DHX.m</i>	Main file containing mass and energy balances in nested loops for iterative solution procedure.	None.
<i>n_S.m</i>	Function containing separation model.	Gas velocity, particle mass flow, temperature, pressure and geometric parameters and k_2 .
<i>n_E.m</i>	Function containing entrainment model.	Gas velocity, particle mass flow, temperature, pressure and geometric parameters and k_4 .
<i>rho_gas.m</i>	Function computing gas velocity, assuming ideal gas behaviour.	Temperature and Pressure.
<i>visc.m</i>	Function computing the gas viscosity using Sutherlands formula[149].	Temperature.
<i>func_v_gas.m</i>	Function computing local gas velocities assuming ideal gas behaviour	Temperature and pressure.
<i>Import_Model.m</i>	Import function reading values from the input file	Input file name and identification number of desired experiment.
<i>Opti_k.m</i>	Optimization routine for experimentally determined constants. Calls Model.m and generates plots	None.
<i>Model.m</i>	Function with similar content as Main2DHX, used for optimization of constants	k_4 , k_4 and heat loss constant.
<i>Inputfile.csv</i>	Input file containing geometric and operational parameters and experimentally obtained data. Data given as comma separated values.	None.

Name	Description	Input
<i>ceil2.m</i>	Generic function ceiling a number with desired steps[150].	A number and a target ceiling step.
<i>fminsearchbnd.m</i>	Generic optimizing function searching for the optimum solution within a specified range of parameter values[150].	Target function, initial guess, upper and lower parameter value limits. Solution options are optional.

Tolerances for the iteration loops have been set to $1 \cdot 10^{-7}$, $1 \cdot 10^{-4}$ and $1 \cdot 10^{-6}$ for the mass flow loop, temperature loop and overall loop, respectively. The target functions for the loops are the differences between guessed values and computed values. Table 62 displays the effect and selection criteria of the tolerances.

Table 62 – Determination of tolerances. Tolerances chosen marked by bold. Values computed from PoC#1.

	$1 \cdot 10^0$	$1 \cdot 10^{-1}$	$1 \cdot 10^{-2}$	$1 \cdot 10^{-3}$	$1 \cdot 10^{-4}$	$1 \cdot 10^{-5}$	$1 \cdot 10^{-6}$	$1 \cdot 10^{-7}$	$1 \cdot 10^{-8}$
$\dot{m}_{P,E,3}$ [kg/s]	-	-	-	0.022733	0.023115	0.023077	0.023078	0.023079	0.023079
$T_{v,3}$ [K]	463.385	512.448	512.446	512.446	512.447	512.447	-	-	-
$\eta_{Sep,3}$ [-]	-	-	-	0.789429	0.785670	0.786009	0.786037	0.786037	0.786037

Appendix F

Inspectional and Dimensional Analysis

Inspectional Analysis

When the governing equations for the process under consideration are known differential equations, dimensionless groups relevant for scaling the process can be identified by inspectional analysis. The groups will appear as factors in the non-dimensionalized equations.

For particle-gas systems, including the 2D-HX and fluidized beds, the governing equations are determined equations of motion and conservation of mass. Assuming constant μ and ρ the Newtonian equation of motion for the fluid reduces to the Navier-Stokes equation, Eq. 84. Furthermore, assuming diluted particle concentration (no particle interaction) the particles are described by Eq. 85. Eq. 82 and Eq. 83 are the conservation of mass for fluid and particles, respectively [128].

$$\nabla \cdot (\varepsilon \mathbf{v}_G) = 0 \quad \text{Eq. 82}$$

$$\nabla \cdot ((1 - \varepsilon) \cdot \mathbf{v}_P) = 0 \quad \text{Eq. 83}$$

$$\varepsilon \cdot \rho_G \cdot \left(\frac{\partial}{\partial t} \cdot \mathbf{v}_G + \mathbf{v}_G \cdot \nabla \mathbf{v}_G \right) + \nabla P + \chi \cdot (\mathbf{v}_G - \mathbf{v}_P) + \varepsilon \cdot \rho_G \cdot \mathbf{g} = 0 \quad \text{Eq. 84}$$

$$\rho_P (1 - \varepsilon) \cdot \left(\frac{\partial}{\partial t} \cdot \mathbf{v}_P + \mathbf{v}_P \cdot \nabla \mathbf{v}_P \right) - \beta \cdot (\mathbf{v}_G - \mathbf{v}_P) + (1 - \varepsilon) \cdot \rho_P \cdot \mathbf{g} = 0 \quad \text{Eq. 85}$$

where χ is the drag force between gas and particles. Introducing the following non-dimensional parameters:

$$\check{v}_G = v_G/v_0, \check{v}_P = v_P/v_0, \check{t} = v_0/(d_p/t), \check{\nabla} = d_p \cdot \nabla, \check{p} = p/\rho_P \cdot v_P^2$$

where v_0 is the characteristic velocity in the system. Eq. 82 to Eq. 85 transform into:

$$\nabla \cdot (\varepsilon \check{v}_G) = 0 \quad \text{Eq. 86}$$

$$\nabla \cdot ((1 - \varepsilon) \cdot \check{\mathbf{v}}_p) = 0 \quad \text{Eq. 87}$$

$$\varepsilon \cdot \rho_G \cdot \frac{v_0^2}{d_p} \cdot \left(\frac{\partial}{\partial t} \cdot \check{\mathbf{v}}_G + \check{\mathbf{v}}_G \cdot \check{\nabla}(\check{\mathbf{v}}_G) \right) + \frac{\rho_P \cdot v_0^2}{d_p} \check{\nabla}(\check{p}) + v_0 \cdot \chi \cdot (\check{\mathbf{v}}_G - \check{\mathbf{v}}_p) + \varepsilon \cdot \rho_G \cdot \mathbf{g} = 0 \quad \text{Eq. 88}$$

$$(1 - \varepsilon) \cdot \rho_P \cdot \frac{v_0^2}{d_p} \cdot \left(\frac{\partial}{\partial t} \cdot \check{\mathbf{v}}_p + \check{\mathbf{v}}_p \cdot \check{\nabla}(\check{\mathbf{v}}_p) \right) - v_0 \cdot \chi \cdot (\check{\mathbf{v}}_G - \check{\mathbf{v}}_p) + (1 - \varepsilon) \cdot \rho_P \cdot \mathbf{g} = 0 \quad \text{Eq. 89}$$

The non-dimensional form is obtained by multiplication each term with $d_p/(\rho_{par} \cdot v_0^2)$:

$$\varepsilon \cdot \left(\frac{\rho_G}{\rho_P} \right) \cdot \left(\frac{\partial}{\partial t} \cdot \check{\mathbf{v}}_G + \check{\mathbf{v}}_G \cdot \check{\nabla}(\check{\mathbf{v}}_G) \right) + \check{\nabla}(\check{p}) + \left(\frac{d_p \cdot \chi}{v_0 \cdot \rho_P} \right) \cdot (\check{\mathbf{v}}_G - \check{\mathbf{v}}_p) + \left(\frac{d_p \cdot \mathbf{g}}{v_0^2} \right) \cdot \left(\frac{\rho_G}{\rho_P} \right) \cdot \varepsilon = 0 \quad \text{Eq. 90}$$

$$(1 - \varepsilon) \cdot \left(\frac{\partial}{\partial t} \cdot \check{\mathbf{v}}_p + \check{\mathbf{v}}_p \cdot \check{\nabla}(\check{\mathbf{v}}_p) \right) - \left(\frac{d_p \cdot \chi}{v_0 \cdot \rho_P} \right) \cdot (\check{\mathbf{v}}_G - \check{\mathbf{v}}_p) + \left(\frac{d_p \cdot \mathbf{g}}{v_0^2} \right) \cdot (1 - \varepsilon) = 0 \quad \text{Eq. 91}$$

The term $d_p \cdot \chi / (v_0 \cdot \rho_{par})$ can be substituted with Re , as the drag force, χ , depends on Re [128]. Characteristic length scale can be normalized with d_p . The following non-dimensionalized groups can be identified:

$$\frac{\rho_G}{\rho_P}, Eu, Re, Fr, \frac{L_S}{d_p}, \frac{L_D}{d_p}$$

which is the relevant parameters for scaling purposes of the 2D-HX according to this analysis. The geometry is represented by the characteristic length of the separation chamber, L_{Sep} , and the depth of the system, L_D , normalized by d_p . Note that from an inspectional analysis point of view, the hydrodynamic behavior of all particle-gas systems can be described by the parameter set provided. This assumes that the particle-particle interaction is neglected, however. The particle-particle interaction can be expressed mathematically in various ways [151,152], and may yield additional scaling parameters. These are typically derived for fluidized beds, where particle-particle interaction is pronounced.

The requirement of governing equations capable of describing all relevant phenomena in the process is one of the short comings of the inspectional analysis.

Note that the model developed in Chapter 8 describing the separation process could also have been subjected to investigational analysis instead of the more general equations of motion and mass conservation. The result would have been that the separation process depends on Fr and

c_0 . The model has not been used for the inspectional analysis as it has not been verified over a wide range of equipment sizes and therefore cannot be accepted as generally valid.

Dimensional Analysis and Pi-theorem

The dimensional analysis is an alternative to the inspectional analysis, which, contrary to the inspectional analysis, does not require a complete model describing the process of interest. According to Zlokarnik [133], a typical dimensional analysis involves the following steps: (a) Definition of relevance list, (b) application of pi-Theorem⁸, (c) generation of dimensionless groups, and (d) identification of independent groups. For details on the procedure and the pi-theorem, please refer to Zlokarnik [133].

The relevance list is the list of process parameters relevant for the process. These parameters may be process-, geometry-, physical- or material related and may be either dimensional or non-dimensional. For the separation process in the 2D-HX, the relevance list is identified as:

$$\eta_{Sep} = f(d_p, PSD, \Phi, Agg, \rho_p, \mu_G, \rho_P, (\rho_P - \rho_G), geometry, c_0, v_G, g, \Delta p)$$

In a first approximation, agglomeration of particles is neglected and the particles are assumed spherical, which removes Agg and Φ from the list. Furthermore, PSD and c_0 are already dimensionless, why they for now can be omitted from the relevance list:

$$\eta_{Sep} = f(d_p, \rho_P, \mu_G, \rho_P, (\rho_P - \rho_G), geometry, v_G, g, \Delta p)$$

By application of the pi-Theorem it is possible to non-dimensionalize the above parameters. The core parameters are chosen to be ρ_P , d_p , and v_G . The resulting dimensional matrix is given in Table 63. The transformed unity matrix is also shown.

Table 63 – Original and transformed dimensional matrix for the separation process.

Original dimensional matrix										
	ρ_P	d_p	v_G	g	L_S	L_D	ρ_G	$\rho_P - \rho_G$	μ_G	Δp
Mass M	1	0	0	0	0	0	1	1	1	1
Length L	-3	1	1	1	1	1	-3	-3	-1	-1
Time T	0	0	-1	-2	0	0	0	0	-1	-2
Transformed dimensional matrix										
Z1 = M	1	0	0	0	0	0	1	1	1	1

⁸ Also known as the Buckingham pi-theorem.

Z2 =	0	1	0	-1	1	1	0	0	1	0
L+3M+T										
Z3 = -T	0	0	1	2	0	0	0	0	1	2

This yields the set of non-dimensional parameters presented in Table 64, remembering the two dimensionless groups from the relevance list.

Table 64 – Identified dimensionless groups for relevant scaling of 2-D HX.

Pi-sets	Manipulation of the Pi-sets
$\Pi_1 = g d_p / v_G^2$	$\Pi_1 \rightarrow \Pi_1^{-1} \cdot \Pi_2 = v_G^2 / (g \cdot d_p) = Fr$
$\Pi_2 = L_{sep} / d_p$	$\Pi_2 \rightarrow \Pi_6^{-1} \cdot \Pi_2^{-1} = (d_p \cdot \rho_G \cdot v_G) / \mu_G \cdot (d_p / L_S) \propto Stk$
$\Pi_3 = L_D / d_p$	$\Pi_3 \rightarrow \Pi_2^{-1} \cdot \Pi_3 = L_D / L_{sep}$
$\Pi_4 = \rho_g / \rho_P$	It is typically assumed that Π_5 and express the same Π_4 [133], why Π_4 (or Π_5) can be neglected
$\Pi_5 = (\rho_P - \rho_G) / \rho_P$	$\Pi_5 \rightarrow \Pi_5 \cdot \Pi_4^{-1} = (\rho_P - \rho_G) / \rho_P \cdot \rho_P / \rho_G = (\rho_P - \rho_G) / \rho_G$
$\Pi_6 = \mu_g / (d_p \cdot \rho_P \cdot v_G)$	$\Pi_6 \rightarrow \Pi_6^{-1} \cdot \Pi_2 = (L_S \cdot \rho_G \cdot v_G) / \mu_G = Re$
$\Pi_7 = PSD$	-
$\Pi_8 = c_0$	-
$\Pi_9 = \Delta p / (\rho_P \cdot v_G^2)$	$\Pi_9 = Eu$

According to the dimensional analysis, the parameters needed describe the separation process are:

$$\frac{(\rho_P - \rho_G)}{\rho_G}, Stk, Re, Fr, Eu, PSD, c_0, \frac{L_D}{L_{sep}}$$

Keeping these parameters constant during scale-up should ensure physical and dynamical similarity between the bench-scale and the full-scale system. Note that Π_6 could also have been transformed into Re_p . Additional geometry parameters could also have been introduced, if desired.

Appendix G

Publications

Two publications have been made in relation to this work:

- A patent, covering the modular construction of the 2D-HX concept, filled in October 2011,
- A short article summarizing the work investigating the powder flowability properties of raw meal, accepted by Powder Technology

Furthermore, a manuscript covering the experimental work on the PoC set-up is under preparation at the time of printing.

The two published items are found here after.



- (51) **International Patent Classification:**
B01J 8/12 (2006.01) F27B 7/20 (2006.01)
F27B 1/00 (2006.01)
- (21) **International Application Number:**
PCT/EP2012/070262
- (22) **International Filing Date:**
12 October 2012 (12.10.2012)
- (25) **Filing Language:** English
- (26) **Publication Language:** English
- (30) **Priority Data:**
11185241.4 14 October 2011 (14.10.2011) EP
61/547,298 14 October 2011 (14.10.2011) US
- (71) **Applicant:** DANMARKS TEKNISKE UNIVERSITET [DK/DK]; Anker Englundsvvej 1, DK-2800 Lyngby (DK).
- (72) **Inventors:** DAM-JOHANSEN, Kim; Frydsvej 19A, DK-3300 Frederiksvaerk (DK). RASMUSSEN, Claus Maarup; Skovlyporten 4-3, DK-2840 Holte (DK).
- (74) **Agents:** HERTLING, Peter et al.; Inspicos A/S, P.O. Box 45, Kogle Allé 2, DK-2970 Hørsholm (DK).
- (81) **Designated States** (unless otherwise indicated, for every kind of national protection available): AE, AG, AL, AM, AO, AT, AU, AZ, BA, BB, BG, BH, BN, BR, BW, BY, BZ, CA, CH, CL, CN, CO, CR, CU, CZ, DE, DK, DM, DO, DZ, EC, EE, EG, ES, FI, GB, GD, GE, GH, GM, GT, HN, HR, HU, ID, IL, IN, IS, JP, KE, KG, KM, KN, KP, KR, KZ, LA, LC, LK, LR, LS, LT, LU, LY, MA, MD, ME, MG, MK, MN, MW, MX, MY, MZ, NA, NG, NI, NO, NZ, OM, PA, PE, PG, PH, PL, PT, QA, RO, RS, RU, RW, SC, SD, SE, SG, SK, SL, SM, ST, SV, SY, TH, TJ, TM, TN, TR, TT, TZ, UA, UG, US, UZ, VC, VN, ZA, ZM, ZW.
- (84) **Designated States** (unless otherwise indicated, for every kind of regional protection available): ARIPO (BW, GH, GM, KE, LR, LS, MW, MZ, NA, RW, SD, SL, SZ, TZ, UG, ZM, ZW), Eurasian (AM, AZ, BY, KG, KZ, RU, TJ, TM), European (AL, AT, BE, BG, CH, CY, CZ, DE, DK, EE, ES, FI, FR, GB, GR, HR, HU, IE, IS, IT, LT, LU, LV, MC, MK, MT, NL, NO, PL, PT, RO, RS, SE, SI, SK, SM,

[Continued on next page]

(54) **Title:** AN APPARATUS FOR CONDUCTING PHYSICAL, CHEMICAL, OR BIOLOGICAL INTERACTION BETWEEN GASES AND SOLID PARTICLES

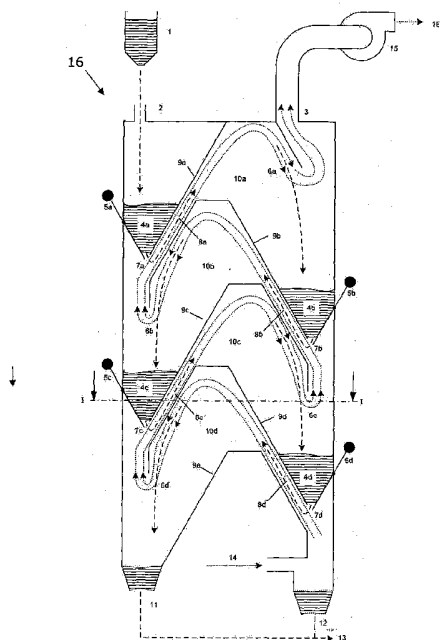


Fig. 1

(57) **Abstract:** The invention provides an apparatus for conducting interaction between gases and solid particles. The apparatus has a vertical hollow shaft with a vertical row of constrictions formed internally and defining a series of intercommunicating chambers in the shaft for guiding the gas and particles e.g. in counter current to effect interaction there between, e.g. for transferring thermal energy. To enable redesign of the apparatus and to enable an improved match between need for capacity and size of the apparatus, the invention provides an apparatus where the shaft comprises a stack of separate modules arranged vertically above each other or side-by-side whereby the apparatus becomes modular.

WO 2013/053890 A1



TR), OAPI (BF, BJ, CF, CG, CI, CM, GA, GN, GQ, GW, — *of inventorship (Rule 4.17(iv))*
ML, MR, NE, SN, TD, TG).

Declarations under Rule 4.17:

— *as to the applicant's entitlement to claim the priority of
the earlier application (Rule 4.17(iii))*

Published:

— *with international search report (Art. 21(3))*

AN APPARATUS FOR CONDUCTING PHYSICAL, CHEMICAL, OR BIOLOGICAL INTERACTION BETWEEN GASES AND SOLID PARTICLES

INTRODUCTION

The invention relates to an apparatus for conducting interaction between gases
5 and solids or between different solid particles, e.g. for conducting physical
and/or chemical and/or biological reactions between gases and solid particles,
e.g. for exchanging thermal energy and/or performing reactions between gas
and solid particles. More particularly, the invention relates to an apparatus
10 comprising a vertical hollow shaft comprising a vertical row of constrictions
formed internally and defining a series of intercommunicating chambers in the
shaft. The chambers are interconnected by gas conduits and by solids conduits.
The apparatus further comprises means for introducing and removing the solid
particles and gas into and out of the shaft in one or more vertically offset levels.

BACKGROUND OF THE INVENTION

- 15 Exchange of thermal energy between gas and solid particles is a challenge in
numerous industrial processes, due to the poor thermal conductivity in bulk
powders as well as the non-floating properties of solid particles and thereby the
need for mechanical or pneumatic forces to transport or agitate the solid
particles.
- 20 The purposes of the heat exchange process can be several, however often it is
desired to obtain a high efficiency in the heat transfer, i.e. obtain the highest
particle outlet temperature for heat exchange of a hot gas with cold particles, or
to obtain a controlled heating profile and specific outlet temperatures, i.e. in the
production of food, foodtech, biotech, or pharmaceutical components.
- 25 Heat exchangers for exchanging thermal energy between gas and solid particles
exist in different variants. One way of obtaining an efficient heat exchange is to

bring particles in direct contact with gas while moving gas and particles in opposite directions. This heat exchange principle is referred to as counter-current heat exchange. Typically, it is convenient to introduce the particles in top of a chamber and to establish an upwardly directed current of gas in the chamber. During descent of the particles against the current of the gas under influence of gravity, thermal energy is transferred between gas and particles, depending on the temperature difference and other system specific parameters.

In practise, it is difficult to achieve counter-current heat exchange since the gravimetric settling velocity of fine particles relative to the gas velocity is low. Therefore, in traditional gas and solid heat exchange systems, particles are typically suspended and transported with the gas. Once the suspended particles and the gas obtain a uniform temperature, the particles are separated from the gas to retrieve the particles. The particles are now, depending on the purpose of the process, either colder or hotter, than the particles fed to the process. The opposite applies for the gas. This mixing, transport, and separation process constitutes a stage in a gas/solid heat exchange process. Arranging several stages in a series, the heat exchange process obtains an overall counter-current-like pattern with increased thermal performance as a result, compared to the performance of a single stage. The actual performance will, among other things, depend on the number of stages in the series.

Typically, various chemical processes may result in transformation of substance during the process, and often, it is required to combine the thermal exchange process with other processes, e.g. for removing unwanted substances, to promote reactions of certain kinds, or to condition particles by e.g. grinding, agglomeration, or coating.

In bulk-industry, efficient thermal exchange processes are typically very important for the overall thermal efficiency of the plant and, depending on the specific purpose, also expensive to construct. In cement manufacturing, taken as an example, solid particles of different composition, e.g. fine calcium carbonate particles mixed with clay and other materials are typically heated in a pre-heater tower to near the calcination temperature before entering the

calciner and the rotary kiln. The particulate material is today heat exchanged in a cyclone based heat exchanger arranged in a kind of counter-current pattern with waste gas from the calcination and/or kiln processes.

The heat exchange is typically carried out in discrete steps whereby carbon or sulphur containing components may evaporate and/or partly oxidize forming
5 unwanted gases which may be emitted from the process. Furthermore, the very large heat exchangers are custom made and offer little flexibility with regards to the amount of material which is processed. Furthermore, the heat exchangers and the support structure are expensive to construct.

10 Heat exchangers are described in various publications including GB1039470, AU2109870, US 4,188,184, and GB1038965.

GB1039470 discloses a heat-exchange apparatus with a zig-zag shaft the bottom of which forms both an inlet for gas and an outlet for particles. Particles are feed to the upper part of the shaft and falls under gravity in the gas while
15 heat is exchanged between the gas and the particles.

AU 2109870 discloses an apparatus for conducting heat between gases and fine-grained solids. The apparatus consists of several separating chambers connected with each other by a gas channel such that material in one chamber can reach the chamber situated beneath via a material outlet. The material outlet opens
20 into the connecting channel leading gas from the chamber situated beneath. The disclosed apparatus is not very easy to scale up and down in size depending on the needed capacity, and typically, a device of the disclosed kind will be made in a "standard-size" which may not be suitable with a specific production in mind. This apparatus also does not enable different modules combined, e.g.
25 combustion sections etc. It is solely a heat exchanger for fine powders.

GB1038965 discloses a method of and apparatus for exchanging heat between solid particles and gases, GB1297185 discloses an apparatus for contacting a finely divided material with a hot gas, and US2888096 discloses a horizontal centrifuge separator.

US 4,188,184 discloses a container with deflectors.

DESCRIPTION OF THE INVENTION

The invention emanates from the existing heat exchangers, e.g. as described in AU2109870. It is an object of embodiments of the invention to overcome the disadvantages detailed above, particularly with regard to the size, cost, and lack of flexibility by use of the existing heat exchangers and to have an easily scaleable system.

Accordingly, the invention, in a first aspect, provides an apparatus as defined in claim 1.

10 According to the invention, at least the constrictions, or alternatively both the constrictions and the hollow shaft are modular whereby the apparatus can be configured and reconfigured with different numbers, sizes or shapes of constrictions or reconfigured with different distances between adjacent constrictions.

15 Herein "*modular*" refers to the feature that the apparatus comprises a number of predefined constrictions and/or shaft modules. The modules may be physical modules arranged against each other and being assembled rigidly to form an apparatus, or the modules may be design modules, i.e. virtual modules available for the designer of an apparatus. Accordingly, the apparatus can be designed
20 based on a number of predefined parameters, e.g. based on a width, height, or depth of the shaft or based on a number of chambers and thereby a number of constrictions or based on the distance between adjacent constrictions. In the following, this will be referred to as parametric design of the apparatus.

Herein, "*width*" refers to a dimension in a horizontal plane, "*height*" refers to a
25 dimension in a vertical plane and "*depth*" refers to a dimension in a horizontal plane and being perpendicular to the width. I.e. the terms are defined by the direction of gravity in a normal use situation for the apparatus.

Particularly, the modules may be detachably fixed to adjacent modules to enable reconfiguration of the apparatus.

The predefined modules may particularly have predefined interfaces determining the connectivity and/or the detachability between the module and adjacent
5 modules. As an example, the predefined interfaces may determine the way two adjacent modules are joined, it may determine a capability obtained by joining two predefined modules, it may determine a necessary resource required for assembling the modules, it may determine an expected duration for assembling the modules etc.

10 The predefined interface may e.g. comprise a horizontal interface adapted for joining the module with horizontally or at least substantially horizontally adjacent modules. Such an interface enables configuration and reconfiguration of an apparatus by changing its width and/or depth for a particular purpose.

The predefined interfaces may also comprise a vertical interface adapted for
15 joining the module with vertically adjacent modules. Such an interface enables stacking of the modules on top of each other and thereby enables configuration and/or reconfiguration of an apparatus by changing the height of the apparatus.

The vertical interface may e.g. include a specification of a capability of a module to carry a load, e.g. specified in an amount of modules of a specific kind which
20 can be carried by the module. Additionally, it may specify the weight of the module and thereby the load which a lower module is charged with.

The apparatus may comprise blinding elements adapted to blind an interface of a module at locations where no adjacent modules are foreseen. As an example, it may be desired to make an apparatus from a vertical row of modules. In this
25 case, all horizontal interfaces are blinded by blinding elements.

In one embodiment, the entire apparatus is made from prefabricated modules which can be moved by a truck and assembled on the location where the apparatus is to be used. The prefabricated modules could e.g. be detachably

fixed to each other such that the apparatus can be disassembled after use, moved to a new location and assembled again, either in an identical configuration and size or in different configuration and size.

Particularly, the hollow shaft may be assembled from wall elements or panels which are detachably joined. In that way, the total height, width, or depth of the apparatus may be amended based on a specifically required capacity. Several assembled panels may form an outer part of the apparatus, i.e. panels may form a boundary to the surrounding space. Particularly, such panels may be assembled in such a way that single panels or groups of panels can be removed to thereby provide access to an inner space within the apparatus, e.g. for maintenance purpose or for replacing single elements, e.g. for replacing the constrictions etc.

Additionally, several assembled panels may form an inner part of the apparatus.

As an example, an apparatus can be completely defined by a number of constrictions, say e.g. 5 constrictions arranged in a standard shaft with a homogeneous or gradually changing distance between each constriction due to thermal expansion of the gases. Should another task require a larger capacity, a new apparatus can be defined by a higher number of constrictions, or a higher height, width or depth of the shaft, i.e. the number of constrictions, the size of the constrictions, and/or the distance between the constrictions can change.

According to the invention, each module or each constriction may be selected based on a desired process. As an example, a number of modules may be for gas/solid heat exchange and other modules and constrictions may be for combustion, gasification or other reactions. The predefined module may therefore have a predefined purpose. The apparatus may e.g. include fluidized modules e.g. including heat transfer tubes. A bottom of the apparatus could e.g. be constituted by a fluid bed combustion reactor, or a calcinator.

To improve flexibility with regards to configuration and reconfiguration and to make scaling easy, the constriction may particularly have a 2-dimensional shape.

By definition, the 2-dimensional shape means that the shape of the constriction is defined in a 2-dimensional plane and that the last, third, dimension in space is defined merely by shifting the two dimensional shape along a vector extending in the third dimension e.g. perpendicular to the before mentioned plane.

- 5 If each constriction has a particular shape, e.g. the shape of a V or the shape of an L, e.g. in a plane in the X-Y directions of a Cartesian space, then this shape is maintained along the Z-direction in this space. Particularly, the 2-dimensional shape may be a shape in a vertical plane such that the Z-direction becomes out of the vertical plane, e.g. in a horizontal plane.
- 10 This feature is hereafter termed a 2-dimensional shape, and it enables easy scaling in the previously mentioned vertical Z-direction. Accordingly, the feature enables an easier reconfiguration of the apparatus either in the design phase or in the construction phase.

To further improve the scalability by use of constrictions with a 2-dimensional shape, the shaft may have a quadrangular or rectangular shape in a cross section perpendicular to a vertical axis. In this way, the constrictions may e.g. have straight edges and/or the constrictions may have a 2-dimensional shape.

Due to the 2-dimensional shape, it is possible to expand the constrictions in the third dimension and thereby to increase the capacity of the apparatus without expanding the constrictions in the first and second dimension or without changing the shape of the constrictions.

Accordingly, it becomes easy to match a specific need for capacity and/or size of the apparatus. The 2-dimensional shape is closely related to the aforementioned horizontal interface since it enables modification of the width and/or the depth of the apparatus depending on the actual need.

Particularly, it may be an advantage if all constrictions have identical shape and size. In that case, the production rate of the apparatus may be obtained by selection of a specific number of constrictions or by selection of a specific

distance between the constrictions in the shaft. In this way, an apparatus can be made by selecting constrictions from a library and using any number sufficient for a specific purpose. Also the attachment of the constrictions in the shaft may be standardised such that attachment of the constrictions in the shaft becomes
5 easy. Again, this is facilitated by the modularity – i.e. the apparatus may include a plurality of identical modules assembled by standardised interfaces.

The identical constrictions may e.g. be arranged in two groups such that every second constriction is in identical orientation and every other second constriction is in identical orientation being rotated by 180 degrees about a vertical axis
10 relative to the constrictions of the other group of constrictions. This provides a mirrored configuration where one group of constrictions corresponds essentially to the other group being mirrored in a central, vertical plane of symmetry.

The apparatus may e.g. comprise a top module, three heat exchange modules and a bottom module. All modules could be designed for heat exchange of raw
15 meal with hot process gas. In this example, the three heat exchange modules could include a number of identical and 2-dimensional constrictions. The top and bottom modules may be different from the modules with the identical constrictions, and the top and bottom modules may e.g. have a larger capacity for separation of particles from the gas. This apparatus may easily be scaled by
20 insertion of removal of constrictions and/or by changing the size of the constrictions in the third direction. The capacity may also be changed by amending the distance between the constrictions.

The 2-dimensional constrictions could be assembled e.g. from planar plates or from plates which are shaped or curved only in the mentioned 2-dimensions, i.e.
25 not double curved.

Generally, the apparatus may be for any kind of reaction or interaction between gas and solid particles or even between solids particles and other solid particles, e.g. reduction of ore with coke, clinker formation reactions etc.

Examples of physical interaction include transfer of thermal energy between the gas and particles, adsorption of gas species on particles, volatilization of liquid or solid material from the particles during heating i.e. drying of particles.

5 Examples of chemical interaction include: Combustion, gasification, pyrolysis, catalytic reactions, e.g. to reduce unwanted emissions.

Examples of biological interaction between gases and solid particles include gas phase enzymatic catalysis, sterilization and protein denaturation and degeneration

The apparatus can be used e.g. for the following purposes:

- 10 — Preheating of raw meal;
- Calcination of raw meal and other minerals;
- Formation of cement clinker;
- Heating of raw meal with insertion of Ca(OH)_2 or CaO at optimal temperatures for absorption of sulphur compounds;
- 15 — Steam production in exterior or interior walls and horizontal constrictions for utilization for e.g. power production. Note that the steam can also be heat exchanged in counter current relative to the gas to thereby achieve the best possible effect;
- Heating of raw meal with insertion of combustible compounds, e.g.
20 waste materials or fossil fuels;
- Removal of moist from particles, i.e. drying of grain;
- Heterogeneous catalytic processes, e.g. catalytic cracking , catalytic oxidation and catalytic reduction;

- Homogeneous gas phase reactions, e.g. selective non-catalytic reduction (SNCR) of NO by NH₃;
- Gas cleaning by heterogeneous reactions, e.g. sulphur absorption and HCl absorption processes;
- 5 — Heat treatment of solids, e.g. controlled sintering or sterilization;
- Coating of particles;

By the arrangement of the separate modules above each other in the vertical direction, also the chambers become vertically arranged above each other.

10 The gas and solids conduits extend between the chambers and thereby facilitate transport of the gas and solid particles between the chambers, i.e. the solids conduit extends from the particle bed of one chamber to an adjacent chamber.

During use of the apparatus, the particles and gas are introduced into the shaft. Typically the gas is introduced at the bottom or lower end of the shaft from where the gas flows from chamber to chamber via the gas conduits. The
15 particles are introduced at the top or upper end of the shaft into a first chamber in the vertical downward array of chambers.

Typically a stage in the process will consist of two chambers, each facilitating a mixing and a separation process, respectively. The particles are introduced into the first chamber and thereafter transported through the first chamber by the
20 stream of gas and during this step, the gas and particles can interact e.g. by transferring thermal energy from the gas to the particles. During this step, the constrictions will guide the gas and particles.

In the second chamber, the particles are separated from the gas and they are transferred via the particle conduit to the second chamber located below the first
25 chamber. For this purpose, the chambers may e.g. form a particle bed with a certain solid storage capacity. The particle bed thereby acts as a guard against

short-circuiting gas streams. If needed, the conduction of particles from chamber to chamber may be facilitated by mechanic or acoustic vibration or by application of pneumatic forces. Such means may be included in selected or in each of the modules, i.e. the modules may have predefined mechanical
5 actuation means for conducting the transport of particles.

In the consecutive stages, the process is repeated; the particles decent down into the first chamber and are transported to the second chamber with the stream of gas moving upwards in the chamber.

Each constriction could be a standard module designed to perform a specific task,
10 and the stack of modules can thereby be designed for specific process purposes by mixing constriction modules of different kind and size.

As an example, the individual constrictions could be adapted to constitute a stage in gas/solid heat exchange process consisting of a mixing and a separation process, a combustion chamber, a gas/solid reactor, or a catalytic reactor. The
15 constrictions may also be adapted to match different classes or types of particles, e.g. classes as defined by Geldart [D. Geldart, Types for Gas Fluidisation, *Powder Technology*, 7 (1973)] .

The solid particles and the gas may additionally be introduced and removed at different levels between the upper end of the shaft and the lower end of the
20 shaft depending on the process, temperature etc. Thus depending on the actual process conditions several gas and particle inlets and outlets can be used to optimize the process thermally or chemically. In some cases it can also be advantageous to design the system such that the internal gas and particle streams in the apparatus bypass one or more stages.

25 Internal valve means may be arranged relative to the constrictions and inner wall of the shaft such that flow of the solid particles between adjacent chambers can be controlled, i.e. valves, loop seals or local fluidization may control the flow in the particle conduits.

The valve means may form part of the shaft or they may form part of the constrictions. Particularly, the internal valve means may be comprised in each separate module.

Depending on the desired interaction, the apparatus may comprise modules with
5 different internal structure, e.g. relating to different processes selected from the group consisting of particle/gas heat exchange, drying, clinker formation, reactions including oxidation and reduction reactions, combustion, gasification, steam production, melting, granulation, condensation, absorption, adsorption, desorption, calcination, pyrolysis, sterilization, heat treatment or other
10 processes of similar kind and combinations thereof.

The planar design of the constrictions and walls enables steam production or process cooling using simple planar heat transfer surfaces incorporated in the constrictions or wall of the apparatus.

To ensure an even distribution of both gas and particles over the entire available
15 cross sectional area inside the apparatus, each module can be fitted with devices or guiding aids to ensure that the gas and particle streams are directed in the optimal direction. Thus the risk of gas and particles short circuiting a stage is minimized. This also makes it possible to operate only a part of the apparatus, as gas and particle streams are confined to the active area.

20 Particularly, it is an object to enable easy scaling of the apparatus. For that purpose, the apparatus may be delivered in the form of an assembly kit with components, e.g. planar panels, which can be assembled by use of pre-defined assembly elements to form a modular apparatus according to the invention.

In a second aspect, the invention provides an assembly kit for making an
25 apparatus of the kind described above. The assembly kit comprises a plurality of modules adapted for being assembled with adjacent modules to form the apparatus.

In a third aspect, the invention provides the use of an apparatus according to any of the preceding claims for manufacturing cement or minerals.

In a fourth aspect, the invention provides a method of designing or making an apparatus of the kind described above. The method comprises the steps of:

- 5 - providing a number of predefined modules each having a predefined configuration, the configuration including a predefined shape, size, and purpose in the assembled apparatus;
- selecting a number of modules;
- selecting a position of each module relative to adjacent modules;
- 10 - assembling the modules to form a vertical hollow shaft with a vertical row of constrictions formed internally and defining a series of intercommunicating chambers in the shaft,
- providing at least one gas conduit and at least one solids conduit connecting adjacent chambers,
- 15 - providing means for introducing and removing the solid particles and gas into and out of the shaft,

Each of the predefined modules may be assigned an expected capacity contribution of that module when assembled to other modules, and an expected total capacity could be calculated from the expected capacity contribution of each module.

The method may further comprise the step of determining a desired total capacity for the apparatus and selecting predefined modules for the apparatus until the expected total capacity corresponds to the desired capacity.

The method may further comprise the step of providing predefined modules with different configuration.

The method may comprise the step of providing a predefined interface between the modules and adjacent modules.

- 5 Particularly, the modules may include any of the features mentioned relative to the first aspect of the invention, e.g. the 2-dimensionally shaped constrictions and the mirrored arrangement of identical constrictions etc.

The process conditions may be of such kind, that the introduced particles will melt during the physical and/or chemical interactions with the gas and/or a
10 second a type of introduced particles. Thus the bottom stages can be designed to handle a liquid outlet.

The apparatus may contain access points, e.g. inspection manholes for access to the interior of the apparatus for cleaning, removal of deposits, repairs or inspection.

- 15 The method may comprise the step of introducing the solid particles into the particle inlet and introducing a gas which is hot relative to the solid particles into the gas inlet and providing interaction between the solid particles and gas within the chambers, e.g. such that the solid particles are melted during a physical and/or a chemical interaction with the gas and/or a second type particles which
20 are introduced into the shaft.

BRIEF DESCRIPTION OF THE DRAWINGS

The invention will now be described by way of an example with reference to following figures in which:

Figs. 1 and 2 illustrate an apparatus according to the invention;

- 25 Fig. 3 illustrates a section along line II in Fig. 1;

Figs. 4 and 5 illustrate details of modular designs, particularly with regards to extension of the apparatus in the Z-direction due to the 2-dimensional shape of the constrictions;

Fig. 6 Illustrates a combustion and gasification module between two heat
5 exchange modules;

Figs 7-12 illustrates different configurations of the apparatus and different shapes of the constrictions; and

Figs. 13-15 illustrate different valves for controlling flow out of the particle beds.

DETAILED DESCRIPTION OF EMBODIMENTS

10 Further scope of applicability of the present invention will become apparent from the following detailed description and specific examples. However, it should be understood that the detailed description and specific examples, while indicating preferred embodiments of the invention, are given by way of illustration only, since various changes and modifications within the scope of the invention will
15 become apparent to those skilled in the art from this detailed description.

The module based process design approach also provides option for easy expansion of a existing module based process, as a new stack of modules similar to the existing can be constructed adjacent to the existing, thus reducing complexity of expansion process, reducing the time of refurbishing the existing
20 process and reducing the overall complexity of the equipment, compared to expansions performed in the chemical industry today, where a new process is often designed and constructed independently from the existing design. Furthermore it is possible to stock different types of modules that can be combined for application in different kinds of systems.

25 Referring now to Figs. 1 and 2, an apparatus according to the invention comprises a vertical hollow shaft 16 with a vertical row of constrictions 9a, 9b, 9c, 9e formed internally and defining a series of intercommunicating chambers

10a, 10b, 10c, 10d in the shaft. The chambers are connected by gas conduits 8a, 8b, 8c, 8d each conducting a mix of gas and particles from one chamber to an adjacent chamber. The chambers are also connected by solids conduits 7a, 7b 7c, 7d which conduct solid particles from a particle bed 4a, 4b, 4c, 4d in one
5 chamber to a chamber located below that particle bed.

The constrictions 9a, 9b, 9c', 9e each have a shape which is defined in the illustrated 2-dimensional plane drawing of Fig. 2. This means that the third dimension is merely a height of the illustrated constrictions without changing the shape. Herein this is termed a 2-dimensional shape. As illustrated, the 2-
10 dimensional shape of all constrictions 9a, 9b, 9c', 9e are defined in a vertical plane.

During use, cold particles are fed from a feed tank 1 or fed from a preceding process in a continuous process facility. The particles enter the shaft through the inlet means 2 which facilitate introduction of the solid particles into the shaft.
15 From the inlet means 2, the particles move to a top particle bed 4a at the top stage. Hot process gas is introduced at the bottom of the system via the inlet 14 which constitutes the means for introducing the gas into the shaft.

The particles from the bottom of particle bed 4a are released via the solids conduit 7a and mixed with gas which flows in the chamber 10b located below
20 the particle bed 4a. At the exit of the solids conduit 7a, the particles are caught and form a combined gas and particle flow in the gas conduit 8a. At this location, the gas and particles flow in the same direction.

The rate of the particles leaving the particle bed 4a is controlled by an internal valve means 5a which thereby forms a particle rate control device.

25 The process repeats it self from the top toward the bottom. In this process, the solid particles are transported from particle bed to particle bed in descending direction.

I.e. The heat exchange between the hot gas and the cold particles takes place in the gas conduits 8a, 8b, 8c, 8d. Each chamber comprises a particle separation section 6a, 6b, 6c, 6d. At this point, the particles are separated from the gas and at the top of the shaft, the gas exits through the outlet means 3 supported by the fan 15. The particles separated from the gas fall to one of the particle beds 4a, 4b, 4c, 4d and via a particle bed, the particles are reintroduced into the gas stream below that particle bed.

The above described is taking place in all intermediate stages/modules.

At the bottom, two particle outlets 11 and 12 are located. The particles separated from the gas at 6d end at the particle outlet 11 and is joined with the material from the secondary particle outlet 12 and transported to the calciner (not shown but indicated by numeral 13). The secondary particle outlet leads out all particles not caught by the gas at 7d.

As the particles are fed through the particle inlet 2 are cold and the process gas introduced at the gas inlet 14 is hot, gradual heating of the particles and cooling of the gas takes place as the particles travel down through the process.

Additional separation systems, e.g. comprising a cyclone, an electrostatic filter etc. can be applied on the gas outlet 3 before the fan 15 to thereby obtain a particle free gas. Such a cyclone or filter would be suitable if the gas that leaves the system contains too high a load of particles for the induced draft fan 15.

Fig. 2 illustrates schematically the apparatus in a perspective view. In this view, it is illustrated that the outer walls of the shaft are made of modular panels 17. In the illustration only the two side walls 18, 19 are shown. The apparatus also comprises front and rear walls 20, 21 such that the shaft becomes closed between the top and bottom. The panels are essentially identical and they are assembled based on a need for a specific height, width or depth. By use of the panels, not only the constrictions but also the shaft becomes modular.

According to the invention, the constrictions are modular. That means that the number of constrictions, the size of the constrictions, and/or the distance between the constrictions can change but the constrictions have the same shape.

Fig. 2 also illustrates how the size of the constrictions can be changeable by
5 making the constrictions from panels 22, 23.

Fig. 3 illustrates that a section along line I-I in Fig. 1. In this view it is clear that the constriction can be scaled in the Z direction indicated by the arrow. Since the constrictions are 2-dimensional, the shape does not change when making this scaling, and the apparatus can be designed parametrically by specifying
10 merely the length in the Z-direction.

Fig. 4 illustrates that the apparatus can be made from modules $n-1$, n , $n+1$ where each module comprises a number of wall panels 17 and a number of constrictions 24 which again could be made from a number of separate panels as illustrated in Fig. 2. In Fig. 5 it is illustrated how the modules can be arranged
15 side-by-side to form different sizes of the apparatus in the depth, i.e. in the Z-direction. Again, due to the 2-dimensional shape, the Z-dimension does not change the shape of the constrictions and the scaling of the apparatus in the Z-dimension becomes easy to manage.

Fig. 6 illustrates details of a process where fuel and/or combustion air is injected
20 through an inlet 25 in one of the wall panels. Generally, any one of the mentioned modules, panels or constrictions may comprise process relevant features not mentioned specifically herein, including injection or rejection openings for feeding or removing substances from the shaft, structures for providing a homogenous flow or for enhancing the interaction between the
25 particles and gas. Level indicated with 26 is gas/solid heat exchange modules. And level indicated with 27 is a combustion/gasification module. Combustion takes place in chamber 28 and gasification takes place in the particle bed 29. The arrow 30 illustrates a fuel particle trajectory.

Figs. 7a, 7b, and 7c illustrate examples of different kinds of combustion modules
30 incorporated in the bottom stage. Level indicated with 31 is gas/solid heat

exchange modules. Heat exchange gas is provided in the inlet 32, Fluidisation air is provided in the inlet 33. A fluid bed module 34 with an air outlet 35 is formed in the bottom. A distribution plate 36 is provided in the bottom. The apparatus further comprises an overflow 37.

- 5 Referring to Fig. 7b, solid fuel and combustion air is provided at the inlet 38, particle outlet is provided at the outlet 39 and ash is removed from the bottom at 40. 41 is a grate firing module and grate firing takes place in the grate firing chamber 42. Heat exchange gas is provided at 43.

- 10 Numbering in Fig. 7b also applies in Fig. 7c. Herein 44 is a suspension firing module and suspension firing takes place in chamber 45.

Fig. 8a illustrates an apparatus with an intermediate gas inlet and outlet configuration. Fig. 8b illustrates an apparatus with several inlets for higher particle outlet temperature. Fig. 8c illustrates one way of configuring particle inlets and outlets.

- 15 In Figs. 8a, 8b and 8c, the following numbers apply. 46 is a particle inlet, 47 is a gas outlet, 48 is a gas inlet and 49 is a particle outlet.

Figs. 9-12 illustrate different shapes for horizontal constrictions. Numbers from Figs. 8a-8c apply.

- 20 Figs. 13-15 illustrate different internal valve structures for controlling a particle flow rate. Fig. 13 illustrates a loop seal-like control valve where 50 is an air supply for particle flow rate control. Fig. 14 illustrates a local fluidization control device, and Fig. 15 illustrates the same device with a mechanical control structure 51 which rotates about its centre of rotation 52.

EMBODIMENTS

- 25 Any of the below mentioned embodiments may apply:

Embodiment 1. An apparatus for conducting physical and/or chemical and/or biological interaction between gases and solid particles, the apparatus comprising a vertical hollow shaft having at least one gas inlet for introducing the gas into the shaft, at least one particle inlet for introducing the solid particles
5 into the shaft, at least one gas outlet for removing the gas from the shaft, and at least one particle outlet for removing the solid particles from the shaft, the shaft forming inside a series of intercommunicating chambers separated by a plurality of constrictions such that at least one gas conduit and at least one solids conduit connect adjacent chambers, wherein the constrictions are modular.

10 I.e. the invention may generally relate to an apparatus which is modular, i.e. constructed and assembled from predefined modules

Embodiment 2. An apparatus according to embodiment 1, comprising
constriction with a 2-dimensional shape.

15 Embodiment 3. An apparatus according to embodiment 1 or 2, comprising a plurality of identical constrictions.

Embodiment 4. An apparatus according to embodiment 3, where constrictions of a first series corresponds to constrictions of a second series being mirrored in a vertical plane extending centrally through the shaft.

20 Embodiment 5. An apparatus according to embodiment 4, wherein the constrictions of the first series are arranged between constrictions of the second series.

Embodiment 6. An apparatus according to any of the preceding embodiments, wherein the constrictions are releasably attached in a vertical row of modules in the shaft.

25 Embodiment 7. An apparatus according to any of the preceding embodiments, wherein the shaft has a quadrangular cross section perpendicular to a vertical axis.

Embodiment 8. An apparatus according to any of the preceding embodiments, wherein the means for introducing the solid particles into the shaft is adapted for introduction of the particles in an upper end of the shaft and the means for introducing the gas into the shaft is adapted for introduction in a lower end of the shaft.

Embodiment 9. An apparatus according to embodiment 8, wherein at least one of the means for introducing the solid particles and the gas into the shaft is adapted for introduction of the particles or gas in different levels between the upper end of the shaft and the lower end of the shaft.

Embodiment 10. An apparatus according to any of the preceding embodiments, where each chamber forms a particle bed in which the solid particles will accumulate as a result of flow conditions in the chamber, and where the chamber is designed such that the particle bed acts as a guard against short-circuiting gas streams.

Embodiment 11. An apparatus according to embodiment 10, wherein each solids conduit extends from the particle bed of one chamber to an adjacent chamber.

Embodiment 12. An apparatus according to any of embodiments 10-11, where each particle bed and corresponding solids conduit is shaped such that transport of particles from each particle bed to the adjacent chamber is facilitated and controlled by mechanic means, acoustic vibration or by application of pneumatic forces or a combination thereof.

Embodiment 13. An apparatus according to any of the preceding embodiments, where the constrictions and the hollow shaft are formed by individual components to enable reconfiguration with different numbers, sizes or shapes of constrictions or reconfiguration with different distances between adjacent constrictions.

ADDITIONAL EMBODIMENTS

The invention may further provide embodiments with any of the below numbered features or combinations thereof.

1. An apparatus comprising internal valve means arranged relative to the
5 constrictions to control a flow of fine-grained solids between adjacent chambers.
2. An apparatus wherein the internal valve means is comprised in each separate module.
3. An apparatus comprising modules with different internal structure.
4. An apparatus wherein the difference in structure relates to different processes
10 selected from the group consisting of particle/gas heat exchange, drying, clinker formation, reactions including oxidation and reduction reactions, combustion, gasification, steam production, melting, granulation, condensation, absorption, adsorption, desorption, calcination, pyrolysis, sterilization, heat treatment and combinations thereof.
- 15 5. An apparatus wherein the constrictions are constituted by planar plates or plates curved in only one plane.
6. An apparatus further comprising at least one additional stack of separate modules arranged vertically above each other whereby each module forms one chamber of the series of intercommunicating chambers or at least forms a part
20 of one chamber of the series of intercommunicating chambers.
7. An apparatus further comprising wall elements comprising heat transfer surfaces which can be used for process cooling or steam production.
8. An apparatus further comprising particle distribution structures arranged internally in the shaft or arranged external to the shaft, the particle distribution
25 structures improving particle distribution within the apparatus.

9. An apparatus where the hollow shaft is formed with at least one opening of a size allowing a person to enter into at least one of the chambers.

CLAIMS

1. An apparatus for conducting physical and/or chemical and/or biological interaction between gases and solid particles, the apparatus comprising a vertical hollow shaft having at least one gas inlet for introducing the gas into the shaft, at least one particle inlet for introducing the solid particles into the shaft, at least one gas outlet for removing the gas from the shaft, and at least one particle outlet for removing the solid particles from the shaft, the shaft forming inside a series of intercommunicating chambers separated by a plurality of constrictions such that at least one gas conduit and at least one solids conduit connect adjacent chambers, wherein at least one of the constrictions and the shaft comprises a number of predefined modules.
2. An apparatus according to claim 1, wherein modules are detachably fixed to adjacent modules.
3. An apparatus according to claim 1 or 2, wherein each predefined module has a predefined interface specifying connectivity to adjacent modules.
4. An apparatus according to claim 3, where the predefined interface comprises a horizontal interface adapted for joining the module with horizontally adjacent modules.
5. An apparatus according to claim 3 or 4, where the predefined interface comprises a vertical interface adapted for joining the module with vertically adjacent modules.
6. An apparatus according to any of the preceding claims, comprising blinding elements adapted to blind an interface of a module at locations where no adjacent modules are foreseen.
7. An apparatus according to any of the preceding claims, wherein each predefined module has a predefined shape, size and purpose.

8. An apparatus according to any of the preceding claims, comprising
constriction with a 2-dimensional shape.
9. An apparatus according to any of the preceding claims, where constrictions of
a first series corresponds to constrictions of a second series being mirrored in a
5 vertical plane extending centrally through the shaft.
10. An apparatus according to claim 9, wherein the constrictions of the first
series are arranged between constrictions of the second series.
11. An apparatus according to any of the preceding claims, where each chamber
forms a particle bed in which the solid particles will accumulate as a result of
10 flow conditions in the chamber, and where the chamber is designed such that
the particle bed acts as a guard against short-circuiting gas streams.
12. An apparatus according to claim 11, where each particle bed and
corresponding solids conduit are shaped such that transport of particles from
each particle bed to the adjacent chamber is facilitated and controlled by
15 mechanic means, acoustic vibration or by application of pneumatic forces or a
combination thereof, the controlled mechanic means forming part of at least one
of the modules.
13. An assembly kit for making an apparatus according to any of claims 1-12,
the assembly kit comprising a plurality of modules adapted for being assembled
20 with adjacent modules to form the apparatus.
14. Use of an apparatus according to any of the preceding claims in
manufacturing of cement or minerals.
15. A method of designing or making an apparatus according to any of claim 12
comprising the steps of:

- providing a number of predefined modules each having a predefined configuration, the configuration including a predefined shape, size, and purpose in the assembled apparatus;
- selecting a number of modules;
- 5 - selecting a position of each module relative to adjacent modules;
- assembling the modules to form a vertical hollow shaft with a vertical row of constrictions formed internally and defining a series of intercommunicating chambers in the shaft;
- providing at least one gas conduit and at least one solids conduit
- 10 connecting adjacent chambers; and
- providing means for introducing and removing the solid particles and gas into and out of the shaft.

16. A method according to claim 15, comprising the steps of:

- assigning to each of the predefined modules, an expected capacity
- 15 contribution of that module when assembled to other modules;
- calculating an expected total capacity from the expected capacity contribution of each module.

17. A method according to claim 16, comprising the step of determining a desired total capacity for the apparatus and selecting predefined modules for the

20 apparatus until the expected total capacity corresponds to the desired capacity.

18. A method according to any of claims 15-17, where the step of providing predefined modules comprises providing modules with different configuration.

19. A method according to any of claims 15-18, where the step of providing predefined modules comprises providing a predefined interface between the modules and adjacent modules.

20. A method according to claim 19, where predefined interfaces are defined for
5 a vertical configuration where the modules are positioned vertically over or under adjacent modules and/or for horizontal configuration where the modules are positioned horizontally next to adjacent modules.

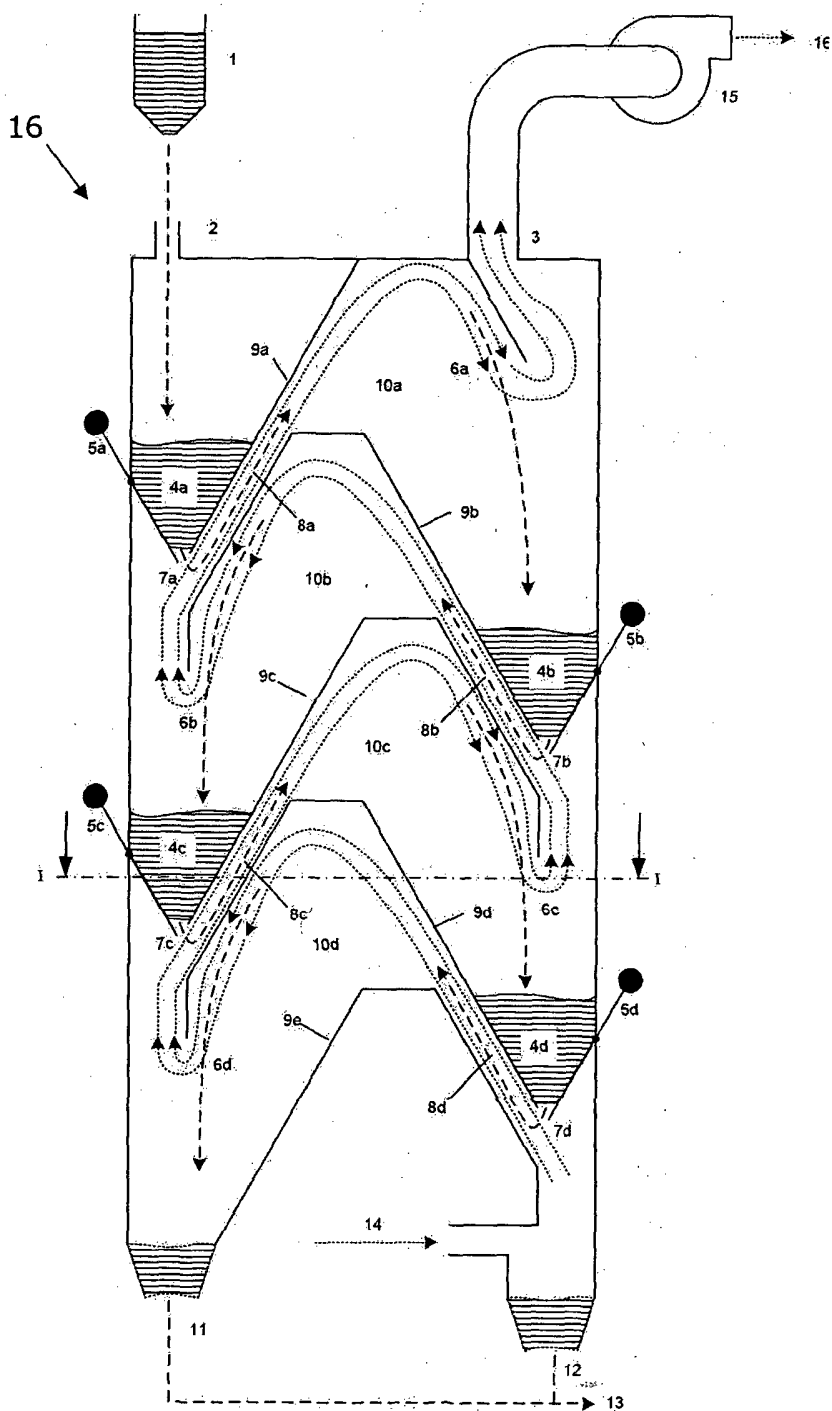


Fig. 1

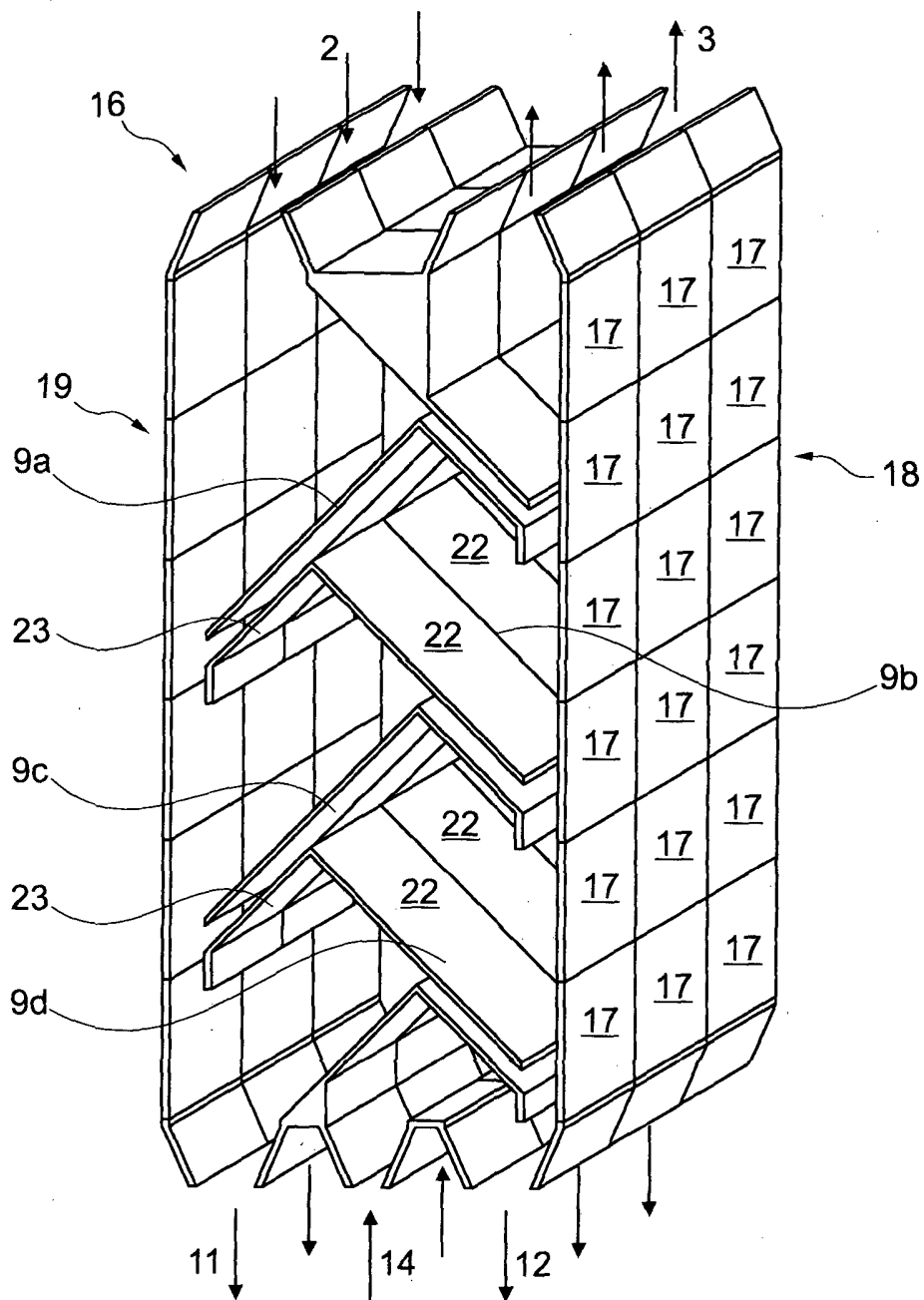


Fig. 2

3/10

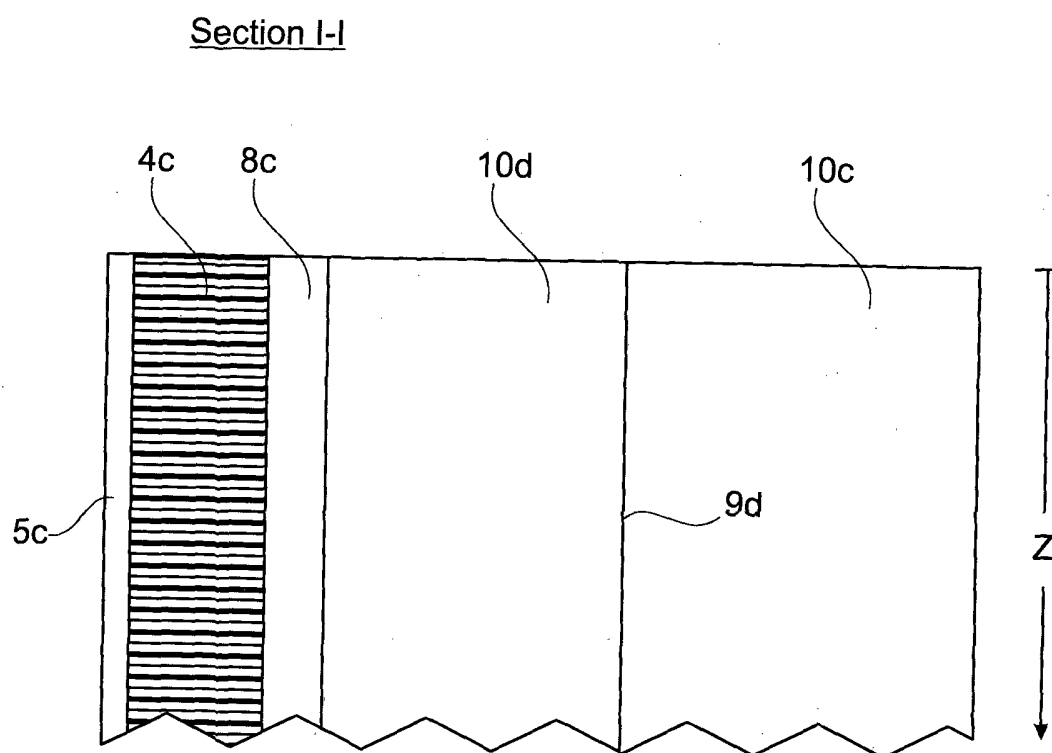


Fig. 3

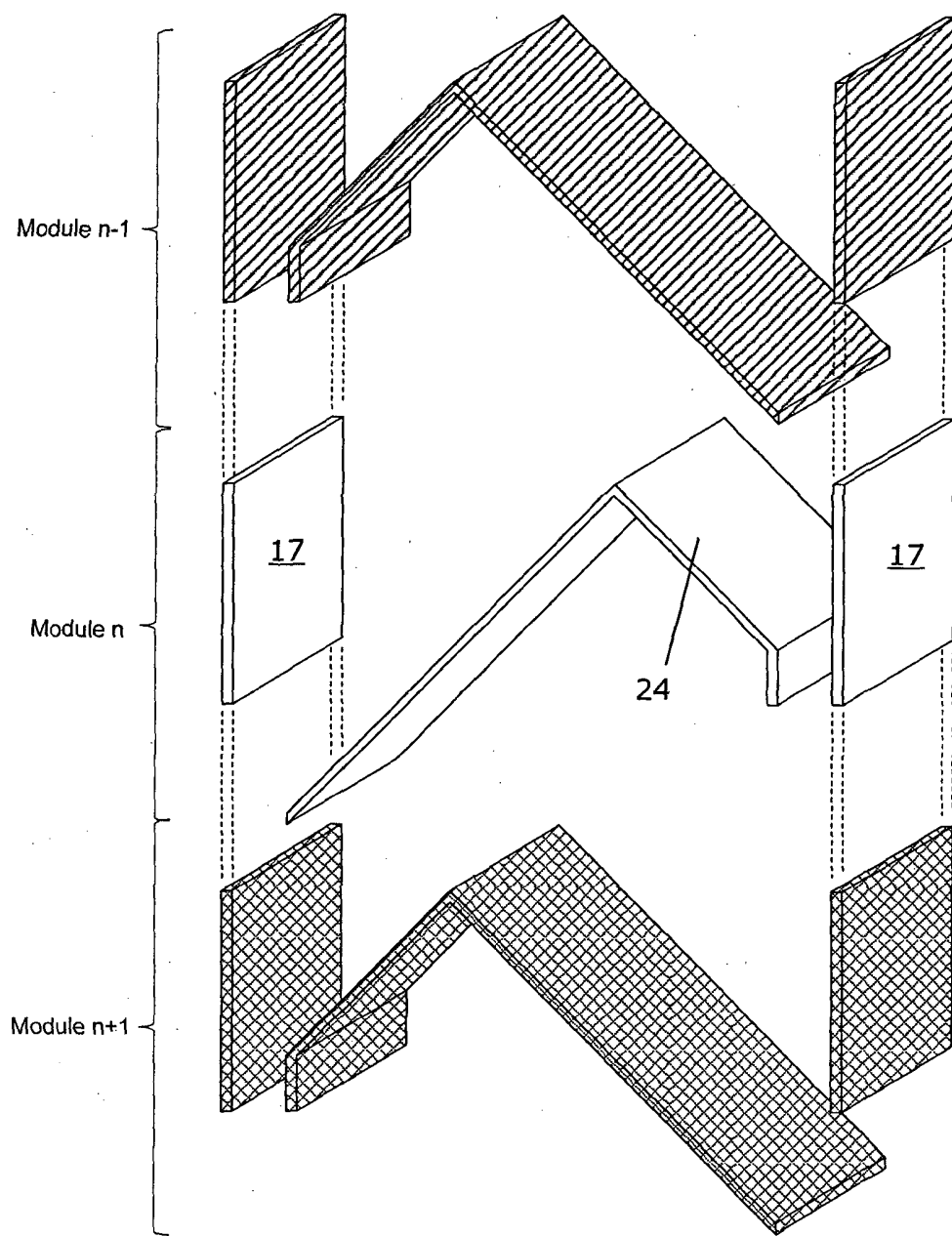


Fig. 4

5/10

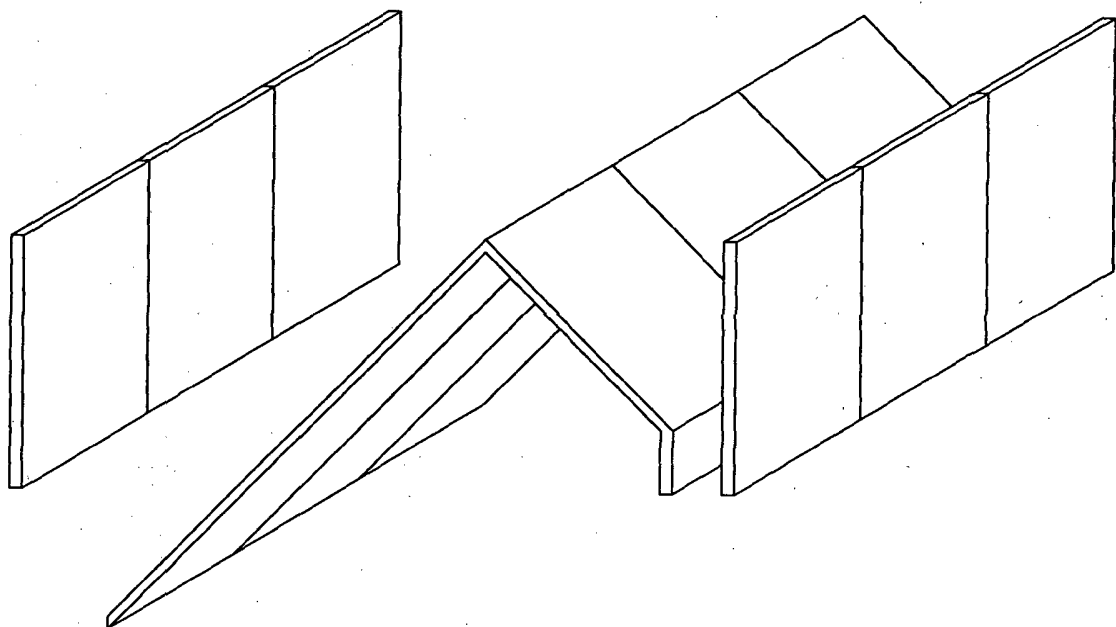
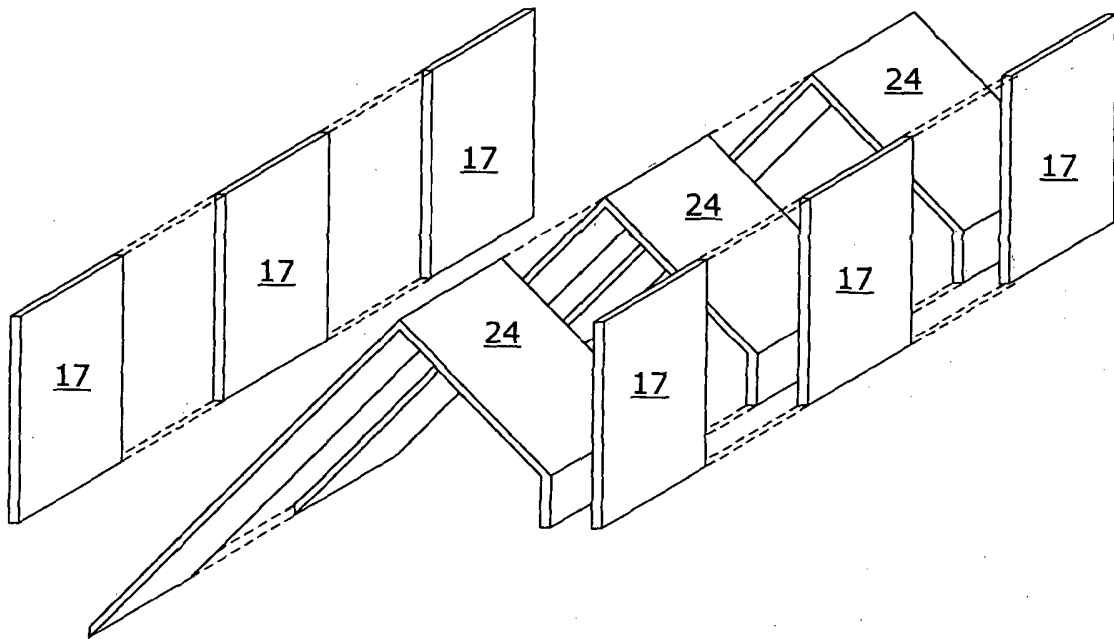


Fig. 5

6/10

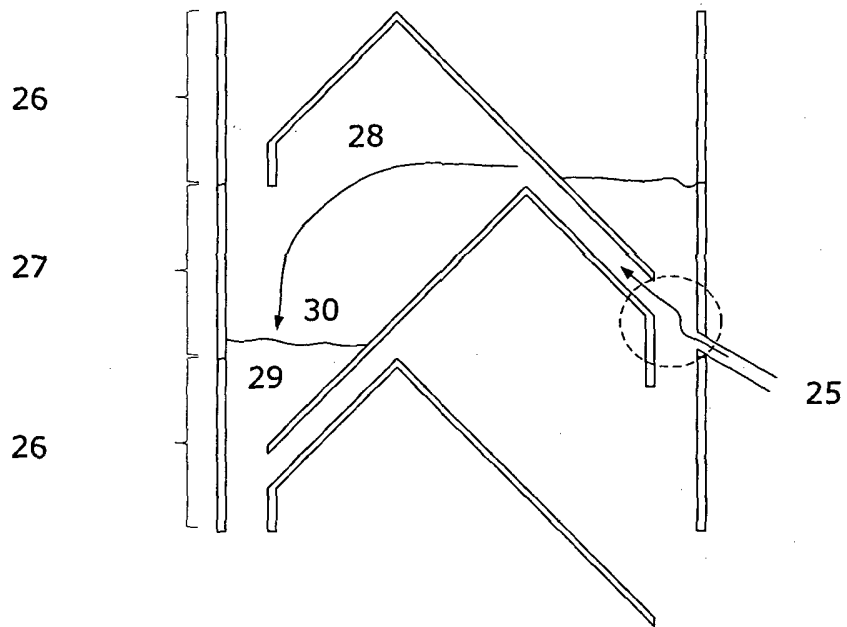


Fig. 6

7/10

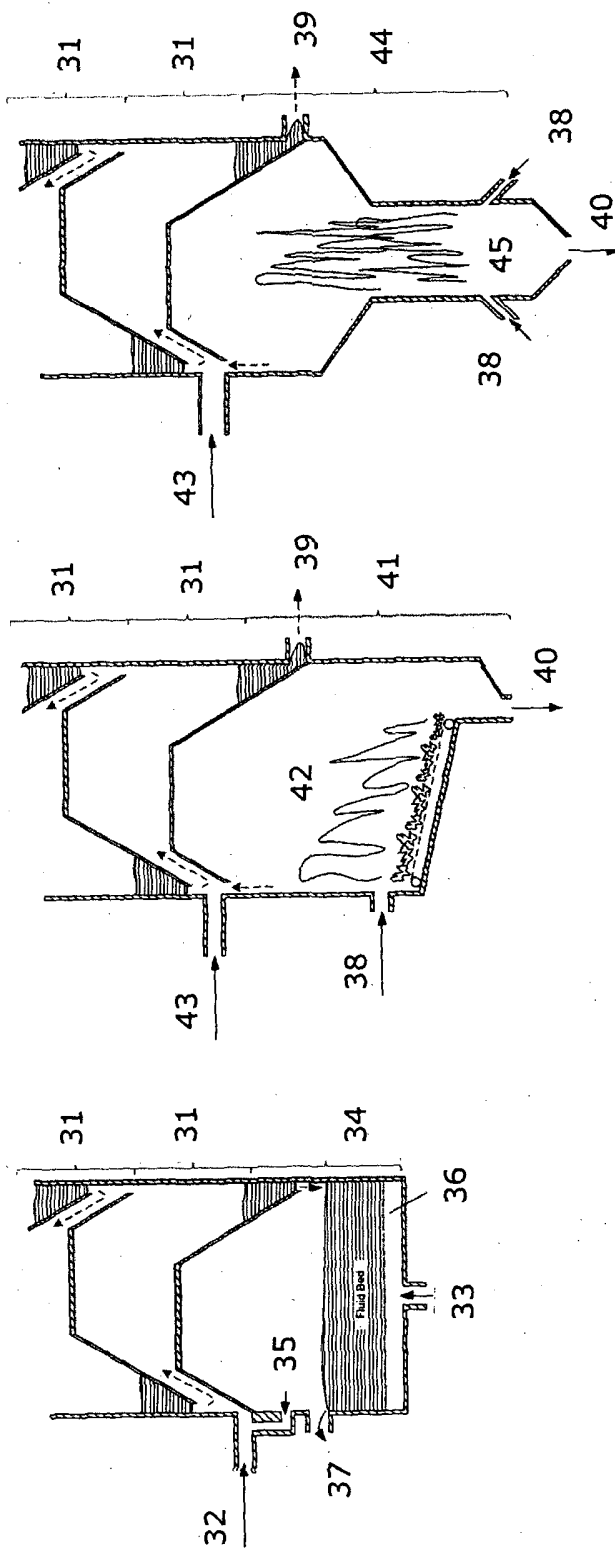


Fig. 7c

Fig. 7b

Fig. 7a

8/10

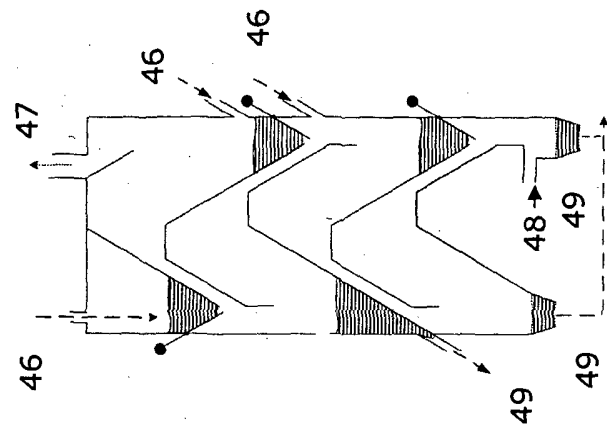


Fig. 8a

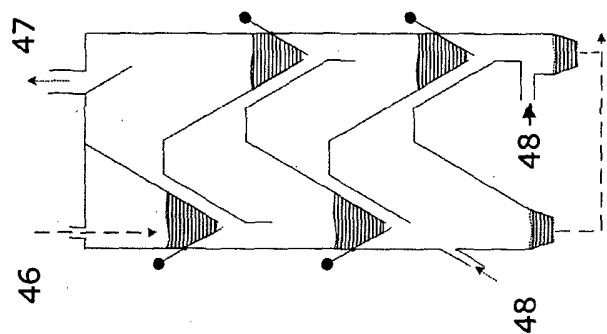


Fig. 8b

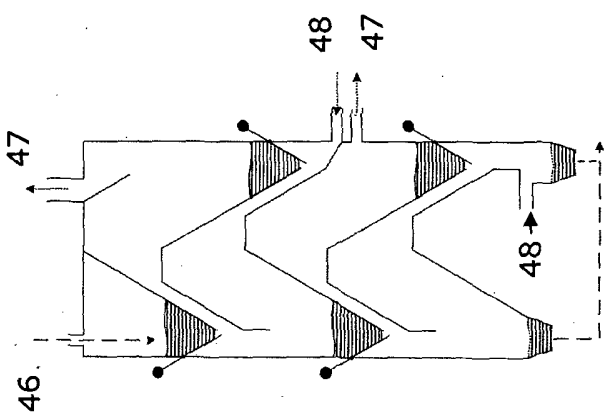


Fig. 8c

9/10

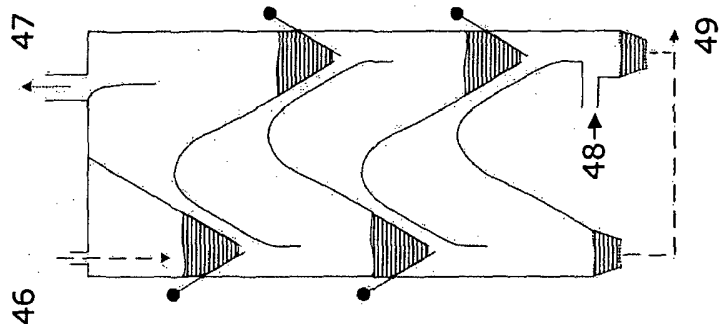


Fig. 9

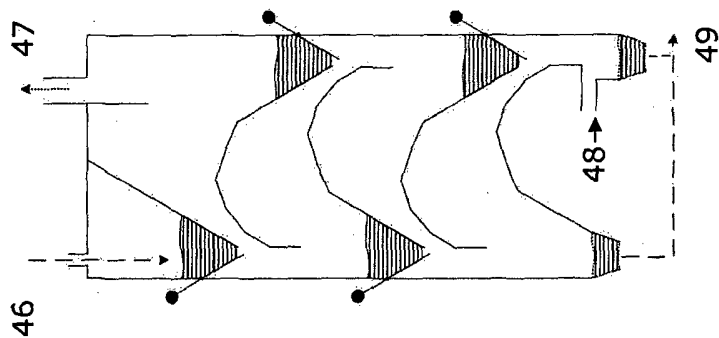


Fig. 10

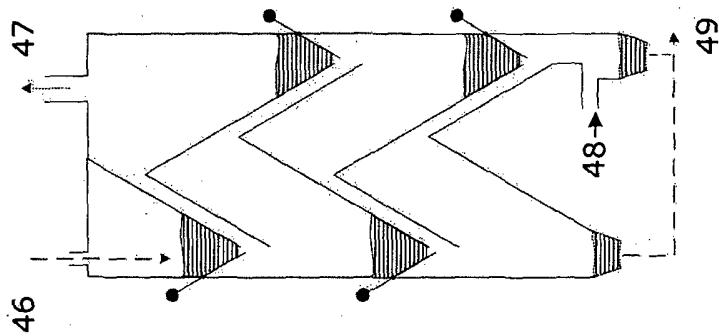


Fig. 11

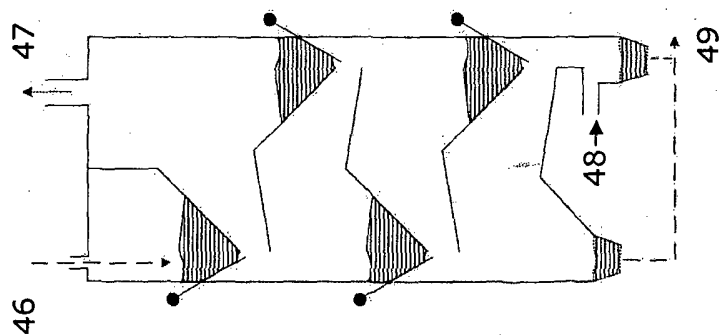


Fig. 12

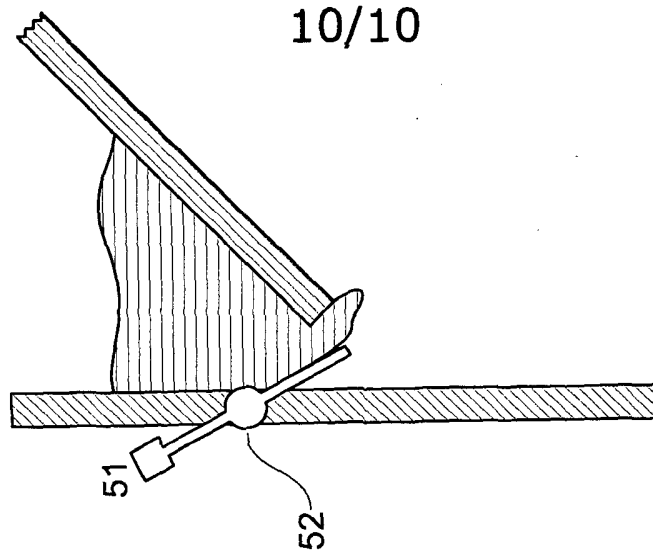


Fig. 15

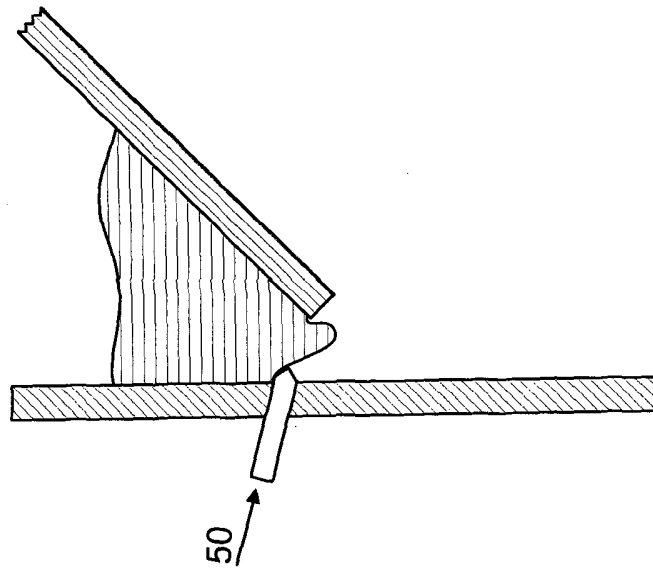


Fig. 14

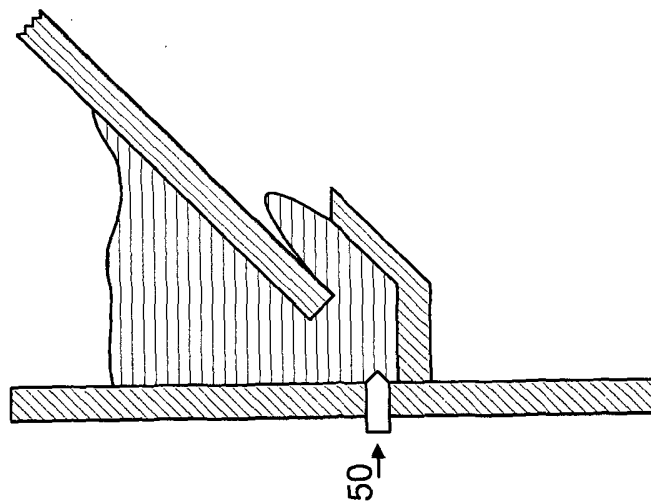


Fig. 13

High Temperature Cement Raw Meal Flowability

Claus Maarup^a, Klaus Hjuler^b, and Kim Dam-Johansen^{a}*

^a Department of Chemical and Biochemical Engineering, Technical University of Denmark, Building
229, 2800 Kgs. Lyngby, Denmark.

5 ^b FLSmidth A/S, Vigerslev Allé 77, 2500 Valby, Denmark

* Corresponding author, email: KDJ@kt.dtu.dk, +45 45 25 28 45

Abstract

The flowability of cement raw meal is investigated at temperatures up to 850°C in a specially designed monoaxial shear tester. Consolidation stresses of 0.94, 1.87 and 2.79 kPa are applied. The results show
10 that the flowability is reduced as temperature is increased above 550°C, indicated by increasing unconfined yield strength and reduced flowability factors. Deviation and reproducibility are acceptable for all temperatures but 850°C where belite formation and possibly also calcination sinter the raw meal.

Keywords

15 Powder flowability, monoaxial shear tester, high temperature, cement raw meal

1. Introduction

In the literature the term powder flowability is often encountered, describing the ability of a powder to flow, but this quantity is not easily defined nor measured [1]. Powder flow properties depend not only on the chemical compounds in the particles, but also on particle size distribution, shape, density,
20 surface texture, moisture content, electrostatic charge, and consolidation stress and time [2]. Furthermore, the flow properties depends on equipment design, i.e. surface roughness, dimension of openings, etc. [1]. The complex nature of powder flowability complicates equipment design from a priori knowledge.

Relations based on semi-theoretical or empirical relations [3,4] between design parameters for
25 powder handling equipment, e.g. siloes and hoppers, and powder properties have been available for
decades. An example is the work of Jenike [5], who developed relations between the measured shear
forces in a Jenike shear test cell and the design parameters of hoppers, which still is widely used today
[3]. Lately, advances in computational particle fluid dynamics have shown that the behavior of some
powders can be represented by a fully theoretical approach [6]. However, the application of these
30 models still seems limited to certain non-cohesive powders [6-8], why powder testing is still essential.

The majority of powder testing procedures involve inducing and measuring a shear force required to
form a shear region in a powder sample, which has been consolidated by a known normal force [4].
The equipment used ranges from simple uniaxial tests [4], to more complex automated ring shear
testers [9,10]. Equipment for characterizing powder flowability by the angle of repose (AOR), such as
35 the device used by Wouters and Geldart [11], are widely used in the industry, but the lack of known
consolidation and shear stresses in these devices only enables qualitative comparisons of powders.

If the unconfined yield strength, σ_c , and the consolidation stress, σ_1 are known, the flow properties of
powders can be expressed numerically as a flowability factor, ff_c , [5]:

$$ff_c = \sigma_1 / \sigma_c$$

40 This parameter is used to classify the powder flowability as indicated in Table 1. Typically ff_c increases
with increasing σ_c , why it is necessary to provide the consolidation stress at which the measurements
are performed [3,12]. Table 2 contains flowability data for selected inorganic powders.

45

Table 1 – Classification of powder flowability by flow index.

Value:	Flow characteristic:
$ff_c < 1$	Not flowing
$1 < ff_c < 2$	Very cohesive
$2 < ff_c < 4$	Cohesive
$4 < ff_c < 10$	Easy flowing
$10 < ff_c$	Free flowing

Table 2 – Mean particle size, Geldart classification and flowability function of selected inorganic powders.

Powder name	Mean particle size [μm]	Geldart classification [13]	Consolidation stress, σ_1 [kPa]	ff_c	Reference
CaCO_3	4.6	C	N/A	1.81	[14]
Cement raw meal A	12.8	C	7.8	2.38	[15]
KCl	481.1	B	N/A	5.75	[14]

50

As mentioned, testing of particle flowability has traditionally been focused on designing silos and hoppers, which are subject to ambient temperatures, atmospheric pressure, varying relative humidity, and storage time [16]. Testing of powders has therefore been performed at these conditions at relevant consolidation stresses. However, in many industrial processes the flow properties at elevated temperatures are of interest, but few tests at elevated temperatures have been reported [16].

55

Pilz [17] constructed a ceramic Jenike-type shear tester for measuring the properties of filter dust from coal combustion up to 850°C, and found that the unconfined yield strength increased with temperature.

Yaojin et al. [18] reports, using a Jenike shear cell, that the flowability of cement raw meal is slightly reduced between 20°C and 700°C, while in the temperature range of 800 – 1000°C, the raw meal

60

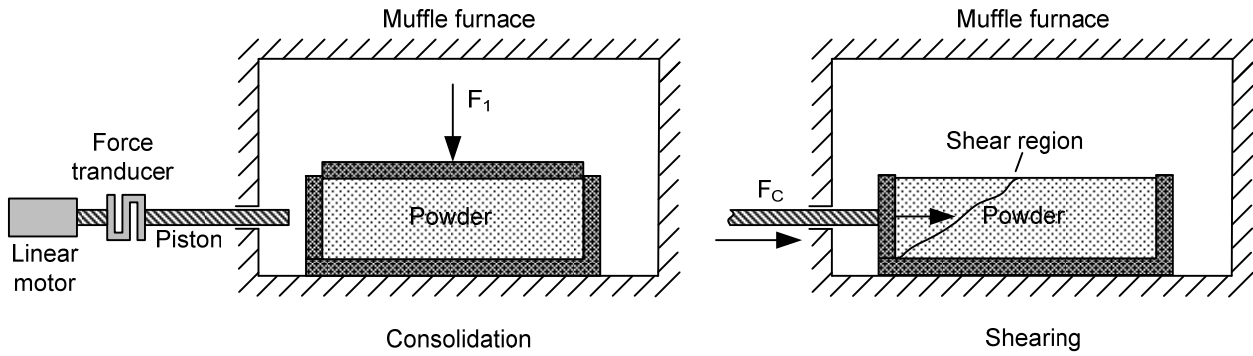
becomes sticky and flowability is significantly deteriorated. Yaojin et al. does not state the reasons for this changed behavior. The sticky tendency is also observed by Telschow [19], who investigated the cement clinker nodulization in a rotary kiln simulator. At 900°C soft nodules of raw meal were formed, indicating significantly changed powder flowability, compared to room temperature behavior. The
65 composition of the nodules showed that calcination of the limestone had taken place and a minor amount (8.5 wt%) of belite (Ca_2SiO_4) had been formed.

For commercial purposes the company *Jenike and Johanson, Inc.* offers flowability testing at temperatures up to 1200°C using modified Jenike cells.

In present work, the powder flowability of cement raw meal is investigated at temperatures up to
70 850°C. Secondly, in order to evaluate the chosen test method, the produced data is compared with data from the more standardized Jenike type shear tester,

2. Equipment

For the purpose of investigating the flowability of cement raw meal at temperatures up to 850°C, a monoaxial shear tester was constructed from high temperature resistant steel. The monoaxial shear
75 test cell was chosen due to its simple geometry, compatibility with an existing muffle furnace, and low cost [3, 16]. However, a major disadvantage of this type of test is the reduced forces due to the anisotropic effects caused by the consolidation and strength measurement not being performed in the same direction and influence of the friction of the sliding wall. A schematic drawing of the system is provided in Figure 1.



80

Figure 1 – Schematic drawing of the monoaxial shear test: Inside a muffle furnace, the sample is consolidated, then after 10 minutes sheared by a piston from outside the furnace wall. Consolidation stress and shearing force are recorded.

85 The powder compartment in the test cell measured 140mm x 100mm x 30mm (length x width x depth) with fixed walls on three sides. The fourth wall is a sliding wall.

The entire setup is placed in a muffle furnace. Through a hole in the side of the furnace, the sliding wall is moved by a piston with a speed of 1mm / s, and the forces exerted by the piston on the sliding wall is continuously recorded at a 100 hertz sampling rate using a tension/compression transducer (S
90 Beam model TCTN-9110, 0 – 50 N). The linear motor driving the piston is a Linak actuator (LA23).

An illustration of the idealized continuous data obtained in each experiment is provided in Figure 2, while an example of actual data is shown in Figure 3.

The powder used was industrial cement raw meal, called Cement raw meal B. Powder specific data are provided in Table 3.

95

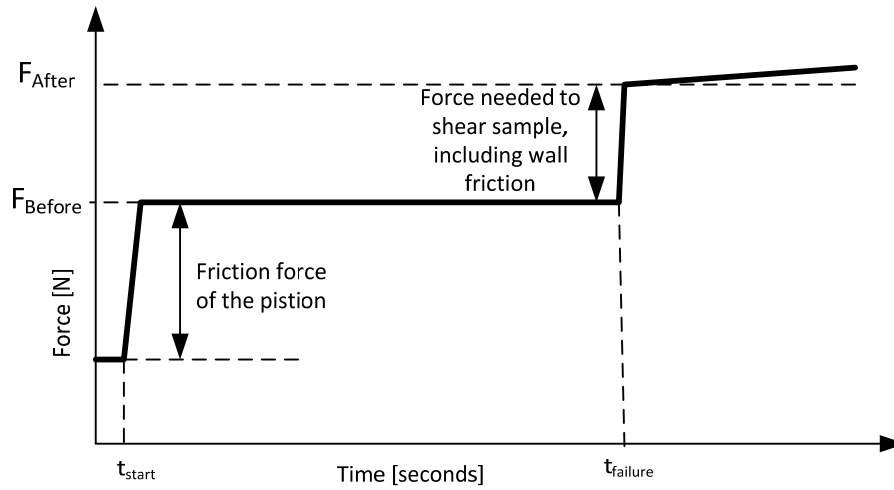
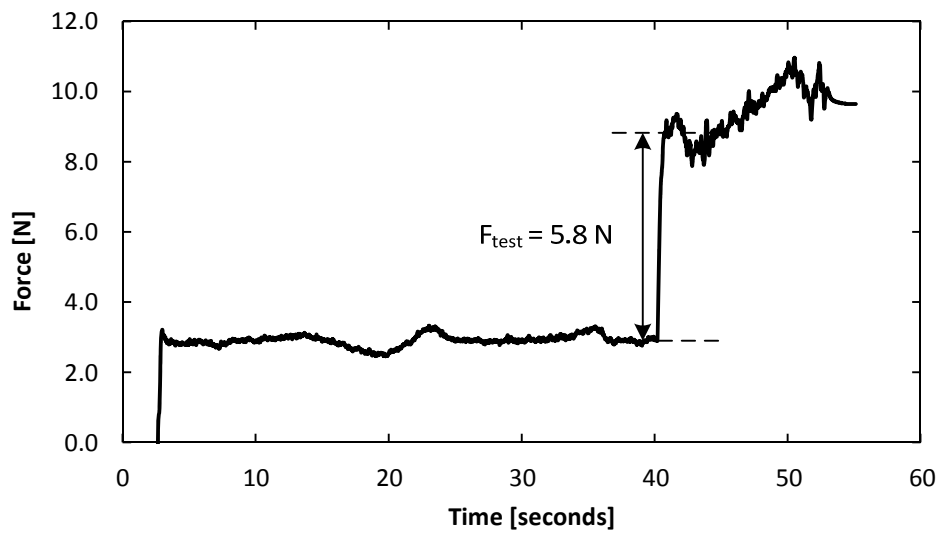


Figure 2 – Idealized continuous force measurement. t_{start} indicates the initiation of the piston movement. $t_{failure}$ indicates the failure of the powder bed.



100

Figure 3- Actual measured data for $T = 550^{\circ}\text{C}$, $\sigma_1 = 2.79 \text{ kPa}$, 1st repetition.

Table 3 – Properties of Cement Raw meal B, [15]

Mean volumetric particle diameter	Packed bulk density	Loose bulk density	Approximate composition	ff_C^A
28.8 μm	1286 kg/m^3	1040 kg/m^3	75 wt% limestone (CaCO_3), 25 wt% clay (mainly SiO_2 , Fe_2O_3 and Al_2O_3)	2.8

^A Measured using a Schulze Ring shear tester at a consolidation stress of 5.8 kPa.

3. Experimental Procedure

150 g of Cement raw meal B is poured into the powder compartment of the test cell and leveled by
105 gently tapping the cell, before the powder level is recorded, before being placed in the preheated
muffle furnace. Consolidation is performed inside the furnace, using different lids corresponding to
consolidation stresses, σ_1 , of 0.94, 1.87, and 2.79kPa. The consolidation time is 10 minutes. Once the lid
is removed, the force required to induce a failure in the powder bed is measured.

At each temperature, a series of references measurements are performed on an empty system
110 enabling correction for the friction of the sliding wall and the piston support. The unconfined yield
strength is given by:

$$\sigma_c = \frac{F_{Test} - F_{System}}{A}$$

Where F is the measured forces, indices *Test* and *System* refer to the powder and reference
measurements, respectively. A is the contact area between the sliding wall and the powder.

115 4. Results

Six temperatures and three consolidation stresses have been investigated. Each powder measurement
is repeated three times, the reference measurements six times.

Pooled variance is used to describe the deviations at each temperature, as the major uncertainty is
assumed to be related to the temperature specific nature of the powder and test cell, and is given as
120 [20,21]:

$$s_p^2 = \frac{\sum_{i=1}^k (n_i - 1) \cdot s_i^2}{\sum_{i=1}^k (n_i - 1)}$$

Where k is the different measurement series, n_i is the number of samples in each series, and s_i is the
variance of each series. Results and computed deviations are provided in Table 4 and Figure 4.

Table 4 – Monoaxial test results of Cement raw meal B at different temperatures.

T [°C]	F _{System} [N]	σ ₁ [kPa]	Area [10 ⁻³ m ²]	σ _c [kPa]			s _p ²
				Repetition #1	Repetition #2	Repetition #3	
22	1.59	0.94	1.89	0.43	0.57	0.23	0,05
		1.87	1.74	0.36	0.62	0.36	
		2.79	1.70	0.71	1.14	1.24	
200	1.12	0.94	1.90	0.11	0.30	0.50	0.31
		1.87	1.78	1.35	1.27	1.24	
		2.79	1.71	0.49	1.65	N/A ^A	
400	2.16	0.94	1.92	0.36	0.16	0.33	0.14
		1.87	1.84	1.01	0.78	0.06	
		2.79	1.78	0.99	0.75	1.15	
550	3.07	0.94	2.00	0.69	0.04	N/A ^A	0.09
		1.87	1.86	0.77	0.68	0.67	
		2.79	1.81	1.52	1.47	1.27	
700	2.80	0.94	2.04	0.89	0.62	0.35	0.11
		1.87	1.88	0.93	1.24	0.77	
		2.79	1.88	1.84	2.21	1.36	
850	4.03	0.94	2.04	4.82	1.86	1.61	2.41
		1.87	1.97	1.11	3.97	2.55	
		2.79	1.95	1.06	3.47	1.32	

^A Conditions replicated twice.

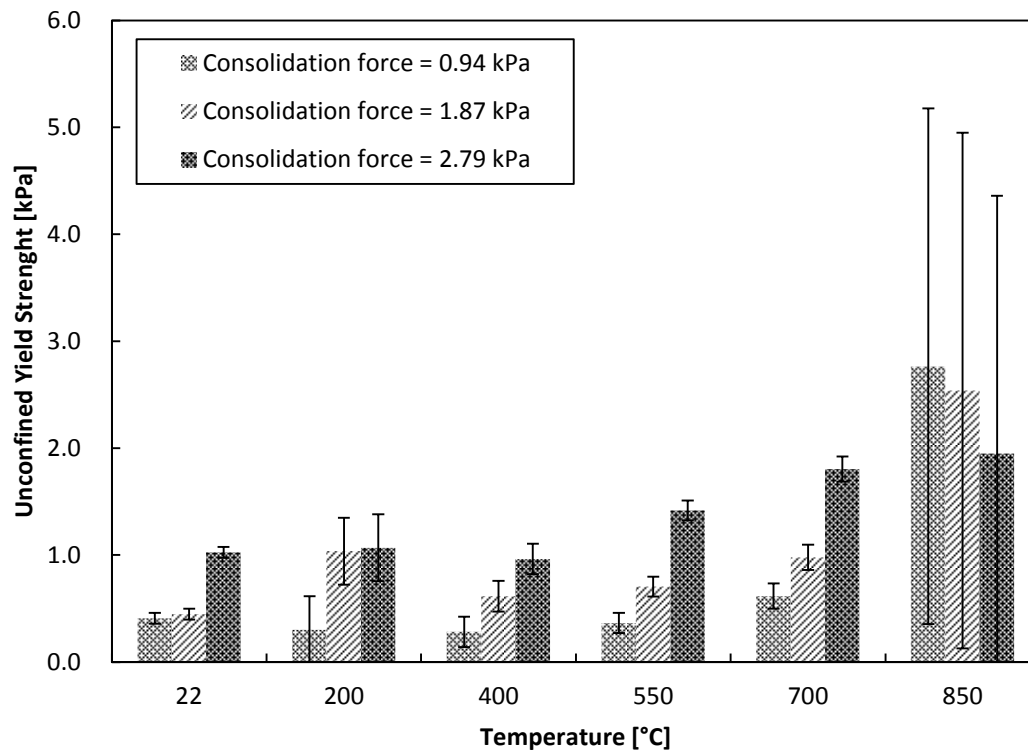


Figure 4 – Measured unconfined yield strength at different consolidation stresses and temperatures of Cement raw meal B. Error bars indicate temperature specific pooled deviations.

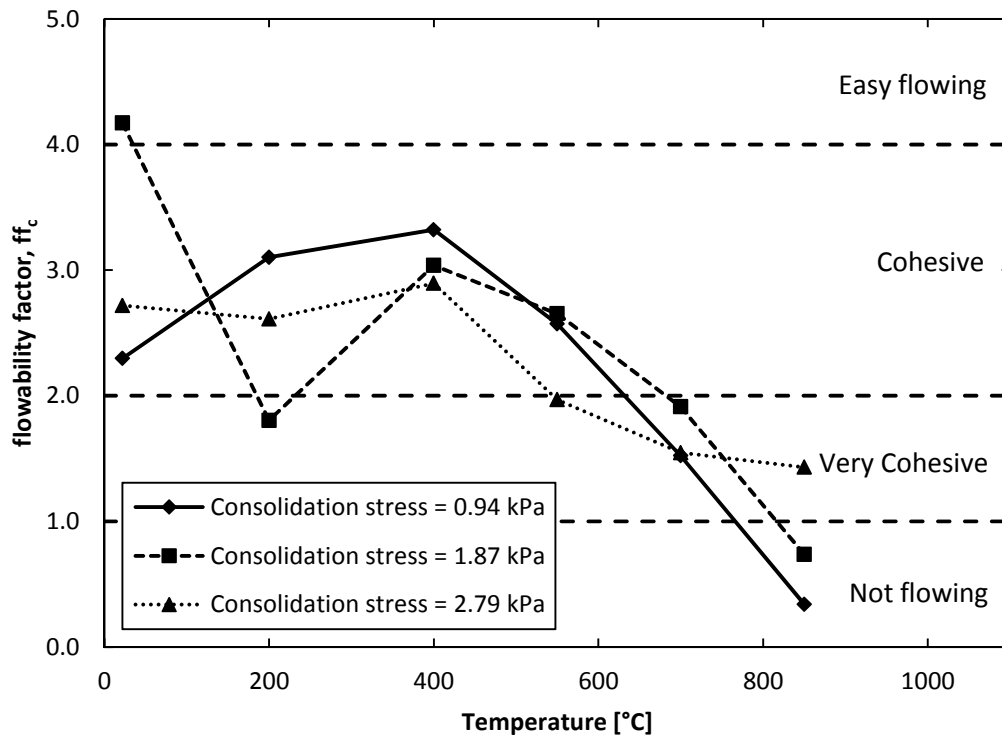
130

The results indicate that the unconfined yield strength is more or less constant until 550°C, where after it increases. Increased consolidation stress increases the unconfined yield strength, as expected. Note the data point $\sigma_1 = 1.87$ kPa at 200°C seems to deviate from the described trends.

135 Reproducibility is acceptable at all temperatures but 850°C. The increased variance at 850°C and the measured force indicate that the flowability of the sample changes significantly between 700°C and 850°C. This is most likely primarily due to initiating belite (Ca_2SiO_4) formation and possible calcination.

If we ignore the anisotropic effects and compute f_{fc} , a classification of the cement raw meal can be made. The results (Figure 5) show that the raw meal sample can be categorized as cohesive in the

140 range from room temperature to 550°C, and as very cohesive/not flowing at 850°C. This trend corresponds with practical observations in the cement industry, suggesting that preheated or calcined raw meal flow more poorly than unheated raw meal. However, it is not yet clear to which degree this is due to calcination, recarbonisation, belite formation, or reaction with components in kiln gases.

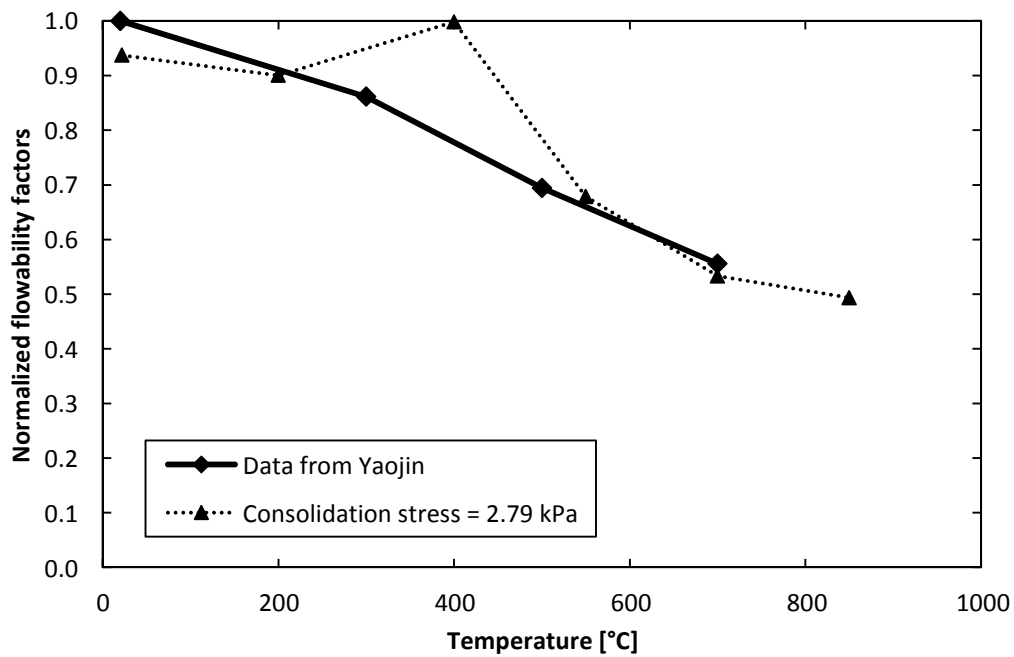


145 **Figure 5** – Flowability functions as a function of consolidation stress and temperature of Cement raw meal B. Powder flowability classifications provided.

5. Discussion

150 Due to the anisotropic effect, the flow factors found using the monoaxial shear tester are expected to be higher than similar measurements performed with a more complete tester, such as the a ring shear tester. Comparable results were obtained with the monoaxial shear tester at 22°C, $ff_c = 2.3 - 4.2$ ($\sigma_c = 0.94 - 2.79\text{kPa}$), and the ring shear tester, $ff_c = 2.8$ ($\sigma_c = 5.9\text{kPa}$). Flowability factors determined using the two different testers should be compared with caution. [3].

Comparing the results of present work with the work of Yaojin et al. [18], similar trends are found in
155 the actual temperature range. A comparison of normalized flowability factors obtained in present
work and by Yaojin et al. [18] is displayed in Figure 6. This indicates that the trends produced using
the monoaxial shear tester are similar to the ones produced using the more complex Jenike shear
tester, thereby enabling hot powders to be classified in a low cost, simple tester.



160 **Figure 6** – Normalized flowability factors from Yaojin et al. [18] compared to the 2.79 kPa data series
of present work displayed as a function of temperature. The data has been normalized to enable
comparison of trends.

The tapping used during preparation of the test cells may cause the particles to interlock with each
165 other, thereby yielding a higher ffc , than obtained in a non-tapped sample. This is, however, not
expected to change the observed trends.

The consolidation stresses applied here, which are lower than in other reported work [2,12,15], are
chosen from two criteria:

1. The consolidation stresses correspond to raw meal layers in the range of 0.1m – 0.3m, which may be found in cyclone preheaters
2. Limited space for applying the consolidation weights inside the muffle furnace, and thereby also size of the lids.

Higher consolidation stresses would have been useful for simulating higher particle levels and reducing the uncertainties. The influence of the low consolidation stress applied, especially $\sigma_1 = 0.94\text{kPa}$, might also be seen from the relative low values of the unconfined yield strength, which is problematic in terms of the signal to noise ratio of the data.

Assuming a reaction in the particle bed takes place, the significant increase in data variance at 850°C can be caused by varying degrees of conversion as a consequence of too short consolidation time, not allowing full conversion in the powder bed. The influence of varying consolidation time has not been further investigated in this work.

The reactions capable of taking place in the powder are either calcination or belite formation. However, further experiments at higher temperatures with simultaneous measurement of carbon dioxide formation, and analysis of the belite content of the sample after testing may clarify the exact mechanisms. In practice, raw meal flowability may be significantly affected by the presence of gaseous components, such as CO_2 , alkali sulfates, and chlorides. Such effects have not been studied in the present work.

6. Conclusion

A simple low cost monoaxial shear tester was constructed for investigating powder flow properties at elevated temperatures. Tests carried out with cement raw meal at three different consolidation stresses, 0.94, 1.87, and 2.79kPa showed that the powder flowability, expressed as either flowability factors or unconfined yield strength is more or less constant from room temperature to 550°C , above which it deteriorates. The reproducibility was satisfactory at all temperatures but 850°C , where large

deviations in the test results were observed. This variance may be due to reactions in the sample, e.g. formation of belite or related to the equipment, e.g. the friction of the sliding wall. The data trends produced with the monoaxial shear tester resembled data trends from Jenike shear tests, confirming that the monoaxial shear tester can be used for high temperature powder classification.

7. Acknowledgement

Acknowledgement is given to Professor Dr.-Ing. Dietmar Schulze for discussions during design of the set-up and evaluation of data, and to M.Sc. Arnau Mestres Rosás for conducting the experiments.

200 Literature cited

- [1] J. Prescott, R. Barnum, On powder flowability, *Pharmaceutical Technology*. October (2000).
- [2] H. Jaeda, *The Use of a Ring Shear Tester to Evaluate the Flowability of Pharmaceutical Bulk Solids*, Heinrich-Heine-Universität Düsseldorf, 2009.
- [3] D. Schulze, *Powders and Bulk Solids*, Springer Berlin Heidelberg, 2008.
- 205 [4] L. Parrella, D. Barletta, R. Boerefijn, M. Poletto, Comparison between a Uniaxial Compaction Tester and a Shear Tester for the Characterization of Powder Flowability, *KONA Powder and Particle Journal*. 26 (2008) 178–189.
- [5] A.W. Jenike, *Storage and flows of solids*, Bull. 123, Engineering Experiment Station, Univeristy of Utah, 1964.
- 210 [6] D.M. Snider, Three fundamental granular flow experiments and CPFDF predictions, *Powder Technology*. 176 (2007) 36–46.
- [7] C. Chen, J. Werther, S. Heinrich, H.-Y. Qi, E.-U. Hartge, CPFDF simulation of circulating fluidized bed risers, *Powder Technology*. 235 (2013) 238–247.
- 215 [8] J. Parker, K. LaMarche, W. Chen, K. Williams, H. Stamato, S. Thibault, CFD simulations for prediction of scaling effects in pharmaceutical fluidized bed processors at three scales, *Powder Technology*. 235 (2013) 115–120.
- [9] D. Schulze, *Flow properties of powders and bulk solids and silo design for flow*, Produktbroschüre, Partec, Nürnberg. (2001) 3–4.
- [10] D. Schulze, *Flow properties of powders and bulk solids*, www.dietmar-schulze.de. (2006).
- 220 [11] I. Wouters, D. Geldart, Characterising Semi-Cohesive Powders using angle of repose, *Particle & Particle Systems*, 13 (1996) 254–259.

- [12] J.J. Fitzpatrick, T. Iqbal, C. Delaney, T. Twomey, M.K. Keogh, Effect of powder properties and storage conditions on the flowability of milk powders with different fat contents, *Journal of Food Engineering*. 64 (2004) 435–444.
- 225 [13] D. Geldart, Types of Gas Fluidization, *Powder Technology*. 7 (1973) 285–292.
- [14] F. Podczeck, Y. Miah, The influence of particle size and shape on the angle of internal friction and the flow factor of unlubricated and lubricated powders, *International Journal of Pharmaceutics*. 144 (1996) 187–194.
- [15] FLSmidth, Laboratory Data, (2011).
- 230 [16] J. Schwedes, Review on testers for measuring flow properties of bulk solids, *Granular Matter*. 5 (2003) 1–43.
- [17] T. Pilz, Zu den Wechselwirkungen bei der Oberflächenfiltration unter besonderer Berücksichtigung der Heißgasreinigung mit keramischen Filtern, Universität Fridericiana Karlsruhe, 1996.
- [18] Z. Yaojin, Y. Li, U. Xuecheng, Preliminary Studies on flowability of cement raw mix at high
235 temperature, *Cement*. 7 (1993).
- [19] S. Telschow, Clinker Burning Kinetics and Mechanism, Ph.D. thesis, Department of Chemical and Biochemical Engineering, Technical Univeristy of Denmark, 2013.
- [20] S. V. Gupta, Measurement Uncertainties, Springer, Berlin Heidelberg, 2012.
- 240 [21] M. Nic, J. Jirat, B. Kosata, A. Jenkins, IUPAC Compendium of Chemical Terminology - The Gold Book, Union of Pure and Applied Chemistry. (2006).